MINISTRY OF EDUCATION AND SCIENCE OF UKRAINE

ODESA STATE ACADEMY OF CIVIL ENGINEERING AND ARCHITECTURE

Pysarenko O. M.

LAMB WAVE-BASED TECHNIQUES FOR NONDESTRUCTIVE MONITORING IN LAYERED COMPOSITES

Monograph

Odesa

OSACEA

2025

UDC 699.88
P 34

Reccomended for publication by the Academic Council
Of the Odessa State Academy of Civil Engineering and Architecture
(Protocol No. 9 of March 20, 2025)

P 34 Pysarenko O.M.

Lamb wave-based techniques for nondestructive monitoring in layered composites :

Monograph. / O.M. Pysarenko. – Odesa. OSACEA, 2025. – 166 p.

ISBN 978-617-8365-09-7

Author:

O. Pysarenko - Associate Professor, Head of the Department of Physics of Odessa State Academy of Civil Engineering and Architecture

Reviewers:

A. Gokhman – Professor of the Department of Applied Mathematics and Informatics of South Ukrainian National Pedagogical University named after K.D. Ushynsky

V. Goczul'skij – Professor, Head of the Department of Physics and Astronomy of Odessa I.I. Mechnikov National University,

The monograph is devoted to the analytical and experimental aspects of using wavelet transforms, namely, Lamb wave transforms, to describe mechanical deformation fields in local volumes of reinforced composite structures. This study examines in detail the issues of detecting mechanical damage at the micro and macro levels. In addition, the results of studies on the propagation, dispersion, scattering, attenuation and interaction of Lamb waves are analyzed. The advantages and disadvantages of the ultrasound scanning technique and the use of piezoelectric sensors for the possibility of detailed recording of local areas of mechanical deformations are analyzed. General issues of monitoring thermal and elastic properties of reinforced composite materials are considered.

Монографія присвячена аналітичним та експериментьальним аспектам використання вейвлет-перетворень, а саме перетворень хвиль Лемба, для опису полів механічних деформацій у локальних об'ємах армованих композитних конструкцій. У даному дослідженні детально розглядаються питання виявлення механісчних деформацій на мікро- та макрорівні. Кпім того, проаналізовано результати досліджень поширення, дисперсії, розсіювання, загасання та взаємодії хвиль Лемба. Проаналізовано переваги та недоліки мтеодики ультразвукового сканування та киористання п'єзоелектричних датчиків для мождивості детальнох реєстрації локальних ділянок механічних деіформацій. Розглянуто загальні питання контролю теплових і пружних влатсивостей армованих композиційних матеріалів.

UDC 699.88
P 34

ISBN 978-617—8365-09-7

CONTENTS

PREFACE

The choice of the topic of this msonography was determined by the extensive use of composite materials in various fields of industry. Research primarily of the mechanical strength of structural elements consisting of composite material most often comes down to the description of the distribution and dynamics of the behavior of micro and macro deformations in the volume and on the surface of composites.

The structure of the monograph includes seven parts. The first, introductory part is devoted to general issues of using wavelet transforms for diagnostics of inhomogeneities of mechanical and thermal fields in the volume of composite material. The second part touches upon issues of using the Lamb transform method in describing mechanical damage in composite materials. The third part of the monograph is devoted to the issues of propagation of Lamb waves. Quantitative characteristics of dispersion, scattering and interaction of Lamb waves are considered in the fourth part of this paper. The use of ultrasound techniques, health monitoring and analytical procedures for modeling wavelet transforms in the study and description of deformations in the volume of reinforced composite structures are considered, respectively, in the fifth, sixth and seventh parts of this study.

CHAPTER 1
INTRODUCTION

The widespread use of composite structures in various industries creates an urgent need for testing and evaluation methods. Such methods could monitor and characterize these complex materials. In addition, as a related goal, it is possible to describe the behavior of such materials during their service life. Numerous experiments and theoretical models have resulted in the development of a wide range of analysis methods, which have been categorized as destructive and non-destructive [1–7]. However, non-destructive methods are often the most attractive, since they do not cause any damage or irreversible changes to the inspected part.

Some non-destructive testing methods are based on Lamb waves. Lamb waves are resonant acoustic excitations guided by the surfaces of a plate structure and are directed along the plate over large distances. These elastic waves are highly dependent on the geometric and material properties of the propagating medium, and thus, the analysis and characterization of Lamb waves propagating in a medium of interest will also help to analyze and understand the medium itself. Non-destructive testing methods using both Lamb waves and body waves have been widely studied in various experimental and theoretical studies for the purpose of characterizing and evaluating various materials and inspecting various structures for any defects or damage [8–14].

Improvement and further development of Lamb wave-based methods can be based on the results of experiments using ultrasonic waves and piezoelectric sensors. In addition, the study of elastic properties, temperature fields and moisture distribution in both laminated and reinforced composite samples can also be significantly improved by using wavelet pre-transformations, including Lamb wave transformations.

A widely used experimental setup for using ultrasound to investigate composite plates is a completely non-contact hybrid system that uses air and laser propagation paths. The results of the experiments form the basis for Lamb wave A0 modes. The method allows the frequency-wavenumber, phase velocity, and group velocity curves for the Lamb wave A0 mode to be measured in anisotropic material quickly using Snell's law and the time-of-flight concept.

The Lamb wave modulation is obtained by imposing a thrust-free boundary condition on the equations of motion. This approach introduces the phenomenon of dispersion, i.e. the wave propagation velocity along the plate is a function of frequency. The dispersion relation of Lamb waves for a linear, homogeneous, and isotropic elastic plate placed in a vacuum, bounded by surfaces $z = \pm h/2$ and infinite in the x and y directions, is given by

$$\frac{\omega^2}{c_T^4} = 4k^2 q^2 \left[1 - \frac{p}{q} \frac{\tan(ph/2 + \gamma)}{\tan(qh/2 + \gamma)} \right], \tag{1.1}$$

where γ = 0 and $\pi/2$ represent *S* and *A* Lamb wave modes,

$$p^2 = \frac{\omega^2}{c_L^2} - k^2, \qquad q^2 = \frac{\omega^2}{c_T^2} - k^2, \tag{1.2}$$

k is the waqvenumber;
ω is the angular frequency;
c_L and c_T are longitudinal and transverse velocities inside the plate, respectively.

Equations (1.1) and (1.2) are written for the time-harmonic wave motion corresponding to the plane strain in the (*x*, *z*) plane of the given plate. In addition, the directed wave field is represented by a propagating wave in the *x* direction and a standing wave in the *z* direction.

Wave interactions depend on the properties of the components, geometry, direction of propagation, and frequency for waves propagating in multilayer composites. The exact dispersion relations of symmetric and antisymmetric wave modes in a plate can be formulated from three-dimensional elasticity theory. The formulation can then be extended to composite laminates with arbitrary stacking sequences. In a single plate, the closed-form dispersion relation relating *x* and *k* in a fixed propagation direction is

$$\begin{aligned} &H_{11}(H_{22}H_{32} - H_{23}H_{32})\tan(\xi_1 h/2 + \varphi) + \\ &+ H_{12}(H_{23}H_{31} - H_{21}H_{33})\tan(\xi_2 h/2 + \varphi) + \\ &+ H_{13}(H_{21}H_{32} - H_{22}H_{32})\tan(\xi_3 h/2 + \varphi) = 0, \end{aligned} \tag{1.3}$$

where φ = 0 and $\pi/2$ represent anti-symmetric and symmetric Lamb wave modes, respectively;
h is the thickness of the single lamina;
ξ_j (j = 1, 2, 3) are the fixed variables;
H_{ij} are quantities that are given by equations

$$H_{1j} = C_{13}k_x + C_{23}k_y R_j + C_{33}\xi_j S_j + C_{36}(k_y + k_x R_j), \tag{1.4}$$

$$H_{2j} = C_{44}(\xi_j R_j + k_y S_j) + C_{45}(\xi_j + k_x S_j), \tag{1.5}$$

$$H_{3j} = C_{45}(\xi_j R_j + k_y S_j) + C_{55}(\xi_j + k_x S_j), \tag{1.6}$$

where
C_{ij} are the elements of the stiffness matrix;

$k_x = k\cos(\phi)$; $k_y = k\sin(\phi)$;

ϕ is the direction of wave propagation in the lamina composite;

R_j, S_j are the real-value coefficient related to the displacement coefficients, elements of stiffness matrix, wavenumbers, frequency and material density.

The Lamb wave velocity can be used to analyze the properties of composite materials. The phase velocity vector using the following formula

$$c_p = \frac{\omega \vec{k}}{k^2}, \tag{1.7}$$

in turn, the modulus of the phase velocity of the Lamb wave is equal to

$$c_p = \frac{\omega}{k}, \tag{1.8}$$

where $\vec{k}$ is the wave vector.

The phase velocity depends only on the wave vector, its modulus and, consequently, the direction of wave propagation in the medium. In isotropic materials, c_p depends only on the modulus of the wave vector $\vec{k}$.

The group velocity (c_g), on the other hand, is defined as

$$c_g = grad_k\left[\omega\left(\vec{k}\right)\right] . \tag{1.9}$$

This velocity has components in the x and y axes as c_{gx} and c_{gy}, respectively, and corresponds to the following matrix

$$\begin{bmatrix} c_{gx} \\ c_{gy} \end{bmatrix} = \begin{bmatrix} \cos\varphi & -\sin\varphi \\ \sin\varphi & \cos\varphi \end{bmatrix} \begin{bmatrix} d\omega/dk \\ d\omega/kd\varphi \end{bmatrix}. \tag{1.10}$$

Under these conditions, the amplitude of the group velocity is equal to

$$c_g = \sqrt{c_{gx}^2 + c_{gy}^2} . \tag{1.11}$$

For the simplest case of an isotropic composite material, it can be concluded that since ω is a function of k only and thus $\partial\omega/\partial\phi = 0$ then the magnitude of the group velocity is

$$c_g = \frac{\partial\omega}{\partial k}. \tag{1.12}$$

In experimental studies, the presence of an air-coupled transducer allows the generation of Lamb waves in composite laminates. The system of control equations is written under the assumption that the laminated composite sample can be considered as an infinite plate immersed in a non-viscous liquid (air). Thus, the plate is excited by a volumetric ultrasonic wave propagating in the air and hitting the boundary between the air and the plate at a certain fixed angle θ.

Partial reflection followed by escape into the air half-space above the plate and partial refraction into the plate is observed when a body wave in air with wave number k_i collides with the surface of the composite plate. The interference of the longitudinal and shear volume Lamb waves generated in the plate, refracted by the upper and lower surfaces of the plate, will be observed along the *x*-direction.

The Lamb wave has a wave number *k*. The horizontal projection of the wave number of the incident wave is k_x. Since $k_x = k_i \sin h$, then

$$k = k_i \sin\theta \qquad (1.13)$$

and

$$k_i = \frac{\omega}{c}, \quad k = \frac{\omega}{c_p}, \qquad (1.14)$$

where *c* is the speed of sound.

In this case

$$\sin\theta = \frac{c}{c_p}. \qquad (1.15)$$

Since the dispersion pattern in Lamb modes depends on the frequency, identifying specific symmetric and antisymmetric modes greatly simplifies the analysis. Experimental methods for detecting damage in structures using Lamb waves estimate the time of flight of scattering waves for damage. At subsequent stages of analysis, the location and size of damage in the volume of the composite sample are determined from the numerical values of phase and group velocities.

The experimental implementation of the hybrid non-contact system includes an air-coupled transducer that generates ultrasonic pressure incident on the surface of a composite plate. The incident pressure waves are partially reflected and partially refracted in the plate, generating longitudinal and shear waves. The out-of-plane velocity measurement of the propagating Lamb wave mode, formed at some distance from the excitation region, is carried out using a laser Doppler vibrometer.

The characteristic dispersion dependencies for the phase c_p and group c_g velocities are given in Figures 1.1 - 1.4.

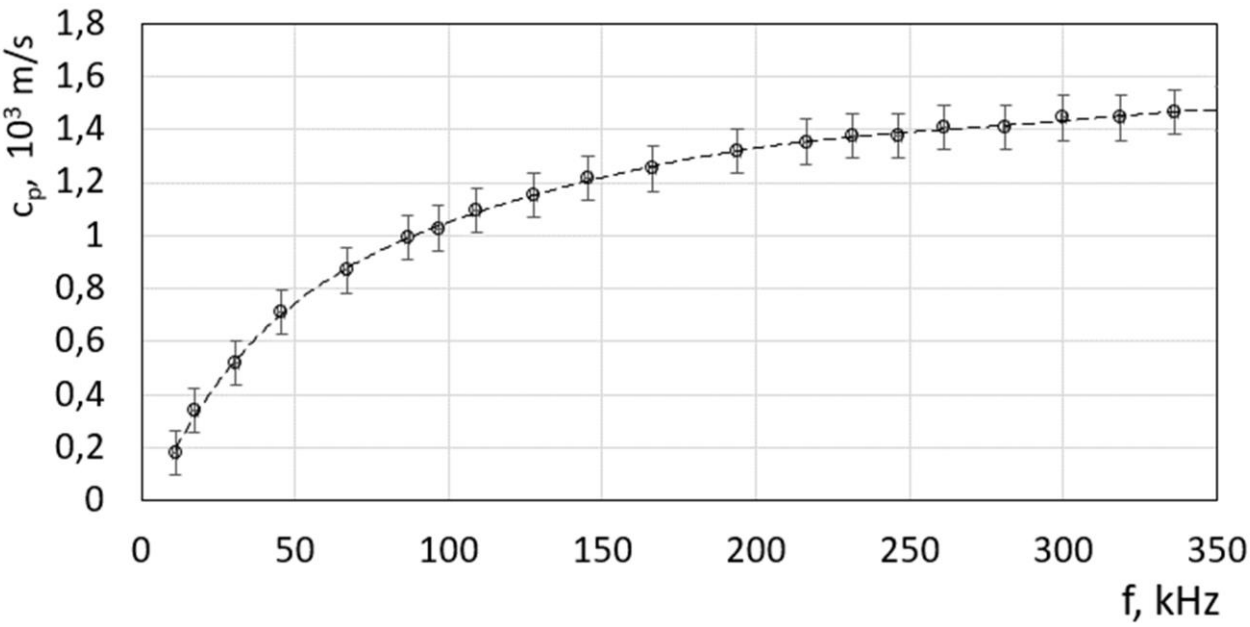

Figure 1.1. Phase velocity dispersion curve $c_p = c_p(f)$ for *A0* mode along 45^0 propagation direction.

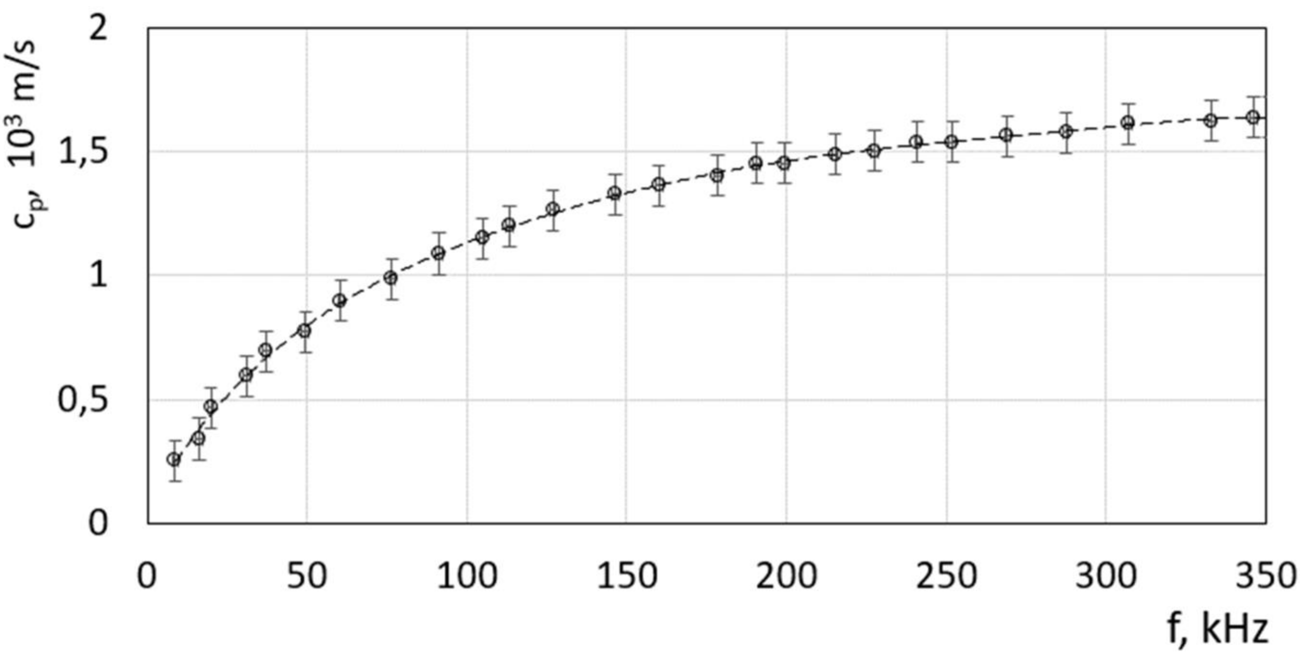

Figure 1.2. Phase velocity dispersion curve $c_p = c_p(f)$ for *A0* mode along 90^0 propagation direction.

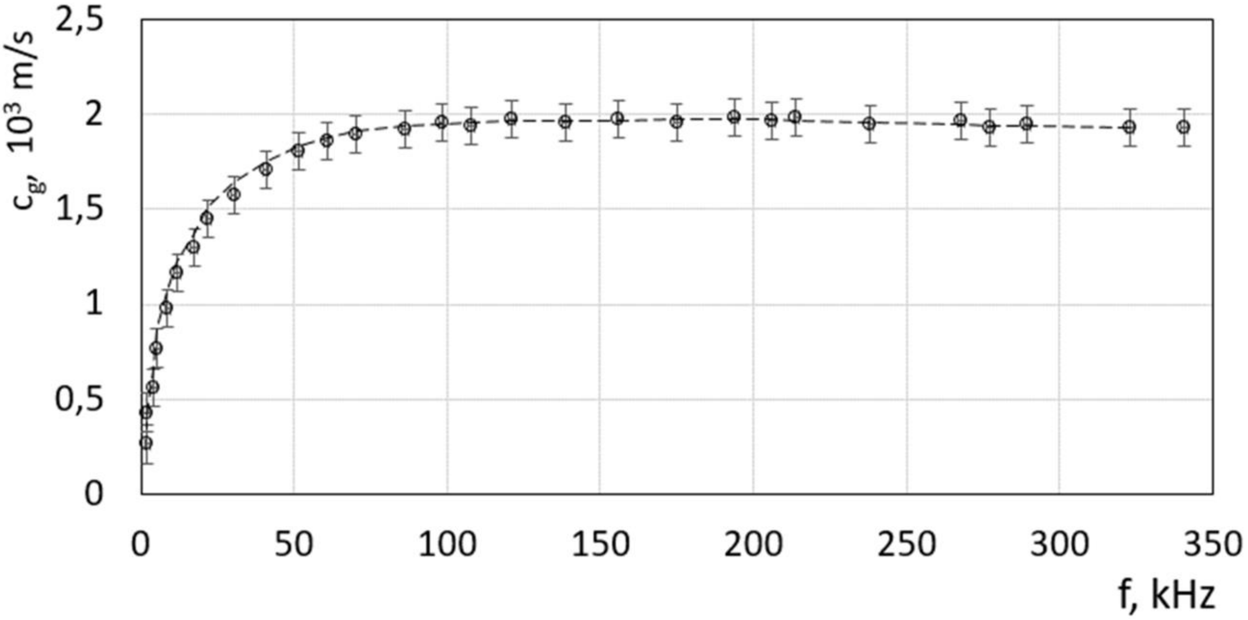

Figure 1.3. Group velocity dispersion curve $c_g = c_g\ (f)$ for *A0* mode along 45^0 propagation direction.

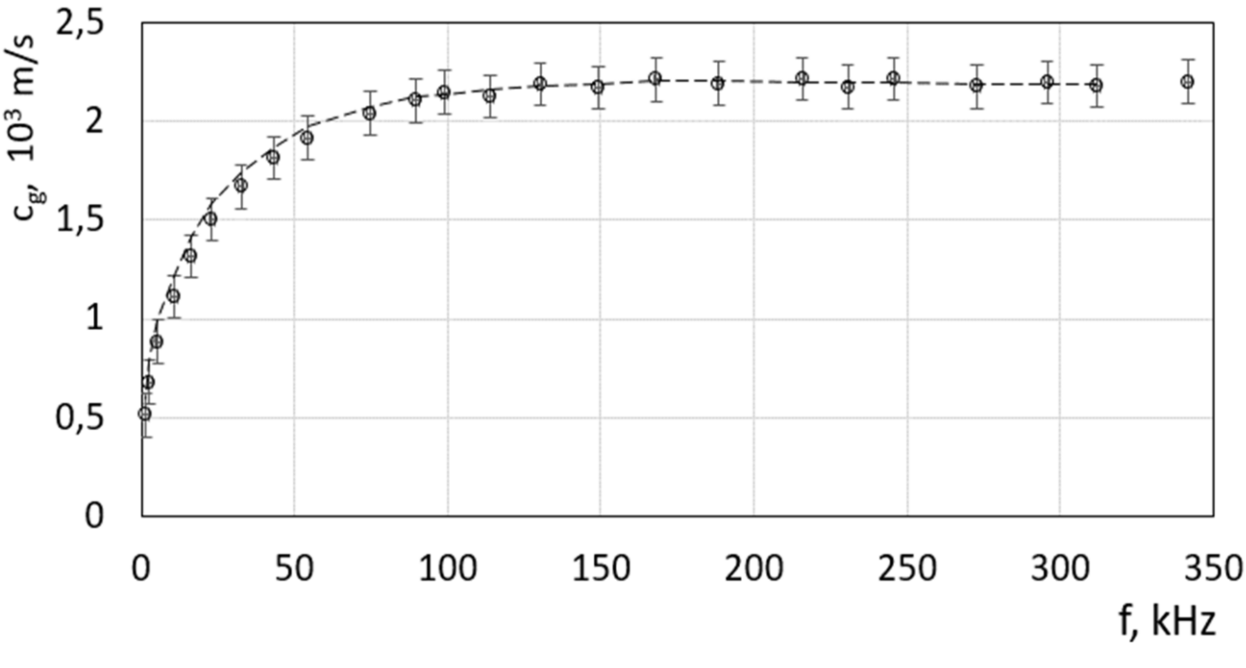

Figure 1.4. Group velocity dispersion curve $c_g = c_g\ (f)$ for *A0* mode along 90^0 propagation direction.

To obtain the group velocity dispersion curve for a given wave propagation direction, the time of flight of wave packets was analyzed. In particular, the Morlet wavelet transform was used to automatically process the received Lamb wave signals in order to improve the accuracy of the time of flight. The time of reaching the maximum is related to the arrival time of the Lamb wave mode A0. The first step of the calculation uses the Morlet wavelet as the mother wavelet, and then divides the propagation distance by the arrival time, which is the time difference between the first and second stored times from the mother wavelet transform. Polar group velocity curves (wave curves) were obtained using the mother wavelet transform method along different propagation directions inside the composite with a step of 15^0. The characteristic wave curves of the laminate for the Lamb wave mode A0 are obtained for different central frequencies. The results clearly indicate the angular dependence of the A0 mode in the laminate with its maximum group velocity along the 0^0 and 45^0 directions.

Currently, researchers are paying attention to the creation of new effective computational methods for calculating the stress-strain state of structures made of composite materials. In addition, for practice, a mandatory addition is the development of non-destructive testing methods and methods for monitoring the technical condition of structures, which are usually based on the analysis of the propagation of elastic waves in layered media. The use of direct numerical methods (in particular, the finite difference method) for modeling composite structures is the most universal approach [15-22]. This approach is aimed at obtaining an approximate solution for objects of any shape. It should be noted that computational methods of this type are the most computationally expensive. An increase in the number of elements is inevitable in areas of rapid changes in solutions or environmental characteristics (corner points, interfaces between contrast layers, etc.) and especially in the case of high frequencies.

One of the successful methods for describing mechanical stresses is the construction of the Fourier transform of the Green's matrix, the poles of which determine the wave numbers of a composite consisting of N anisotropic layers, as well as the study of the dispersion characteristics of the layered structure. he algorithm for recursively calculating the Fourier transform of the Green's matrix requires only the procedure of inversion of 6 x 6 matrices for any number of layers in the composite. This approach allowed us to obtain curves and surfaces describing the wave numbers, phase velocities, and group velocities of the wave front of Lamb waves. The set of Lamb waves can be considered as a network of wave packets that propagate in symmetric and antisymmetric composites with respect to the direction of propagation and the oscillation frequency. Wave packets propagate in an elastic medium and excite deformations that contain all three components of the displacement vector. The basic equations of elasticity theory for each of the three-dimensional layers of a non-uniform anisotropic multilayer (packet of N layers) elastic medium have the form

$$\frac{\partial\sigma_{ij}^{(n)}}{\partial x_i}=\rho^{(n)}\frac{\partial^2 u_j^{(n)}}{\partial t^2}, \qquad (1.16)$$

where j = 1, 2, 3; n = 1, … , N.

The composite sample has a volume of $\infty \leq x$, $y \leq \infty$, $z_{N+1} \leq z \leq 0$, where z_{N+1} is the distance from the lower boundary of the N-th layer to the upper surface, $z_1 = 0$, $\rho^{(n)}$ is the density of the n-th layer. The layer number will be designated by a superscript. The relationship between mechanical stresses and deformation can be described by the equations of the linear theory of elasticity

$$\sigma_{ij}^{(n)}=C_{ijkm}^{(n)}\varepsilon_{km}^{(n)}, \qquad (1.17)$$

where $C_{ijkm}^{(n)}$ is a the stiffness tensor of the n-th layer.

When the coordinate system changes, the tensor coordinates change according to the formula

$$C_{ijkm}^{(n)}=a_{pi}a_{qi}a_{rk}a_{ml}C'^{(n)}_{parl}, \qquad (1.18)$$

where $C'^{(n)}_{pqrl}$ are the coordinates of the stiffness tensor with respect to one coordinate system;
a_{ij} is a 3 x 3 rotation matrix.

The wave characteristics of the composite according to such a model will be determined by the physical characteristics of the layers and the oscillation frequency. In addition, the characteristics of the wave packets and the direction of their propagation in the composite also depend on the direction of the applied load and the local calculated form for the volume of the composite structure.

The calculation model uses a two-dimensional Fourier transform of the displacement vector of the n-th layer $u^{(n)}(x, y, z)$

$$U_j^{(n)}(\alpha_1,\alpha_2,z)=F\left[u_j^{(n)}\right]=\int_{-\infty}^{\infty}\int_{-\infty}^{\infty}u_j^{(n)}(x,y,z)\exp[i(\alpha_1 x+\alpha_2 y)]dxdy. \qquad (1.19)$$

Fourier transforms allow us to write the following matrix relations

$$S^{(1)}U^{(1)}\Big|_{z=z_1}=Q, \qquad (1.20)$$

$$\frac{dU^{(n)}}{dz} = A^{(n)}U^{(n)}, \tag{1.21}$$

$$\left[B^{(n)}U^{(n)} - B^{(n+1)}U^{(n+1)}\right]\Big|_{z=z_{n+1}} = 0, \quad n = 1,\dots,N-1, \tag{1.22}$$

$$S^{(n)}U^{(n)}\Big|_{z=z_{n+1}} = 0, \tag{1.23}$$

where $U(n)$ is the Fourier transform of the vector of displacement components and their ordinary derivatives with respect to z

$$U^{(n)} = \left\{U_1^{(n)}, U_2^{(n)}, U_3^{(n)}, U'^{(n)}_1, U'^{(n)}_2, U'^{(n)}_3\right\}. \tag{1.24}$$

$$A^{(n)} = \begin{pmatrix} 0 & 1 \\ A^{(n,20)-1}\tilde{A}_1 & A^{(n,20)-1}\tilde{A}_2 \end{pmatrix}, \tag{1.25}$$

where

$$\tilde{A}_1 = A^{(n,01)}\alpha_1^2 + A^{(n,02)}\alpha_2^2 + A^{(n,03)}\alpha_1\alpha_2 - A^{(n,04)}, \tag{1.26}$$

$$\tilde{A}_2 = i\left[A^{(n,11)}\alpha_1 + A^{(n,12)}\alpha_2\right], \tag{1.27}$$

where
$A^{(n,ik)}$ are the matrices with elements $C_{ik}^{(n)}$;
$B^{(n)}$ are matrices that characterize the interaction of layers.

The matrices $A^{(n)}$, $B^{(n)}$ depend only on the material properties of each layer, the oscillation frequency ω and the Fourier variables α_1 and α_2.

The method presented here is related to a linear problem, therefore it is possible to expand the Fourier transform of the displacement component vector with respect to the components of the applied load $Q = \{Q_1, Q_2, Q_3\}$ as follows

$$U^{(n)}(\alpha_1,\alpha_2,z) = U_1^{(n)}(\alpha_1,\alpha_2,z)Q_1 + U_2^{(n)}(\alpha_1,\alpha_2,z)Q_2 +$$

$$+U_3^{(n)}(\alpha_1,\alpha_2,z)Q_3 = \sum_{p=1}^{3} U_p^{(n)}Q_p\,. \tag{1.28}$$

For each layer n in the Fourier domain, the solution to this problem can be represented in matrix form

$$U^{(n)}(\alpha_1,\alpha_2,z)=K^{(n)}(\alpha_1,\alpha_2,z)Q(\alpha_1,\alpha_2), \qquad (1.29)$$

where $K^{(n)}$ is the Green's matrix of the problem.

The displacement vector $u(n)$ gives the solution to the problem as a result of the inverse Fourier transform to the displacements $U(n)$ found in the Fourier domain

$$u^n(x,y,z)=F^{-1}\left[U^{(n)}\right]=\frac{1}{4\pi^2}\int_{-\infty}^{\infty}\int_{-\infty}^{\infty}U^{(n)}(\alpha_1,\alpha_2,z)\exp\left[-i(\alpha_1 x+\alpha_2 y)\right]d\alpha_1 d\alpha_2\,. \qquad (1.30)$$

The phase velocity of the mode k can be found via

$$c_p^{(k)}(\omega,\gamma)=\frac{\omega}{\zeta^{(k)}(\omega,\gamma)}, \qquad (1.31)$$

and the partial derivative is defined as a group velocity for a direction γ by

$$\frac{\partial\omega}{\partial\zeta^{(k)}(\gamma,\omega_0)}=\frac{\omega_1-\omega_0}{\zeta^{(k)}(\omega_1,\gamma)-\zeta^{(k)}(\omega_0,\gamma)}. \qquad (1.32)$$

The calculation method is based on the consideration of dimensionless frequencies $\omega h/cT$ and dimensionless velocities c_p/c_T, with which symmetric and antisymmetric modes propagate. The wave packet velocity vectors were located in two directions: in the xy plane at an angle of $c = p/6$ relative to the x axis, and along a straight line at an angle of $c = p/4$ to the x axis in the xy plane. A significant number of studies on the features of Lamb wave propagation in composite structures analyzed the phase velocity graphs depending on the propagation directions for fixed numerical values of the dimensionless frequency xh/c_T (in particular, for the dimensionless frequency, the following values can be specified: 4 and 1.78). The theoretical analysis of the propagation features of Lamb waves is conveniently performed for the following package of dimensionless quantities: dimensionless frequency xh/c_T, dimensionless wave numbers $\zeta\cdot h$, dimensionless phase velocity c_p/c_T and dimensionless group velocity of the wave front c_g/c_T, where x is the angular frequency in rad/s, h is the total thickness of the composite, f are the dimensional wave numbers, c_p, c_g are the phase and group velocities.

The dispersion curves for the propagation of wave groups are characterized by dimensionless propagation velocities c_p/c_T of symmetric and antisymmetric modes for dimensionless frequency xh/c_T. he change in phase velocities depending on the direction of propagation was characterized by the values of the dimensionless frequency xh/cT equal to 3.4 and 1.72, respectively.

The numerical method considered is quite universal and allows uniformly study not only Lamb waves, but also any oscillations in a package of anisotropic layers with arbitrary elastic anisotropy and arbitrary spatial orientation. This theoretical analysis for each layer in a large frequency range based on a single formalism uses the Fourier transform of the Green's matrix. The formalism considered here, despite its redundancy for the task of studying dispersion curves, is quite universal. The numerical method allows one to study in detail practically any combination of elastic characteristics of a layer package, their alternation, orientation, type of symmetry, etc.

It should be noted that various combinations of layers consisting of only one material can be considered as elastic waveguides with different properties. The change in the sequence of mutual orientation of the layers had only a slight effect on the nature of the phase velocity surfaces and group wave surfaces. In some cases, changing the mutual orientation of the layers and the number of layers led to the appearance of a noticeable anisotropy of their characteristics, in other cases to almost complete anisotropy. For almost all experiments, the A0 mode had a pronounced dispersion of phase velocities and a wave front group in the low-frequency range. On the other hand, for the S0 and SH0 modes, the group and phase velocities were practically independent of frequency, but they exhibited a more pronounced anisotropy.

The occurrence of multivalued group velocities of the wave front in the low-frequency range was quite typical for non-quasi-isotropic composite stackings. Experimenters and analysts expect that such a feature may manifest itself for most directions. ncreasing the number of wave packet modes for the high-frequency range does not require a change in the calculation methodology, but leads to a significant increase in the computational load.

Structural components made of composite materials are widely used in various industries. The reasons for this popularity include the following advantages over conventional metallic materials: higher strength-to-weight ratio and higher stiffness-to-weight ratio [23-25]. However, normal service conditions of structures involve frequent changes in environmental conditions such as temperature. During thermal cycling, thermal stresses are generated in composite laminates. Cyclic thermal stresses can cause damage. These damages and deformations are similar to those observed under mechanical cyclic loading, namely transverse matrix cracks, delamination. In addition, the need for long-term service life of composite parts and the importance of operational safety should be taken into account. Even small damages accumulated due to thermal fatigue often pose a great danger to preventing unpredictable catastrophic failures caused by microdamages. The combination of these factors is the reason why non-destructive detection of thermal fatigue at an early stage is of great importance in the long-term operation of composite parts and structures.

The most promising tool for non-destructive testing of the quality and integrity of structures, especially those made of laminar composites, is the ultrasonic wave technique based on the use of Lamb waves. However, most of both experimental and theoretical methods were limited to using the linear characteristics of Lamb waves only for detecting macrodamages located within local areas in the volume of the composite [26-28]. Linear ultrasonic wave methods are less sensitive to detecting microdefects. Therefore, special attention has been paid to the development of nonlinear ultrasonic techniques as a potential means for detecting microdefects. The few studies have focused mainly on the use of nonlinear elastic wave spectroscopy to assess impact damage in composite materials. The nonlinear elastic wave approach has been shown to be more sensitive to microdamage than linear acoustic methods. The high sensitivity of the nonlinear ultrasonic approach and the advantages of the nonlinear Lamb wave method have attracted considerable attention. In particular, nonlinear ultrasonic Lamb waves have been successfully used to assess microdamage in metallic structures. However, the use of nonlinear ultrasonic Lamb waves has rarely been applied to detect microdamage in composite structures. An obstacle in applying the nonlinear technique to composites is that it becomes difficult to control the tiny second harmonic amplitudes reliably in highly attenuated composites. Furthermore, the dispersive and multimode nature of Lamb modes potentially complicates efficient second harmonic generation.

Consequently, the studies on the application of nonlinear methodology to composite structures have focused on the study of the second harmonic generation characteristics of Lamb wave propagation in laminar composites. In particular, the Lamb mode “phase matching” method was chosen to detect the second harmonic. The difficulties arising from the multimode nature of Lamb wave propagation were overcome by using the group delay approach. This technique allowed the thermal fatigue damage to be assessed in the specimens. Composite specimens were subjected to artificial thermal fatigue to simulate the effect of temperature change in operational composite structures. A correlation was found between the acoustic nonlinear parameter and thermal cycles. In studies using a similar technique, the sensitivity thresholds of linear and nonlinear ultrasonic parameters to thermal fatigue damage were estimated.

A nonlinear phenomenon in which the propagation of a monochromatic ultrasonic wave over a certain distance in a composite material with nonlinear characteristics leads to the generation of an additional two-frequency harmonic wave is called second harmonic generation. The dispersive nature of Lamb waves results in the second harmonic generation effect being quite weak. An important step in the calculation method is to describe the second harmonic generation together with the cumulative propagation of Lamb waves. In this case, the cumulative effect of the second harmonic amplitude allows the nonlinear effect to be measured with a sufficient signal-to-noise ratio. The second harmonic modes of Lamb waves exhibit a cumulative effect under the conditions of "phase matching" and non-zero power transfer from the fundamental mode to the second harmonic. Except for A0 and S0, the two fundamental Lamb modes in the plate structure, all other modes satisfy the non-zero power flow condition.

The mode with the minimum characteristic frequency is selected for the study as the fundamental frequency mode, since this mode satisfies the phase matching condition. This condition results in the two-frequency Lamb mode (S2 mode) being generated by the cumulative effect. The two-frequency Lamb wave, based on the fundamental mode S1, has the same phase velocity and group velocity. This factor was the reason for the combined analysis of both the fundamental mode (mode S1) and the two-frequency second harmonic Lamb mode (mode S2).

For the experimental generation of Lamb waves, a laboratory technique of combining a piezoelectric transducer and a wedge was used. The angle of incidence for the generation of Lamb wave modes was determined by Snell's law

$$c_p = \frac{c_1}{\sin\theta}, \tag{1.33}$$

where

c_1 is the longitudinal wave velocity in the wedge material;

c_p is the phase velocity of the Lamb mode;

θ is the incident angle.

Experimental studies have shown that the generation of the S1 mode is correlated with the generation of the A1 mode. The reason for this correlation is their relative proximity to each other in the phase velocity dispersion curve. This, in turn, is due to the multimode nature of Lamb wave propagation. However, the group velocity of the S1 mode is very different from that of the A1 mode, since it is noticeably faster than A1. It is found that after the multimode signal propagates for a certain distance, the S1 wave packets containing the dual-frequency content of the S2 and A1 modes are eventually separated.

If the propagation distance is short, the multimodes will not be separated correctly. As the propagation distance increases, the mode separation becomes visible, since the time-of-flight gap due to the group velocity difference becomes noticeable. As a result, only a portion of the S1 mode can be selectively selected.

Therefore, the frequency spectrum analysis for filtering the second harmonics is performed within a time gate placed above the S1-S2 wave packet, maintaining a propagation distance comparable to the dimensions of the composite sample to avoid the influence of A1 and other modes. The measured signal generated by the Lamb wave in the time domain is processed by the fast Fourier transform to obtain the frequency spectrum. The frequency spectrum allows us to analyze the behavior of the amplitude of the fundamental Lamb mode S1 (A1) and the two-frequency second harmonic of the mode S2 (A2).

Spectral dependences for the phase and group velocity of Lamb wave modes are illustrated in Figures 1.5 - 1.10 ($c'_p = c_p / c_{ch}$, $c'_g = c_g / c_{ch}$, $f' = f / f_{ch}$, where c_{ch} and f_{ch} are the characteristic speed and frequency, respectively).

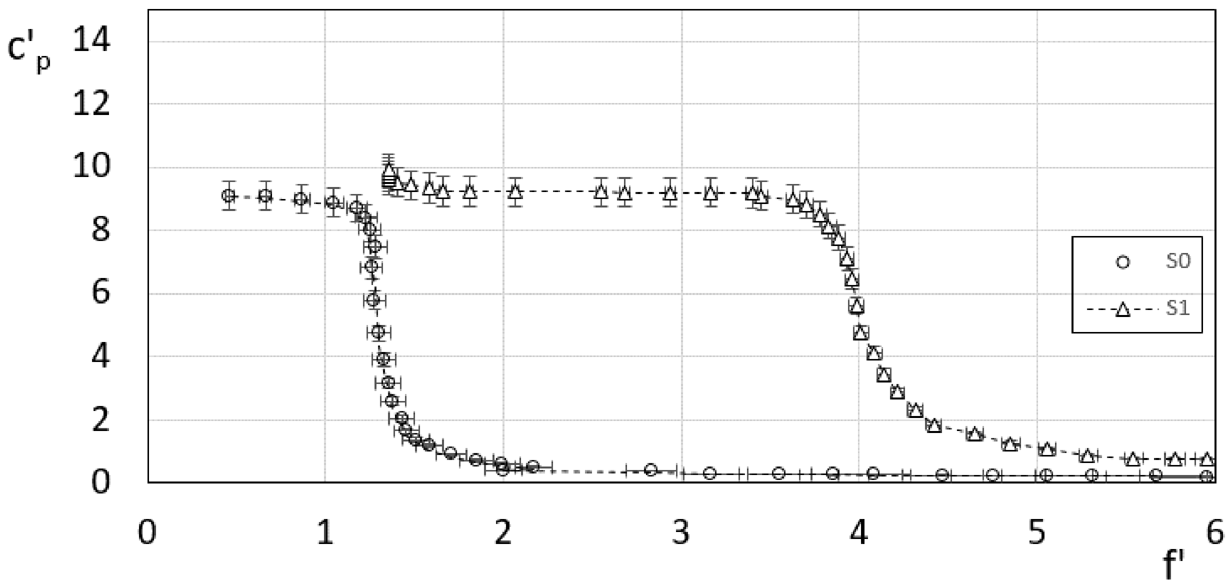

Figure 1.5. Phase velocity dispersion curve $c'_p = c'_p(f')$ for *S0 and S1* modes of Lamb wave.

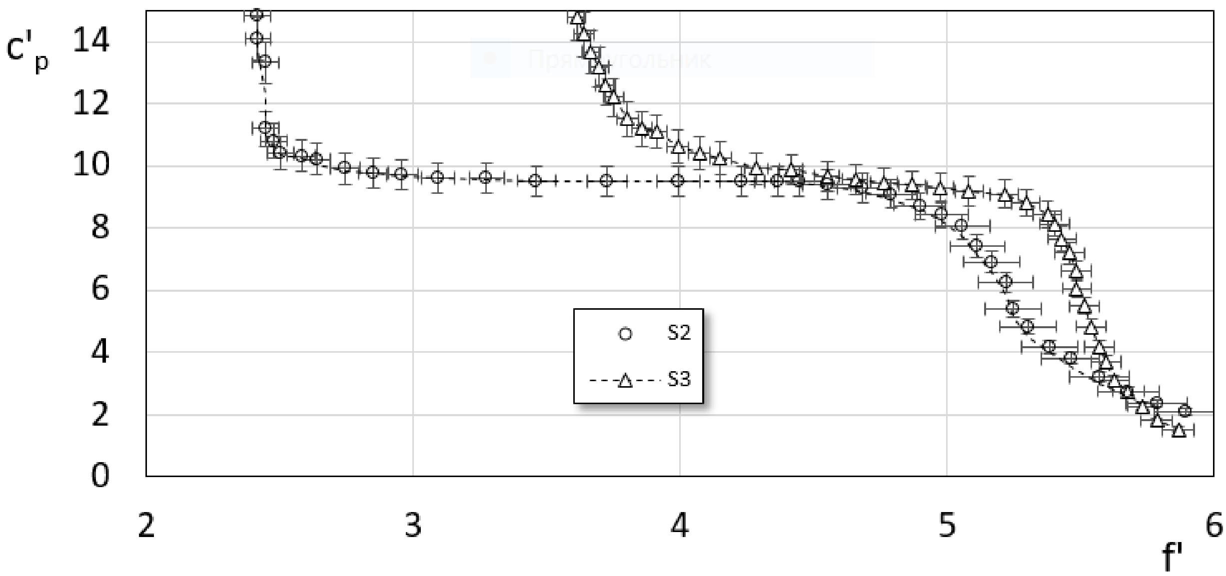

Figure 1.6. Phase velocity dispersion curve $c'_p = c'_p(f')$ for *S2 and S3* modes of Lamb wave.

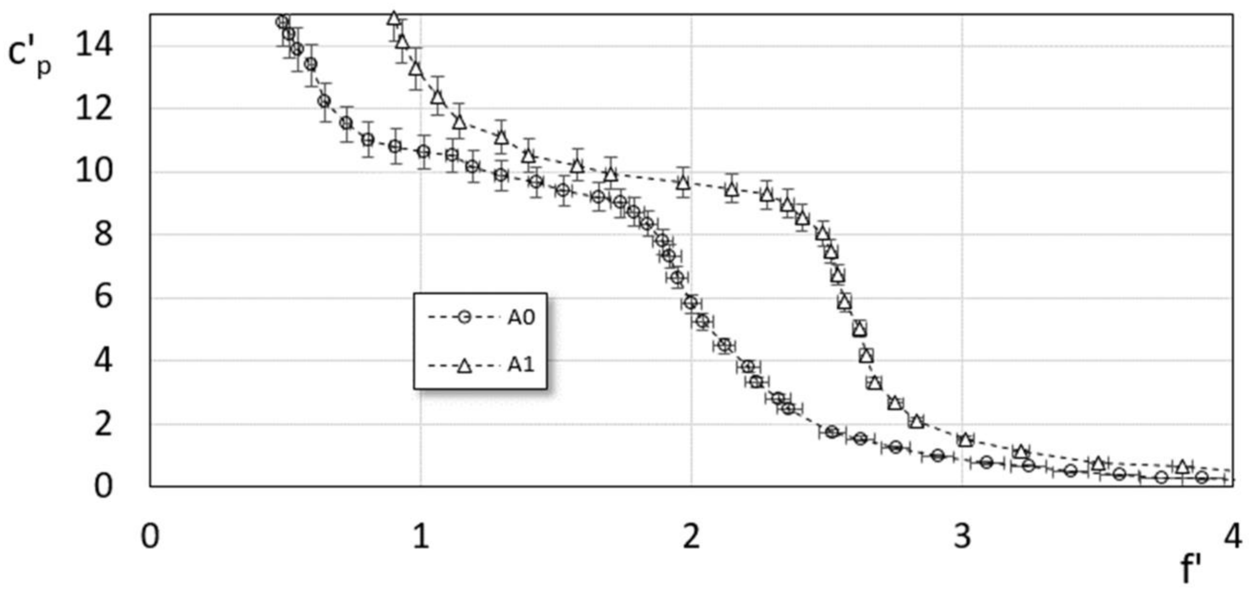

Figure 1.7. Phase velocity dispersion curve $c'_p = c'_p\,(f')$ for *A0 and A1* modes of Lamb wave.

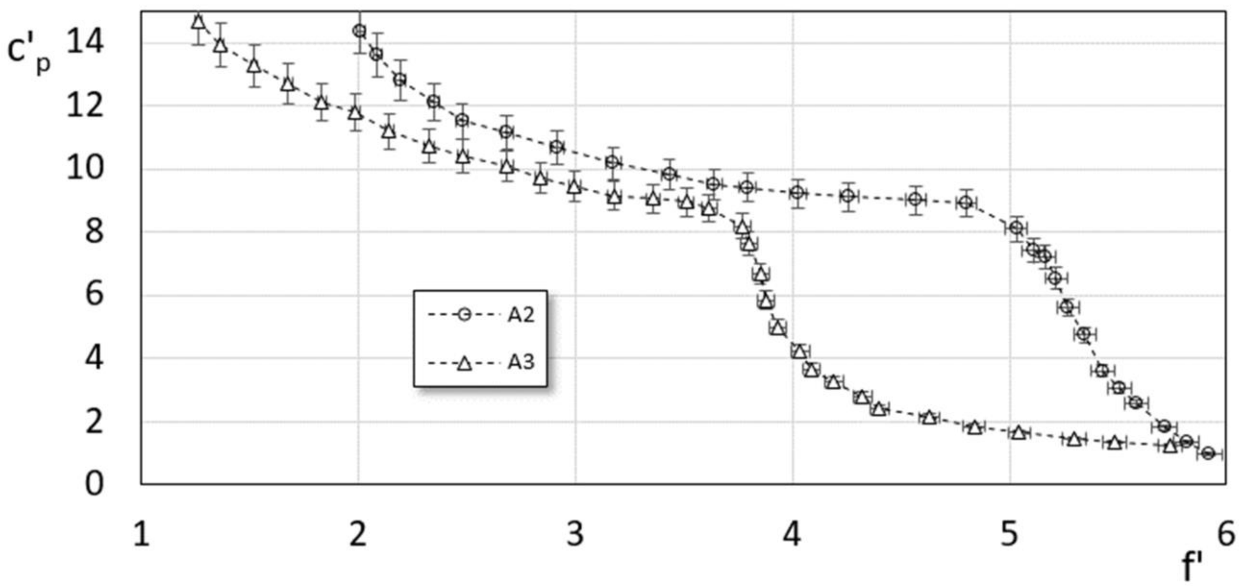

Figure 1.8. Phase velocity dispersion curve $c'_p = c'_p\,(f')$ for *A2 and A3* modes of Lamb wave.

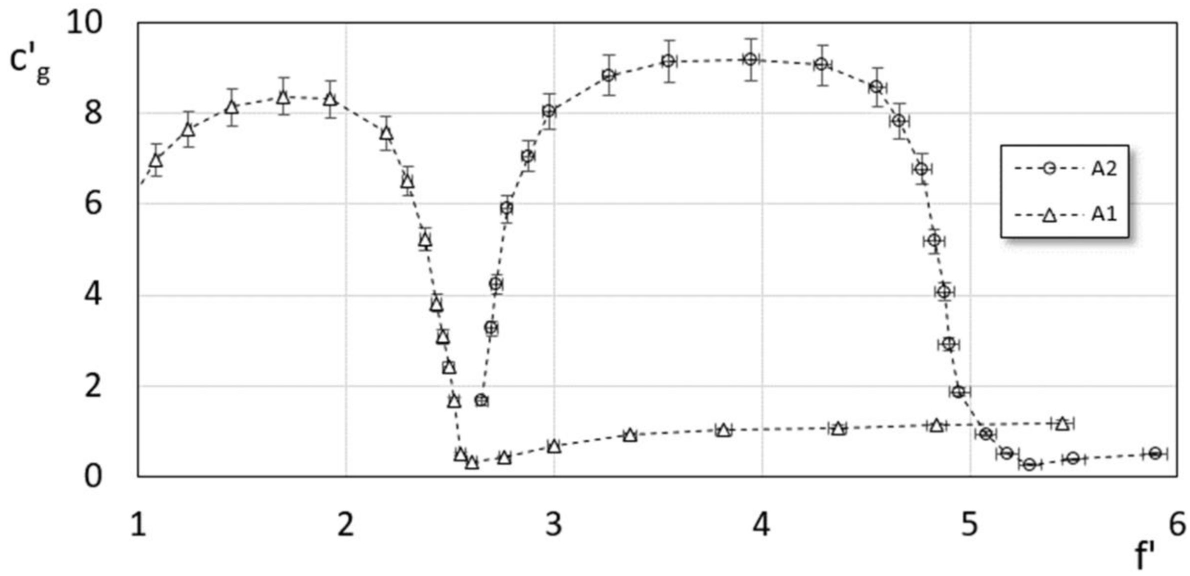

Figure 1.9. Group velocity dispersion curve $c'_g = c'_g(f')$ for *A1 and A2* modes of Lamb wave.

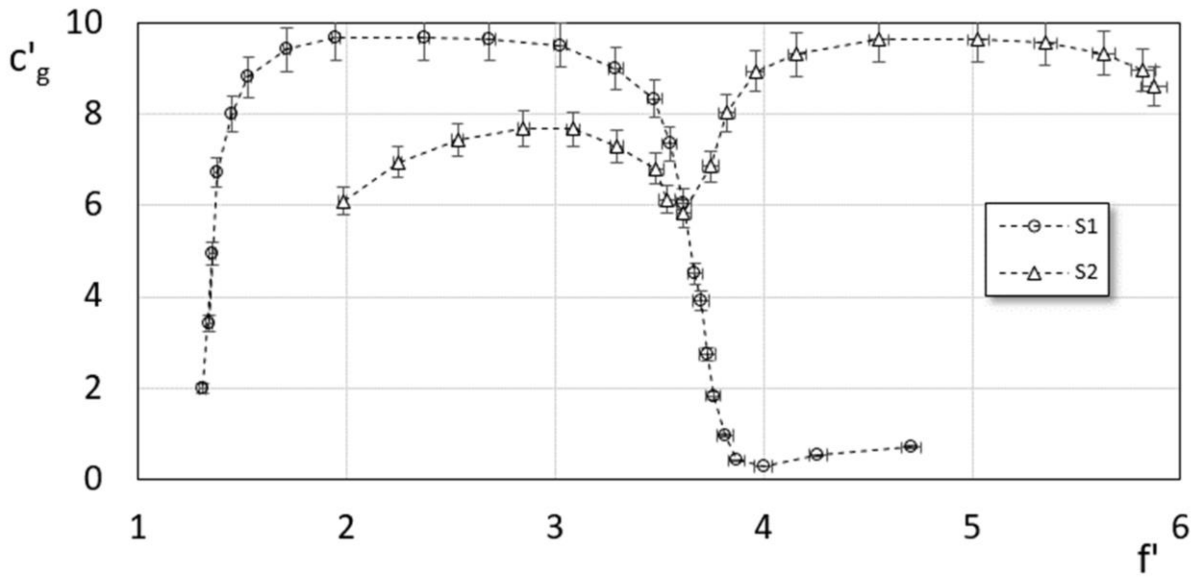

Figure 1.10. Group velocity dispersion curve $c'_g = c'_g(f')$ for *S1 and S2* modes of Lamb wave.

The A1 mode is an independent incident mode, which is separated from the S1 mode packet by the group delay method. It should be noted, however, that the two-frequency Lamb mode (S2), which is controlled by the fundamental mode S1, depends on the fundamental mode (S1). The group packet of S1 modes, passing through the volume of the composite structure, transfers the fundamental and the two-frequency second harmonic wave.

The analysis of the dispersion curves allows us to conclude that the fundamental mode (S1) and the second harmonic mode (S2) have the same phase velocity and group velocity. The detected tendency is similar to the phase condition in resonant vibration, since the generated S2 mode has the same phase and group velocity as the fundamental mode S1. Separation of these two modes in the time domain spectrum is not an ordinary task. However, the study of the frequency spectrum allows us to obtain their amplitudes in the frequency spectrum. The spectra of the fundamental mode S1 and the second harmonic mode S2 are clearly separated in the frequency domain.

A large number of experimental and analytical studies on the propagation characteristics of Lamb pulses in the volume of composites lead to the conclusion that there are two main mechanisms of amplitude attenuation, which are "material attenuation or damping" and "wave packet propagation" corresponding to the wave dispersion effect.

Since the guided wave modes in this study are selected in the non-dispersive frequency range, it is assumed that the amplitude decay is mainly affected by the attenuation. Attenuation is an important characteristic of the propagation of the Lamb guided wave. The attenuation effect is equivalent to the decrease in signal strength after the wave travels a certain distance. The attenuation of the wave is determined by the attenuation coefficient.

A typical experimental technique using Lamb pulse echo to measure the attenuation coefficient is to compare two amplitudes of a particular mode captured at two corresponding travel distances. We denote the attenuation value as α. The magnitude of the attenuation uniquely determines the decrease in the wave amplitude depending on the frequency and mode. Therefore, the following relationship is true

$$\ln\frac{A_{x1}}{A_{x2}} = \alpha\left(x_2 - x_1\right), \tag{1.34}$$

where

A_{x1} and A_{x2} are the amplitudes of the wave mode signal;

x_1 and x_2 are the corresponding signal travel distances at which the specified amplitudes are recorded.

In general, an ultrasonic Lamb wave propagates as a wave packet. This wave packet contains a number of adjacent frequency components around a central frequency. The velocity of the wave packet can be considered as the group velocity. The phase velocity is equal to the velocity of a pure single-frequency wave mode. The phase velocity also determines the speed of energy carried by the wave packet. The relationship between the group velocity and the energy carried by the wave packet is observed for inviscoelastic materials when directional propagation is considered.

In the Lamb wave experiments, unidirectional samples of laminar composites were analyzed. Lamb waves in these samples propagated along the fiber direction. The experimental group velocity of the Lamb wave, measured by a piezoelectric transducer operating at a fixed frequency, can be determined quite easily. The most effective method for such determination is to compare the time difference between two different receiver positions in a given range with a theoretically predicted value. The theoretically determined value is calculated by numerical differentiation from the phase velocity dispersion curve. The Lamb wave group velocity changes significantly with the material properties and depends on the thickness of the specimens. When the wave passes through a damaged region with reduced stiffness, the group velocity will be affected.

The nonlinear parameter of the second harmonic of the Lamb wave satisfies the following relation

$$\beta = \frac{8A_2}{k^2 A_1^2 x} f_x, \tag{1.35}$$

where
k is the wavenumber of the Lamb wave;
x is the wave propagation distance;
A_1 and A_2 are the amplitude of the second harmonic and fundamental wave, respectively;
f_x is the special function of the Lamb wave nonlinear parameter β.

This special function is described by the following mathematical relationship

$$f = \frac{\cos^2(ph)}{\cosh(2ph)}\left[1 - \frac{\left(k^2 + q^2\right)}{2k^2}\right], \tag{1.36}$$

where
h is the thickness of the waveguide;
$p = \sqrt{k^2 - k_l^2}$;
$q = \sqrt{k^2 - k_t^2}$;

k_l and k_t are the wave numbers of longitudinal and transverse waves;

The functional dependence for the nonlinear parameter of Lamb waves leads to the unambiguous conclusion that this parameter is determined as a function of frequency, mode type, material properties and waveguide geometry. The characteristic mode of the wave is chosen to detect acoustic nonlinearity in samples with constant thickness at a fixed input fundamental frequency. When studying the acoustic nonlinearity S1 at fixed frequencies, the influence of the characteristic function can be neglected.

Theoretical analysis has shown that the normalized amplitude of the second harmonic can be represented as the ratio of the amplitude of the second harmonic divided by the square of the amplitude of the fundamental wave (A_2/A_1^2). In terms of graphical illustration, such a feature corresponds to the slope of the line relating the actual acoustic nonlinear parameter β to the propagation distance x for a fixed wave number k and nonlinearity function f. In this case, the normalized amplitude of the second harmonic can be written as

$$\overline{\beta} = \frac{A_2}{A_1^2} \alpha\beta x. \tag{1.37}$$

The normalized amplitude of the second harmonic increases with the propagation distance due to the presence of a cumulative effect. The increase is observed up to a certain point, when the material attenuation becomes dominant.

Checking for this cumulative effect in measurements is important. Namely, the presence of the effect ensures that the measurements from the samples are not due to the uncertainty of the measuring system, but to the nonlinearity caused by the damage.

The phase matching of the wave mode pair (S1, S2) to generate the cumulative second harmonic wave avoids the dispersive and multimode nature of the Lamb ultrasonic wave propagation. The group delay method is used to effectively separate a large number of wave packet modes. The basis of this method is the difference in group velocities among the different Lamb modes. Experimental work has revealed a correlation between the acoustic nonlinearity of the Lamb ultrasonic wave and the thermal degradation of composite laminates.

The nonlinear Lamb wave method is a promising tool for early detection of thermal damage in composite materials.

Hydrothermal aging of composite materials is caused by two main types of influences. According to the first mechanism, physical aging occurs below the glass transition temperature (T_g) of the composite material, and is partially reversible and leads to plasticization. The second aging mechanism is chemical in nature and is observed above the glass transition temperature. The second aging mechanism is completely irreversible and leads to hydrolysis. Water absorption by composite materials can cause serious degradation, the level of which can vary depending on the temperature and exposure time.

The presence of moisture in most cases leads to swelling of composite materials. In this case, microcavities inside the volume of the composite are filled. Microcracks filled with moisture create microcracks at the boundaries between the fibers and the matrix. Therefore, measuring the mechanical properties of composite materials can be a way to assess the moisture content [29-31].

The C-scan immersion ultrasound method for measuring the phase and group velocities of broadband pulse echo is often used to monitor the moisture content of composite materials. The results of this technique allow us to determine the elastic modulus in the direction normal to the material plate. Over time, when the material plate is subjected to hydrothermal aging, both the phase velocity and the attenuation of the bulk waves are studied. Experimental techniques use piezoelectric transducers, either implanted in the sample (contact technique) or through a water connection (immersion technique). The measured acoustic parameters are then related to the viscoelasticity and microstructure of the propagation medium, which change with the level of humidity.

The moisture content of the reinforced composite plates can be controlled using Lamb waves. The wave packet modes are generated and detected using air-coupled ultrasonic transducers. The transducers are located on one side of the composite sample. Due to these features, it can be stated that the method is contactless and one-sided. This satisfies the limitations of industrial non-destructive testing. The methodology is complemented by a quantitative assessment of the complex wave numbers of the guided Lamb wave modes.

The numerical model can also be used to predict the wave number dispersion curves for Lamb modes. The experimental technique allows to investigate the sensitivity of Lamb waves to changes in viscoelastic moduli. Hydrothermal aging, similar to the humid conditions encountered during the operation of structures, is applied to the composite plate.

Subsequent dehydration of the composite sample is used to control the reversibility of the absorption phenomenon. During several stages of hydrothermal aging and drying, the changes in the plate weight and the complex wave numbers of the three Lamb modes A0, S0 and S1 are measured. Analysis of the results of ultrasonic measurements with numerical predictions allows us to formulate and solve the inverse problem for deriving the material properties, i.e. the complex viscoelastic moduli of the plate.

The changes in these moduli are compared with the weight changes. Such a synthesis of experimental and analytical methods allows us to make predictions about the potential of non-contact, one-way, ultrasonic technology for monitoring the moisture content of composite materials.

The method of surface impedance matrices is used to construct dispersion curves (complex wave numbers $K = K' + iK''$ depending on the frequency-thickness).

In this case, the wave modes are directed along the x_2 of the plate (or x_3, since the planes P_{12} and P_{13} are identical). The method of describing the properties of laminated composites is based on the use of complex viscoelastic moduli, $C_{ij} = C'_{ij} + C''_{ij}$, of the equivalent material, which were measured using the classical immersion ultrasound technique. These moduli are defined on the coordinate axes x_1 (perpendicular to the plane of the laminate), x_2 and x_3 (located in the plane of the laminated composite).

Spectral dependences (argument f/d, where f is the frequency and d is the thick of a sample) of viscoelastic moduli for different Lamb wave modes are shown in Fig. 1.11 – 1.14. As for the real and imaginary parts of the wave numbers, it should be noted that the real part K' is associated with the phase velocity of the modes, and the imaginary part K'' is associated with their attenuation.

The sensitivity of Lamb waves to changes in viscoelastic moduli has also been analyzed in detail. The first step in the analysis was to determine the numerical values of the viscoelastic moduli carried by the different Lamb modes. Dispersion curves have been plotted for the A0, S0, and S1 modes, first using fixed values of the complex C_{ij}, and then increasing by a quarter either the real or the imaginary part of one of these moduli.

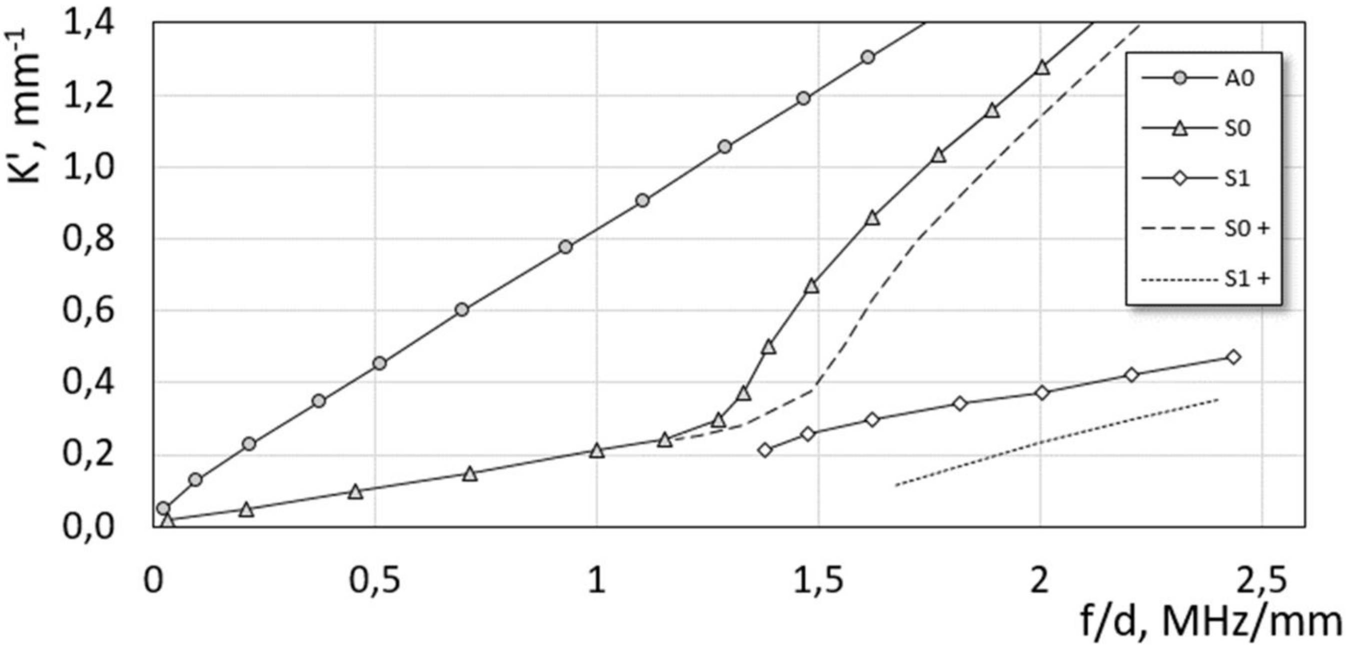

Figure 1.11. Effect of ¼ change of C'_{11} on real-part complex number K' (index "+" for modified part).

Comparisons between the different plots thus obtained show the individual effect of each C'_{ij} or C''_{ij} on the complex wave numbers. Figures 1.15 – 1.16 show the changes in both the real and imaginary parts of the complex wave numbers befor and after drying.

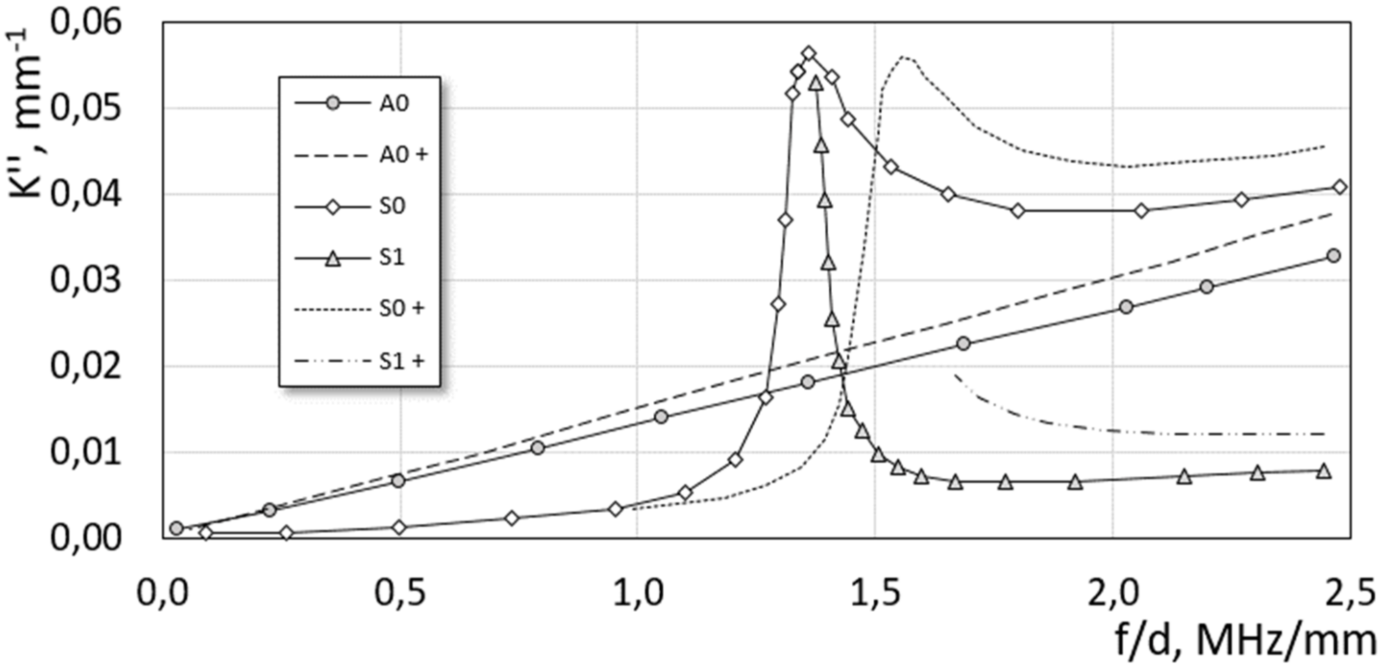

Figure 1.12. Effect of ¼ change of C'_{11} on imaginary-part complex number K'' (index "+" for modified part).

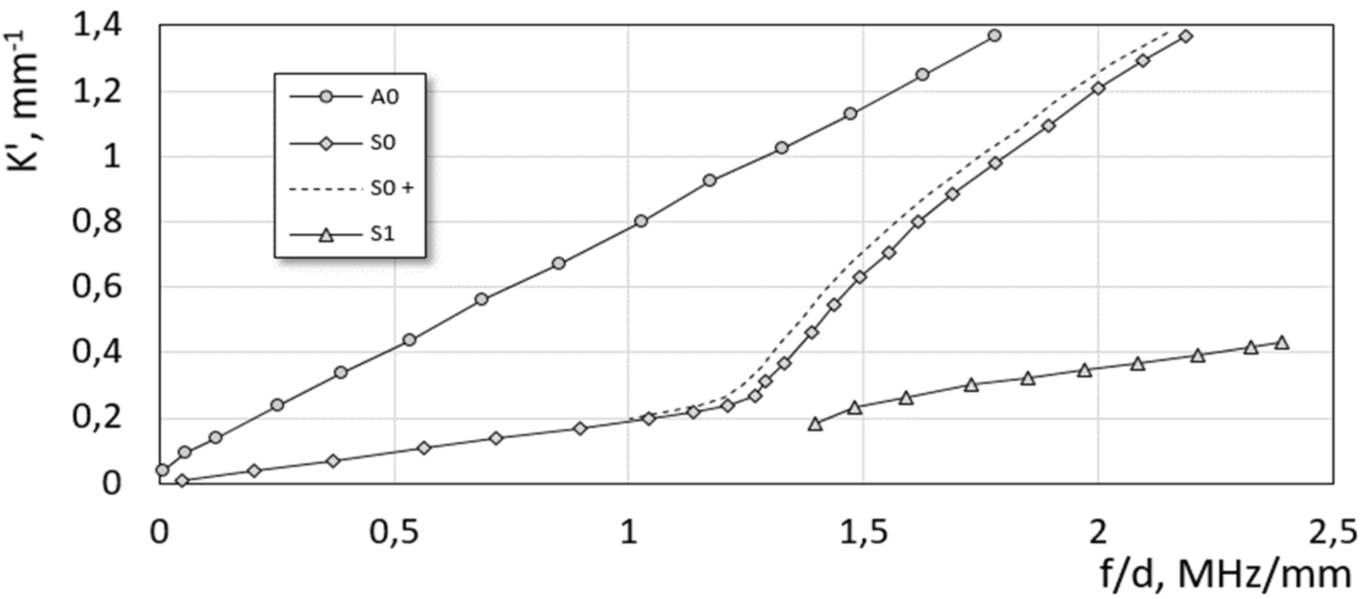

Figure 1.13. Effect of ¼ change of C'_{22} on real part complex number K' (index "+" for modified part).

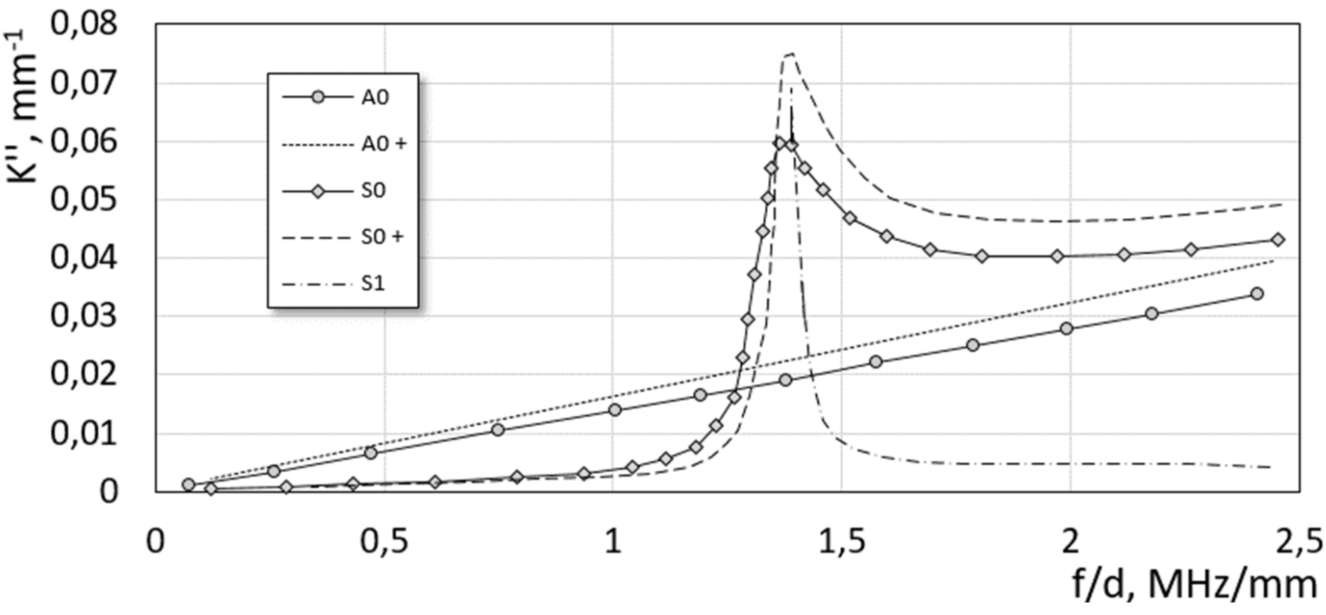

Figure 1.14. Effect of ¼ change of C'_{22} on imaginary-part complex number K'' (index "+" for modified part).

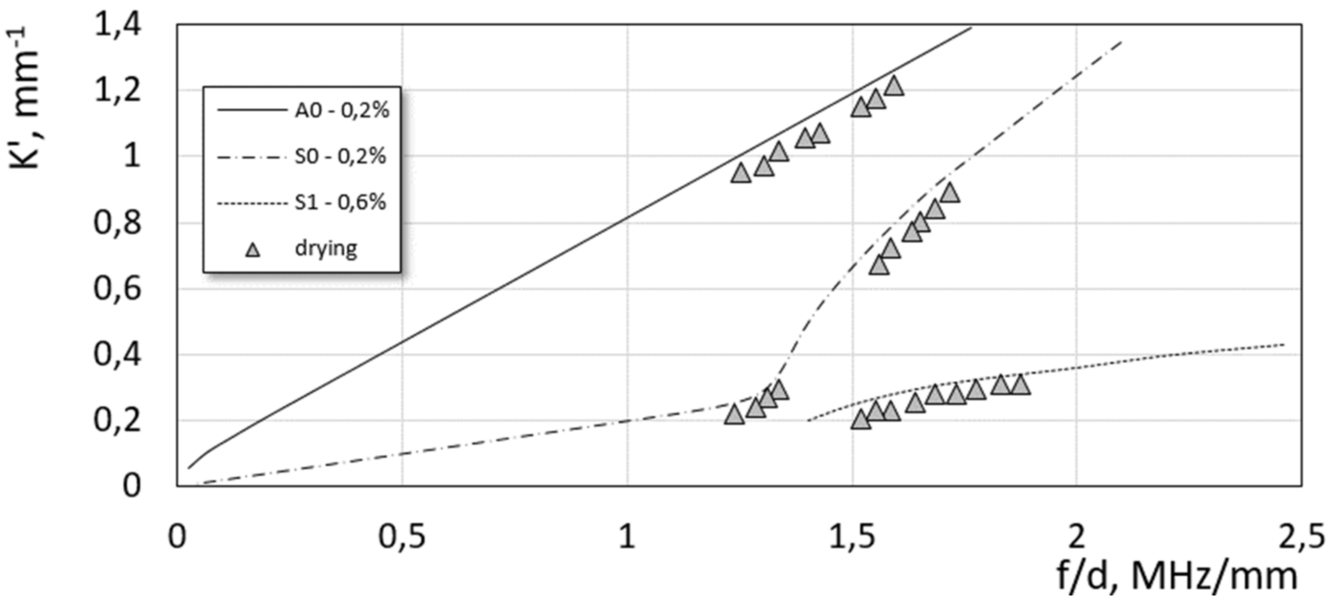

Figure 1.15. Measurements real part complex number K' before (lines) and after (triangles) drying.

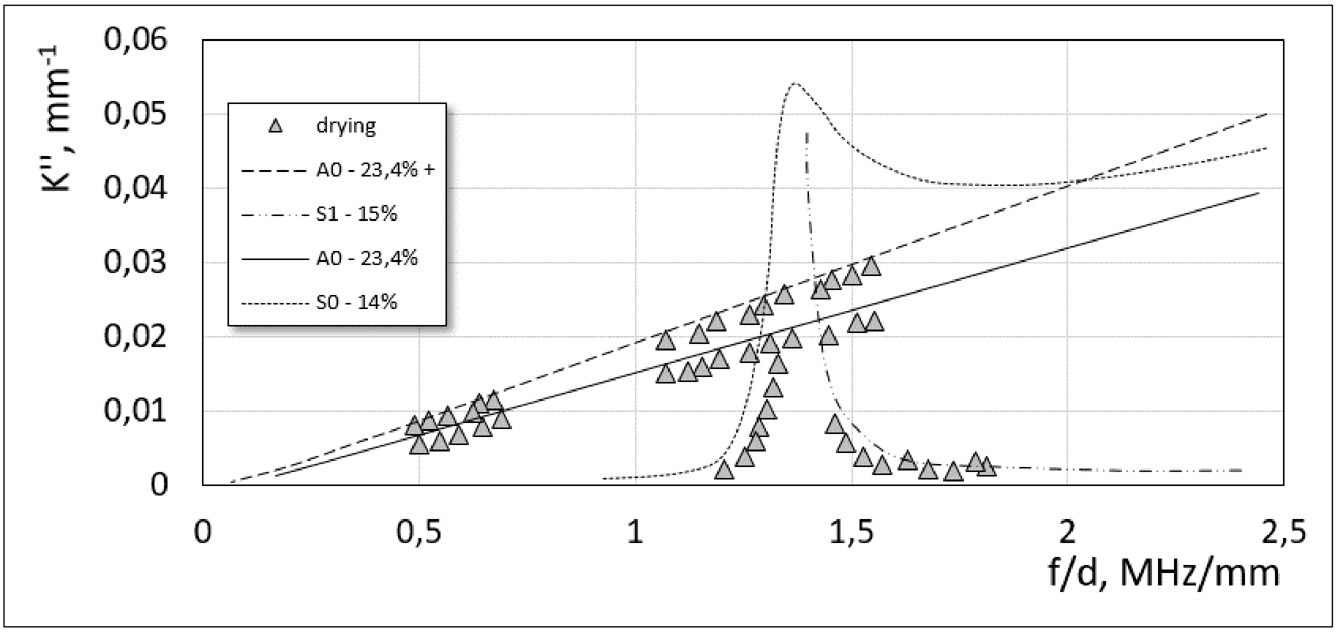

Figure 1.16. Measurements imaginary-part complex number *K''* before (lines) and after (triangles) drying.

Experiments indicate a significant sensitivity of Lamb waves to the moisture content of laminated composite plates. It can be argued that the A0 mode decay is a good indicator of the moisture content of the material, since its changes during the aging-drying processes very well follow the changes in the weight of the plate. In addition, the A0 mode decay is found to be sensitive to the imaginary part of the Coulomb modulus in the plane of propagation.

CHAPTER 2
DAMAGE IDENTIFICATION

The advantage of using Lamb waves in damage detection is that they are highly sensitive to disturbances in the propagation path, such as a fault or boundary. In addition, Lamb waves can propagate over long distances even in highly attenuating materials such as carbon fiber-reinforced composites. As a result, a wide area can be quickly investigated in experimental studies of, for example, laminated composites. The entire thickness of the laminate can also be related to different Lamb modes. This makes it possible to detect both internal and surface damage. The range of potential damage types that Lamb wave analysis can detect is quite wide.

In general, the Lamb wave approach to damage detection is characterized by (the ability to inspect large structures while preserving coating and insulation. In addition, the ability to inspect the entire cross-sectional area of the structure is preserved. The Lamb wave packet-based technique has high sensitivity to multiple defects with high identification accuracy. The analysis of Lamb wave propagation in anisotropic viscoelastic media is quite a challenging task.

With very high speed, waves reflected from boundaries can easily hide components scattered by damage in signals. To ensure accuracy, the structure to be tested can be relatively large and with a relatively small detection area. Lamb waves are usually characterized by several wave modes. The dispersion properties of such wave formations are not identical throughout the thickness of the composite, even for the same mode, but in different frequency ranges. Existing methods of both experimental and theoretical studies provide the possibility of identifying damage using Lamb waves for fiber-reinforced composite structures. Lamb waves propagating in composite structures have unique characteristics of dispersion processes. The features of Lamb wave propagation in composite laminates provide a free choice of their generation mode.

Lamb waves, consisting of a superposition of longitudinal and shear modes, are observed in relatively thin laminated composite plates. Their propagation characteristics vary with the angle of entry, excitation, and structural geometry. Lamb waves, consisting of a superposition of longitudinal and shear modes, are observed in relatively thin laminated composite plates. Their propagation characteristics vary with the angle of entry, excitation, and structural geometry. A Lamb mode can be either symmetric or antisymmetric and are described, respectively, by the following relations:

symmetric modes

$$\frac{\tan(qh)}{\tan(ph)} = -\frac{4k^2qp}{\left(k^2 - q^2\right)^2}, \tag{2.1}$$

anti-symmetric modes

$$\frac{\tan(qh)}{\tan(ph)} = -\frac{\left(k^2 - q^2\right)^2}{4k^2 qp}, \tag{2.2}$$

$$p^2 = \frac{\omega^2}{c_L^2} - k^2, \quad q^2 = \frac{\omega^2}{c_T^2} - k^2, \quad k = \frac{\omega}{c_p}, \tag{2.3}$$

where
h is the plate thickness;
k is the wavenumber;
c_L is the velocity of longitudinal mode;
c_T is the velocity of transverse mode;
c_p is the velocity of phase mode;
ω is the circular frequency of Lamb wave.

The relationship between propagation speed and frequency implies that Lamb waves, regardless of mode, are dispersive (speed depends on frequency). The presence of Lamb wave modes is accompanied by a transverse (shear) motion different from normal shear waves (vertical shear mode) in laminated composites. Perpendicular to the plane of the composite cross-section of propagation, such a mode has been accordingly called the shear horizontal (SH) mode (Lave wave).

The anisotropic properties of composite structures give rise to physical processes such as direction-dependent velocity and the difference between phase and group velocities. In an N-layer composite laminate, the Lamb wave can generally be described using its displacement field, *u*, satisfying the Navier displacement equations in each layer

$$\mu^n \nabla^2 u^n + \left(\lambda^n + \mu^n\right) \nabla(\nabla u^n) = \rho^n \frac{\partial^2 u}{\partial t^2}, \quad n = 1, 2, ..., N, \tag{2.4}$$

where
ρ^i is the density of the *i*th layer;
λ^i is the first Lame' constan of the *i*th layer;
μ^i is the second Lame' constant of the *i*th layer.

In most cases, when propagating through the volume of a composite, there is attenuation in magnitude, a change in the propagation speed, and a change in wave number, called dispersion.

Analysis of experimental measurements shows that Lamb waves are capable of propagating over relatively large distances even in composites. Larger propagation distances are typically observed in carbon fiber-based materials than in glass fiber-reinforced materials. Artificial or natural stiffening can slightly increase attenuation. The most serious influence on attenuation is exerted by the presence of surface coating materials, which can cause very significant attenuation.

Accurate consideration of the boundary conditions on each layer of the laminar composite leads to a complex dispersion equation

$$\left| A\left(\omega, k, \lambda^{n}, \mu^{n}, h_{n}\right) \right| = 0, \tag{2.5}$$

where the conditional dependence can be considered: $\omega = \omega\,(k, h_n, \lambda_n, \mu_n)$.

Lamb wave fault identification essentially depends on the interpretation of the captured wave signals. Determining the signatures useful for fault identification from the collected Lamb wave signal typically involves a number of interferences. Such interferences include: contamination by various noises, interference from natural structural vibration, confusion of several modes, and set of the sample data. In this regard, various signal processing and identification methods have become widespread, in particular, time series analysis, frequency analysis, and integrated time-frequency analysis.

Time domain signal analysis can detect damage both globally and locally. In particular, delamination in a composite beam can be detected by measuring the time of flight in the final Lamb signal. Time series analysis can be applied to waveforms for damage detection using a two-stage prediction model. As a result of applying this technique, it can be found that the difference in time domain signals between the defective structure and the reference, defined as the residual error, will be greatest for sensors near the damage.

A slightly different approach to structural damage detection is based on the combination of independent component analysis in the time domain. This technique allows the detection of key features from the measured vibration signals. However, with the exception of a few successful applications in fault localization, direct time series analysis is usually unable to isolate information scattered across defects properly from noise in different frequency ranges. In addition, a reference signal is needed for comparison.

A significant number of works are devoted to the study of a dynamic signal in the frequency domain using the Fourier transform. This transform mathematically transforms the time-dependent Lamb wave signal, $f(t)$, into frequency space according to the equation

$$F(\omega) = \int_{-\infty}^{\infty} f(t) \exp(-j\omega t)\,dt, \tag{2.6}$$

where ω is the angular frequency;

j is the unit complex;
$F(\omega)$ is the Fourier counterpart of $f(t)$.

The fast Fourier transform and its two-dimensional form, which are derived from the Fourier transform but with improved capabilities, are often used to analyze Lamb wave signals, and can significantly speed up the calculation process. A simplification of the explicit analysis of multimode Lamb waves can be obtained by measuring the response of a composite plate at a number of equally spaced positions on the surface and then applying a 2*D* Fourier transform. In subsequent steps, different modes at different frequencies in the frequency-wavenumber domain can be distinguished.

As an example of an experimental setup, a laser ultrasound system for generating Lamb waves in the direction perpendicular to the laser beam can be mentioned. In this case, the spatial orientation of the laser line source was controlled by mirror translation. Subsequently, a two-dimensional Fourier transform was applied to the signals collected from different positions using a Michelson interferometer along the scanning path. In this way, dispersion curves could be obtained.

A similar principle was used as the basis for the experimental setup, where a pair of transducers was used to measure signals at equally spaced positions. The second stage involved analyzing the two-dimensional Fourier transform. This analysis ended with the separation of symmetric and antisymmetric Lamb modes. The resulting Lamb wave spectrogram in the frequency-wave number region contained a region where several modes were already separated, even for those in the same frequency band.

The deficiencies of dynamic Lamb wave analysis in the time or frequency domain can be addressed by introducing a packet that combines time information with frequency data. Most time-frequency algorithms can be summarized as follows

$$P(t,\omega)=\frac{1}{2\pi}\int\limits_{\delta}\int\limits_{\tau}\int\limits_{\theta}\exp[-i(\theta t+\tau\omega+\theta\delta)]\phi(\theta,\tau)f^{*}\left(\delta-\frac{\tau}{2}\right)f\left(\delta+\frac{\tau}{2}\right)d\theta\, d\tau\, d\delta, \quad (2.7)$$

where
$P(t, \omega)$ is the energy intensity;
t - is the current moment in time;
ω is the frequency;
f – is the Lamb wave signal;
f^* is the complex conjugate of f;
$\phi(\theta, \tau)$ is the characteristic function depending on $f(t)$.

In practice, instead of direct time-frequency analysis, some variants of equation (2.7) are more popular, such as the short-time Fourier transform, the Winger-Ville distribution, and the wavelet transform.

In particular, the wavelet transform uses a wavelet with a portion of the waveform that is limited in time. The average amplitude of such a portion of the wave is zero. The time-dependent signal is mapped into a two-dimensional representation with scale and time. The scale of such a representation can be related to the frequency by defining the scale value at which the scalogram reaches its maximum.

With the wavelet transform analysis, the dynamic wave signal can be examined using a localized fragment to fully display the hidden characteristics. The hidden characteristics include trends such as breakpoints or discontinuities and self-similarity. Continuous wavelet transform and discrete wavelet transform are two typical forms of wavelet transform. For Lamb wave signal, in general, continuous wavelet transform is especially effective for analysis and visualization. On the other hand, discrete wavelet transform is more useful for signal denoising, filtering, compression and feature extraction.

The Lamb wave signal *f* (*t*) applied with the basic orthogonal function Ψ (*t*), obtained from the sensor can be transformed into a quadratic expression using the scale of the dual parameters, *a*, and time, *b*

$$W(a,b)=\frac{1}{\sqrt{a}}\int_{-\infty}^{\infty} f(t)\Psi^*\left(\frac{t-b}{a}\right)dt\,, \tag{2.8}$$

where

W (*a*, *b*) is the continuous wavelet-transform coefficient;

Ψ *(*t*) is the complex conjugate of Ψ (*t*).

The non-stationary nature of the wave energy in the region is illustrated by the relation

$$E=\int_{-\infty}^{\infty}\int_{a>0}^{\infty}\left|W(a,b)\right|^2 dadb\,, \tag{2.9}$$

where

$|\Psi(a,b)|^2$ can be considered as a scalogram.

Calculating the wavelet coefficients at each scale point is computationally expensive. For simplicity, equation (2.8) can be performed in discrete scale and time using binary variables *m* and *n*

$$W'(m,n)=a_0^{-m/2}\int f(t)\Psi\left(a_0^{-m}t-nb_0\right)dt\,, \quad (2.10)$$

$$a=a_0^m\,,\quad b=n\,a_0^m\,b_0,\quad m,n\in Z\,, \quad (2.11)$$

where
a_0 and b_0 are constants determining sampling intervals along the time and scale axes.

The decomposition of the signal into separate bands of relatively higher and lower frequencies can be accomplished using equation (2.10). Typically, the signal components of different frequencies are separated into a fixed number of levels by applying the discrete wavelet transform.

The simplest methods for localizing mechanical damage in composites employ logical signal analysis. Time-of-flight, defined as the time delay from the moment a sensor detects a signal reflected by a damage to the moment the same sensor detects an incident signal, can be incorporated into a simple method for damage triangulation. As a two-dimensional extension of this concept to composite structures, a series of sensors were used to cover the region of interest, and the transit times were extracted from the signals obtained from each possible actuator-sensor path. For example, four piezoelectric sensors, each serving as both an actuator and a sensor, were attached to the four corners of a reinforced composite plate. The transit times T_{1i} were extracted from the signals obtained from each possible actuator-sensor path with noise cancellation

$$T_{1,i}=\frac{L_{AD}}{V_{S0}}+\frac{L_{DS}}{V_{Sd}}-\frac{L_{AS}}{V_{S0}}\,, \quad (2.12)$$

where
V_{Sd} and V_{S0} are the velocities of damage-induced shear mode and incident symmetric mode S0, respectively;
L_{AD}, L_{DS}, L_{AS} are the distances between damage centre (x, y) and the ith sensor;
Index “1” represents the damage centre.

The representation of distances in Cartesian coordinates is

$$L_{AD}=\sqrt{x^2+y^2}\,,\quad L_{DS}=\sqrt{(x-x_i)^2+(y-y_i)^2}\,,\quad L_{AS}=\sqrt{x_i^2+y_i^2}\,, \quad (2.13)$$

where (x_i, y_i) represents the coordinates of the i-th transducer in the present coordinate system.

The hybrid of the analytical model and its hardware implementation included a nonlinear system that consisted of four sets of equations, with each piezoelectric actuator (P_i, i = 1, …, 4) acting in turn as an actuator based on its own reference frames, the mathematical solution of which led to the location of the damage (see Fig. 2.1).

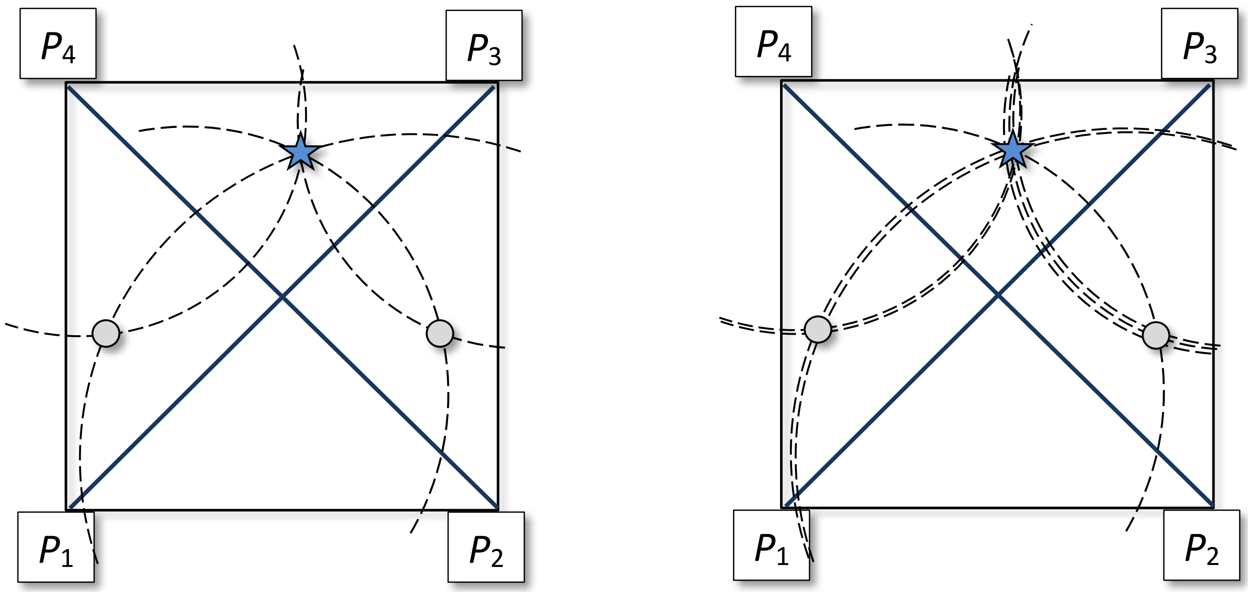

Figure 2.1. Detection of delamination location: blue stars - diagnostic results; gray circles - accompanying pseudo-results; left figure - diagnostics by 4 pathways; right figure - diagnostics by 8 pathways.

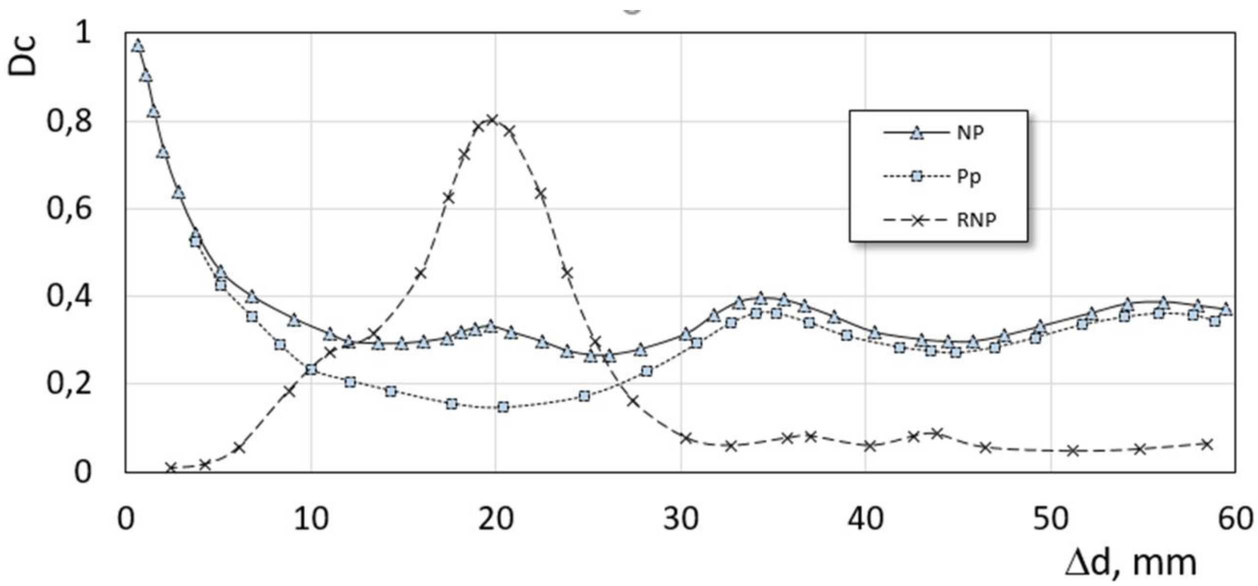

Figure 2.2. Damage identification using time-reversal approach. NP – correlation notched plate; Pp – correlation perfect plate; RNP – ratio notched plate; Dc - correlation.

The wave packet transit time technique enables time-reversed imaging for wave-based fault detection. The Lamb wave governing equations in an ideal (lossless, time-independent) structure contain only second-order time derivatives. The set of any waves that are generated by the source and subsequently scattered, reflected, and refracted by the fault can be mapped to another set of waves. The second wave packet can exactly replicate all paths and converge synchronously at the original source, as if time were running backwards.

Due to the fact that the composite material is generally inhomogeneous, the scattered Lamb waves measured by different actuator-sensor paths can be time-reversed, which is realized by replacing the actuator and sensor and vice versa. In this case, the Lamb wave should propagate from the sensor to the actuator. All these time-reversed wave signals, each of which exhibits a time delay due to the presence of the fault, will converge simultaneously at one point, namely the scattering point (of the fault). The results of applying the equivalent time reversal technique to localize mechanical damage in a composite plate are illustrated in Fig. 2.2.

The propagation of elastic waves in composite materials depends on the particular arrangement and interaction of the constituent microparticles. Lamb waves can be recorded in thin plates (with flat dimensions much greater than the thickness and with a wavelength of the order of the thickness), which provide upper and lower boundaries for the direction of continuous wave propagation. In a thin isotropic and homogeneous plate, wave packets, regardless of the mode, can generally be described in the form of a Cartesian tensor notation, namely

$$\mu u_{ij} + (\lambda + \mu) u_{ij} + \rho f_i = \rho \ddot{u}_i , \tag{2.14}$$

where

u_i is the displacement in the x_i direction;

f_i is the bodyforce in the x_i direction;

ρ is the density;

μ is the shear modulus of the composite plate;

$$\lambda = \frac{2\mu\nu}{1 - 2\nu}, \tag{2.15}$$

where

λ is the Lame constant;

ν is the Poisson ratio.

The displacement potential technique based on the Helmholtz equation is the basis of potential analysis and can be used as an effective approach to decompose equation (2.14) into two independent parts under the plane strain condition for governing longitudinal and transverse modes, accordingly

$$\frac{\partial^2\phi}{\partial x_1^2}+\frac{\partial^2\phi}{\partial x_3^2}=\frac{1}{c_L^2}\frac{\partial^2\phi}{\partial t^2}, \tag{2.16}$$

$$\frac{\partial^2\psi}{\partial x_1^2}+\frac{\partial^2\psi}{\partial x_3^2}=\frac{1}{c_T^2}\frac{\partial^2\psi}{\partial t^2}, \tag{2.17}$$

where

$$\phi=\left[A_1\sin(px_3)+A_2\cos(px_3)\right]\cdot\exp\left[i(kx_1-\omega t)\right], \tag{2.18}$$

$$\psi=\left[B_1\sin(px_3)+B_2\cos(px_3)\right]\cdot\exp\left[i(kx_1-\omega t)\right], \tag{2.19}$$

A_s, B_s, s = 1, 2, 3, 4 are the constants determined by the boundary conditions;
k is the wavenumber;
ω is the circular frequency;
index ”*L*” stands for the longitudinal modes;
index ”*T*” stands for the transverse/shear modes.

Velocities of longitudinal and transverse/shear modes are

$$c_L=\sqrt{\frac{E(1-\nu)}{\rho(1+\nu)(1-2\nu)}}=\sqrt{\frac{2\mu(1-\nu)}{\rho(1-2\nu)}}, \tag{2.20}$$

$$c_T=\sqrt{\frac{E}{2\rho(1+\nu)}}=\sqrt{\frac{\mu}{\rho}}, \tag{2.21}$$

E denotes the Young’s modulus of the medium.

The plane deformation of the displacement in the direction of propagation of the wave packet index "1" and the normal direction (index "3") is described by the equations

$$u_1=\frac{\partial\phi}{\partial x_1}+\frac{\partial\psi}{\partial x_3}, \tag{2.22}$$

$$u_2=0,\qquad u_3=\frac{\partial\phi}{\partial x_3}-\frac{\partial\psi}{\partial x_1}. \tag{2.23}$$

In this case, the following system of equations holds for the components of mechanical stresses

$$\sigma_{31} = \mu\left(\frac{\partial u_3}{\partial x_1} + \frac{\partial u_1}{\partial x_3}\right) = \mu\left(\frac{\partial^2 \phi}{\partial x_1 \partial x_3} - \frac{\partial^2 \psi}{\partial x_1^2} + \frac{\partial^2 \psi}{\partial x_3^2}\right), \quad (2.24)$$

$$\sigma_{33} = \lambda\left(\frac{\partial u_1}{\partial x_1} + \frac{\partial u_3}{\partial x_3}\right) + 2\mu\frac{\partial u_3}{\partial x_3} =$$

$$= \lambda\left(\frac{\partial^2 \phi}{\partial x_1^2} + \frac{\partial^2 \phi}{\partial x_3^2}\right) + 2\mu\left(\frac{\partial^2 \phi}{\partial x_3^2} - \frac{\partial^2 \psi}{\partial x_1 \partial x_3}\right). \quad (2.25)$$

Three types of boundary conditions can be distinguished for a plate with free upper and lower surfaces

$$u(x,t) = u_0(x,t), \quad (2.26)$$

$$t_i = \sigma_{ij} n_j, \quad (2.27)$$

$$\sigma_{31} = \sigma_{33} = 0, \quad x_3 = \pm\frac{d}{2} = \pm h, \quad (2.28)$$

where
d is the plate thickness;
h is the half thickness.

For brevity, it is noted that the standard symbols for Lamb wave applications are “S” and “A”, which denote symmetric and antisymmetric modes. The subscript indicates the mode order of the wave packet. S modes mainly have in-plane radial displacement of particles. On the other hand, A modes mainly have out-of-plane displacement. Therefore, the symmetric wave mode is often described as "compressional", showing bulging and compression of the thickness. Accordingly, the antisymmetric mode is known as "bending", showing a bending of constant thickness. It should be noted that higher-order antisymmetric modes have increasingly complex thickness displacements. Under the same excitation conditions, the magnitude of S modes (in-plane motion) is usually smaller than that of A modes.

The analysis of Lamb wave propagation in a plate with free surfaces can be extended to the condition of non-free surfaces, such as a plate immersed in a liquid, which creates transverse constraints on the plate.

For example, when a composite plate is immersed in water, the S modes will be largely confined in the plate, since it is difficult for in-plane particles to cross the plate-liquid interface. The net effect of such physical processes is that there is no significant energy leakage from the plate to the surrounding water for the S modes. However, some of the energy of the out-of-plane A mode will leak into the water. This phenomenon is known as Lamb wave leakage in a plate with a surrounding liquid.

Multilayer structures made of composite material are characterized by anisotropic nature. This feature is the reason for the appearance of many unique phenomena. Among such phenomena are: directional dependence of wave velocity, differences in phase and group velocities, change in direction, shape and deceleration of the wave, as well as many subtler features.

The propagation of Lamb waves within a plate composed of macroscopically uniform layers involves not only scattering at the top and bottom surfaces, but also reflection and refraction between the layers. Extending the governing equation to an *N*-layer laminate, the displacement field *u* within each layer must satisfy the Navier displacement equations for the *n*th layer,

$$\mu_n \nabla^2 (u_n) + (\lambda_n + \mu_n)\left(\nabla^2 u_n + \nabla u_n\right) = \rho_n u_n^{''} . \tag{2.29}$$

Besides the two fundamental Lamb modes, S and A are fundamental, i.e. those that dominate the radial in-plane and out-of-plane (vertical) particle motion in the plate, respectively.

In addition, there is another type of possible particle motion, namely in-plane but in the direction perpendicular to the wave propagation direction. In this direction, the wave packet propagates along the x_1 direction, while the particles vibrate only in the x_2 direction and are confined to the $x_1 - x_2$ plane. This wave is called the horizontal (SH) shear wave mode, in contrast to the out-of-plane (vertical) antisymmetric motion (i.e., the A mode). The A mode of the Lamb wave is called the vertical shear mode. SH waves can occur along free surfaces. Like Lamb waves, the wave modes in the SH family are either symmetric or antisymmetric.

Three-dimensional finite element modeling as well as experimental studies have demonstrated SH modes using models that allow particle motion in all directions. From a definitional point of view, SH waves are governed by the following coordinate equation

$$(u_2)_{x_1}^{''} + (u_2)_{x_3}^{''} - c_T^{-2} (u_2)_t^{''} = 0 . \tag{2.30}$$

The solution to Equation (2.30) has the form

$$u_2(x_1, x_2, t) = A \exp(-b x_3) \cdot \exp[i(k x_1 - \omega t)], \tag{2.31}$$

where
A is the constant;

$$b = k\left[1-\left(\frac{\omega}{kc_T}\right)^2\right]^{0.5}. \tag{2.32}$$

As a characteristic mode, we can mention the propagation of the Lamb SH wave in a medium that is covered with a layer of another material, as in polymer composite laminates. A typical example of such propagation is the motion of Lamb waves in a layer (ρ_1, μ_1), which is associated with a half-space (ρ_2, μ_2) and can be described by the equation

$$u_2(x_1, x_2 t) = [A\exp(-b_1 x_3) + B\exp(-b_2 x_3)]\cdot\exp[i(k\,x_1 - \omega t)], \tag{2.33}$$

where

$$b_1 = k\left[1-\left(\frac{\omega}{kc_{T_1}}\right)^2\right]^{0.5}, \tag{2.34}$$

$$b_2 = k\left[1-\left(\frac{\omega}{kc_{T_2}}\right)^2\right]^{0.5}, \tag{2.35}$$

$$c_{T_1} = \sqrt{\frac{\mu_1}{\rho_1}}, \tag{2.36}$$

$$c_{T_2} = \sqrt{\frac{\mu_2}{\rho_2}}, \tag{2.37}$$

c_{T1} is the velocity of transverse mode in the fixed layer;
c_{T2} is the velocity of transverse mode in the half-space.

The propagation of Lamb waves can be characterised by the phase (c_p) and group (c_g) velocities.

The speed at which the general shape of the wave amplitudes (known as the modulation or envelope of the wave) propagates through space can be thought of as the group velocity. The group velocity (the rate at which the wave energy is transferred) is the speed that is measured in most experiments. The group velocity depends on the frequency and the thickness of the plate.

A typical technique for determining mechanical damage in laminated composites using Lajmba wave packets includes the governing equation

$$c_g(f\,d) = d\omega\left[d\left(\frac{\omega}{c_p}\right)\right]^{-1} = d\omega\left[\frac{d\omega}{c_p} - \omega\frac{dc_p}{c_p^2}\right]^{-1} =$$

$$= c_p^2\left[c_p - \omega\frac{dc_p}{d\omega}\right]^{-1} = c_p^2\left[c_p - (f\,d)\frac{dc_p}{d(f\,d)}\right]^{-1}, \tag{2.38}$$

where $f = (2\pi)^{-1}\omega$ is the central frequency of the wave.

For the SH mode of a Lamb wave, the phase and group velocities are defined as follows

$$c_p(f\,d) = 2c_T\left[\frac{f\,d}{\sqrt{4(f\,d)^2 - n^2c_T^2}}\right], \tag{2.39}$$

$$c_g(f\,d) = c_T\sqrt{1-\left(\frac{nc_T}{2f\,d}\right)^2}, \tag{2.40}$$

where

$n \in [0, 2, 4, \ldots]$ for symmetric SH modes;

$n \in [1, 3, 5, \ldots]$ for antisymmetric SH modes.

Lamb waves move with the same speed in all directions when propagating in isotropic plates. The Lamb wave front forms a locus of points equivalent to a circle. For non-isotropic materials, in particular for fiber-reinforced composites, the wave speed depends on the direction of propagation. This fact is the reason why the shape of the wave front differs significantly from a circle and is described by the equation of a generalized ellipse with a fixed slope to the axes of the reference system.

The theoretical (phase velocity) and experimental (group velocity) values for the S0 and A0 modes in carbon fiber reinforced epoxy composite laminates for the case where two Lamb wave modes travel with different velocities in different directions (d_1) and frequencies (f_1 = 1MHz, f_2 = 0.8 MHz) are illustrated in Fig. 2.3 - 2.6.

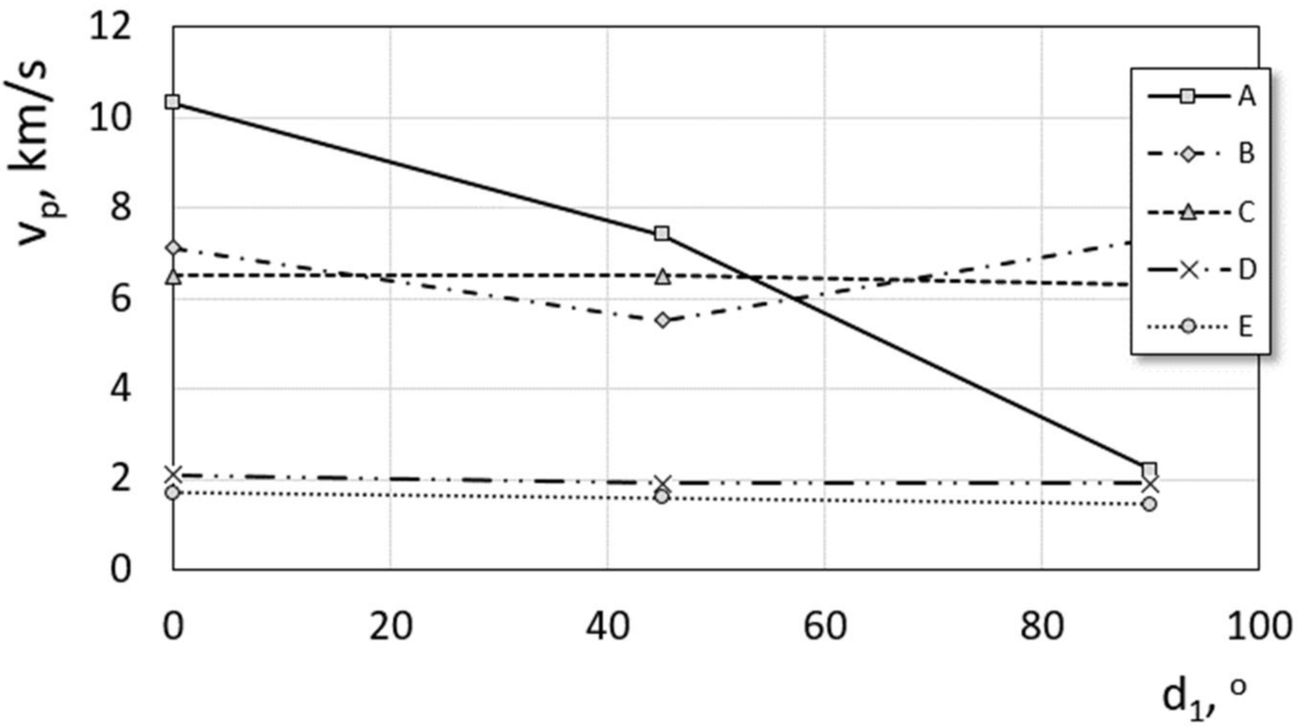

Figure 2.3. Phase velocities of S0 modes in CF/FP composite laminates (for f_1): *A* – $[0]_8$, *B* – $[0/90]_{2s}$, *C* – $[\pm45/0/90]_s$, *D* – $[0/90]_{4s}$, *E* – $[\pm45/0/90]_{2s}$.

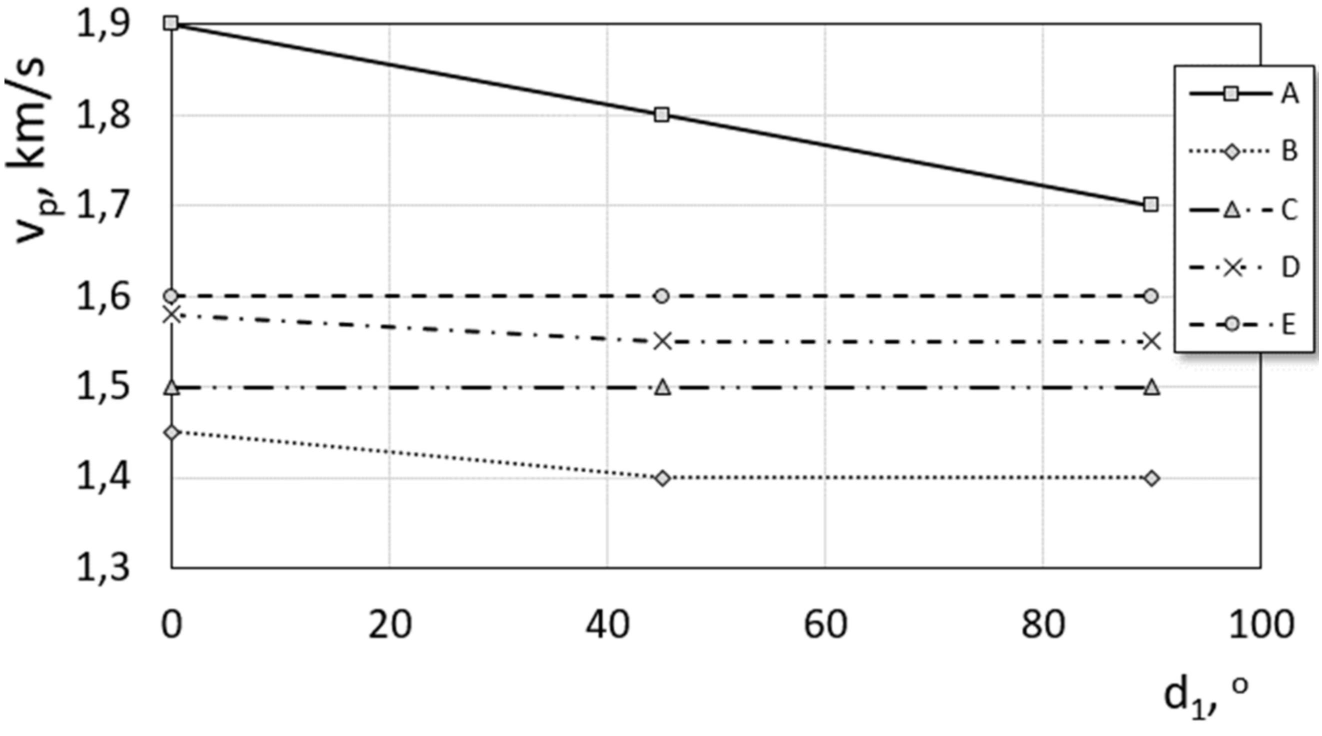

Figure 2.4. Phase velocities of A0 modes in CF/FP composite laminates (for f_1): *A* – $[0]_8$, *B* – $[0/90]_{2s}$, *C* – $[\pm45/0/90]_s$, *D* – $[0/90]_{4s}$, *E* – $[\pm45/0/90]_{2s}$.

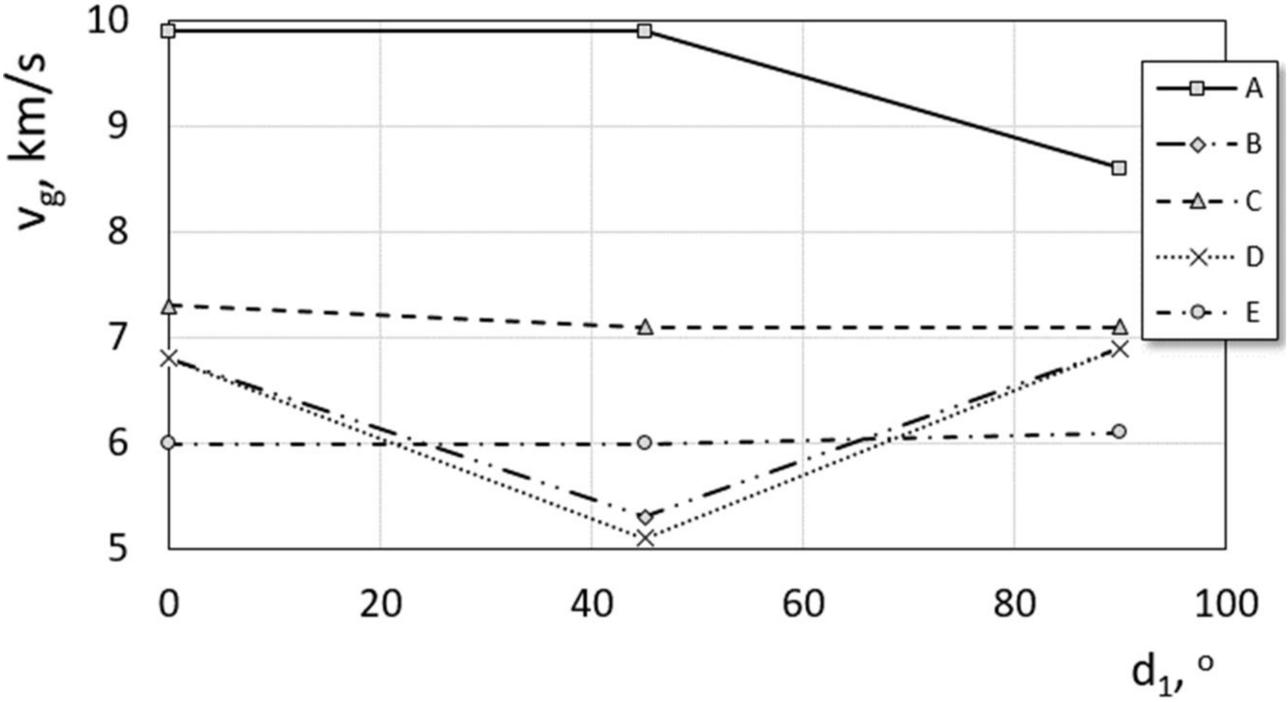

Figure 2.5. Group velocities of S0 modes in CF/FP composite laminates (for f_2): *A* – $[0]_8$, *B* – $[0/90]_{2s}$, *C* – $[\pm45/0/90]_s$, *D* – $[0/90]_{4s}$, *E* – $[\pm45/0/90]_{2s}$.

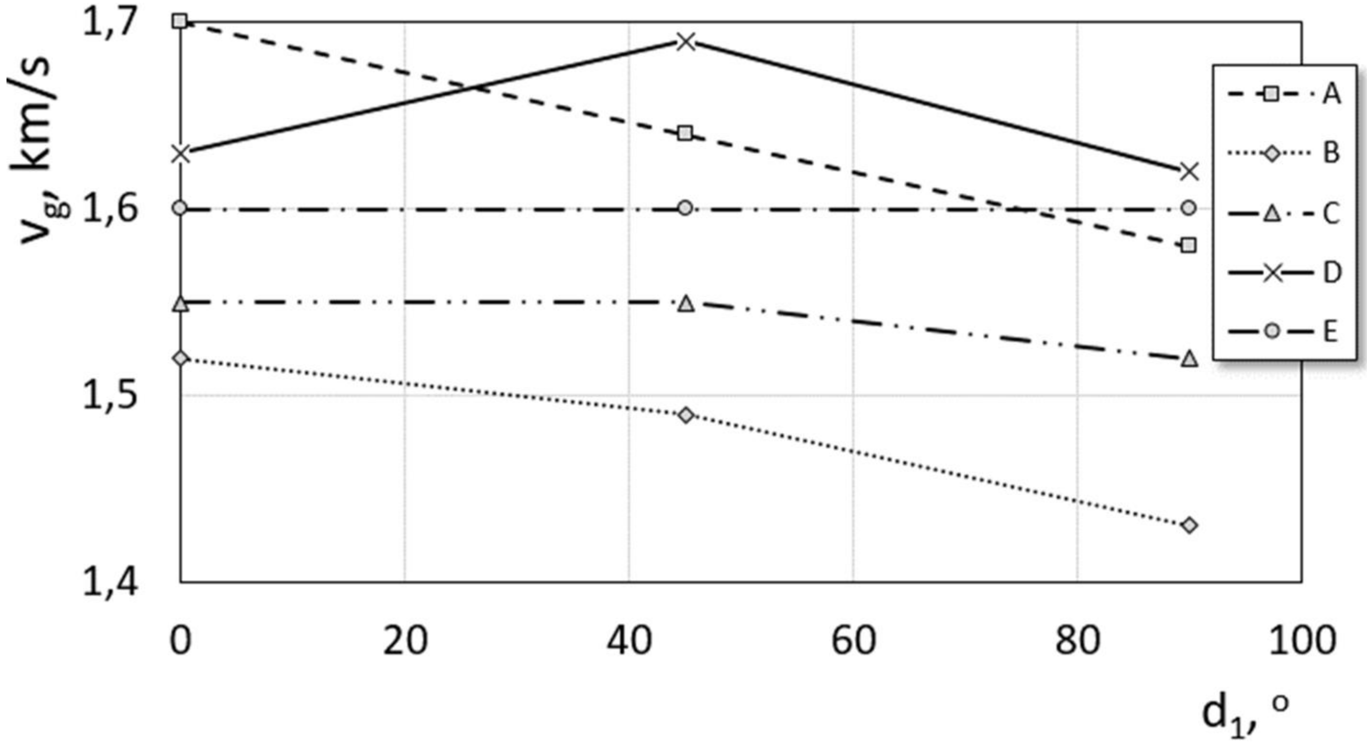

Figure 2.6. Group velocities of A0 modes in CF/FP composite laminates (for f_2): *A* – $[0]_8$, *B* – $[0/90]_{2s}$, *C* – $[\pm45/0/90]_s$, *D* – $[0/90]_{4s}$, *E* – $[\pm45/0/90]_{2s}$.

The difference in the directions of Lamb wave propagation is described by the retardation profile, which is a function of the reciprocal of the direction-dependent propagation velocity, $1/c_g(\vartheta)$ (where ϑ is the direction of wave propagation relative to 0°).

The lowest order modes (S0, A0 and SH0) behave quite differently in different directions of propagation relative to the 0° fiber, but they all become almost directionally independent in a laminate of quasi-isotropic configuration (e.g., $[\pm 45/0/90]_s$). This mechanism is very important for the study of Lamb waves in composite structures.

Detection of matrix cracking in samples with different crack density, as well as evaluation of the elastic modulus decay of cracked samples and comparison with those obtained during ultrasonic Lamb wave propagation testing, is usually carried out by analyzing composite samples in tension. This variational model based on mechanical stress testing is the most developed model for predicting matrix crack density. The lower limit of the elastic modulus E_c of a damaged laminate is determined in this model as follows:

$$\frac{1}{E_c} \leq \frac{1}{E_c^0} + \frac{1}{E_2} k_2^2 \eta(\lambda) \frac{<\chi(\delta)>}{<\delta>}, \tag{2.41}$$

where

$$\eta(\lambda) = \frac{3\lambda^2 + 12\lambda + 8}{60}, \tag{2.42}$$

$$k_2 = \frac{\sigma_2}{\sigma_0}, \qquad \lambda = \frac{t_1}{t_2}, \tag{2.43}$$

t_1 and t_2 are the half of the thickness of 0° and 90° layers, respectively;
σ_2 is stress in 90^0 layers;
σ_0 is the total stress in laminate.

The numerical values of k_2 (relative stiffness of 90^0 layers) as well as E_c^0 (initial stiffness of the laminate) are determined using the classical lamination analysis of an intact composite laminate taking into account the longitudinal and transverse elastic moduli of the composite layers. This analysis is carried out on the basis of the following system of definitions

$$\delta = \frac{a}{t_2}, \tag{2.44}$$

$$\chi(\delta) = 2\alpha\beta\left(\alpha^2 + \beta^2\right)\cdot\left[\frac{\cosh(2\alpha\rho) - \cos(2\beta\rho)}{\alpha\sin(2\beta\rho) + \beta\sinh(2\alpha\rho)}\right], \tag{2.45}$$

$$\alpha = q^{1/4}\cos\left(\frac{\theta}{2}\right), \tag{2.46}$$

$$\beta = q^{1/4}\sin\left(\frac{\theta}{2}\right), \tag{2.47}$$

$$\tan\theta = \sqrt{\frac{4q}{p^2}} - 1, \tag{2.48}$$

where
a is the half of the distance between two adjacent cracks;
p and *q* are the factors that depend exclusively on the layup and mechanical properties of the composite laminate.

A semi-analytical model is often used to obtain the stresses required to induce matrix cracking with different crack densities in specimens. Such a model for describing progressive matrix cracking in composites typically follows a specific scenario for cracking initiation and assumes a regular pattern of cracks created in 90° layers. According to this method, it is assumed that the initial cracks occur in the center of the specimen, then two subsequent cracks occur at both ends of the specimen and subsequently any new cracks occur between the two previous cracks in the bulk of the composite structure. In the case of controlled crack initiation, the crack density is related to the applied stress in the 90° layer based on the following equation

$$\left(\frac{\rho_c}{k}\right)^2 = C_{in}\left(\frac{\sigma_0}{\sigma_{in}} - 1\right), \tag{2.49}$$

where
ρ_c is the crack density;
σ_{in} is the in-situ strength of 900 layers;
σ_0 is the stress in 90^0 layers of the multi-layered composite specimen;
C_{in} is the material-independed factor that is evaluated by fitting the theoretical master curve to the tensile test data;
K is the shear lag parameter which is given for the cross-ply composite specimen as

$$k = \sqrt{\frac{3(d+b)E_cG_{12}G_{23}}{dbE_1E_2\left(bG_{23} + d_{12}\right)}}, \tag{2.50}$$

where

b and d are the thickness of 00 and 900 layers of the laminate, respectively;

E_c is the elastic modulus of composite laminate;

E_1 and E_2 are the longitudinal and transverse elastic modulus of each composite ply, respectively;

G_{12} and G_{23} are the in-ply and out of plane shear modulus, respectively.

The propagation of Lamb waves in composite structures with anisotropic properties is accompanied by such nonlinear phenomena as the difference in group and phase velocities, as well as the direction-dependent velocity. The wave motion in an N-layer laminated composite is governed by the Navier displacement equation by applying appropriate boundary conditions in each layer.

The sum of the gradient of the scalar potential of the compression wave (ϕ) and the curl of the vector potential of the shear wave (ψ), for example, $u = \nabla\varphi + \nabla \times \psi$, can be interpreted as a displacement vector. The problem of wave packet propagation can, under certain restrictions, be reduced to a two-dimensional version. In this case, the correct set of such ψ' = (0, 0, ψ) potentials that satisfies the boundary conditions of a plate medium and thus governs the propagation of a Lamb wave can be expressed as

$$\varphi_1^s = \{a_1 \exp[i\eta(x_1 - x_2)] + a_2 \exp[i\eta(x_1 + x_2)]\}, \tag{2.51}$$

$$\psi_1^s = \{b_1 \exp[i\eta(x_1 - x_2)] + b_2 \exp[i\eta(x_1 + x_2)]\}, \tag{2.52}$$

where

a_1, a_2 are the compression wave characteristics;

b_1, b_2 are the shear wave amplitudes.

For constants η and β we get

$$\eta^2 = k_l^2 - k_c^2, \tag{2.53}$$

$$\beta^2 = k_l^2 - k_s^2, \tag{2.54}$$

where

k_l is the lamb wavenumber;

k_s is the shear wavenumber;

k_c is the compression wavenumder.

The dispersion dependence for k has the form

$$k_s(\omega) = \frac{\omega}{\sqrt{\mu / \rho}}, \tag{2.55}$$

$$k_c(\omega) = \frac{\omega}{\sqrt{\dfrac{\lambda + 2\mu}{\rho}}}. \tag{2.56}$$

For the case of linear viscoelastic composites, it is more convenient to use complex values of the corresponding characteristics. The propagation of Lamb wave packets in viscoelastic materials is described by a complex version of the equation for antisymmetric modes

$$\frac{\tanh(\hat{\eta} h)}{\tanh(\hat{\beta} h)} = \frac{4\hat{k}_l^2 \hat{\eta}\hat{\beta}}{\left(2\hat{k}_l^2 - \hat{k}_s^2\right)^2}. \tag{2.57}$$

For shear and compression velocities we get

$$\left(\frac{\hat{c}_s}{\hat{c}_c}\right)^2 = \frac{1 - 2\nu}{2 - 2\nu}. \tag{2.58}$$

In turn, the displacement on the plate surface ($x_2 = h$) in a viscoelastic composite material is equal to

$$\hat{u}_2(i\omega, x_1) = \left[\hat{\eta} A_1 \cosh(\hat{\eta} h) - i\hat{k}_l B_2 \cosh(\hat{\beta} h)\right] \cdot \exp\left(i\hat{k}_l x_1\right), \tag{2.59}$$

where for the complex Lamb wavenumber we get

$$\hat{k}_l(\omega) = \alpha(\omega) - i\beta(\omega), \tag{2.60}$$

and

$$\hat{\eta}^2 = \hat{k}_l^2 - \hat{k}_c^2. \tag{2.61}$$

The displacement component u_2 at two locations along propagation direction x_1 with a distance L from each other is

$$\frac{\left\|\hat{u}_2\left(x_1^2, \omega\right)\right\|}{\left\|\hat{u}_2\left(x_1^1, \omega\right)\right\|} = \exp[\beta(\omega) L]. \tag{2.62}$$

where || || denotes the absolute value of a complex number. On the other hand, the real part of the Lamb wavenumber, is

$$\alpha(\omega)=\frac{\omega}{c_l}. \tag{2.63}$$

where the Lamb wave phase velocity (c_l) is obtained from the experiments.

The complex shear modulus is defined as

$$\hat{G}(\omega)=G'(\omega)+iG''(\omega), \tag{2.64}$$

where

$G'(\omega)$ is the storage shear modulus;

$G''(\omega)$ is the loss shear modulus.

Complex shear modulus satisfies the expression

$$\hat{G}(\omega)=\frac{\rho\omega^2}{\hat{k}_s^2}. \tag{2.65}$$

Dispersion dependencies for G', G'' and η have the form

$$G'(\omega)=\rho\omega^2\frac{1}{\left[\alpha_s^2(\omega)-\beta_s^2(\omega)\right]}, \tag{2.66}$$

$$G''(\omega)=2\rho\omega^2\frac{\alpha_s(\omega)\cdot\beta_s(\omega)}{\left[\alpha_s^2(\omega)-\beta_s^2(\omega)\right]^2}, \tag{2.67}$$

$$\eta=\tan\delta=\frac{2\alpha_s(\omega)\cdot\beta_s(\omega)}{\alpha_s^2(\omega)-\beta_s^2(\omega)}. \tag{2.68}$$

The formation of matrix cracks in polymer matrix composite laminates depends on various factors such as layup, cross-sectional strength of composites, impact strength and rigidity of the polymer matrix, strength, rigidity of fibers, etc. The experimental study of the mechanical damage field in the volume of the composite material must necessarily be accompanied by an assessment of the crack density in the composite samples. Such an assessment is necessary due to the fact that the base of some cracks was not fully opened, and some cracks did not grow in a straight line. To avoid any uncertainties, cracks crossing the entire area of 90^o layers were counted at a fixed distance approximately in the middle of the sample volume.

Figure 2.7 illustrates the average induced crack densities ρ_c (mm^{-1}) in the test set of specimens for different applied stress levels θ_L (MPa), predicted by the elastic model and also obtained from tensile tests.

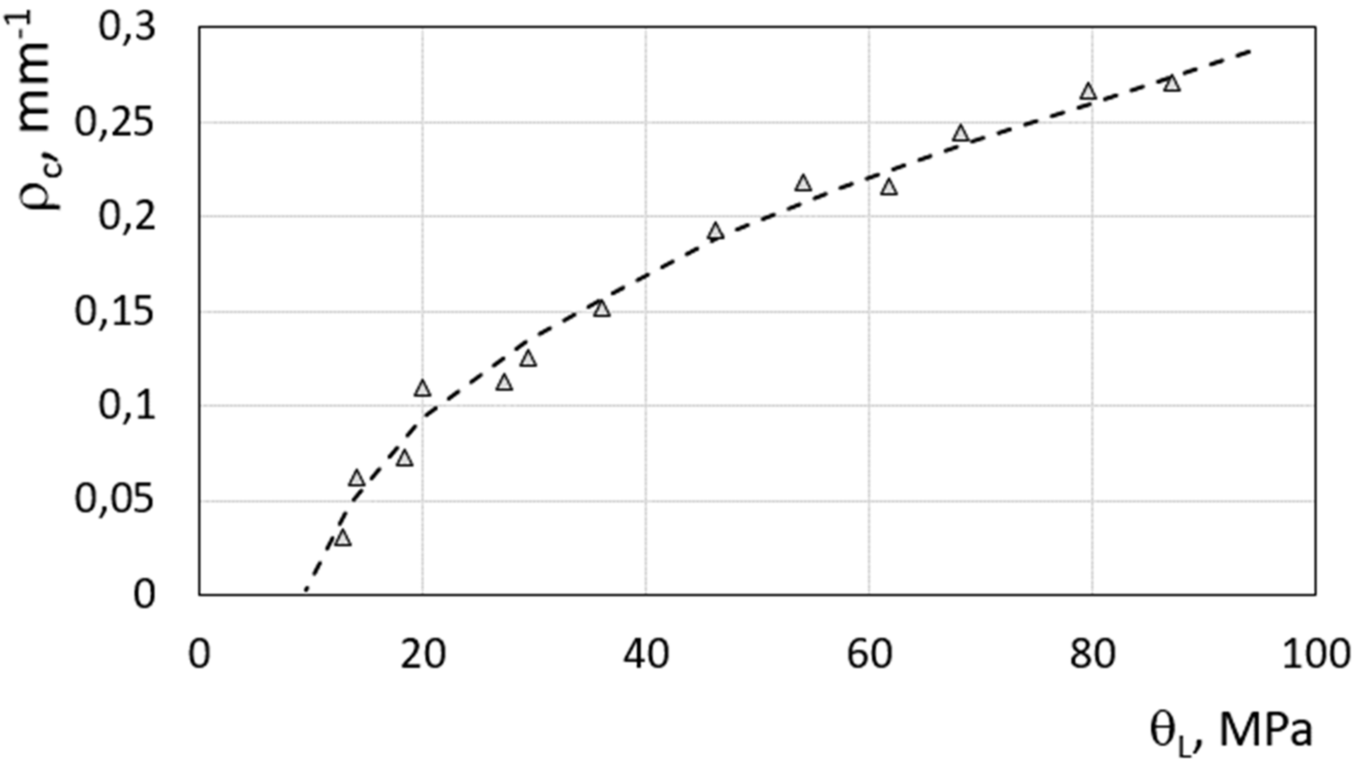

Figure 2.7. Dependence of crack density on stress level in 90^0 layers.

Lamb wave multipath scattering is effectively used for mechanical damage monitoring in laminar composites. In Lamb wave-based structural health monitoring, it is common to pre-record baseline signals when the structure is free of damage. On this basis, the residual field U^{rs}, which subtracts these baseline signals from the measured signals, isolates the effects of the unknown damage introduced between the two measurements. In the single scattering approximation, the residual field only takes into account the direct scattering path of the damage. Therefore, the following relation holds

$$U^{rs}(\omega;s,r)=F(\omega)G_0(\omega;\|u-s\|)\psi(\theta;\theta_1,\theta_2)G_0(\omega;\|r-u\|), \tag{2.69}$$

$$G_0(\omega;d)=\frac{\exp[ik(\omega)d]}{\sqrt{\dfrac{d}{d_r}}}, \tag{2.70}$$

where
$F(\omega)$ is the frequency domain excitation;
ψ (ω; θ_1, θ_2) is the part of scaterring pattern;
$s = [s_x,s_y]^T$ is the location of transmitter;
$r = [r_x,r_y]^T$ is the location of receiver;
$u = [u_x,u_y]^T$ is the location of damage;
θ_1 is the incoming angle;
θ_2 is the outcoming angle;
d is the actual propagation distance;
d_r is the reference distance;
$k = \omega/c_p$ is the wavenumber;
c_p is the phase velocity.

Obstacles that can scatter Lamb waves are associated not only with sources of unknown damage, but also with previously known features in the structure, such as edges, stiffeners, lap joints, and rivets. The residual signal may also include waves that are scattered multiple times between these known scatterers and the target (i.e., the damage).

The residual signal may also include waves that are scattered multiple times between these known scatterers and the target (i.e., the damage). This scattering is considered under the assumption that there are no waves that interact with obstacles more than once. In particular, if we consider waves doubly scattered from both a single scatterer and the damage, the residual field satisfies,

$$U^{rs}(\omega;s,r)=U^{ss}(\omega;s,r)+U^{ds}(\omega;s,r), \qquad (2.71)$$

where

$$U^{ds}(\omega;s,r)=\sum_i\left[F(\omega)G_0(\omega;\|v_i-s\|)G_0(\omega;\|u-v_i\|)G_0(\omega;\|r-u\|)\right]\times$$

$$\times\psi(\omega;\theta_1,\theta_2)\mu_i(\omega;\theta_{1i},\theta_{2i})+$$

$$+\sum_j\left[F(\omega)G_0(\omega;\|u-s\|)G_0\left(\omega;\left\|v^j-u\right\|\right)G_0\left(\omega;\left\|r-v^j\right\|\right)\right]\times$$

$$\times\psi(\omega;\theta_1.\theta_2)\mu_j\left(\omega;\theta_{j1}.\theta_{j2}\right), \qquad (2.72)$$

v_1, v_2 are the coordinates of the scatterers;
μ_1, μ_2 are the coefficients of scattering patterns.

The residential field may be modified as

$$U^{rs}[\omega,r,s]=U^{ss}[\omega,r,s]+U^{ds}[\omega,r,s]+U^{ts}[\omega,r,s], \tag{2.73}$$

where

$$U^{ts}[\omega,r,s]=\sum_{i\neq j}\sum_{j}[F(\omega)G_0(\omega;\left\|v^i-s\right\|G_0\left\|u-v^i\right\|G_0\left\|v^i-u\right\|G_0\left\|r-v^i\right\|\times$$

$$\times[\psi(\omega;\theta_1,\theta_2)\mu_i(\omega;\theta_{i1},\theta_{i2})\mu_j(\omega;\theta_{j1},\theta_{j2})+$$

$$+\sum_{i\neq j}\sum_{j}[F(\omega)G_0(\omega;\left\|v^i-s\right\|)G_0(\omega;\left\|v^j-v^i\right\|)G_0(\omega;\left\|u-v^j\right\|)G_0(\omega;\left\|r-u\right\|)\times$$

$$\times[\psi(\omega;\theta_1,\theta_2)\mu_i(\omega;\theta_{i1},\theta_{i2})\mu_{ij}(\omega;\theta_{j1},\theta_{i2})+$$

$$+\sum_{i\neq j}\sum_{j}[F(\omega)G_0(\omega;\left\|u-s\right\|)G_0(\omega;\left\|v^j-u\right\|)G_0(\omega;\left\|v^j-v^i\right\|)G_0(\omega;\left\|r-v^j\right\|)\times$$

$$\times[\psi(\omega;\theta_1,\theta_2)\mu_{ji}(\omega;\theta_{i1},\theta_{j2})\mu_{ij}(\omega;\theta_{j1},\theta_{i2}). \tag{2.74}$$

In equation (2.74), the theoretical analysis technique used allows us to neglect waves interacting with a single scatterer more than once. Statistical analysis has shown that multipath scattering produces more types of damage than can be obtained with forward scattering. Better resolution imaging can be achieved by extending the imaging technique to handle these multipath scattering signals.

The entire set of known singularities in composite structures can be classified as linear reflectors (e.g. ribs and stiffeners) and point scatterers (e.g. rivets) according to their dimensions. An additional improvement of the above technique is related to the inclusion of multipath scattering characteristics between linear reflectors and damage in the analysis area.

Fermat's principle can be applied to the propagation of acoustic rays. This principle leads to the presence of six possible propagation paths, since the transmitter s = $[s_x,s_y]^T$ and the receiver r = $[r_x,r_y]^T$ are present near two adjacent edges of the structure (i.e. the damage is located at u = $[u_x,u_y]^T$).

A large number of experimental studies on Lamb wave propagation in the volume of anisotropic laminated composites indicate that each linear reflector can be considered as a mirror, creating a virtual transmitter or receiver in a symmetrical position. The location of this virtual transmitter or receiver is determined by the position of the actual and mirror, and is independent of the location of the damage.

The physical effects associated with the presence of multiple scattering paths can be described under the simplifying assumption of the shape of their trajectory as direct scattering paths from virtual/actual transmitters to the damage and back to actual/virtual receivers. All these factors allow us to conclude that taking into account multiple scattering paths is equivalent to increasing the reading paths of the sensor network. In this case for the value of U^{ds} we get

$$U^{ds}(\omega;s,r)=\sum_i F(\omega)[\mu_i(\omega;\theta_1,\theta_2)G_0(\omega;\|u-s^i\|)]\psi(\omega;\theta_1,\theta_2)G_0(\omega;\|r-u\|)+$$

$$+\sum_j F(\omega)G_0(\omega;\|u-s\|)]\psi(\omega;\theta_1,\theta_2)[\mu_j(\omega;\theta_{j1},\theta_{j2})G_0(\omega;\|r^i-u\|)], \quad (2.75)$$

where
$s_1 = [-s_x, s_y]^T$;
$s_2 = [s_x, -s_y]^T$;
$r_1 = [-r_x, r_y]^T$;
$r_2 = [r_x, -r_y]^T$ are the coordinates of the virtual transmitters and receivers.

At the second stage the value Uts can be modified as follows

$$U^{ts}(\omega;s,r)=\sum_i F(\omega)G_0\left(\omega;\|u-s^i\|\right)\mu_i(\omega;\theta_{i1},\theta_{i2})\psi(\omega;\theta_1,\theta_2)G_0\left(\omega;\|r^j-u\|\right)\times$$

$$\times\left[G_0\left(\omega;\|r^j-u\|\right)\mu_j\left(\omega;\theta_{j1},\theta_{j2}\right)\right], \quad (2.76)$$

The presence of multipath scattering associated with one transmitter-receiver pair allows to extend the sensor network consisting of real sensor elements with virtual ones. It should be noted that in this case with such a matrix of sensors, conventional elliptic methods cannot be directly used for damage visualization.

A necessary condition for the application of elliptic methods is that the probability of damage occurrence at any point (*x*, *y*) can be expressed as a linear summation of the probability density functions calculated for each possible transmitter-receiver pair.

In the presence of such effects, the complexity of the application of the considered technique arises. Despite the fact that the residual signal consists of several wave packets due to multipath scattering, the wave packet associated with the virtual pair of sensors cannot be identified, since the location of the damage site is actually unknown. Thus, the probability density function associated with the virtual pair of sensors cannot be obtained.

However, the wave packet for each possible pair of sensors (either real or virtual) can be included in the residual signal. As a rule, the residual signal is a consequence of the effects of an unknown damage introduced between the two measurements. Different wave packets can correspond to the same damage (but with different scattering paths). Taking advantage of this, a modified elliptic method is established for damage visualization.

Multipath scattering of Lamb waves is characterized by a strong influence of the set of scattering patterns μ_i (ω; θ_1, θ_2) and μ_j (ω; θ_1, θ_2) on the amplitude of the wave packet. To suppress their effects, a Gaussian distribution function $f(z_{ij})$ is introduced, which is a function of the time of flight of the wave packet, but not of the amplitude or envelope

$$f\left(z_{ij}\right)=\sum_{n}\frac{1}{\sigma\sqrt{2\pi}}\left[-\frac{z_{ij}(n)^2}{2\sigma^2}\right], \tag{2.77}$$

$$z_{ij}(n)=\sqrt{\left(x-s_x^i\right)^2+\left(y-s_y^i\right)^2}+\sqrt{\left(x-r_x^i\right)^2+\left(y-r_y^i\right)^2}-v_0 t_f\,, \tag{2.78}$$

where
σ is the standart variance;
v_0 is the group velocity at the central particulary effective to produce a resulting image by considering information from al input images;

$$S_1\left(u_x,u_y\right)=\left(\prod_{ij} f\left(z_{ij}\right)\right)^{1/I}, \tag{2.79}$$

where
I is the number of wave packets.

CHAPTER 3
LAMB WAVE PROPAGATION

Non-destructive testing, as well as structural health monitoring, determine the integrity and degradation of composite structures to ensure their operability. The working object of active diagnostics is the ultrasonic transient wave. In order to detect damage, localize and subsequently evaluate damage, understanding the wave propagation characteristics of composites is essential for the successful application of diagnostic methods.

The effects of wave propagation in composites are complex due to the nature of the component heterogeneity, inherent material anisotropy and multilayer construction. These features are the reason why the wave mode velocity is macroscopically dependent on the laminate layup, the direction of wave propagation, frequency and interface conditions.

The propagation of elastic waves in isotropic plate structures is characterized by repeated reflections on the upper and lower surfaces alternately. As a result, the propagation of waves from their mutual interference is guided by the surfaces of the plates. The guided wave can be modeled by imposing surface boundary conditions on the equations of motion.

The effects of wave propagation in composite structures are accompanied by the phenomenon of dispersion, i.e. the propagation velocity of a guided wave along the plate is a function of frequency or, equivalently, wavelength. In particular, guided waves propagating along the plane of an elastic plate with tension-free boundaries are called Lamb waves. Since guided waves remain confined within the structure, they can propagate over large distances, allowing a large area to be surveyed with only a limited number of sensors.

This property makes them well suited for continuous monitoring techniques for ultrasonic testing of entire structures and their elements, which are used in various industrial fields. In isotropic plates, guided waves can be classified into three types according to their polarization (direction of the displacement vector).

Lamb waves polarized in the plane perpendicular to the plate, in the *x-z* plane, are called symmetric (or longitudinal, S) waves and antisymmetric (or flexural, A) waves, while those polarized in the plane of the plate (along the y-axis) are called shear horizontal (SH) waves. SH waves can also be either symmetric or antisymmetric about the midplane.

S and A waves are controlled by plane strain state (displacements *u* and *w*); while SH waves are controlled by antiplane strain (displacement *v* only). Conventionally, S_n and A_n with index n = 0, 1, 2, 3... represent symmetric and antisymmetric Lamb wave modes, respectively; SHn with even and odd index n denote symmetric and antisymmetric SH waves, respectively.

Wave interactions of waves propagating in multilayer composites depend on the properties of the components, geometry, direction of propagation, frequency, and conditions at the interface. For the case when the wavelengths are significantly larger than the dimensions of the composite components (fiber diameters and spacing), each plate can be considered as a sample made of an equivalent homogeneous orthotropic or transversely isotropic material. Such a material is characterized by an axis of symmetry parallel to the fibers.

Scattering of tensile waves was recorded in experimental studies under conditions when the wavelength had the same order of magnitude as the fiber diameter. It should be noted that for flexural waves, scattering appeared when the wavelength was more than an order of magnitude greater than the fiber diameter.

Composite laminates consist of macroscopically homogeneous layers. In this case, wave interactions include not only reflection at the surfaces, but also reflection and refraction between the layers, manifested in the form of resultant waves. These interfering wave packets propagate along the plane of the plate.

The process of Lamb wave propagation in the composite is characterized by the following features. The velocity of the wave packet depends on the direction of its propagation. In addition, a consequence of elastic anisotropy is the loss of pure wave modes. The dependence of the wave velocity on the direction of propagation implies that the direction of the group velocity in general does not coincide with the wave vector (or wave normal).

The distinction between the wave mode types in composites is rather arbitrary. The reason for this is that the three wave mode types are usually related. Engineering practice usually uses symmetric laminates when designing composite structures. Lamb waves in symmetric laminates can be divided into symmetric and antisymmetric modes. For the symmetric modes, one type is designated as quasi-extended. In this case, the dominant component of this symmetric mode of the polarization vector is located along the direction of propagation. The second type of symmetric mode is quasi-horizontal shear. For quasi-horizontal shear, the polarization vector is mainly parallel to the plane of the plate.

In exactly the same way, quasi-flexural and quasi-horizontal shears are generated for antisymmetric types of wave modes. In theoretical analysis, two approaches can be distinguished for the study of Lamb waves in composites. The first method is associated with exact solutions according to the three-dimensional theory of elasticity. The second method is characterized by the inclusion of approximate solutions according to theories of plates.

The dispersion relations of Lamb waves in a composite plate can be obtained by analyzing the mechanical elasticity in three dimensions. Further extension of the transfer matrix methodology in different types of composites was used to obtain the dispersion curves.

The exact solutions of Lamb wave dispersion in composite shells are compared with the results of the Flugge shell theory. It should be noted that the scope of applicability of this methodology is limited only to the case of dispersion relations of phase, but not group velocity.

Calculation of dispersion characteristics of multilayer composites is quite complex due to the presence of transcendental equations. In addition, such calculations should take into account the transient wave response of composites.

Lamb wave packets that propagate in composites along an arbitrary direction generally cause a perturbation in the mechanical strain field. Such a change in the field characteristics involves three components of displacement, i.e., a generalized plane strain arising from the anisotropy of the material.

The displacement of plane harmonic waves can be described in general using 3-D elasticity. The initial stage of the analysis investigates the characteristics of Lamb waves in a single plate (monoclinic plate). In this case, a compact closed dispersion relation can be obtained by separating symmetric and antisymmetric modes using trigonometric functions through the plate thickness.

Special cases are when the waves propagate along the symmetry axis of the material in such a way that mutual separation of S- and A waves as well as SH waves is considered. The final stage of the analysis generates a modified exponential form in the thickness direction to derive the dispersion relation for the composite laminate with special emphasis on symmetric laminates.

The propagation of wave packets is considered in a Cartesian coordinate system with the *z*-axis perpendicular to the midplane of the composite laminate spanned by the *x*- and *y*-axes. The two outer surfaces of the laminate are defined by the coordinates $z = \pm h/2$.

An arbitrary direction θ of the Lamb wave packet is defined counterclockwise with respect to the x-axis. In this case, a fixed layer of the composite laminate with an arbitrary orientation in the global coordinate system (x, y, z) is considered as a monoclinic material having x–y as a plane of symmetry. This fact causes the stress–strain relationships to take the following matrix form:

$$\begin{bmatrix} \sigma_x \\ \sigma_y \\ \sigma_z \\ \tau_{yz} \\ \tau_{xz} \\ \tau_{xy} \end{bmatrix} = \begin{bmatrix} C_{11} & C_{12} & C_{13} & 0 & 0 & C_{16} \\ C_{21} & C_{22} & C_{23} & 0 & 0 & C_{26} \\ C_{31} & C_{32} & C_{33} & 0 & 0 & C_{36} \\ 0 & 0 & 0 & C_{44} & C_{45} & 0 \\ 0 & 0 & 0 & C_{54} & C_{55} & 0 \\ C_{61} & C_{62} & C_{63} & 0 & 0 & C_{66} \end{bmatrix} \cdot \begin{bmatrix} \varepsilon_x \\ \varepsilon_y \\ \varepsilon_z \\ \gamma_{yz} \\ \gamma_{xz} \\ \gamma_{xy} \end{bmatrix}. \tag{3.1}$$

The case where the global coordinate system (x, y, z) does not coincide with the main coordinate system of the material (x', y', z) of each layer, but forms an angle φ with the *x*-axis is considered separately (Fig. 3.1). For such conditions, the stiffness matrix C_{ij} (i, j = 1, 2, 3, 6) in the system (x, y, z) can be obtained from the plate stiffness matrix C_{0ij} in the system (x_0, y_0, z) using the transformation matrix method. The composite material specimen is orthotropic or transversely isotropic with respect to the main axes of the material in (x_0 , y_0, z). The plate stiffness matrix C_{0ij} can be calculated from the plate material properties E_k, ν_{kl} and G_{kl} (k, l = 1, 2, 3).

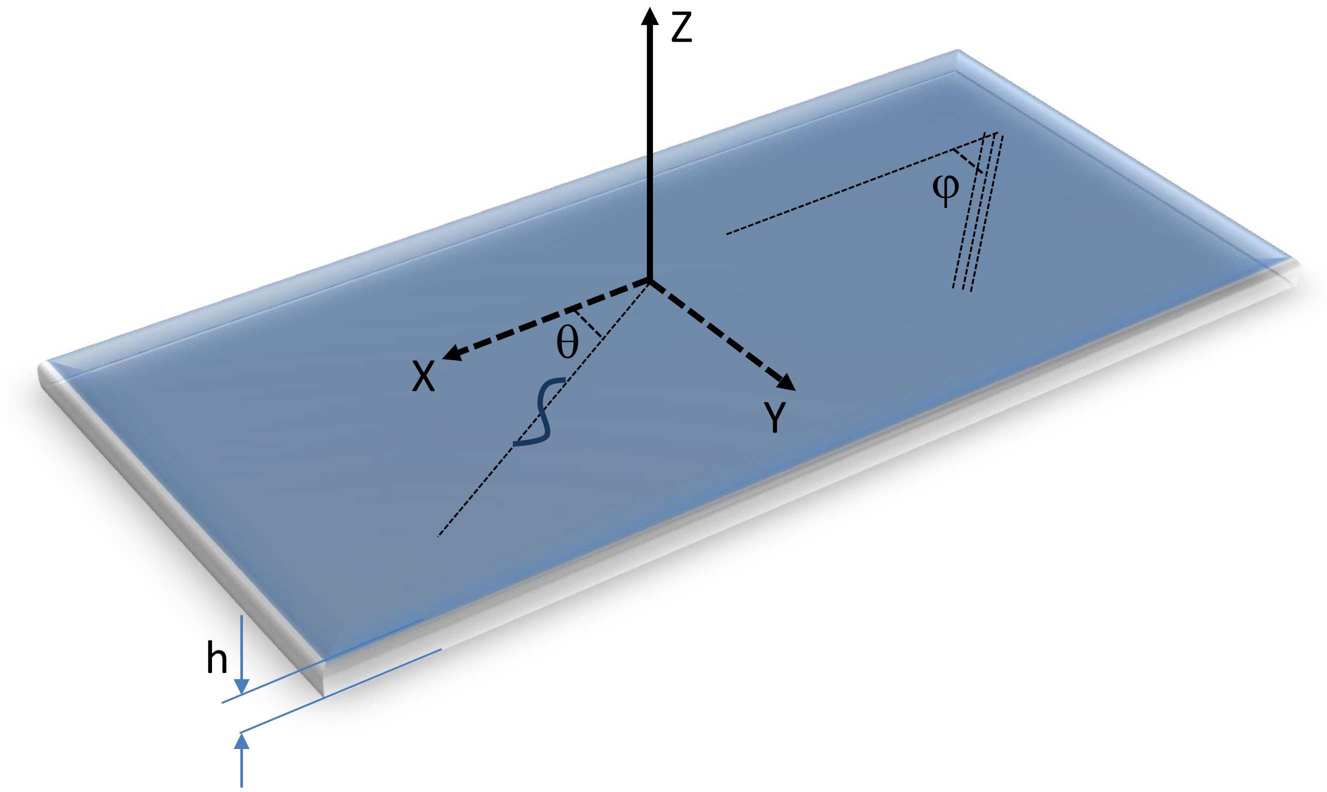

Figure 3.1. Lamb waves propagating in a composite laminate.

The relationships between deformations and displacements are as follows

$$\varepsilon_x = u_x, \ \varepsilon_y = \upsilon_y, \ \varepsilon_z = w_z, \ \gamma_{yz} = \upsilon_z + w_y,$$

$$\gamma_{xz} = u_z + w_x, \ \gamma_{xy} = u_y + \upsilon_x, \tag{3.2}$$

where
u is the displacement in the x direction;
υ is the displacement in the y direction;
w is the displacement in the z direction.

For the case of absence of external forces, the equations of motion can be expressed using the following relationships

$$\sigma_{xx} + \tau_{xy,y} + \tau_{xz,z} = \rho \ddot{u}, \tag{3.3}$$

$$\tau_{xy,x} + \sigma_{yy} + \tau_{yz,z} = \rho \ddot{\upsilon}, \tag{3.4}$$

$$\tau_{xz,x} + \tau_{yz,y} + \sigma_{zz} = \rho \ddot{w}, \tag{3.5}$$

where
ρ is the density of fixed lamina.

The boundary conditions on the upper and lower surfaces can be written using the following equations

$$\sigma_z = \tau_{xz} = \tau_{yz} = 0, \quad z = \pm\frac{h}{2}. \tag{3.6}$$

Lamb wave packets propagate along the plane of a plate with boundaries free of additional mechanical stresses. On the other hand, Lamb waves are standing waves in the *z*-direction of the plate. Therefore, the wave motion can be expressed by a superposition of plane harmonic waves. Each plane harmonic wave propagating in the direction of the wave normal *k* can be described by the relation

$$\{u, \upsilon, w\} = \{U(z), V(z), W(z)\} \exp\{i[(k_x x + k_y y) - \omega t]\} , \tag{3.7}$$

where $k = [k_x, k_y]^T$.

Magnitude of *k* is

$$|k| = \sqrt{k_x^2 + k_y^2} = \frac{\omega}{c_p}, \tag{3.8}$$

$$k = \frac{2\pi}{\lambda}, \tag{3.9}$$

where
λ is the wavelength;
ω is the angular frequency;
c_p is the phase velocity.

Mechanical stresses in each layer are

$$\sigma_x = [C_{11} k_x U + C_{12} k_y - iC_{13} W' + C_{16}(k_y U + k_x V)] \times$$
$$\times \exp\{i[(k_x x + k_y y) - \omega t]\} , \tag{3.10}$$

$$\sigma_y = [C_{12} k_x U + C_{22} k_y - iC_{23} W' + C_{36}(k_y U + k_x V)] \times$$

$$\times \exp\{i[(k_x x + k_y y) - \omega t]\} \ , \tag{3.11}$$

$$\sigma_z = [C_{31} k_x U + C_{32} k_y - iC_{33} W' + C_{63} (k_y U + k_x V)] \ \times$$

$$\times \exp\{i[(k_x x + k_y y) - \omega t]\} \ , \tag{3.12}$$

$$\tau_{yz} = [C_{44} (V' + ik_y W) + C_{45} (U' + ik_x W)] \ \times$$

$$\times \exp\{i[(k_x x + k_y y) - \omega t]\} \ , \tag{3.13}$$

$$\tau_{xz} = [C_{54} (V' + ik_y W) + C_{55} (U' + ik_x W)] \ \times$$

$$\times \exp\{i[(k_x x + k_y y) - \omega t]\} \ , \tag{3.14}$$

$$\tau_{xy} = [C_{61} k_x U + C_{62} k_y V - iC_{63} W' + C_{66} (k_y U + k_x V)] \ \times$$

$$\times \exp\{i[(k_x x + k_y y) - \omega t]\} \ , \tag{3.15}$$

The equations for mechanical displacements for an off-axis composite plate allow separation into symmetric (index "s") and antisymmetric (index "a") wave modes. This separation leads to a particularly simple form of the asymptotic representation

$$U_s = A_s \cos \xi z \, , \quad V_s = B_s \cos \xi z \, , \quad W_s = C_s \sin \xi z \, , \tag{3.16}$$

$$U_a = A_a \cos \xi z \, , \quad V_a = B_a \cos \xi z \, , \quad W_a = C_a \sin \xi z \, , \tag{3.17}$$

where ξ is the fixed variable.

The method of analyzing the resulting system of equations for mechanical displacements and stresses can be divided into two successive stages. In the first approximation, only symmetrical modes of Lamb waves are subjected to theoretical analysis during their group motion along the aisotropic medium, which constitutes the volume of the laminated composite. In addition, a set of compact dispersion relations is analyzed separately for both symmetric and antisymmetric Lamb wave modes. This analysis is performed using metric functions for the corresponding wavelet transform for all points in the laminated composite volume. Symmetrical modes are considered first. At the second stage, the entire sequence of solutions of this system is transformed into a matrix form

$$\begin{bmatrix} \Gamma_{11}-\rho\omega^2 & \Gamma_{12} & \Gamma_{13} \\ \Gamma_{21} & \Gamma_{22}-\rho\omega^2 & \Gamma_{23} \\ \Gamma_{31} & \Gamma_{32} & \Gamma_{33}-\rho\omega^2 \end{bmatrix} \begin{Bmatrix} A_s \\ B_s \\ C_s \end{Bmatrix} = 0, \tag{3.18}$$

Matrix elements can be expressed by the following expressions

$$\Gamma_{11} = C_{11}k_x^2 + 2C_{61}k_x k_y + C_{66}k_y^2 + C_{55}\xi^2, \tag{3.19}$$

$$\Gamma_{12} = C_{61}k_x^2 + (C_{12} + C_{66})k_x k_y + C_{62}k_y^2 + C_{45}\xi^2, \tag{3.20}$$

$$\Gamma_{13} = -i[(C_{31} + C_{55})k_x + (C_{63} + C_{45})k_y]\xi \ , \tag{3.21}$$

$$\Gamma_{22} = C_{66}k_x^2 + 2C_{26}k_x k_y + C_{22}k_y^2 + C_{44}\xi^2, \tag{3.22}$$

$$\Gamma_{23} = -i[(C_{36} + C_{45})k_x + (C_{23} + C_{44})k_y]\xi \ , \tag{3.23}$$

$$\Gamma_{33} = C_{55}k_x^2 + 2C_{45}k_x k_y + C_{44}k_y^2 + C_{33}\xi^2, \tag{3.24}$$

A similar technique is consistently applied to the antisymmetric mode. As a result, the resulting matrix becomes equal to (**Γ** – $\rho\omega^2$**I**), where **I** is the identity matrix. For the case when the Hermitian matrix **Γ** is positive definite, it can be shown that the eigenvalues of the symmetric and antisymmetric modes coincide.

The non-trivial solutions A_s, B_s and C_s participate in the zeroing of the determinant of the characteristic matrix (**Γ** – $\rho\omega^2$**I**), which yields the following sixth-order polynomial in ξ

$$\xi^6 + \alpha_1\xi^4 + \alpha_2\xi^2 + \alpha_3 = 0, \tag{3.25}$$

where α_i are real-valued coefficients of C_{ij}, k, and $\rho\omega^2$.

Analysis of the system of characteristic equations showed that there are three solutions. The properties of these solutions include their positivity, nonzero difference, and discreteness. A_s is a rule, such solutions are related to indices n_j (j = 1, 2, 3). For each index nj in the symmetric modes of the wave packets B_s and C_s, which are related to the symmetric modes of Lamb waves in composite structures, the following relationships can be written in terms of A_s

$$B_s = \frac{\left(\Gamma_{11} - \rho\omega^2\right)\Gamma_{23} - \Gamma_{12}\Gamma_{13}}{\Gamma_{13}\left(\Gamma_{22} - \rho\omega^2\right) - \Gamma_{12}\Gamma_{23}} A_s = RA_s , \tag{3.26}$$

$$C_s = \frac{\Gamma_{12}^2 - \left(\Gamma_{11} - \rho\omega^2\right)\left(\Gamma_{22} - \rho\omega^2\right)}{\Gamma_{13}\left(\Gamma_{22} - \rho\omega^2\right) - \Gamma_{12}\Gamma_{23}} A_s = iSA_s . \tag{3.27}$$

As a result, the modified equations for mechanical shears and stresses will have the form

$$\left(\sigma_z , \tau_{yz} , \tau_{xz}\right)\Big|_{z=h/2} = \sum_{j=1}^{3} [H_{1j} \sin\left(\xi_j z + \varphi\right), H_{2j} \cos\left(\xi_j z + \varphi\right) +$$

$$+ H_{3j} \cos\left(\xi_j z + \varphi\right)] A_j = 0, \tag{3.28}$$

where φ = 0 and π/2 represent anti-symmetric and symmetric Lamb wave modes, and

$$H_{11}(H_{22}H_{33} - H_{23}H_{32})\tan\left(\frac{\xi_1 h}{2} + \varphi\right) +$$

$$+ H_{12}(H_{23}H_{31} - H_{21}H_{33})\tan\left(\frac{\xi_2 h}{2} + \varphi\right) +$$

$$+ H_{13}(H_{21}H_{32} - H_{22}H_{31})\tan\left(\frac{\xi_3 h}{2} + \varphi\right) = 0 . \tag{3.29}$$

The numerical calculation methodology for Lamb wave propagation in composite structures assumes that the interfaces between layers are ideally coupled. For each layer, the displacement components in the corresponding z-axis equation must be modified into exponential forms to account for the inhomogeneity of the multilayer laminate.

$$U = A\exp\left(i\xi z\right), \qquad V = B\exp\left(i\xi z\right), \quad W = -iC\exp\left(i\xi z\right). \tag{3.30}$$

The general solution in each lamina is

$$\{U, V, W\} = \exp\left\{i \left[\left(k_x x + k_y y\right) - \omega t\right]\right\} \cdot \sum_j A_j \left\{1, R_j, S_j\right\} \exp\left(i\xi_j z\right). \tag{3.31}$$

Symmetrical and asymmetrical wave modes in conventional laminates cannot be separated. It should be noted that symmetrical laminates are used in engineering practice when designing composite structures. A reliable method for separating the two types of wave modes is to generate boundary conditions on both the upper and middle planes of the surface. For the upper boundary of the laminate, the boundary conditions can be written as follows

$$\left.\{\sigma_z, \tau_{yz}, \tau_{xz}\}\right|_{z=h/2} = 0, \tag{3.32}$$

The symmetry conditions for the entire laminate allow only half of the entire sample to be analyzed. In a subsequent step, the following conditions are imposed on the stress and displacement components in the midplane for symmetric modes

$$\left.\{u, \upsilon, \sigma_z\}\right|_{z=0} = 0, \tag{3.33}$$

The implicit functional form G (ω, $\boldsymbol{k}$) = 0, or G (ω, k, θ) = 0 can be used to formulate the dispersion relation between ω and k. This dispersion relation can be explicitly solved in the form of real roots $\omega = W(\boldsymbol{k})$, or $\omega = W(k, \theta)$.

The number of possible solutions with different functions W tends to infinity. Such solutions correspond to different wave modes. The phase velocity vector for plane modes is defined as $c_p = (\omega/k)\cdot(\mathbf{k}/|\mathbf{k}|)=(\omega/k^2)\mathbf{k}$. Therefore, its magnitude is $c_p = \omega/k$. The set of all statistical samples k from the origin for c_p at a given frequency forms the so-called velocity curve. The radius vectors of the velocity curves in the direction of a given k represent the admissible dispersion of the phase velocity of the different wave modes.

A set of points in phase space or a slowness curve can be defined by fixing the slowness vector $\mathbf{s} = \mathbf{k}/\omega$. The characteristics of the set of phase points can be simply formed from the velocity curve by geometric inversion, i.e. by mapping through the inverse radius.

The directions of the slowness and phase velocity vectors coincide. Thus, the inverse phase velocities can be measured from the origin to the slowness curves. The distance traveled per unit time is defined as the phase velocity. On the other hand, time as slowness is numerically equal to the time required to travel a unit distance. For volume (non-dispersive) waves, it is convenient to use the slowness curve. The reason for this is the fact that this curve does not depend on x.

In isotropic materials, the phase velocity depends only on the magnitude of the wave vector k. The phase velocity of anisotropic materials depends on the wave vector $\mathbf{k}$, its magnitude, and the direction in which the wave propagates. For experimentally measured wave packets, the phase velocities are measured by tracking the wave peaks.

The numerical value for the group velocity can be determined by tracking the wave packet envelopes, namely $c_g = \mathrm{grad}_k W = \partial W/\partial k$. Provided that the closed form of the implicit function G has been previously determined, the group velocity can also be calculated as

$$c_g = -\left(\frac{\partial G}{\partial k}\right)\cdot\left(\frac{\partial G}{\partial \omega}\right)^{-1}. \tag{3.34}$$

The gradient W (grad_k W) in the polar coordinate system has a radial component $\partial W/\partial k$ in the direction $\boldsymbol{k}$ and an angular component $\partial W/k\partial\theta$, perpendicular to $\boldsymbol{k}$. After the coordinate transformation, the group velocity in the Cartesian coordinate system is equal to

$$\begin{Bmatrix} c_{gx} \\ c_{gy} \end{Bmatrix} = \begin{bmatrix} \cos\theta & -\sin\theta \\ \sin\theta & \cos\theta \end{bmatrix} \begin{Bmatrix} \dfrac{\partial W}{\partial k} \\ \dfrac{\partial W}{k\partial\theta} \end{Bmatrix}, \tag{3.35}$$

where indexes “*x*” and “*y*” represent the components in *x*- and *y*-axes, respectively.

The magnitude and direction of group velocity represents this system of equations

$$c_g = \sqrt{c_{gx}^2 + c_{gy}^2}, \qquad \theta_g = \tan^{-1}\frac{c_{gy}}{c_{gx}}. \tag{3.36}$$

The skew angle θ or steering angleis defined as

$$\theta = \theta_g - \theta'. \tag{3.37}$$

It makes sense to introduce the concept of a wave curve (or wave front curve) as the geometric locus of the group (radial) velocity vectors along all choices c_g from the origin at a given frequency. The radius vector connecting the origin (or source point) with a point on the wave curve is numerically equal to the distance traveled by the elastic disturbance per unit time.

In other words, the geometric concept of a wave curve essentially comes down to the concept of a geometric locus of points (or wave front) recorded per unit time by a disturbance emitted by a point source acting through the origin at time $t = 0$. Wave curves are of great importance in detecting mechanical damage.

The dispersion relation written for each Lamb wave mode can be expressed as an explicit function of W(k; θ). This function is associated with a conical surface in a three-dimensional domain. In addition, the deceleration curve $W(k; \theta) = \omega_0$ is geometrically a level surface of $W(k; \theta)$. Differentiating both sides of the equation with respect to θ, the following relation can be obtained

$$\frac{\partial W}{\partial k}\frac{dk}{d\theta}+\frac{\partial W}{\partial \theta}=0, \tag{3.38}$$

As an example of the use of numerical and symbolic methods for recording mechanical damage in a composite material, we can consider the results of the Lamb wave propagation analysis in graphite/epoxy resin AS4/3502. Two laminates are used in the tests: L_1 ($[+45_6/45_6]s$) and L_2 ($[+45/45/0/90]s$). The numerical results consist of dispersion curves (phase and group velocities) and three characteristic wave curves in two different types of laminates. The characteristic dispersion curves are illustrated in Figs. 3.2 - 3.5. The dimensionless frequency $f_d = \omega h/c_T$ and the dimensionless velocity $\upsilon_{d1} = c_p/c_T$ and $\upsilon_{d2} = c_g/c_T$ are used to normalize the physical frequency and velocity, respectively. In addition, c_T is defined as $(G_{12}/\rho)^{0.5}$ is the velocity of the transverse (in-plane shear) wave in the plate.

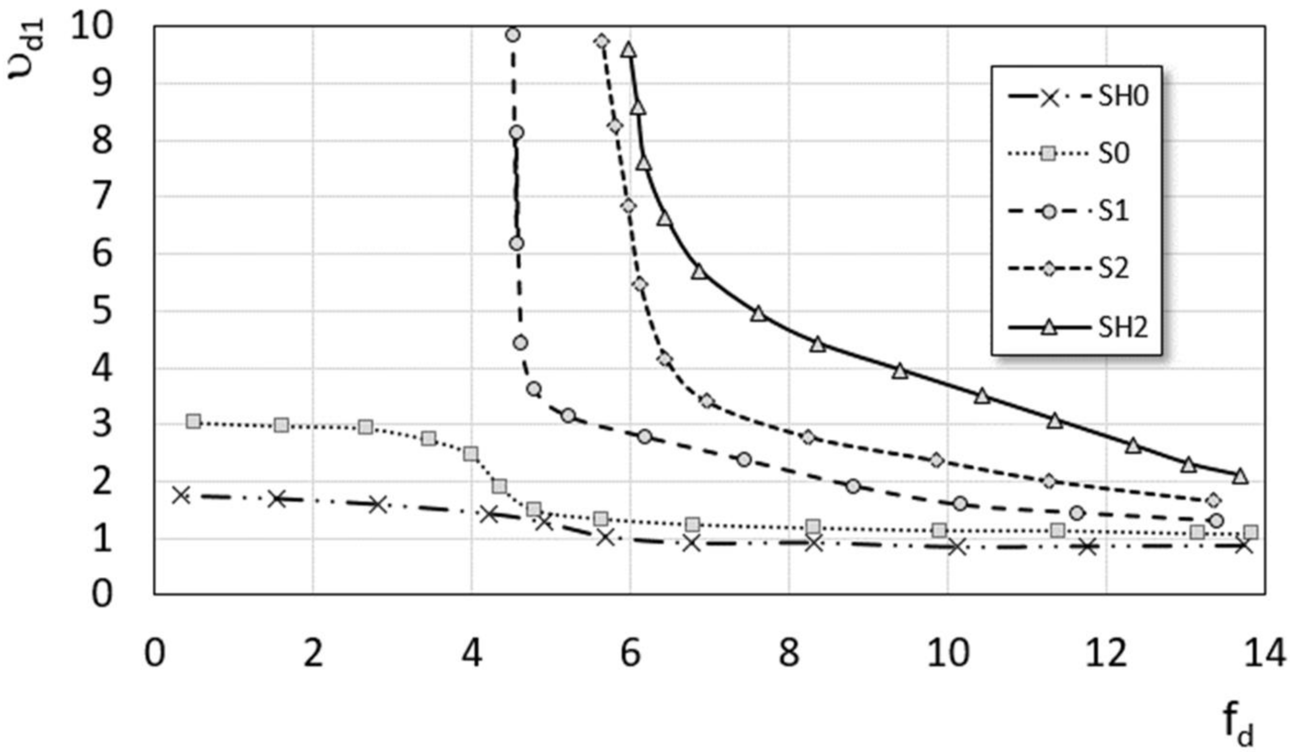

Figure 3.2. Dispersion curves $\upsilon_{d1} = \upsilon_{d1}(f_d)$ of Lamb waves along $\theta = 45^0$ (symmetric modes).

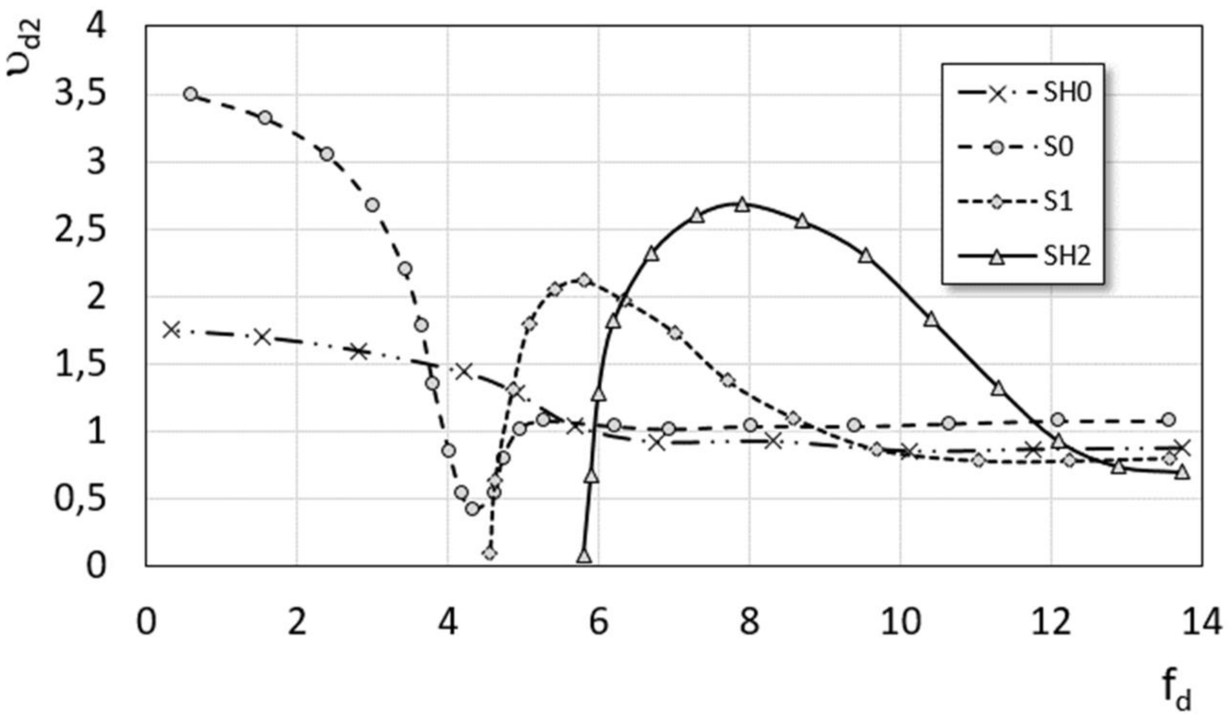

Figure 3.3. Dispersion curves $\upsilon_{d2} = \upsilon_{d2}$ (f_d) of Lamb waves along $\theta = 45^0$ (symmetric modes).

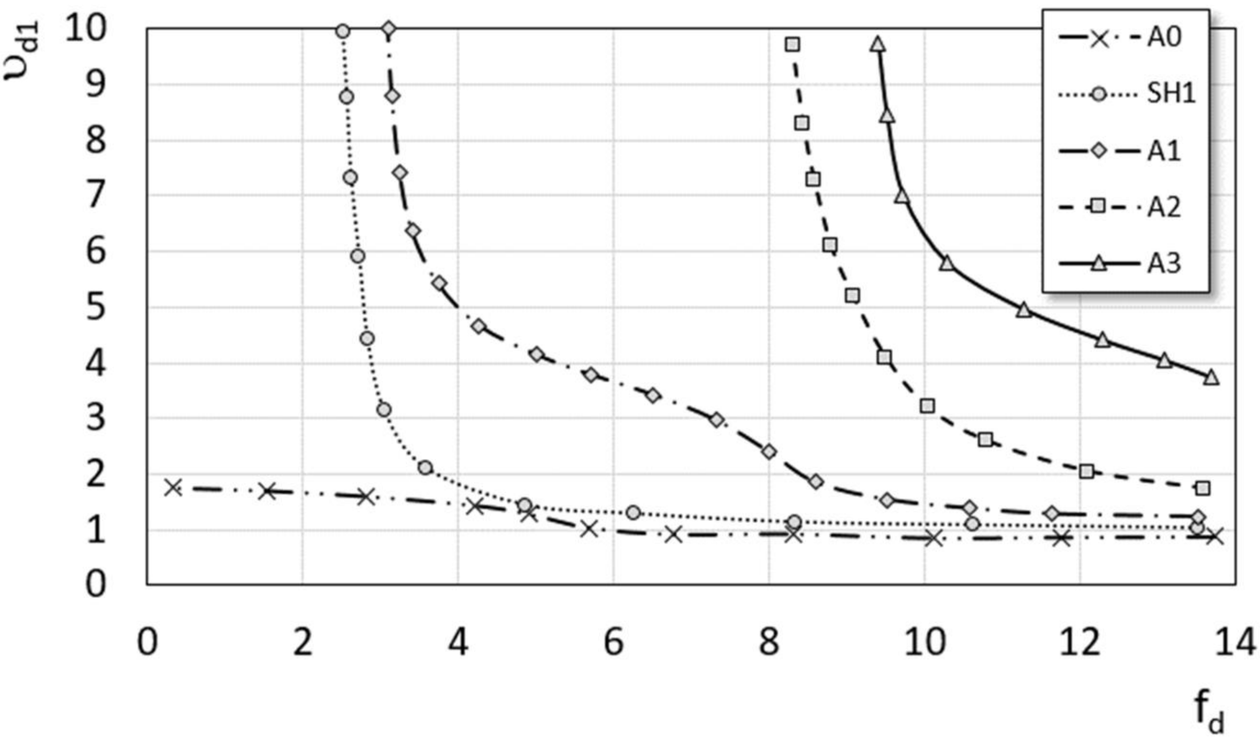

Figure 3.4. Dispersion curves $\upsilon_{d1} = \upsilon_{d1}$ (f_d) of Lamb waves along $\theta = 45^0$ (anti-symmetric modes).

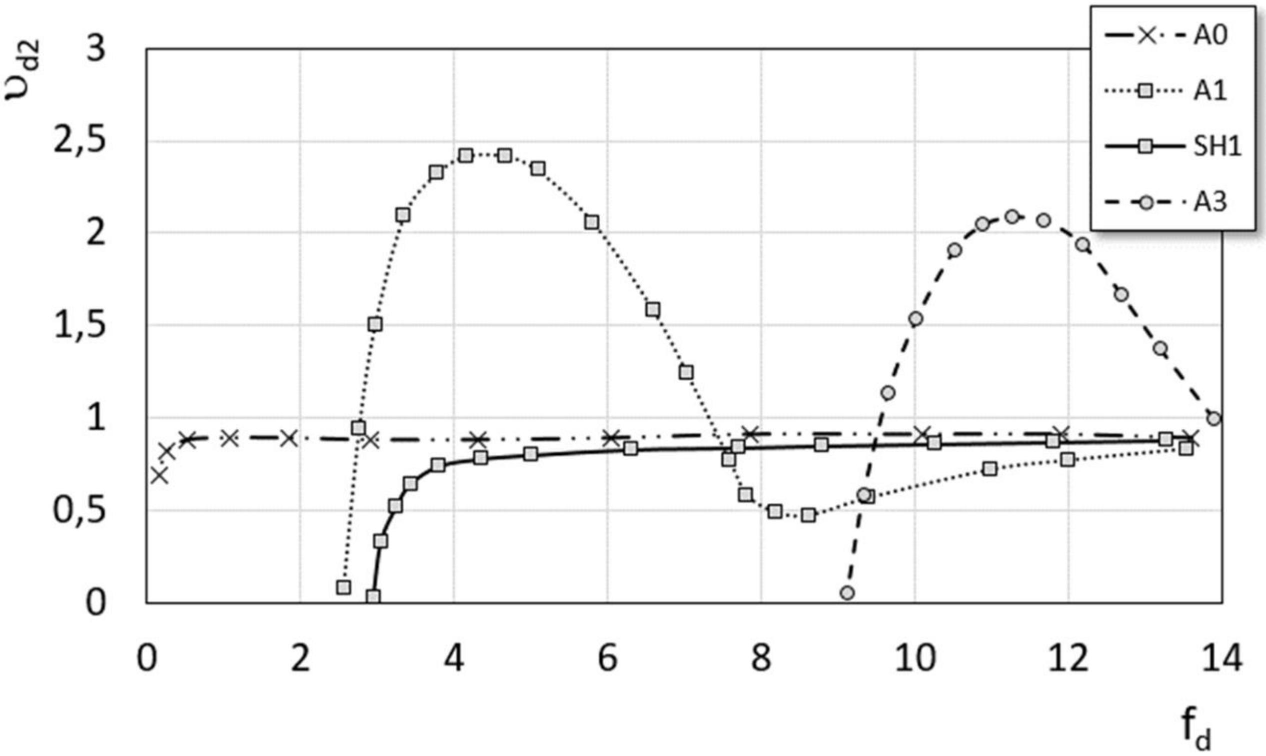

Figure 3.5. Dispersion curves $\upsilon_{d2} = \upsilon_{d2}$ (f_d) of Lamb waves along θ = 45^0 (anti-symmetric modes).

The group velocity of the SH0 and S0 modes has pronounced dispersion characteristics. However, even greater dispersion is observed for symmetric modes in the quasi-isotropic laminate [+45/45/0/90]s . In contrast, the dispersion of the A0 mode in both laminates is weaker beyond $\omega h/c_T = 1$. This feature is effectively used for structural monitoring of laminar composites.

Characteristic wave curves, including velocity, as well as slow Lamb wave curves, propagate in composites at a given frequency. Most of these curves are centrosymmetric about the origin. This feature is a consequence of the fact that the fiber orientation of each individual plate is invariant when h is replaced by $h + p$ (p = const). Moreover, all characteristic wave curves change with frequency due to the dispersion nature.

Characteristic wave curves can be constructed at $\omega h/c_T = 4$ with two symmetric modes (S0 and SH0) and three antisymmetric modes (A0, SH1 and A1). The wavelengths of these modes at a fixed h = 30 are much larger than the fiber diameters and the distance between the fibers. The set of characteristic wave curves considered can vary significantly for different frequencies due to its dispersive nature.

Such a phenomenon as energy focusing is observed for volume waves in anisotropic solids. It should also be noted that energy focusing is also observed for SH wave modes. The deceleration curves have many inflection points. This implies that the same direction of the group velocity can correspond to several directions of wave propagation. The specific directions are determined by the features of the wave front of the Lamb wave packet.

The characteristic frequency of wave packet propagation in thin quasi-isotropic laminated composite is lower than the cutoff frequencies of A1 and S1 modes. Therefore, only fundamental modes (A0, S0 and SH0) exist in thin laminate. The angular dependence of Lamb waves in the laminate [+45/45/0/90] becomes weaker due to quasi-isotropic stacking.

Numerical analysis revealed that the A0 mode has a maximum along 45^0 directions, since the bending of the dominant outer plate is oriented in these directions. The wave curve for each layer of the composite material has no inflection. This fact is a consequence of the quasi-isotropic stacking, not the dispersion characteristics.

Since the velocity curves are approximately independent of the wave propagation direction, the average wavelengths can be estimated using solutions of the characteristic equations. These wavelengths are found to be comparable to the plate thickness, but much larger than the fiber diameters and the fiber spacing. This also shows that the wavelength of A0 is shorter than that of the S0 and SH0 modes.

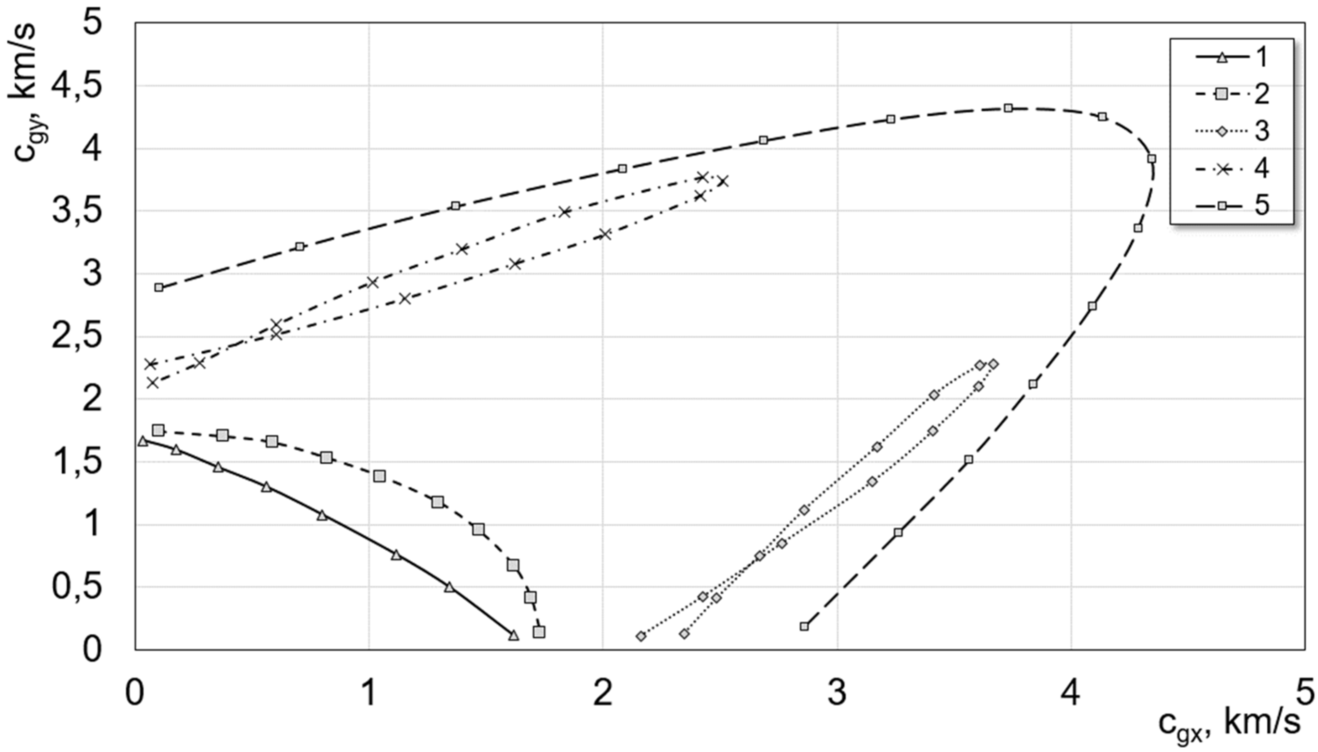

Figure 3.6. Wave curves in the laminate [+456/-456]: 1 – SH1; 2 – A0 (theory); 3 – SH1A; 4 – SH1B; 5 – A1.

Comparison results between theoretical prediction and experimental measurement of Lamb waves in a relatively thick [+45$_6$/ 45$_6$]s laminate are shown in Fig. 3.6. It can be seen from the figure that the exact solutions agree satisfactorily with the experimental results for both symmetric and antisymmetric modes. Even higher modes such as S1 and A1 can be detected experimentally.

The SH0 and S0 modes are difficult to distinguish in the very low frequency range (50 – 150 kHz). This feature is explained by the fact that the difference in arrival time between the two modes is very small. It can be concluded that the two modes have already appeared even before the end of the excitation duration. It should be noted, however, that the exact solution for the S2 modes is not consistent with the experimental results. This difference is determined by the presence of larger scattering signals from inhomogeneities in the high-frequency range for lower wave modes than from the S2 mode itself.

A comparison of the Lamb wave results in the quasi-isotropic [+45/45/0/90]s laminate shows that for excitation frequencies up to 1 MHz, the eight-layer thinner composite exhibits only fundamental guided waves (SH0, S0 and A0) that propagate in the laminate. It should also be noted that the exact solutions are in good agreement with the experimental measurements for both the group velocity dispersions and the wave curves.

Detection of mechanical damage in composites requires the combined use of both the Lamb wave method and the basic concepts of the theory of elasticity and elasticity in non-isotropic media, which in general include laminar composite structures.

The consideration of waves with a fixed wave front shape implies flat deformation conditions in the xz plane, i.e. $\varepsilon_y = \varepsilon_{xy} = \varepsilon_{yz} = 0$, and negligible changes in non-vanishing strains and stresses in the y direction. The basic relations of elasticity theory are the linear stress-strain equations for a rotated composite layer and are given by

$$\sigma = [C]\varepsilon\,, \tag{3.39}$$

where

$\boldsymbol{\sigma} = \{\sigma_x, \sigma_z, \sigma_{xz}\}^T$ is the extended stress vector;

$\boldsymbol{\varepsilon} = \{\varepsilon_x, \varepsilon_z, \varepsilon_{xz}\}^T$ is the extended strain vector.

The ply stiffness matrix [**C**] is

$$[C] = \begin{bmatrix} C_{11} & C_{13} & 0 \\ C_{31} & C_{33} & 0 \\ 0 & 0 & C_{55} \end{bmatrix}. \tag{3.40}$$

For each point in the volume of a sample made of a composite structure, the equilibrium equations for stresses in the x and z directions can be written. The equilibrium equations, in turn, are reduced to equations describing the motion of a wave with a fixed wave front shape. The derivatives of mechanical stresses with respect to y are negligibly small. As a result, the equilibrium equations for mechanical stresses take the form

$$\sigma_{x,x}(x,z,t)+\sigma_{xz,z}(x,z,t)=\rho\ddot{u}(x,z,t), \tag{3.41}$$

$$\sigma_{xz,x}(x,z,t)+\sigma_{z,z}(x,z,t)=\rho\ddot{w}(x,z,t), \tag{3.42}$$

where
u is the displacement component along *x* axis;
w is the displacement component along z axis;
ρ is the average density of the lamina composite.

The thickness displacement variations are satisfactorily described by the kinematic hypothesis of the layer-by-layer theory. The layer-by-layer theory allows for the presence of piecewise (zigzag) fields across the thickness of the composite. The calculation method is simplified by assuming that a typical laminate can be divided into N discrete layers. Each discrete layer can contain one layer, one sublayer, or two sublayers. Consequently, the displacement field in the laminate takes the form

$$u(x,z,t)=\sum_{n=1}^{N}U^n(x,t)\Psi^n(z), \tag{3.43}$$

$$u(x,z,t)=\sum_{n=1}^{N}U^n(x,t)\Psi^n(z), \tag{3.44}$$

where
U^n are the in-plane displacement of fixed layer along *x* axis;
W^n are the in-plane displacement of fixed layer along *y* axis;
$\Psi^n(z)$ are the linear interpolation functions.

The equivalent form of the 2 × N equations of motion across the thickness of the laminate for an infinite strip is:

$$\sum_{n=1}^{N}\left(A_{11}^{mn}U_{xx}^n+B_{13}^{mn}W_x^n-D_{55}^{mn}U^n-B_{55}^{mn}W_x^n+\left[\Psi^m\sigma_{xz}\right]_{-h/2}^{h/2}\right)=\sum_{n=1}^{N}\left(m^{mn}\ddot{U}^n\right). \tag{3.45}$$

$$\sum_{n=1}^{N}\left(B_{55}^{mn}U_x^n + A_{55}^{mn}W_{xx}^n - B_{13}^{mn}U_x^n - D_{33}^{mn}W^n + \left[\Psi^m \sigma_z\right]_{-h/2}^{h/2}\right) = \sum_{n=1}^{N}\left(m^{mn}\ddot{W}^n\right). \quad (3.46)$$

The Fourier transform of the generalized displacement vectors *U* (x,t) and *W* (x,t) for a wave propagating along the *x*-axis of the strip is performed first with respect to the time variable *t*, and then with respect to the spatial variable *x*, following the standard rule

$$\left\{\tilde{U}(x,\omega),\tilde{W}(x,\omega)\right\} = \int_{-\infty}^{\infty}\{U(x,t),W(x,t)\}\exp(-i\omega t)dt, \quad (3.47)$$

$$\left\{\tilde{U}(\xi,\omega),\tilde{W}(\xi,\omega)\right\} = \int_{-\infty}^{\infty}\{U(x,\omega),W(x,\omega)\}\exp(-i\xi x)dx, \quad (3.48)$$

where
ω is the circular frequency;
ξ is the axial wavenumber.

Performing the fast Fourier transform procedure leads to the following form of the main equations

$$\left(\begin{bmatrix} \xi^2 A_{11}^{mn} & -i\xi\left(B_{13}^{mn} - B_{55}^{mn}\right) \\ -i\xi\left(B_{55}^{mn} - B_{13}^{mn}\right) & \xi^2 A_{55}^{mn} + D_{33}^{mn} \end{bmatrix}\right) - \omega^2 \begin{bmatrix} m^{mn} & 0 \\ 0 & 2m^{mn} \end{bmatrix} \begin{Bmatrix} U^n \\ W^n \end{Bmatrix} = \begin{Bmatrix} F_{xz}^m \\ F_z^m \end{Bmatrix}, \quad (3.49)$$

where *m*, *n* = 1, ..., *N*.

The 4*N*-dimensional first-order problem for a given real value of frequency ω and wave number ξ can be formulated as follows

$$[A(\omega) - \xi B(\omega)]\hat{V} = \hat{P}, \quad (3.50)$$

where

$$\hat{P} = \begin{Bmatrix} 0 \\ \hat{F} \end{Bmatrix}_{4N}, \quad \hat{V} = \begin{Bmatrix} \hat{U} \\ \hat{W} \\ \xi\hat{U} \\ \xi\hat{W} \end{Bmatrix}_{4N}, \quad (3.51)$$

$$B(\omega)=\begin{bmatrix} -D_{55}+m\omega^2 & 0 & 0 & 0 \\ 0 & -D_{33}+m\omega^2 & 0 & 0 \\ 0 & 0 & A_{11} & 0 \\ 0 & 0 & 0 & A_{55} \end{bmatrix}, \tag{3.52}$$

$$A(\omega)=\begin{bmatrix} 0 & 0 & -D_{55}+m\omega^2 & 0 \\ 0 & -D_{33}+m\omega^2 & 0 & -D_{33}+m\omega^2 \\ -D_{55}+m\omega^2 & 0 & A_{11} & i(B_{13}-B_{55}) \\ 0 & -D_{33}+m\omega^2 & 0 & A_{55} \end{bmatrix}. \tag{3.53}$$

Non-trivial solutions of the homogeneous part of equation (3.50) are obtained by imposing a boundary condition, the essence of which is that the determinant of the coefficient matrix of the vector *V* must be equal to zero.

This is equivalent to the characteristic dispersion relation of the equation. For a given frequency ω, the characteristic equation has *m* = 1, ... , 4*N* complex eigenvalues $\xi^m = \xi^m_{Re} + i\cdot\xi^m_{Im}$. The complex solutions are the axial wave numbers for all modes existing at the excited frequency.

Among all the derived modes, there are propagating, inhomogeneous, and decaying modes. Accordingly, these modes are characterized by real, complex, and purely imaginary axial wave numbers.

The modal decomposition allows us to decompose the eigenvector *V* in terms of the right eigenvector φ_m as follows

$$\hat{V}=\sum_{m=1}^{4N}V_m\varphi_m=\hat{P}. \tag{3.54}$$

The generalized coefficients V_m can be expressed using the following relationship

$$V_n=\frac{\psi_n^T\hat{P}}{(\xi_n-\xi)D_{mn}}, \tag{3.55}$$

where

$$D_{mn}=\psi_m^T B\,\varphi_m. \tag{3.56}$$

Accordingly, the resulting Green's function in the domain of frequencies and wave numbers has the form

$$\hat{V} = \sum_{m=1}^{4N} \frac{\psi_m^T \hat{P}}{(\xi_m - \xi) D_{mn}} \varphi_m \ . \tag{3.57}$$

The frequency band fluctuations are superimposed on changes in the vector of the external force *F*, which occurs during mechanical displacement. With such superposition, various loading cases can arise. The most common in the deformation of laminar composites are two types of surface loads: a concentrated force at the point $x = x_0$ and a distributed shear force, which is applied over a finite length. The dependence of the force on time can be any. The force vector can be expressed using the following relationship

$$f(x,t) = F_0 \delta(x - x_0) f(t), \tag{3.58}$$

where
F_0 is the amplitude of the force *F*;
$\delta\ (x - x_0)$ is the Dirac delta-function;
F (*t*) is the time dependence of external force.

The double Fourier transform in both time and space variables yields a transformed force vector

$$\hat{F}(\xi,\omega) = F_0 \frac{1}{2\pi} \exp(i\xi\, x_0) F'(\omega), \tag{3.59}$$

where F'(ω) is the transformed forcing vector.

Applied composite sheat stress is

$$\tau_{xy}(x,t) = \tau_0 \left[H(x + \alpha) - H(x - \alpha)\, f(t) \right] \ . \tag{3.60}$$

The shift in the frequency-spatial domain obtained using the inverse Fourier transform has the form

$$\tilde{V}(x,\omega) = \frac{1}{2\pi} \sum_{m=1}^{4\pi} \int_{-\infty}^{\infty} \frac{\psi_m^T \hat{P}}{(\xi_m - \xi) D_{mn}} \varphi_m \exp(i\xi\, x) d\xi \, . \tag{3.61}$$

The integral in equation (3.61) is evaluated numerically using the Cauchy residue theorem. The integrand has singularities only where the denominator is zero, i.e., for the poles $\xi = \xi_m$. Only those poles that lead to propagating Lamb waves are analyzed. Therefore, it is necessary to calculate the residues from these N_d poles

$$\tilde{V}(\xi,\omega) = -i\sum_{m=1}^{N_d}\frac{\psi_m^T\hat{P}}{D_{mn}}\varphi_m \exp(i\xi_m x). \tag{3.62}$$

For a given excitation frequency ω, equation (3.62) represents the frequency response of the system. To decide which poles produce the correct propagating waves, we calculate the group velocity for each eigenvalue from equation

$$c_{gm} = \frac{\psi_m K_\xi \varphi_m}{2\omega_m \psi_m M\, x_m}. \tag{3.63}$$

Verification numerical calculations using the features of Lamb wave propagation in the composite volume were performed according to the following model. A pair of concentrated normal forces of equal magnitude was applied to the upper and lower surfaces of the sample in two different configurations.

The first configuration corresponded to the unidirectionality of the applied forces. In this case, the generation of antisymmetric wave modes was assumed. The second configuration included oppositely directed external deformation forces. Forces of this direction excited symmetric wave modes. In addition, the calculations were performed under the assumption that the time dependence of the applied load *f* (*t*) was modeled by a Gaussian 3-cycle sinusoidal tone burst.

The predicted time response of the fringe at a distance comparable to one third of the specimen length, measured from the point of application of the external force, was calculated in terms of the u and w displacement components. The calculated results showed good agreement with the experimental results for the propagation of the A0 and S0 waves. It should be noted that the widely used semi-analytical finite element method leads to worse predictions for the identification of mechanical damage in the bulk of the composite.

Transit time of each mode is consistent with the predicted group velocity. The S0 mode wave has a high dispersion at the selected excitation frequency. It should be noted that the comparison of the predicted wave response will be sensitive to small errors in the numerical calculation of the wave characteristics. In addition, a small oscillatory component is observed at the beginning of the time response. The initial times are compared with the arrival time of the guided wave mode, which is introduced by the inverse Fourier transform applied to obtain the results.

The use of generalized models of layered laminates allowed us to obtain semi-analytical solutions for the directed propagation of a direct Lamb wave with a fixed profile in laminated composite strips. The model describing the propagation of Lamb wave packets in composite inhomogeneous structures is solved analytically in axial propagation. Three-dimensional theory of layered laminates was used to analyze the variation of displacement with thickness. A double Fourier transform transformed the problem into the frequency-wavenumber domain, where the modal properties of the structure were extracted. Finally, two inverse Fourier transforms provide a solution to the problem in terms of displacements.

High-speed dynamic events in laminar composites with short dynamic response times are described quite effectively by explicit dynamic analysis of Lamb wave propagation. The explicit central-difference
time integration rule satisfies the equations of dynamic equilibrium at the beginning of each time increment *t*. The instantaneous accelerations calculated at time t are used to further determine the velocity at time $t + \Delta t/2$. On the other hand, the displacement solution is related to time $t + \Delta t$. The equations of motion for the body are integrated as

$$\dot{u}_{i+1/2} = \dot{u}_{i-1/2} + \frac{\Delta t_{i+1} + \Delta t_i}{2}\ddot{u}_i, \tag{3.64}$$

$$u_{i+1} = u_i + \Delta t_{i+1}\dot{u}_{i+1/2}, \tag{3.65}$$

where *u* is the displacement vector.

For this model, the source of deformation regions in a laminar composite is a piezoelectric sensor, the coordinates of which are fixed on the side surface of the composite sample are assumed to be known.

An additional limitation of the calculation model is that the mechanical property of the piezoelectric sensor is transversely isotropic. The direction of placement of the sensor is coaxial with the polarization direction, which is specified by the Z axis (perpendicular to the disk plane, as shown in Fig. 3.7). In this case, the associated linear electromechanical constitutive relations can be expressed as

$$\begin{Bmatrix} q_1 \\ q_2 \\ q_3 \\ \varepsilon_{11} \\ \varepsilon_{22} \\ \varepsilon_{33} \\ \varepsilon_{23} \\ \varepsilon_{13} \\ \varepsilon_{12} \end{Bmatrix} = \begin{bmatrix} D_1 & 0 & 0 & 0 & 0 & 0 & 0 & d_{15} & 0 \\ 0 & D_1 & 0 & 0 & 0 & 0 & d_{15} & 0 & 0 \\ 0 & 0 & D_3 & d_{31} & d_{31} & d_{33} & 0 & 0 & 0 \\ 0 & 0 & d_{31} & S_{11} & S_{12} & S_{13} & 0 & 0 & 0 \\ 0 & 0 & d_{31} & S_{12} & S_{11} & S_{13} & 0 & 0 & 0 \\ 0 & 0 & d_{33} & S_{13} & S_{13} & S_{33} & 0 & 0 & 0 \\ 0 & d_{15} & 0 & 0 & 0 & 0 & S_{44} & 0 & 0 \\ d_{15} & 0 & 0 & 0 & 0 & 0 & 0 & S_{44} & 0 \\ 0 & 0 & 0 & 0 & 0 & 0 & 0 & 0 & 2(S_{11} - S_{12}) \end{bmatrix} \cdot \begin{Bmatrix} E_1 \\ E_2 \\ E_3 \\ \sigma_{11} \\ \sigma_{22} \\ \sigma_{33} \\ \sigma_{23} \\ \sigma_{13} \\ \sigma_{12} \end{Bmatrix}, \tag{3.66}$$

where
q_i is the electric displacements;
E_i is the electric field;

ε_{ij} are the mechanical strains;
σ_{ij} are the mechanical stresses;
d_{ij} are the piezoelectric strain constants;
s_{ij} are the compliance constants.

Simplification of material equations in a plane-stressed state is possible under the assumption that for a piezoelectric sensor there is no electric field in the plane $E_1 = E_2 = 0$. In this case, the following representation is valid for the material equations

$$q_3 = D_3 E_3 + d_{31}(\sigma_{11} + \sigma_{22}), \quad (3.67)$$

$$\sigma_{11} = \frac{E}{1-\upsilon^2}\left[(\varepsilon_{11} + \upsilon\varepsilon_{22}) - (1+\upsilon)d_{31}E_3\right], \quad (3.68)$$

$$\sigma_{22} = \frac{E}{1-\upsilon^2}\left[(\varepsilon_{22} + \upsilon\varepsilon_{11}) - (1+\upsilon)d_{31}E_3\right], \quad (3.69)$$

where
E is the Young's module;
υ is the Poisson's ratio in the plane of piezoelectric sensor.

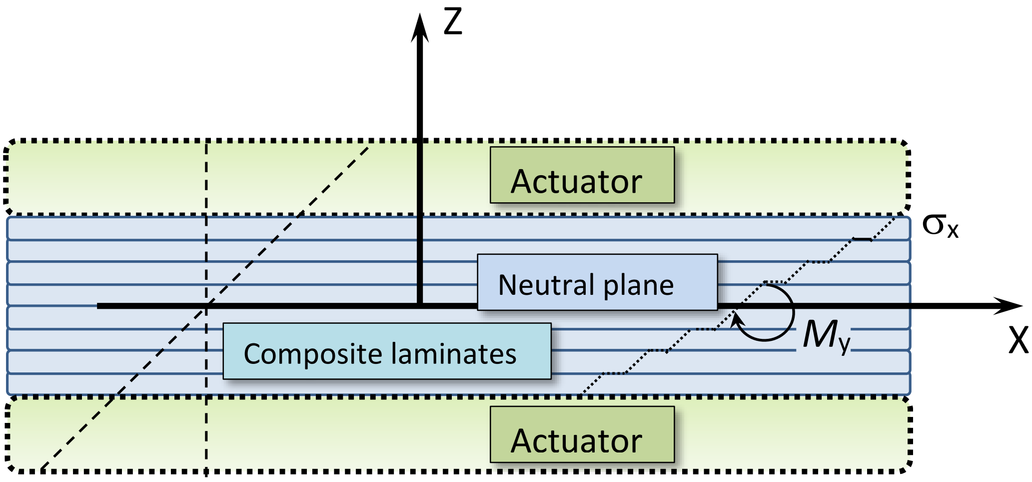

Figure 3.7. Variations in deformation and mechanical stress in composite laminate.

The resulting values of the forces and moments of forces acting in the volume of a mechanically stressed laminar composite satisfy the following relationships

$$\begin{Bmatrix} N_x \\ N_y \\ N_{xy} \end{Bmatrix} = \int_{-t_p/2}^{+t_p/2} \begin{Bmatrix} \sigma_x \\ \sigma_y \\ \sigma_{xy} \end{Bmatrix} dz . \tag{3.70}$$

The most common two configurations correspond to the arrangement of disk sensors with a symmetric composite plate. The first configuration includes a single-disk sensor. In this case, both symmetric (S0) and asymmetric (A0) Lamb wave modes can be excited simultaneously. The reason for this effect is that the composite plate is activated by shear and bending.

In the case of a double-disk sensor, the corresponding sensors produce either pure shear or pure bending. Therefore, symmetric and asymmetric Lamb wave modes can be generated separately.

The resulting displacement, shear force and bending moment generated by the circular disk of the piezoelectric sensor on symmetric quasi-isotropic composite plates are uniform along the edges of the sample.

In this case, elastic waves are excited in the main plates and propagate in the direction perpendicular to the edge of the sensors. In the relatively "low frequency" region, a single piezoelectric sensor simultaneously excites the S0 and A0 modes of the Lamb wave. On the other hand, double disks can generate S0 or A0 modes separately. The relationship between mechanical stresses and strains in the *x*- and *y*- directions is described by the following equations

$$\sigma_x = \frac{E}{1-\upsilon}\left[\frac{\varepsilon_x + \upsilon\varepsilon_y}{1+\upsilon} - d_{31}E_3\right] = \frac{E}{1-\upsilon}\left[\frac{\varepsilon_x + \upsilon\varepsilon_y}{1+\upsilon}\frac{z}{t_n} - \Lambda\right] , \tag{3.71}$$

$$\sigma_y = \frac{E}{1-\upsilon}\left[\frac{\varepsilon_y + \upsilon\varepsilon_x}{1+\upsilon} - d_{31}E_3\right] = \frac{E}{1-\upsilon}\left[\frac{\varepsilon_y + \upsilon\varepsilon_x}{1+\upsilon}\frac{z}{t_n} - \Lambda\right] , \tag{3.72}$$

where Λ is the piezoelectric strain.

In the neutral plane region of the integrated configuration of the piezoelectric sensors and the base plate (see Fig. 3.8), for the case of one sensor, the bending moment per unit length can be given as

$$M_x = \int_{-t_n}^{t_p - t_n} \sigma_x^{(p)} z\, dz , \quad z = 0 , \tag{3.73}$$

and for assymmetric mode

$$M_x = \int_{-t_n/2}^{t_p/2} \sigma_x^{(p)} z\,dz\,, \qquad z = 0\,. \tag{3.74}$$

The proposed finite difference stress excitation models work effectively and provide very good excitation of Lamb waves at fixed frequencies for both isotropic plates and quasi-isotropic composite laminates. The calculation results are illustrated in Fig. 3.8.

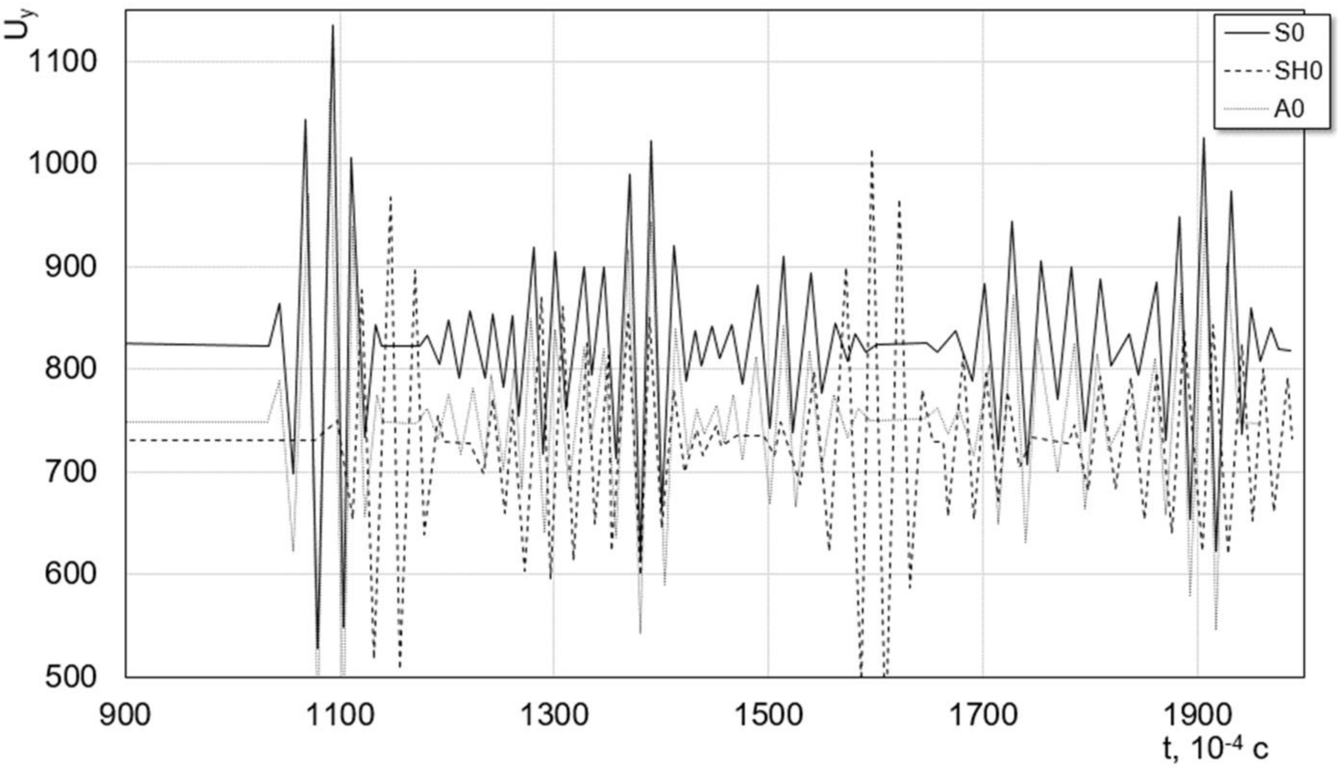

Figure 3.8. Finite element model’s results for 3-D shell elements x-displacement mode.

A single piezoelectric sensor can excite both S0 and A0 modes simultaneously. Alternatively, with multiple sensors evenly spaced over the side surface of a laminated composite sample, either S0 or A0 can be excited separately. Numerical calculations with the finite difference model, which uses the 3-D method with displacement and shear force excitation, indicate that the group velocities of the A0 mode corresponding to one and several sensors are significantly different. However, there is no such difference for the S0 mode.

CHAPTER 4
DELAMINATION DETECTION IN COMPOSITES

Lamb waves are elastic disturbances resulting from the superposition of longitudinal waves (P-waves) and shear waves (S-waves). Shear displacements occur both in the direction of wave propagation and perpendicular to it. Compared to body waves, which propagate in solids far from the boundaries of the free surface, Lamb waves can propagate over large distances. With this type of propagation, energy losses are minimal, as is the attenuation of the amplitude.

This feature allows Lamb waves with different signal-to-noise ratios to be detected. Detailed detection is possible even in highly dispersed/fading materials, such as polymer matrix composites. The slight attenuation of wave packets is caused by the presence of two closely spaced parallel free boundaries of the surface compared to the wavelength. This condition is most often satisfied for plate or shell structural elements. The propagation of Lamb waves inside a composite material is determined by the presence of defects and damages, like any other boundary condition. This phenomenon is the basis for the use of Lamb waves in detecting mechanical damage in non-destructive testing methods.

Two-mode Lamb waves can exist simultaneously in symmetric (Sn) and antisymmetric (An) states. These modes can propagate independently of each other. The subscript (n) is an integer indicating the mode order or the number of inflection points found in the wave deformation field across the thickness.

When a wave packet propagates in a composite sample of finite thickness, there is an infinite number of multimode symmetric and antisymmetric Lamb waves. The shear components of horizontal (SHn) waves differ from each other in their phase and group velocities, as well as in the distribution of displacements and stresses across the thickness of the plate.

Most of the experimental studies use only input signals that excite uniquely fundamental (without inflection points) antisymmetric (A0) and symmetric (S0) Lamb waves. Such a technique helps to avoid the increased complexity in interpreting the collected wave signals, which contain interference of multiple modes.

In addition to the existence of several wave modes, Lamb waves are dispersive, i.e. the propagation velocity of each wave mode and their order/excitation depend on the excitation frequency. This behavior is predicted by the corresponding characteristic equations of Lamb waves and is represented by dispersion curves, i.e. curves of the dependence of the propagation velocity on the frequency and thickness.

The use of composite allows for the application of individual designs, applying appropriate strength/stiffness in the required directions, while minimizing the weight of the structure. It should be noted that the response to damage of composite structures on the one hand and metallic (isotropic) systems on the other is fundamentally different.

The use of Lamb waves has shown significant promise for damage detection in composite structures. However, most of the theoretical developments in the analysis that allow accurate application of Lamb waves have been performed mainly for isotropic materials or for anisotropic materials with orthotropic and higher symmetry.

Lamb wave propagation in composites is quite difficult to predict. The reason for the poor predictability is the significant anisotropy of the material, as well as the strong attenuation/dispersion behavior of the wave. Composite material parameters such as fiber volume fractions, stacking sequence, and types of matrices/reinforcements used greatly affect wave propagation characteristics.

The direction of propagation of wave packets in composite plates is directly related to the wavefront velocity, which varies with frequency. Composite laminates in simplified analysis models are assumed to have orthotropic or higher symmetry to generate dispersion curves.

One of the simplest methods for generating Lamb wave dispersion curves is to use the effective stiffness approach. In this methodology, a geometrically weighted average of the component property values is used as the average material constants for the entire laminate.

An additional methodology is based on the classical laminated plate theory. It should be noted that the classical laminated plate theory cannot accurately predict the dispersion behavior of Lamb waves at sufficiently high frequencies.

Both analytical techniques have high computational efficiency. However, the classical laminated plate theory and higher order theories are only approximations and cannot accurately predict the higher modes of Lamb waves at higher frequencies.

The solution to this problem, at least partially, is the approximation method for a multilayer transversely isotropic material. The approximation method is based on the analysis of a set of stiffness characteristics. Such an analysis assumes the possibility of approximation by polynomial interpolation functions for the thickness displacement distribution.

An additional hybrid method involves the use of a semi-analytical finite element, which uses the finite element method to discretize the cross-section and describes the displacement along the wave propagation using analytical simple harmonic functions. The most accurate method for calculating the propagation characteristics of Lamb waves in composites is the linear 3D elastic properties method.

Analytical equations can describe the propagation of Lamb waves in the principal plane (with simultaneous shear-horizontal mode separation) in a single-layer monoclinic composite plate. A generalization of these analytical equations includes a solution for an n-layer plate based on the transfer matrix approach.

The state of a general monoclinic laminate composite under stress-free conditions can only be described by a discrete set of analytical dispersion equations.

The propagation of the fundamental mode Lamb wave in an arbitrary orthotropic laminate can be analyzed in detail based on three-dimensional linear elasticity theory and the transfer matrix. Numerical calculation of the energy distribution through the thickness is performed as a result of the analysis of the real part of stress and mechanical strain.

For a periodically layered composite with orthotropic symmetry, a closed-loop algebraic solution for elastic wave propagation is an effective technique. The corresponding numerical calculations are reduced to the use of a sixth-order matrix equation and a transfer matrix analysis. A composite material with monoclinic symmetry provides the Lamb wave packet propagation dynamics based on the slowness vector and the transfer matrix approach for propagation along the symmetry axis.

The existence of a coupling between longitudinal and shear waves is the reason for the plate wave for the n-layer orthotropic laminate. The analysis of the plate wave dynamics is based on both the transfer matrix and global matrix approaches.

The propagation and dispersion characteristics of Lamb waves can be derived and analyzed on the basis of orthotropic and higher symmetry for n-layer composite laminates, including several simplifications and approximations (characterizing wave propagation only in certain directions). The adoption of the orthotropic hypothesis may be invalid if the actuators and sensors in an orthotropic or transversely isotropic laminate are mounted in a non-principal direction or if the layup is symmetric but not balanced.

This leads to a lower monoclinic symmetry, for which the solution is provided for only one layer. Therefore, to significantly improve this analysis technique, a complete derivation of the Lamb wave equations for n-layer monoclinic composite laminates based on 3D linear elasticity is needed. The existence of an effective coupling between Lamb waves and horizontal shear waves is in turn related to the existence of displacement fields in all three directions.

The computational method uses the partial wave method in combination with the global matrix approach to numerically solve the Lamb wave equations. A robust step-by-step solution for generating Lamb wave dispersion curves is the main objective for this part of the Lamb wave packet propagation analysis.

First of all, it is necessary to consider the shear-stress relationship. The tensor form of the stress-strain relationship in a Cartesian coordinate system for an anisotropic solid medium assuming linear elastic behavior is as follows

$$\sigma_{ij} = c_{ijkl}\varepsilon_{kl}, \tag{4.1}$$

$$\varepsilon_{ij} = s_{ijkl}\sigma_{kl}, \tag{4.2}$$

where
c_{ijkl} is the stiffness tensor;
s_{ijkl} is the compliance tensor.

The dependence of the linear elastic deformation on the mechanical displacement can be determined by the following relationship

$$\varepsilon_{ij} = \frac{1}{2}\left(\frac{\partial u_i}{\partial x_j} + \frac{\partial u_j}{\partial x_i}\right). \tag{4.3}$$

In turn, the generalized equation of motion is determined by the components of the displacement

$$\frac{\partial \sigma_{ij}}{\partial x_j} = \rho \frac{\partial^2 u_i}{\partial t^2}. \tag{4.4}$$

Each layer in the laminar composite according to the calculation model is described by a local $\{x_1^*, x_2^*, x_3^*\}$ and global $\{x_1, x_2, x_3\}$ coordinate system.

The mechanical stress in the global system is equal to

$$\{\sigma\} = [T_\sigma]\{\sigma^*\}, \tag{4.5}$$

where $[T_\sigma]$ is the stress transformation matrix.

The local coordinate x_3^* coincides with the global coordinate (x_3), thereby defining φ as the rotation angle around the x_3 axis. In this case, the stress transformation matrix $[T_r]$ is defined by the matrix form

$$[T_\sigma] = \begin{bmatrix} c^2 & s^2 & 0 & 0 & 0 & 2cs \\ s^2 & c^2 & 0 & 0 & 0 & -2cs \\ 0 & 0 & 1 & 0 & 0 & 0 \\ 0 & 0 & 0 & c & -s & 0 \\ 0 & 0 & 0 & s & c & 0 \\ -cs & cs & 0 & 0 & 0 & c^2 - s^2 \end{bmatrix}, \tag{4.6}$$

where
c = cos φ;
s = sin φ.

The transformation of the stiffness matrix from the local to the global coordinate system can be performed using the following algorithm

$$[c]=[T_\sigma][c^*][T_\varepsilon]^{-1}. \tag{4.7}$$

The propagation of Lamb wave packets is described by the governing equations for the case of composite materials that exhibit orthotropic and higher degrees of symmetry.

It should be noted, however, that it is necessary to consider lower monoclinic symmetry for the excitation and propagation mode of wave packets in an orthotropic or transversely isotropic laminate along a non-principal direction, or if the stacking is symmetric but not balanced. For example, this will be observed as a result of the installation of wave signal generators that can be fixed in a non-principal direction of the commonly used orthotropic or lower symmetry of the plate.

These factors lead to the fact that the Lamb wave equations will be derived for monoclinic symmetry, which can be used for any material symmetry that is higher than monoclinic.

The stress-strain relationship for monoclinic composite material can be expressed as

$$\begin{Bmatrix} \sigma_{11} \\ \sigma_{22} \\ \sigma_{33} \\ \sigma_{23} \\ \sigma_{13} \\ \sigma_{12} \end{Bmatrix} = \begin{bmatrix} c_{11} & c_{12} & c_{13} & 0 & 0 & c_{16} \\ c_{12} & c_{22} & c_{23} & 0 & 0 & c_{26} \\ c_{13} & c_{23} & c_{33} & 0 & 0 & c_{36} \\ 0 & 0 & 0 & c_{44} & c_{45} & 0 \\ 0 & 0 & 0 & c_{45} & c_{55} & 0 \\ c_{16} & c_{26} & c_{36} & 0 & 0 & c_{66} \end{bmatrix} \begin{Bmatrix} \varepsilon_{11} \\ \varepsilon_{22} \\ \varepsilon_{33} \\ 2\varepsilon_{23} \\ 2\varepsilon_{13} \\ 2\varepsilon_{12} \end{Bmatrix}. \tag{4.8}$$

Let us consider in more detail the model of Lamb wave propagation in a monoclinic material in order to derive representative equations. At the first stage, we will analyze the displacement field in all three directions in comparison with the consideration of only the propagation of wave packets along the principal directions.

The consideration of Lamb waves can be non-isotropic for all directions in a laminar composite sample. Substituting the displacement fields ui with The general equilibrium equations for the displacement field ui have the form

$$K_{ij}(k_3)U_j = 0, \tag{4.9}$$

where the matrix elements have the form

$$K_{11} = c_{11}k_1^2 + c_{66}k_2^2 + c_{55}k_3^2 + 2c_{16}k_1k_2 - \rho\omega^2, \tag{4.10}$$

$$K_{12} = c_{16}k_1^2 + c_{26}k_2^2 + c_{45}k_3^2 + (c_{12} + c_{66})k_1k_2 , \tag{4.11}$$

$$K_{13} = (c_{13} + c_{55})k_1k_3 + (c_{36} + c_{45})k_2k_3 , \tag{4.12}$$

$$K_{22} = c_{66}k_1^2 + c_{22}k_2^2 + c_{44}k_3^2 + 2c_{26}k_1k_2 - \rho\omega^2 , \tag{4.13}$$

$$K_{23} = (c_{36} + c_{45})k_1k_3 + (c_{23} + c_{44})k_2k_3 , \tag{4.14}$$

$$K_{33} = c_{55}k_1^2 + c_{44}k_2^2 + c_{33}k_3^2 + 2c_{45}k_1k_2 - \rho\omega^2 . \tag{4.15}$$

The condition for the presence of a set of non-trivial solutions to a system of equations can be reduced to the form

$$\det(K_{ij}) = 0 \tag{4.16}$$

or

$$D_1k_3^6 + D_2k_{31}^4 + D_3k_3^2 + D_4 = 0 . \tag{4.17}$$

The three roots of k_3^2 correspond to one pair of quasi-longitudinal and two pairs of quasi-shear modes. The six roots of k_3 can be divided into three pairs, with the constituent elements of each pair being negative with respect to each other. Each pair represents an ascending and descending traveling wave making the same angle with the x_1 axis.

The relationship between mechanical stresses and stiffening elements for the case of boundary conditions without tension takes the form

$$\sigma_{33} = c_{13}\frac{\partial u_1}{\partial x_1} + c_{23}\frac{\partial u_2}{\partial x_2} + c_{33}\frac{\partial u_3}{\partial x_3} + c_{36}\left(\frac{\partial u_2}{\partial x_1} + \frac{\partial u_1}{\partial x_2}\right), \tag{4.18}$$

$$\sigma_{13} = c_{45}\left(\frac{\partial u_2}{\partial x_3} + \frac{\partial u_3}{\partial x_2}\right) + c_{55}\left(\frac{\partial u_3}{\partial x_1} + \frac{\partial u_1}{\partial x_3}\right), \tag{4.19}$$

$$\sigma_{23} = c_{44}\left(\frac{\partial u_2}{\partial x_3} + \frac{\partial u_3}{\partial x_2}\right) + c_{45}\left(\frac{\partial u_3}{\partial x_1} + \frac{\partial u_1}{\partial x_3}\right). \tag{4.20}$$

Free boundary conditions at the top and bottom surfaces of lamina composites are

$$\sigma_{33}\big|_{x_3=\pm h} = \sigma_{13}\big|_{x_3=\pm h} = \sigma_{23}\big|_{x_3=\pm h} = 0\,. \tag{4.21}$$

The displacements (u_1, u_2, u_3) can be represented as functions of unit amplitude (U_{1q}), by defining the ratios of the displacement components as $V_q = U_{2q}/U_{1q}$ and $W_q = U_{3q}/U_{1q}$, namely

$$V_q = \frac{K_{11}(\chi_q)K_{23}(\chi_q) - K_{12}(\chi_q)K_{13}(\chi_q)}{K_{13}(\chi_q)K_{22}(\chi_q) - K_{12}(\chi_q)K_{23}(\chi_q)}, \tag{4.22}$$

$$W_q = \frac{K_{11}(\chi_q)K_{23}(\chi_q) - K_{12}(\chi_q)K_{13}(\chi_q)}{K_{33}(\chi_q)K_{12}(\chi_q) - K_{13}(\chi_q)K_{23}(\chi_q)}. \tag{4.23}$$

The total displacement interms of V_q and W_q are

$$u_1 = \sum_{q=1}^{6} U_{1q} \exp\left[i\left(k_1 x_1 + k_2 x_2 + \chi_q x_3 - \omega t\right)\right], \tag{4.24}$$

$$u_2 = \sum_{q=1}^{6} V_q U_{1q} \exp\left[i\left(k_1 x_1 + k_2 x_2 + \chi_q x_3 - \omega t\right)\right], \tag{4.25}$$

$$u_3 = \sum_{q=1}^{6} W_q U_{1q} \exp\left[i\left(k_1 x_1 + k_2 x_2 + \chi_q x_3 - \omega t\right)\right]. \tag{4.26}$$

And the total stress can be simplified as

$$\sigma_{33} = i\sum_{q=1}^{6} D_{1q} U_{1q} \exp\left[i\left(k_1 x_1 + k_2 x_2 + \chi_q x_3 - \omega t\right)\right], \tag{4.27}$$

$$\sigma_{13} = i\sum_{q=1}^{6} D_{2q} U_{1q} \exp\left[i\left(k_1 x_1 + k_2 x_2 + \chi_q x_3 - \omega t\right)\right], \tag{4.28}$$

$$\sigma_{23} = i\sum_{q=1}^{6} D_{3q} U_{1q} \exp\left[i\left(k_1 x_1 + k_2 x_2 + \chi_q x_3 - \omega t\right)\right], \tag{4.29}$$

where

$$D_{1q} = k_1\left(c_{13} + c_{36}V_q\right) + k_2\left(c_{36} + c_{23}V_q\right) + c_{33}W_q\chi_q, \tag{4.30}$$

$$D_{2q} = c_{55}W_qk_1 + c_{45}W_qk_2 + \chi_q\left(c_{55} + c_{45}V_q\right), \tag{4.31}$$

$$D_{3q} = c_{45}W_qk_1 + c_{44}W_qk_2 + \chi_q\left(c_{45} + c_{44}V_q\right). \tag{4.32}$$

The layers of composite structures consist of a linear elastic material with perfectly bonded interfaces with a continuous strain distribution and that the stresses at each interface are equal. The composite fiber aggregate is sufficiently rigidly bonded to the matrix. There is stress/strain compatibility at the fiber-matrix interface.

The most commonly used methods for generating Lamb wave dispersion curves of layered anisotropic media are based on three-dimensional linear elasticity in combination with global matrix and transfer matrix approaches. This technique uses only the global matrix approach, since the transfer matrix is considered stable only for the low-frequency thickness product.

The global matrix concept analysis methodology is based on examining all the equations from each layer to form a single global matrix (Fig. 4.1). This matrix describes the displacement and stress fields associated with wave propagation. The global matrix method consists of X (n - 1) equations for n layers, where X represents the number of expected partial waves. This method is robust and remains stable for any frequency-thickness product, since it does not rely on wave coupling from one interface to another.

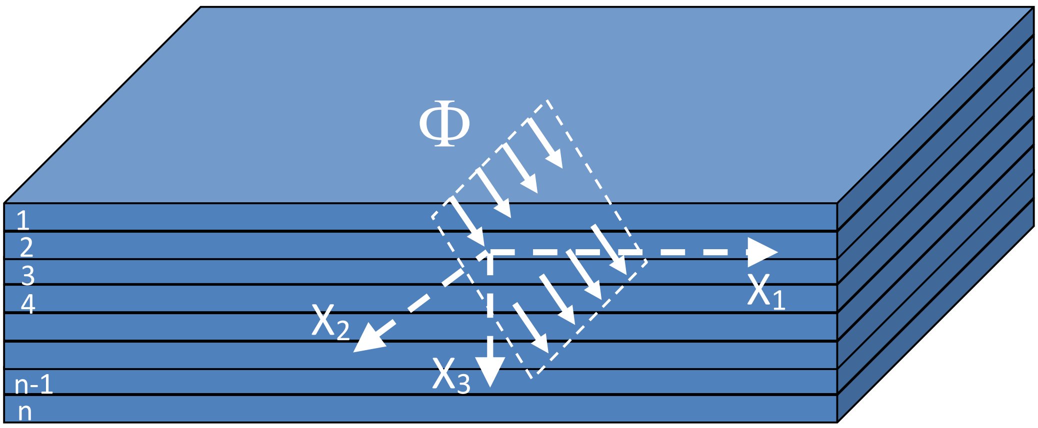

Figure 4.1. N-layered composite laminate.

For the *k*-th layer of a monoclinic plate with thickness d*k*, the displacement ui and stress rij can be written as follows

$$(u_1, u_2, u_3)_k = \left[\sum_{k=1}^{6} (1, V_q, W_q) U_{1q} \exp\{i(k_1 x_1 \sin\varphi + k_2 x_2 + \chi_q x_3 - \omega t)\} \right]_k , \qquad (4.33)$$

$$(\sigma_{33}, \sigma_{13}, \sigma_{23})_k = \left[i \sum_{k=1}^{6} (D_{1q}, D_{2q}, D_{3q}) U_{1q} \exp\{i(k_1 x_1 \sin\varphi + k_2 x_2 + \chi_q x_3 - \omega t)\} \right]_k , \qquad (4.34)$$

where

φ is the incident angle relative to the *x*-axis.

By linking together, the matrix elements for mechanical stress, shear, and the energy component of a wave packet as it moves in a fixed direction within a laminated composite, the following matrix equation can be written

$$\begin{Bmatrix} u_1 \\ u_2 \\ u_3 \\ \sigma_{33} \\ \sigma_{13} \\ \sigma_{23} \end{Bmatrix}_k = \begin{bmatrix} 1 & 1 & 1 & 1 & 1 & 1 \\ V_1 & V_1 & V_3 & V_3 & V_5 & V_5 \\ W_1 & -W_1 & W_3 & -W_3 & W_5 & -W_5 \\ iD_{11} & iD_{11} & iD_{13} & iD_{13} & iD_{15} & iD_{15} \\ iD_{21} & -iD_{21} & iD_{23} & -iD_{23} & iD_{25} & -iD_{25} \\ iD_{31} & -iD_{31} & iD_{33} & -iD_{33} & iD_{35} & -iD_{35} \end{bmatrix}_k \times$$

$$\times \begin{Bmatrix} U_{11} \exp[i(k_1 x_1 \sin\varphi + k_2 x_2 + \chi_1 x_3 - \omega t)] \\ U_{12} \exp[i(k_1 x_1 \sin\varphi + k_2 x_2 + \chi_1 x_3 - \omega t)] \\ U_{13} \exp[i(k_1 x_1 \sin\varphi + k_2 x_2 + \chi_1 x_3 - \omega t)] \\ U_{14} \exp[i(k_1 x_1 \sin\varphi + k_2 x_2 + \chi_1 x_3 - \omega t)] \\ U_{15} \exp[i(k_1 x_1 \sin\varphi + k_2 x_2 + \chi_1 x_3 - \omega t)] \\ U_{16} \exp[i(k_1 x_1 \sin\varphi + k_2 x_2 + \chi_1 x_3 - \omega t)] \end{Bmatrix}. \qquad (4.35)$$

The part of the matrix equation (4.35) that contains the displacement and stress vectors is denoted as P_k. Accordingly, the right-hand side is denoted as X_k, the displacement amplitude is U_k, and the wave equation is denoted as D_k. In this case, the short form of the matrix equation is

$$\{P_k\} = [X_k] \cdot [D_k] \cdot \{U_k\}. \qquad (4.36)$$

Each layer of the monoclinic plate of the laminar composite has six partial waves, denoted as (L+/), (SV+/) and (SH+/). These Lamb waves can be interpreted as quasi-longitudinal, quasi-shear vertical and quasi-shear horizontal waves, respectively. Positive and negative signs represent downward and upward traveling waves. The characteristic equations of Lamb waves can be written as a result of the analysis of displacements and shears in the second interface (*i*2), which consists of the lower surface of layer 2 (*l*2) and the upper surface of layer 3 (*l*3).

Mechanical displacements and shifts in a fixed layer are subject to a system of equations

$$\{P_{l2,b}\} = [[X_{l2,b}][D_{l2,b}]\{U_{l2,b}\}] \ , \tag{4.37}$$

$$\{P_{l3,b}\} = [[X_{l3,b}][D_{l3,b}]\{U_{l3,b}\}] \ . \tag{4.38}$$

The condition of continuity of displacement within one layer has the form

$$[[Z_{l2,b}][-Z_{l3,b}]]\begin{Bmatrix} \{U_{l2,b}\} \\ U_{l3,t} \end{Bmatrix} = \{0\}, \tag{4.39}$$

where indexes “b” and “t” are the nearest surfaces of fixed layer.

The global matrix combines the conditions for all layers and the five partial Lamb waves that propagate in the monoclinic laminate

$$\begin{bmatrix} [Z_{l1,b}] & [-Z_{l2,t}] & [0] & [0] & [0] \\ [0] & [Z_{l2,b}] & [-Z_{l3,t}] & [0] & [0] \\ [0] & [0] & [X_{l3,b}] & [-Z_{l4,t}] & [0] \\ [0] & [0] & [0] & [X_{l4,b}] & [-Z_{l5,t}] \end{bmatrix} = \{0\}. \tag{4.40}$$

The boundary conditions for Lamb waves specify that the mechanical stresses on the top and bottom surfaces are zero. The solution to this boundary condition can be obtained by splitting the submatrix of the top and bottom layers in the equation into their associated mechanical stresses and displacements. This split allows a new matrix to be formed in the next step.

In the next step after the separation, only the components of mechanical stress are analyzed to obtain the dispersion curves of Lamb waves. Assuming that the displacement components from the upper and lower layers of the equation are negligible, the newly obtained matrix can be separated.

The solution for Lamb wave propagation (Fig. 4.2) and hence the dispersion curves are obtained by finding a non-trivial solution to the previously written characteristic equation [Z] {U} = 0 where [Z] is the global matrix and {U} is the amplitude vector. Numerical determination of equation $|Z| = 0$ leads to the construction of the Lamb wave dispersion curve.

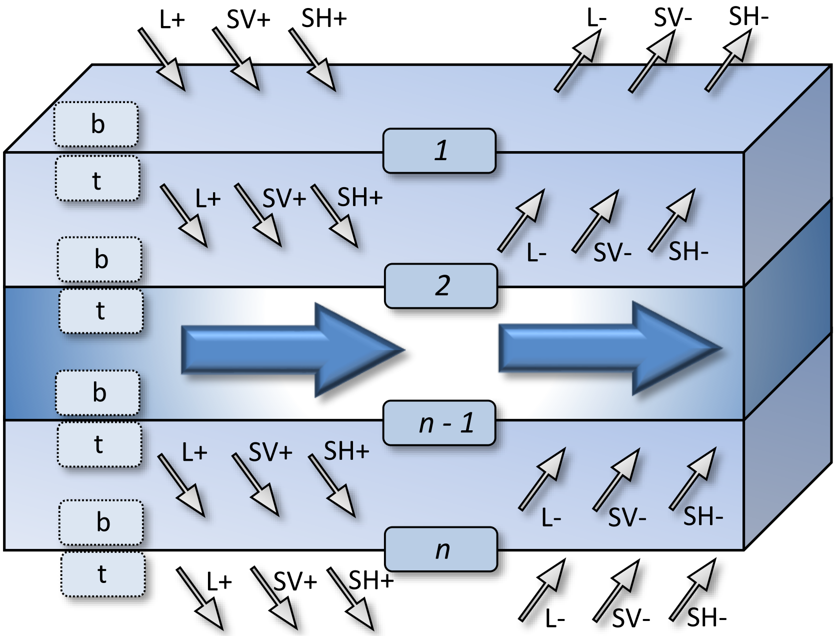

Figure 4.2. Partial waves in monoclinic composite plate.

Comparison of the calculated and experimental data indicates numerical values of 2.4, 5.6 % for antisymmetric and symmetric Lamb waves, respectively. The modulus of the theory-experiment difference increases slightly for high Lamb wave frequencies and in the direction coaxial with the symmetry axis of the laminate specimen can be explained by the difference in the stiffness of the composite material between its rolling direction and transverse direction.

To confirm the efficiency of describing the field of mechanical stresses and shears in the bulk of the laminar composite, a broadband Lamb wave was investigated. The Lamb wave packet was propagated in a quasi-isotropic laminate of 3.4 mm thickness ([45/0/−45/0]3s). The frequency generator and receiver were separated by a distance of 100 mm and were fixed on the surface of the laminate. The input signal was a single-cycle sine wave at a frequency of 400 kHz with a Hamming window. The input waveform had a characteristic region with a single-peak profile. This input wave is broadband up to a value of 1 MHz. The full width at half maximum of the Fourier spectrum is about 600 kHz.

The Lamb wave sets were averaged during processing to reduce noise. The resulting waveform was analyzed using the Fast Fourier Transform. The continuous wavelet transform was implemented using the complex Morlet wavelet. The

Fourier spectrum was characterized by a large number of peaks due to the frequency dispersion of the Lamb waves in the laminate.

To identify the Lamb wave modes, theoretical dispersion curves of Lamb wave packets were calculated. The group velocities of all modes propagating in a quasi-isotropic laminate of fixed thickness were calculated for each frequency. The time for symmetric and antisymmetric modes was determined from the phase and group velocities. The corresponding dispersion curves are shown in Fig. 4.3.

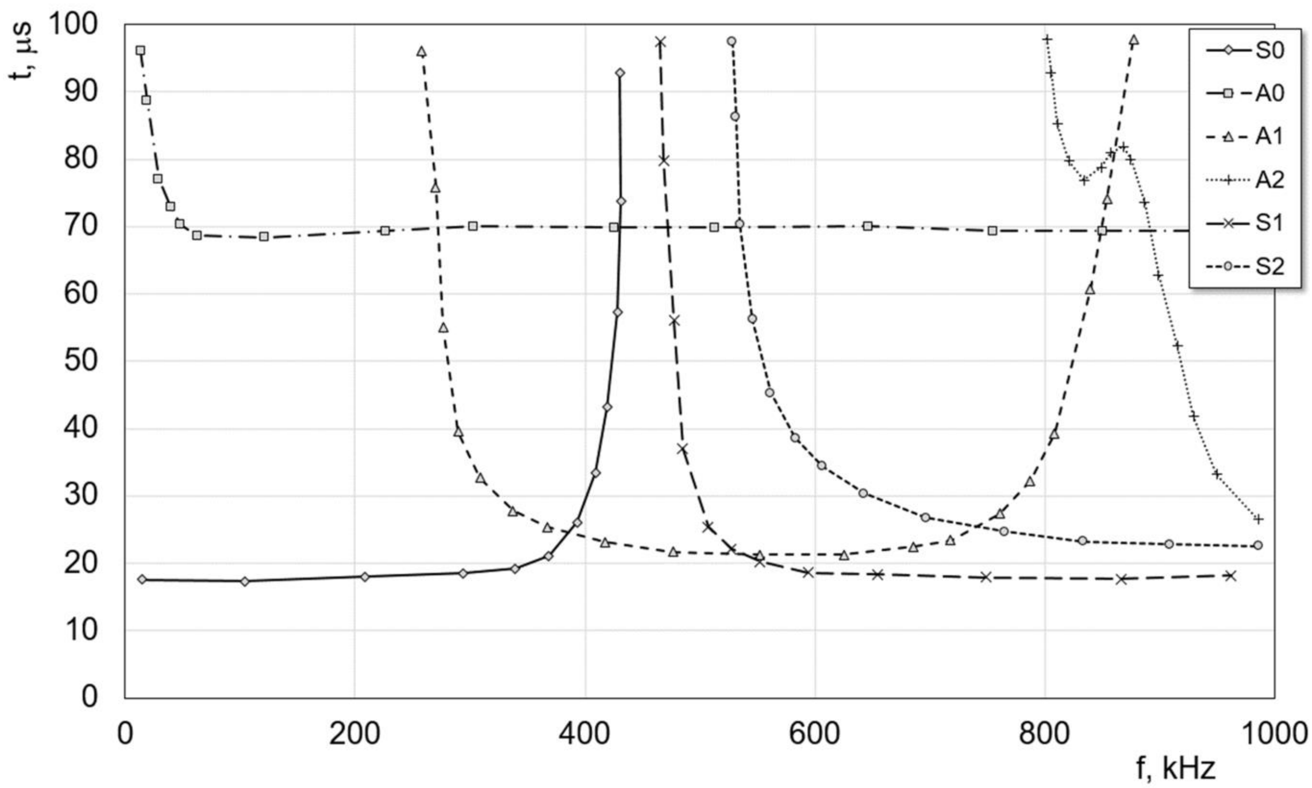

Figure 4.3. Dispersion curves for all modes of Lamb waves.

Most often, Lamb wave packets transform their modes at fixed points. For these regions of the composite volume, the plate thickness changes and some modes are reflected back. To explain this effect, it should be taken into account that the mode dispersion curves strongly depend on the plate thickness.

The results of the analysis of the dispersion curves for a quasi-isotropic laminate with an insignificant thickness indicate that the frequency on the horizontal axis doubled. This frequency doubling was observed under the condition that the thickness was halved. Comparison of the mode composition of Lamb wave packets for different thicknesses of composite plates leads to the following results. Three modes A0, S0 and A1 are present at a fixed frequency in a thick laminate. On the other hand, the A1 mode cannot propagate in a thin laminate. Therefore, in regions of space where the laminate thickness experiences a significant (multiple) decrease, the A1 mode will be transformed into S0 and A0. On the contrary, with increasing thickness, part of the energy of the S0 and A0 modes will be transformed into A1.

For the case where there is a delamination in the middle of the laminate thickness, the frequency dispersion curves of the Lamb wave packets that pass through the delamination region will change. The reasons for this change can be attributed to the mode transformations at both ends of the delamination. This phenomenon can be used to quantitatively detect delamination damage in the laminate.

The intact region before delamination is characterized by the presence of antisymmetric modes A0 and A1, which are generated by the antisymmetric excitation. In addition, the analysis results indicate the existence of small S modes. These modes were reflected from both ends of the delamination after mode conversion.

It was found that the A1 mode propagated weakly in the frequency range above the cutoff frequency in the stratified region. Most of the wave energy of the A1 mode was converted into S0. The amplitude of the A1 mode increased significantly after passing through the stratification. The reason for this increase in amplitude is the mode transformation from S0 to A1 at the end point of the stratification.

In symmetric modes, the weak modes S1 and S2 appeared twice with different arrival times. The dispersion curve analysis showed that the faster modes S1 and S2 were transformed from S0 and A1, and the slower ones were transformed from A0. The results of the analysis of the characteristics of the transformed modes in the delamination region are consistent with the available experimental results.

The combined analysis of both the calculated dependences and the experimental results indicates the following features of the behavior of the Lamb wave packet modes. The A1 mode in the undamaged region is transformed into the S0 mode at the initial point of delamination, which is present in the middle of the thickness of the quasi-isotropic laminate. On the other hand, the S0 mode is transformed into the A1 mode at the final point of delamination.

The observed features of the mode conversion can be used as a basis for a method for detecting delamination in quasi-isotropic laminates. In particular, the key effect whose characteristics should be used in the method is the excitation of antisymmetric modes.

The antisymmetric mode A1 is converted to the mode S0 in the delamination region. In this case, the group velocity dispersion differs between the mode A1 in the intact region of the thick laminated composite sample and the mode S0 in the delamination region of the thin sample. Since the mode S0 is faster than the mode A1, the arrival time of the mode A1 at the detection sensors decreases with increasing delamination length.

This difference in velocity increases with decreasing frequency. Therefore, it can be concluded that the frequency dispersion of the mode A1 will change depending on the delamination length. These expected phenomena were investigated in numerical simulations.

The trend of the dispersion changes for the peaks of the maximum of the A1 mode depending on the delamination length is illustrated in Fig. 4.4. With an increase in the delamination length, the amplitude of the A1 mode decreased. The slope of the dispersion curve also changed. Comparison of the calculation results with the available experimental measurements indicates that the considered method of using Lamb wave dispersion is effective for detecting delamination damage.

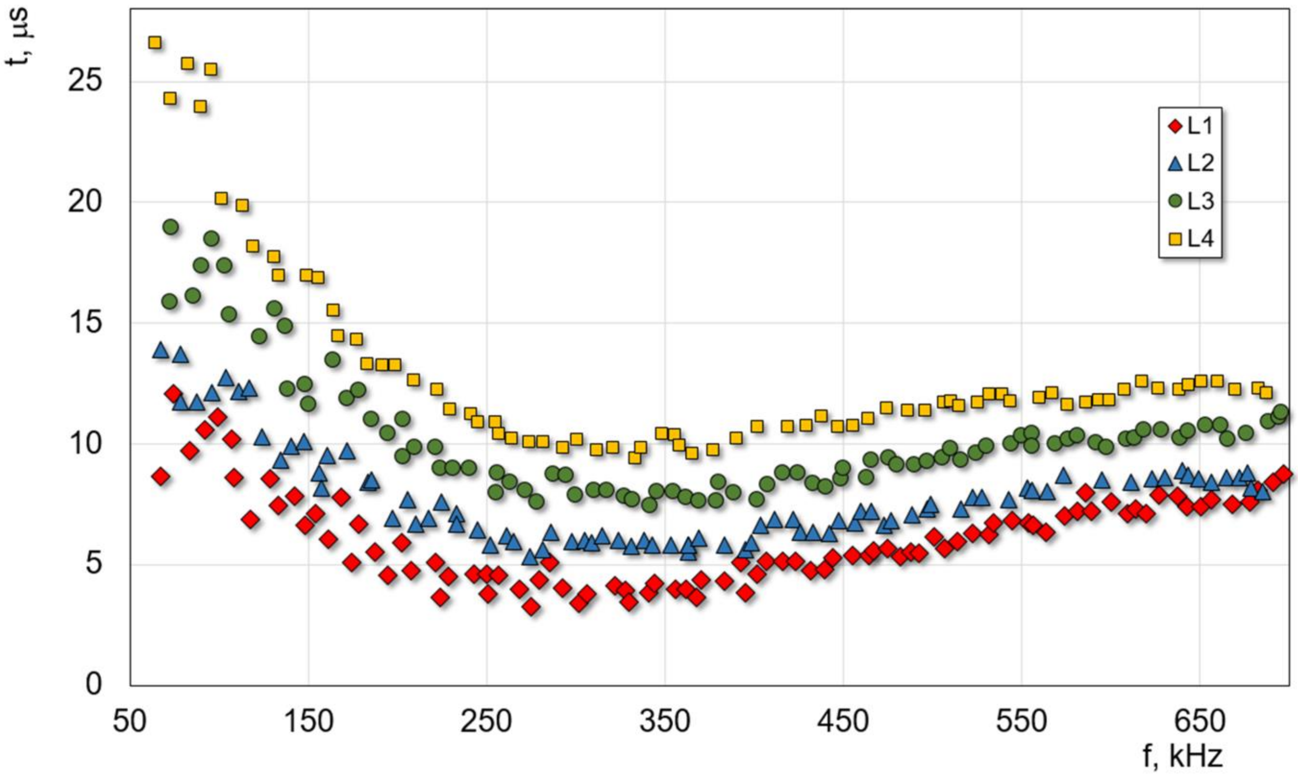

Figure 4.4. Maximum points of A1 mode: L1 – 0.5 mm; L2 – 20 mm; L3 – 40 mm; L4 – 60 mm.

The interaction of waves with laminar composite bulk delamination and lateral surface effects is fairly easy to detect in the time-space wave field. However, the implicit characteristics of wave packet propagation, such as the content of the wave mode and how the modes change along the wave path, are not easily visible.

Wave data analysis, representing the characteristics of a wave number set by the locus of wave front points, has abundant information regarding the existence of different wave modes and wave propagation characteristics.

Localization of a two-dimensional Fourier transform, where the wave number is a function of distance, can be realized by methods of transforming the wave field into a time-space representation of the wave number.

Spectral analysis of Lamb waves in time and space using a two-dimensional Fourier transform allows one to write the frequency-wave number representation (*f* - *k*) as

$$V(f,k)=\int_{-\infty}^{\infty}\int_{-\infty}^{\infty}v(t,x)\exp[-i(2\pi\, f\, t-kx)]dt\,dx\,, \qquad (4.41)$$

where
V (*f*, *k*) is the resulting frequency-wavenumber representation;
f is the frequency variable;
k is the wavenumber variable.

For spatial information in the resulting *f* - *k* representation *V* (*f*, *k*), the spatial component is lost during the transformation. However, it is often desirable to know how the wave number varies along the propagation distance of the wave. In order to preserve and subsequently transform spatial information, a new short spatial two-dimensional Fourier transform was developed to obtain the space-frequency-wave number representation.

This technique can be viewed as a straightforward extension of the short-time Fourier transform to two-dimensional problems, i.e., breaking up the time-space wave field into small segments along the spatial dimension before applying the Fourier transform.

The first step in the numerical implementation of such a technique is that the wavefield data are multiplied by a window function of fixed size. This function is not zero only for a short period in space, but is constant over the entire time dimension.

In a subsequent step, a two-dimensional Fourier transform is applied to the resulting wavefield segments. As the window slides along the spatial dimension, a set of windowed wavefield segments is generated. A two-dimensional Fourier transform is again applied to these segments, resulting in a set of frequency and wavenumber spectra, which are indexed by the window location.

Spatial information can only be preserved by this method. The window space is realized using the two-dimensional Fourier transform technique and has the form

$$S(\bar{x}, f, k)=\int_{-\infty}^{\infty}\int_{-\infty}^{\infty}v(t,x)W^*(t,x-\bar{x})\exp[-i(2\pi\, f\, t-kx)]dt\,dx\,, \qquad (4.42)$$

where
$\bar{x}$ is the retained spatial argument;

W (*t*, *x*) is the window function.

For the case of laminar composites, it is advisable to choose the Hanning function for constructing the window *W* (*t*, *x*) in the form

$$W(t,x)=\begin{cases} |x|\le \dfrac{D_x}{2},\ 0.5\left[1+\cos\left(2\pi\dfrac{x}{D_x}\right)\right] \\ |x|>\dfrac{D_x}{2},\ 0 \end{cases}, \tag{4.43}$$

where D_x is the window length in specific space dimension.

The nature of the change in the frequency component, as well as the resulting spectrum of the space-frequency-wave number in space, can be determined by shifting the window along the spatial dimension. This procedure is usually carried out using a two-dimensional Fourier transform.

In the spectrum of the delaminated plate, new *f* - *k* components appear between the original A0 and S0 modes, including both positive (forward propagating) and negative (backward propagating) analogues. The set of emerging *f* - *k* components correlates with the wave propagation in the delamination region. This correlation can be explained by assuming that the delamination is the only difference from the original plate.

The reconstructed wave field represents the back and forth propagation of waves between the delamination boundaries. The combination of analytical predictions and experimental data indicate that the new *f* - *k* components are created by waves trapped in the delamination region when the waves pass above and below the delamination. In this case, the trapped waves are above the delamination, since the wave field characteristics correspond to the upper surface of the laminated composite in the form of a thin plate.

The processing of the numerical characteristics of the wave fields using the two-dimensional Fourier transform at short distances indicates that the wave number changes along the propagation path of the wave packet in the local volume of the laminar composite.

It should be noted that the space-wave number of both A0 and S0 modes remains constant in wave number and continuous in space along the propagation path. Naturally, the absence of changes corresponds only to the ideal case. The presence of delaminations in the bulk of the composite leads to a significant change in the spectrum of space-wave numbers.

The region of significant concentration of delaminations in the volume of the laminated composite corresponds to the discontinuity of wave numbers along the spatial dimension. The size of the gap is directly related to the length of the delamination. The analysis of the delamination spectrum indicated that new wave numbers representing forward and backward propagation can be identified and are present only in the delamination region.

The final conclusion can be formulated as follows. New wave numbers are present in the delamination region and are related to the propagation of Lamb wave packets in this region. The considered methods of wave number analysis can be used in engineering practice to detect delamination and estimate its length in space.

It is of interest to improve the method for determining the depth of the layer under which delamination occurs. The problem of determining the depth of delamination is reduced to determining the number of layers above the delamination. Obviously, the number of layers below the delamination can then be found by subtracting this result from the total number of layers.

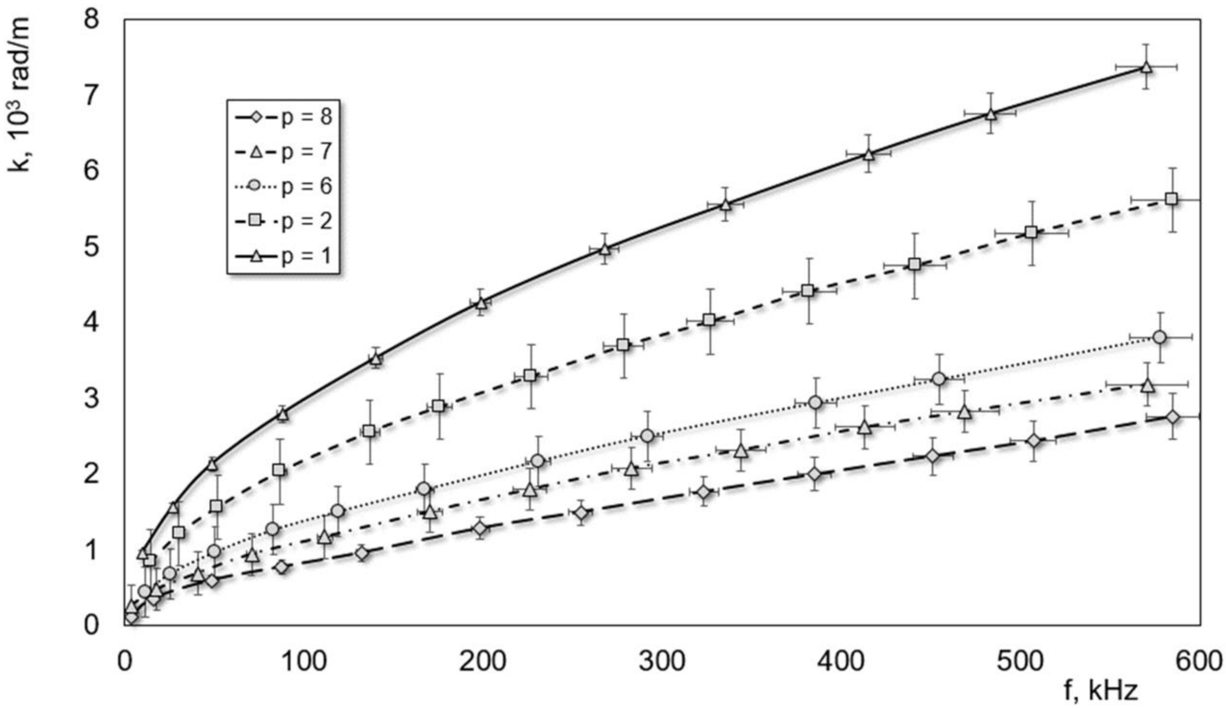

Figure 4.5. Frequency (*f*)-wavenumber (*k*) dispersion curves for fixed plies (*p*).

Analysis of the material properties at the layer level of the composites under study allows one to construct a set of theoretical dispersion curves with a corresponding set of wave numbers. The dispersion curves for laminates of 1–8 layers are shown in Fig. 4.5. For example, a five-layer laminate will consist of five upper layers, [0/0/90/90/0].

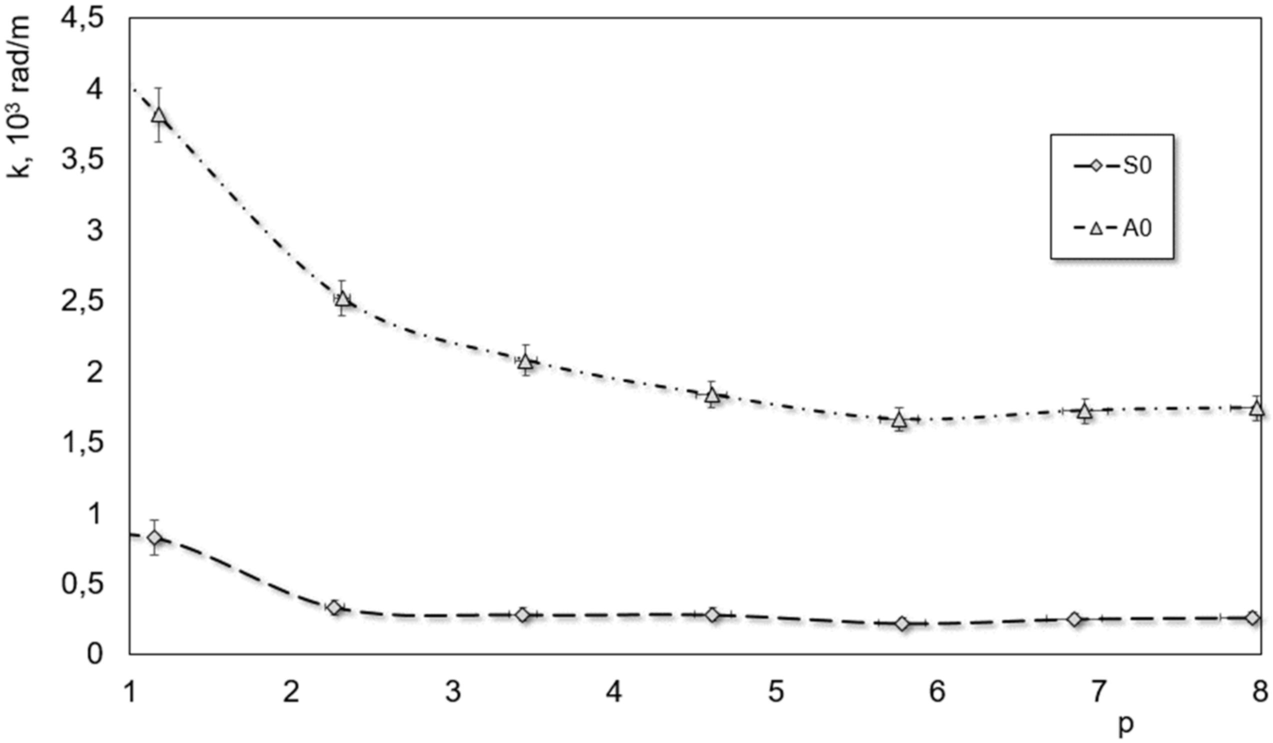

Figure 4.6. Wavenumbers (*k*) at 300 kHz versus of plies (*p*).

Figure 4.6 shows the wave numbers at 300 kHz for laminates of 1 – 8 layers. The detection of the delamination depth is carried out when new wave numbers are present in the wave number spectrum. The new wave numbers will correspond to the theoretical dispersion curves (for the frequency-wave number spectrum) and/or the theoretical wave numbers (for the space-wave number spectrum).

Numerical calculations have confirmed that wave packets propagate through the delamination region and can be reflected back and forth between the delamination entrance and exit. In such reflection, the propagation of wave packets is characterized by the appearance of new in-plane and out-of-plane wave numbers.

A mechanical deformation such as a simple delamination that separates an initially composite specimen into two parts will result in the propagation of Lamb waves above and below the delamination. The composite material above and below the damage will have different layers and thicknesses compared to the original intact plate. Lamb waves propagating on the outer surface of the plate above (or below) the damage will have modified propagation characteristics and wave numbers (which will depend on the number of layers in the separated parts). To determine the depth of delamination, it is necessary to determine the number of layers above the delamination.

The appearance of a set of new wavenumbers allows the depth of the delamination layer to be determined. The new wavenumbers will correspond to the theoretical dispersion curves (for the frequency-wavenumber spectrum) and/or the theoretical wavenumbers (for the space-wavenumber spectrum). The spectrum of the in-plane f - k component from the simulation data is verified by comparing it with the dispersion curves of plates with different numbers of layers.

The analysis of numerical experiments showed that the dispersion curves for the case of a two-layer thick laminate best fit these new frequency-wavenumber components. In particular, the new f - k components fit well the theoretical curves of the S0 mode in a two-layer [0/0] laminate. Summarizing these results, it can be stated that the position of the delamination in terms of the number of layers can be determined using frequency and wavenumber analysis.

The dispersion curves show new frequency-wavenumber components that correspond to the A0 mode in the two upper [0/0] layers. These components can be identified using the same comparison technique (although in this case the waves are much weaker compared to the waves outside the delamination region).

It should be noted that the delamination in this case is detected below the second layer. In the space-wavenumber spectrum at 300 kHz, the new wavenumbers are present in the delamination region and coincide well with the A0 mode at 300 kHz in the two-layer [0/0] laminate.

The good agreement between the experimental results and numerical simulation data confirms the possibility of using layer depth detection through wavenumber fitting to quantify delamination.

CHAPTER 5
LAMB MODES DISPERSION AND SCATTERING

The main advantages of Lamb waves as a tool for identifying a wide variety of damage types in the volume of composite samples are their propagation over long distances with high sensitivity to small changes, as well as their ability to scan a large area of the objects or structures being examined. Lamb wave packets with a fixed propagation direction not only cover large objects, but are also quite sensitive to local mechanical damage. However, the nonlinear characteristics of directed wave packets complicate the task of extracting information about the features of a defect. In this regard, the method of processing signals recorded by wave receivers is also complicated.

Both phase and group velocities of guided waves are among the main parameters for assessing the deviation or change in material properties. Waves of a fixed direction have an infinite number of dispersion modes. and each of them is described by two frequency-dependent velocities: phase and group. Dispersion curves are used to show the changes in velocities c depending on the frequency f. Changes in the velocity of a guided wave can indicate the location and size of a defect.

Taking these features into account, it can be argued that a signal processing method that allows reconstructing the dispersion curves of guided waves propagating in a given structure is very relevant. However, most of the algorithms for reconstructing group and phase curves of the dispersion of the velocity of guided waves encounter difficulties in estimating time-dependent changes in the frequency spectrum of the signal. In this regard, these methods should contain an improved frequency-time analysis of guided wave signals.

One of the types of guided waves propagating in thin plates with parallel free boundaries are ultrasonic Lamb waves. Information about the dependence of the phase velocity c_p on the product of the frequency f and the plate thickness d can be obtained by analyzing the phase velocity dispersion curves of Lamb waves. In general, the dispersion curves are different for different wave modes.

All modes, namely the asymmetric An mode and the symmetric Sn mode (except for the horizontal shear SH) are strongly dependent on frequency. Since the phase velocity is defined for any particular frequency, the wavelength λ of the mode can also be estimated. The wavelength λ of the Lamb wave is a critical parameter because it determines the sensitivity to the size and geometry of the detector. The phase velocity dispersion curve is an important parameter for detecting inhomogeneities in elastic properties and/or localizing defects in unknown material objects under test.

The hybrid signal processing methodology is generally free of the above-mentioned shortcomings. This method uses spectral decomposition and zero-crossing methods to analyze non-stationary signals. The first stage of the improved method requires analyzing broadband signals, characterizing the dispersion, and reconstructing segments of the phase velocity dispersion curve of both lower fundamental Lamb wave modes. The main objective of this technique is to study the suitability of the proposed algorithm for signal processing in a dispersive medium for estimating the dispersive phase velocity and for reconstructing segments of this velocity dispersion curve in the widest possible frequency ranges.

A promising method for measuring the phase velocity of the Lamb wave is the zero crossing method. The peculiarity of this technique is that the parameters in both the time and frequency domains are calculated and related to each other as a segment of the phase velocity dispersion curve. The zero crossing method provides several advantages, such as identifying the fundamental A0 and S0 modes operating in low or high dispersion zones. In addition, this technique allows reconstructing segments of the phase velocity dispersion curves of the A0 and S0 modes in the case of Lamb wave packets.

According to the zero-crossing technique, at least two signals are required, recorded by two receivers located at two different and relatively close positions x_i and x_{i+1}. The Lamb wave source is characterized by constant coordinates and is excited by a broadband packet $s(t)$. In general, these signals contain information about the phase velocity $c_p(f)$, which must be extracted by signal processing.

The velocity of the wave packet on the surface of the plate affects the Lamb wave signal $u_i(t)$ at a distance x_i

$$u_i(t) = FT^{-1}\left[S(f) \cdot H(f)\right]. \tag{5.1}$$

where
FT^{-1} is the inverse Fourier transform;
$S(f)$ is the Fourier transform of the incident pulse $s(t)$.

The transfer function for Lamb waves propagation has the form

$$H(f) = \exp\left[-j\frac{2\pi f x_i}{c_p(f)}\right]. \tag{5.2}$$

The zero crossing method is based on the delay times t_{im} and $t_{(i+1)m}$ of the propagating waves. The delay times are calculated from the characteristics of the signals recorded at different positions x_i and x_{i+1}. These signals are analyzed according to the zero crossing algorithm for relative amplitude A' (see Fig. 5.1). The number of measured zero crossing moments is m = 1, 2, …, M, where M is the total number of analyzed zero crossing moments. In the second stage of the zero crossing technique, the phase velocity c_{pm} of the propagating wave at a given distance can be estimated using the following formula

$$c_{pm} = \frac{\Delta x_i}{\Delta t_{im}} = \frac{x_{i+1} - x_i}{t_{(i+1)m} - t_{im}}. \quad (5.3)$$

where
Δx_i is the distance between two neighboring positions;
Δt_{im} is the signals delay time difference.

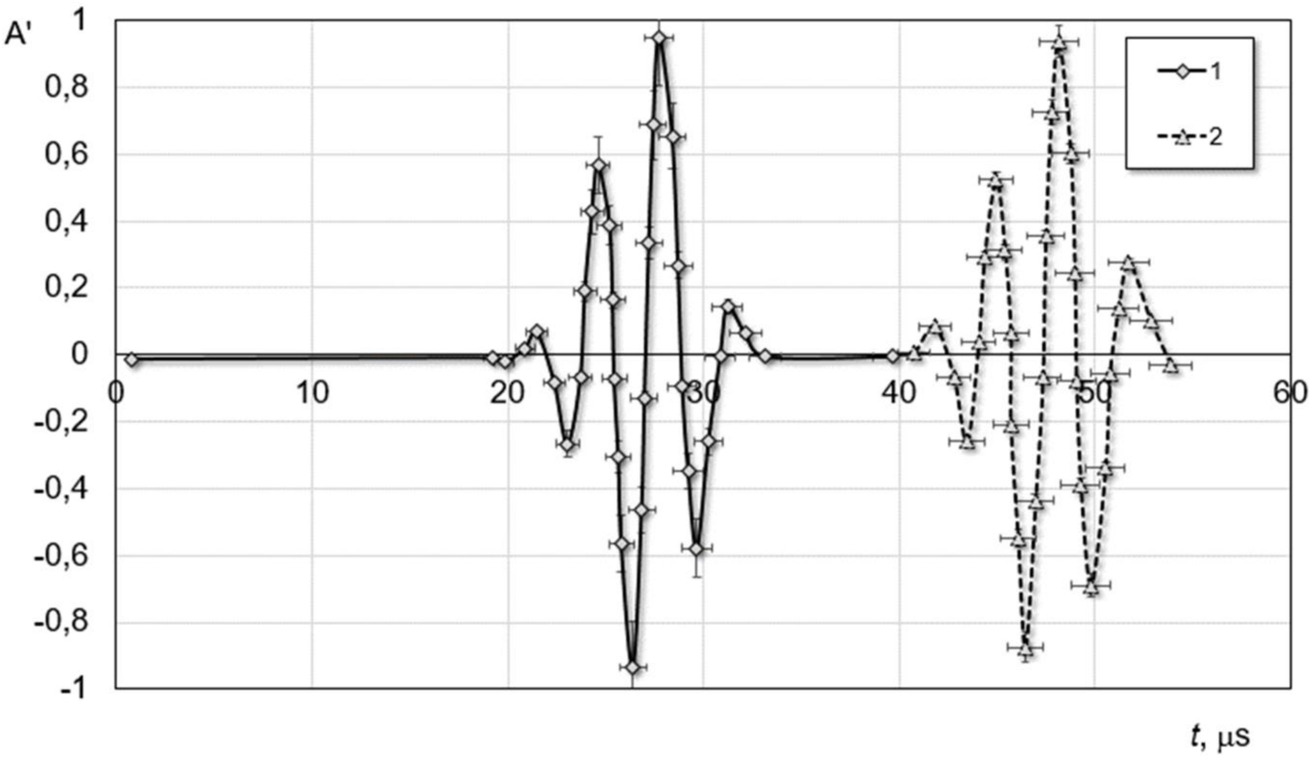

Figure 5.1. Wave form of received signals: 1 – $u_i(t)$, 2 – $u_{i+1}(t)$.

The time delay Δt_{im} can be calculated based on the data on the delay times of the zero-crossing t_{im} and $t_{(i+1)m}$. The frequencies f_m, to which the calculated phase velocities c_{pm} correspond, are calculated for the duration of half the period between two adjacent zero-crossing points m and $m + 1$

$$f_m = \frac{1}{2[t_{i(m+1)} - t_{im}]}. \quad (5.4)$$

Each segment of the dispersion curve is uniquely defined by a set of phase velocity and frequency pairs D (f_m, c_{pm}). Analysis of the calculated propagation characteristics of Lamb wave packets showed that the proposed measurement method has one main limitation. The phase velocity dispersion curves are reconstructed only in a relatively limited bandwidth around the central frequency of the signal. Consequently, information on a part of the frequency spectra of the signal was lost. To solve this limitation and reconstruct the phase velocity dispersion curves of guided waves in the widest possible frequency ranges, it was proposed to use the spectral decomposition method.

According to Fourier theory, any signal *s* (*t*) can be expanded into trigonometric functions as follows

$$S(j\omega) = \int_{-\infty}^{\infty} s(t)\exp(-j\omega t)dt = S(\omega)\exp[-j\varphi(\omega)]. \qquad (5.5)$$

where

ω is the angular frequency;

$j = \sqrt{-1}$;

$S(\omega)$ is the amplitude frequency response;

$\varphi(\omega)$ is the phase frequency response.

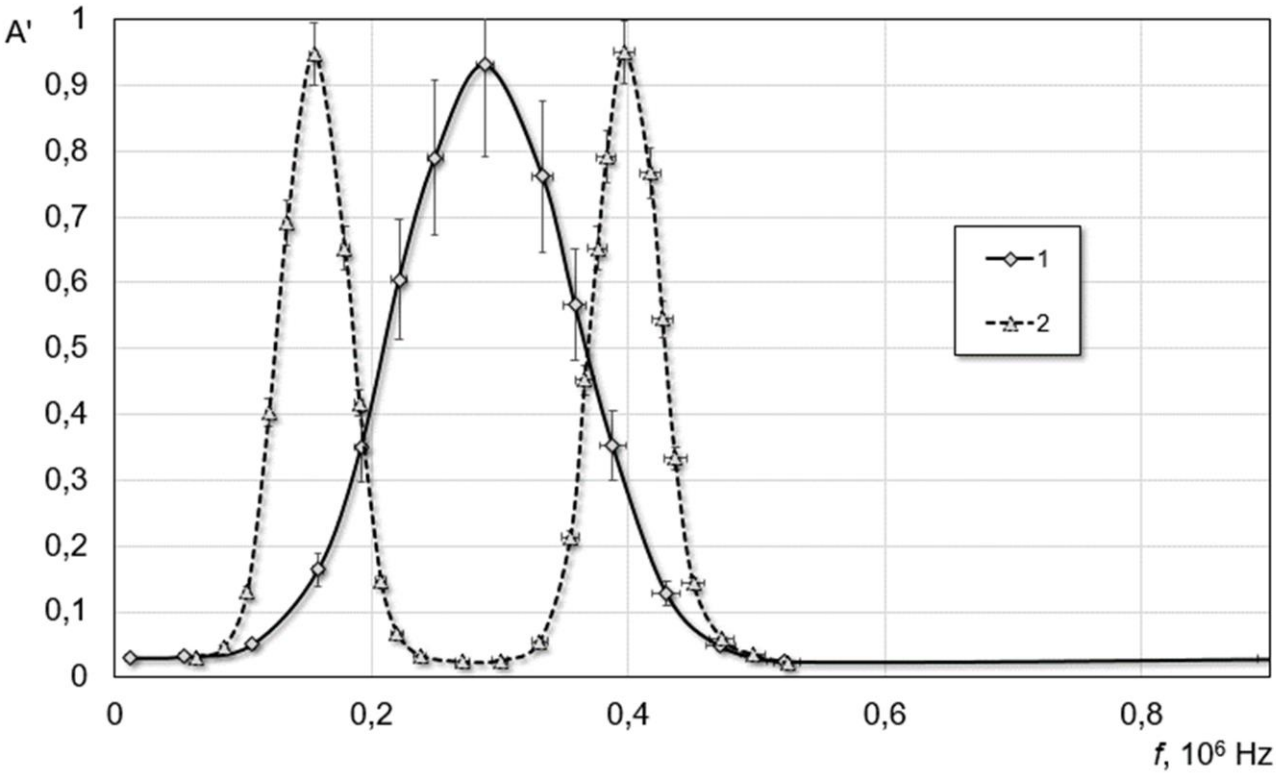

Figure 5.2. Frequency spectrum of Lamb wave signal: 1 – signal; 2 - filter *B*.

It can be stated that the frequency response of the signal corresponding to the Lamb wave packets is the result of such a decomposition. The modulus of the complex spectrum represents the amplitudes of the various frequency components. The signal spectrum corresponds to the interval in which the dominant frequency components are concentrated in the frequency band around the maximum of the spectrum. These features are the reason that without filtering the phase velocity dispersion curve will be reconstructed in a narrow frequency band around the central frequency. Therefore, a necessary condition for increasing the sensitivity of the signal processing method to frequency components with small amplitudes is the procedure of filtering the frequency components that correspond to higher amplitudes (see Fig. 5.2).

The zero-crossing algorithm assumes the possibility of decomposing the measured signals $u_i(t)$ at different distances into a set of signals with a limited bandwidth $u_{ik}(t)$. Such a procedure becomes possible provided that the signals $u_i(t)$ are filtered using bandpass filters with a narrower bandwidth than the bandwidth of the incident spectrum.

At the next step for each filtered signal uik(t) the delay times t_{imk} and $t_{(i+1)mk}$ are estimated. In this way, the phase velocities c_{pmk} and frequencies f_{mk} are calculated. Then, the obtained sets (f_{mk}. c_{pmk}) can be represented as segments of the phase velocity dispersion curve.

Each section of the dispersion curve obtained using one of the filters can be reconstructed in a relatively narrow passband. In addition, scanning the filter's central frequency in wide frequency ranges will allow covering a large part of the falling spectrum.

The frequency spectrum of two adjacent signals can be represented as

$$U_i(f)=FT[u_i(t)]. \tag{5.6}$$

$$U_{i+1}(f)=FT[u_{i+1}(t)]. \tag{5.7}$$

where

$u_i(t)$ is the signal measured at distance $x_i(t)$;

$u_{i+1}(t)$ is the signal measured at distance $x_{i+1}(t)$;

FT is the Fourier transform.

Adjacent bands of the frequency spectra are filtered by k Gaussian bandpass filters with predetermined parameters

$$U_{ik}(f)=U_i(f)\cdot B_k(f). \tag{5.8}$$

$$U_{(i|+1)k}(f)=U_{i+1}(f)\cdot B_k(f). \tag{5.9}$$

where the frequency response of *k*-th bandpass filter is

$$B_k(f) = \exp\left\{4\ln(0.5)\cdot\Delta B^{-2}\cdot[f - f_L - (k-1)df]^2\right\}. \quad k = 1,2,...,K. \tag{5.10}$$

where
f_L is the left frequency filter edge;
f_H is the central part of frequency filter edge;
ΔB is the filter bandwidth;
the frequency domain d*f* is

$$df = \frac{f_H - f_L}{K-1}. \tag{5.11}$$

The signal reconstruction using the Fourier transform has the following form

$$u_{ik}(t) = FT^{-1}[U_{ik}(f)]. \tag{5.12}$$

$$u_{(i\backslash+1)k}(t) = FT^{-1}\left[U_{(i+1)k}(f)\right]. \tag{5.13}$$

At the next stage of the numerical method. the phase velocity can be estimated according to the following relation

$$c_{pmk} = \frac{x_{i+1} - x_i}{t_{(i+1)mk} - t_{imk}}. \tag{5.14}$$

Using the data on the duration of the half-periods of the first signal, it is possible to estimate the equivalent frequencies to which the calculated values of the phase velocity should be assigned

$$f_{imk} = \frac{0.5}{t_{i(m+1)k} - t_{imk}}. \tag{5.15}$$

Comparison of the results obtained using the proposed hybrid method and the previous version of the reference zero-crossing method showed that the zero-crossing method recovers the phase velocity dispersion curve in the frequency range of 286–319 kHz. This bandwidth is only 8% of the original signal bandwidth.

Meanwhile, the proposed spectrum decomposition approach allows us to recover the phase velocity dispersion curve in a significantly wider frequency range. This range covers almost the entire bandwidth of the incident Lamb wavelet signal. *t* should be noted that the frequency ranges in which the dispersion curve is reconstructed depend significantly on the bandwidth of the filters used in the spectrum decomposition approach.

For example, for the 120 kHz filter, 70% coverage of the incident signal bandwidth was achieved. Finally, the best results were achieved with the narrowest filter (40 kHz bandwidth). For this narrowed filter, the reconstructed dispersion curve covers 90% of the original bandwidth.

In summary, it can be argued that narrow filters are more efficient, but this leads to a large number of filters, which generates more computational resources and longer processing times.

Typical B-scan results for the propagation of the A0 Lamb wave mode in a 2 mm thick laminated composite sample are presented in Table 5.1. The dispersion curve data for the relative amplitude are divided into three ranges: A-band (0 - 150 kHz). B-band (150-300 kHz) and C-band (300-500 kHz).

Table 5.1. Dispersion dependences for A0 mode of the Lamb wave.

A-band		B-band		C-band	
f, kHz	*A′*	*F*, kHz	*A′*	*F*, kHz	*A′*
15.9304	0.0152	157.2193	0.5169	304.7936	0.5203
25.3012	0.0338	158.1551	0.4882	311.3182	0.5458
34.6720	0.1083	162.8342	0.5017	318.7750	0.5085
41.2316	0.2183	170.3209	0.4595	322.5033	0.5864
47.7912	0.2470	176.8717	0.5456	328.0959	0.6661
58.0991	0.2369	185.2941	0.5253	327.1638	0.7322
62.7845	0.3063	187.1658	0.6284	333.6884	0.6898
61.8474	0.4856	195.5882	0.7128	341.1451	0.7254
69.3440	0.6125	199.3316	0.7010	343.9414	0.6644
74.0295	0.4399	199.3316	0.7517	347.6698	0.5458
78.7149	0.3012	203.0749	0.7973	356.9907	0.5746
85.2744	0.4467	209.6257	0.7720	361.6511	0.6085
87.1486	0.5330	213.3690	0.7483	364.4474	0.5339
89.9598	0.6261	213.3690	0.8142	363.5153	0.4864
96.5194	0.5753	217.1123	0.8953	362.5832	0.3814
104.0161	0.7547	218.9840	0.9865	366.3116	0.2712
111.5127	0.5381	233.0214	0.8666	377.4967	0.1780
113.3869	0.6819	237.7005	0.6791	387.7497	0.1051
115.2610	0.7902	246.1230	0.7500	399.8668	0.1322
122.7577	0.9306	248.9305	0.8497	411.9840	0.1797
126.5060	0.8190	254.5455	0.9662	424.1012	0.1102
136.8139	0.7580	263.9037	0.9578	430.6258	0.0678
143.3735	0.7733	266.7112	0.8868	441.8109	0.1186

The measurement results using different sets of the filters (where P is the number of filters) are obtained and compared with the dispersion curve of zero-crossing method (ZCM) for A0 mode of the Lamb wave ($f \in 0 \div 500$ kHz). The results for phase velocity c_p (measured in m/s) are presented in Table 5.2.

Table 5.2. Dispersion curves for different methods.

$P = 4$		$P = 12$		ZCM	
f, kHz	c_p, m/s	f, kHz	c_p, m/s	f, kHz	c_p, m/s
76.923	1207.41	59.64	1047.13	65.22	1047.20
88.942	1304.38	78.31	1183.57	76.09	1114.29
102.163	1393.27	104.22	1332.40	88.77	1186.34
123.798	1522.56	123.49	1429.15	99.03	1258.39
142.428	1608.75	135.54	1483.72	109.90	1340.37
156.851	1654.55	149.40	1548.22	122.58	1370.19
164.063	1724.58	175.30	1652.40	140.10	1459.63
177.885	1746.13	204.82	1759.07	152.78	1504.35
183.894	1805.39	224.10	1791.32	174.52	1603.73
197.716	1837.71	246.39	1890.54	191.43	1638.51
212.740	1905.05	268.67	1930.23	210.14	1740.37
228.966	1937.37	295.18	1997.21	230.68	1780.12
234.375	1983.16	310.84	2017.05	254.23	1852.17
253.005	2020.88	322.89	2051.78	269.93	1899.38
265.625	2090.91	339.76	2074.11	289.25	1926.71
284.856	2115.15	355.42	2126.20	300.12	1968.94
302.885	2150.17	384.94	2163.41	322.46	1996.27
316.707	2198.65	396.39	2190.70	346.01	2055.90
332.933	2195.96	413.25	2203.10	375.00	2088.20
345.553	2263.30	419.28	2230.39	402.17	2147.83
362.380	2268.69	431.33	2230.39	423.31	2165.22
385.216	2325.25	439.76	2250.23	434.18	2190.06
405.649	2338.72	450.60	2255.19	445.05	2197.52
426.082	2389.90	463.25	2292.40	469.20	2222.36
449.519	2419.53	481.33	2299.84	486.11	1249.69

A comparison of the results presented in Table 5.2 shows that the experimental method using only four filters gives overestimated values of phase velocity and, therefore, does not have sufficient accuracy for the engineering practice of monitoring the propagation of Lamb wave packets in the volume of laminar composites.

The finite element method is also a promising tool for describing shear strain kinetics and detecting mechanical damage. In particular, a dynamic finite element code is used to calculate acoustic emission waveforms in isotropic and anisotropic laminar composites. However, when using the finite element method, computational problems often arise related to the interpretation of the obtained results.

As an alternative, various semi-analytical methods have been recently developed. The waveguide finite element method and the spectral finite element method are two alternative modeling methods. Due to their numerical efficiency, these methods have been successfully applied to composites of various structures.

The theoretical problem for a laminar composite plate is a homogeneous plate consisting of a transversely isotropic material with an axis of symmetry perpendicular to its surface. Representing the laminar composite as a honeycomb sandwich panel allows us to reduce the problem to considering a three-layer transversely isotropic plate consisting of a honeycomb core attached to composite shells.

In this model, a single layer of a homogeneous isotropic elastic composite plate is described by dispersion relations of the following type symmetric and antisymmetric modes of Lamb waves

$$\left(2k^2 - k_2^2\right)^2 \cosh(\eta_1 H)\sinh(\eta_2 H) - 4k^2\eta_1\eta_2 \sinh(\eta_1 H)\cosh(\eta_2 H) = 0. \quad (5.16)$$

Accordingly, for antisymmetric modes of Lamb waves, the equation can be modified as follows

$$\left(2k^2 - k_2^2\right)^2 \sinh(\eta_1 H)\cosh(\eta_2 H) - 4k^2\eta_1\eta_2 \cosh(\eta_1 H)\sinh(\eta_2 H) = 0, \quad (5.17)$$

where

$$\eta_j = \sqrt{k^2 - k_j^2}, \quad k_j = \frac{\omega}{c_j}, \quad j = 1,2, \quad (5.18)$$

$k = \omega/c$ is the angular wavenumber;
H is half the thickness of the composite sample;
c_1 is the P-wave velocity for lamina composite material;
c_2 is the S-wave velocity for lamina composite material.

The working fluid for the model calculation experiment was a laminar composite consisting of 8 layers with the stacking sequence $[0^0/45^0/0^0/45^0]$s. The composite plate is modeled as a homogeneous transversely isotropic material with the x_3-axis as the axis of symmetry.

Young's modulus E_{22} can be determined from the results of a standard uniaxial tensile test in the x_2 direction. In addition, a stress-strain curve is plotted from the tensile test results. Poisson's ratio ν_{12} in the 1-2 plane is determined from the same test by measuring the strains in both the x_1 and x_2 directions. The shear modulus G_{23} and the elastic constant E_{33} for the composite face sheet are determined from the equations

$$G_{23} = \upsilon_{23}^2 \rho , \tag{5.19}$$

$$E_{33} = \frac{\rho E_{22}(1-\nu_{12})\upsilon_{11}^2}{E_{22}(1-\nu_{12}) + 2\rho \nu_{13}^2 \upsilon_{11}^2}, \tag{5.20}$$

where

υ_{11} is the longitudinal wave velocity;

υ_{23} is the shear wave velocity;

An analytical plane strain model can be considered without loss of generality and this will be sufficient to determine the propagation characteristics of directed waves. For the case of a transversely isotropic composite material, the model problem can be divided into the motions of symmetric and antisymmetric modes of Lamb wave packets. The propagation of symmetric modes is described by the dispersion relation determined by the quantity H

$$\frac{\sinh(kA_1 H)\cosh(kA_2 H)}{\sinh(kA_2 H)\cosh(kA_1 H)} =$$

$$= \frac{A_1\left[A_2^2 - \dfrac{c_{11}}{c_{13}}\left(\dfrac{c^2}{c_{1L}^2} - 1\right)\right]\cdot\left[\dfrac{c_{13}}{c_{33}}\left(\dfrac{c_{13}}{c_{44}} + 1\right) + A_1^2 + \dfrac{c_{11}}{c_{44}}\left(\dfrac{c^2}{c_{1L}^2} - 1\right)\right]}{A_2\left[A_1^2 - \dfrac{c_{11}}{c_{13}}\left(\dfrac{c^2}{c_{1L}^2} - 1\right)\right]\cdot\left[\dfrac{c_{13}}{c_{33}}\left(\dfrac{c_{13}}{c_{44}} + 1\right) + A_2^2 + \dfrac{c_{11}}{c_{44}}\left(\dfrac{c^2}{c_{1L}^2} - 1\right)\right]}, \tag{5.21}$$

and for the case of antisymmetric modes

$$\frac{\cosh(kA_1 H)\sinh(kA_2 H)}{\cosh(kA_2 H)\sinh(kA_1 H)} =$$

$$= \frac{A_1\left[A_2^2 - \frac{c_{11}}{c_{13}}\left(\frac{c^2}{c_{1L}^2} - 1\right)\right]\cdot\left[\frac{c_{13}}{c_{33}}\left(\frac{c_{13}}{c_{44}} + 1\right) + A_1^2 + \frac{c_{11}}{c_{44}}\left(\frac{c^2}{c_{1L}^2} - 1\right)\right]}{A_2\left[A_1^2 - \frac{c_{11}}{c_{13}}\left(\frac{c^2}{c_{1L}^2} - 1\right)\right]\cdot\left[\frac{c_{13}}{c_{33}}\left(\frac{c_{13}}{c_{44}} + 1\right) + A_2^2 + \frac{c_{11}}{c_{44}}\left(\frac{c^2}{c_{1L}^2} - 1\right)\right]}, \qquad (5.22)$$

where

c_{11}, c_{13}, c_{33} and c_{44} are the stiffness constants;

$$A_1 = \frac{\eta_1}{k} = \sqrt{\frac{-A + \left(A^2 - 4B\right)^{0.5}}{2}} = i\sqrt{\frac{A - \left(A^2 - 4B\right)}{2}}, \qquad (5.23)$$

$$A_2 = \frac{\eta_2}{k} = \sqrt{\frac{-A - \left(A^2 - 4B\right)^{0.5}}{2}} = i\sqrt{\frac{A + \left(A^2 - 4B\right)}{2}}, \qquad (5.24)$$

$$A = \frac{c^2}{c_{3L}^2} + \frac{c^2}{c_{3T}^2} - \frac{\left(c_{11}c_{33} - c_{13}^2 - 2c_{13}c_{44}\right)}{c_{33}c_{44}}, \qquad (5.25)$$

$$B = \left(\frac{c^2}{c_{3L}^2} - \frac{c_{11}}{c_{33}}\right)\cdot\left(\frac{c^2}{c_{3T}^2} - 1\right), \qquad (5.26)$$

$$k = \frac{\omega}{c}, \quad c_{1L}^2 = \frac{c_{11}}{\rho}, \quad c_{3L}^2 = \frac{c_{33}}{\rho}, \quad c_{3T}^2 = \frac{c_{44}}{\rho}. \qquad (5.27)$$

The relationships for the compression constants are determined by Young's moduli

$$c_{11} = \frac{E_{11}\left(1 - \nu_{32}\nu_{23}\right)}{\left(1 + \nu_{12}\right)\left(1 - \nu_{12} - 2\nu_{32}c_{23}\right)}, \qquad (5.28)$$

$$c_{33} = \frac{E_{33}\left(1 - \nu_{12}\right)}{\left(1 - \nu_{12} - 2\nu_{32}c_{23}\right)}, \qquad (5.29)$$

$$c_{12} = \frac{E_{11}\left(\nu_{12} + \nu_{32}\nu_{23}\right)}{\left(1 + \nu_{12}\right)\left(1 - \nu_{12} - 2\nu_{32}c_{23}\right)}, \qquad (5.30)$$

$$c_{13}=\frac{E_{33}\nu_{23}}{\left(1-\nu_{12}-2\nu_{32}c_{23}\right)}, \tag{5.31}$$

$$c_{44}=G_{31}. \tag{5.32}$$

At the next stage, it makes sense to apply an alternative approach to the numerical Fourier transform. The motion of Lamb waves in a rectangular laminated composite sample can be modeled by the propagation of Lamb wave packets along waveguides whose geometric dimensions are related to the dimensions of the laminar composite sample.

In particular, the finite element method of a waveguide helps to determine the phase and group velocities of propagating waves in arbitrary waveguides.
For this method, only one segment s of a waveguide with thickness Dx1 needs to be meshed in the finite element modeling process. The dynamics of this waveguide segment are described by the equations of motion

$$M\,\ddot{u}+C\,\dot{u}+K\,u=f\ , \tag{5.33}$$

where
M is the mass of composite sample;
C is the damping coefficient;
K is the stiffness matrix;
u is the displacement;
f is the external force.

The Lamb wave mode dynamic behavior can be expressed as

$$\begin{bmatrix} D_{LL} & D_{LR} \\ D_{RL} & D_{RR} \end{bmatrix}\cdot\begin{bmatrix} u_L \\ u_R \end{bmatrix}=\begin{bmatrix} f_L \\ f_R \end{bmatrix}, \tag{5.34}$$

where the stiffness matrix has the form

$$D=-\omega^2 M-i\omega C+K\ , \tag{5.35}$$

where ω is the angular frequency.

A set of experiments on compression and shear of volume elements of laminar composites showed that for such experiments it is possible to use the conditions of equilibrium and continuity. In this case, equation (5.34) can be rewritten in the form

$$\begin{bmatrix} u_L^{s+1} \\ f_L^{s+1} \end{bmatrix}=\begin{bmatrix} -D_{LR}^{-1}D_{LL} & D_{LR}^{-1} \\ -D_{RL}+D_{RR}D_{LR}^{-1}D_{LL} & -D_{RR}D_{LR}^{-1} \end{bmatrix}\cdot\begin{bmatrix} u_L^{s} \\ f_L^{s} \end{bmatrix}. \tag{5.36}$$

Table 5.3. Phase velocity dispersion in reinforced composite.

f, 10^3 kHz	υ_p, 10^3 m/s				
	S1	A1	S0	A0	A1e
613.833	9.791	9.665	4.538	2.431	9.895
618.156	9.623	9.497	4.496	2.431	9.519
623.919	9.393	9.245	4.475	2.431	9.351
635.447	8.975	9.099	4.433	2.452	9.079
646.974	8.703	8.826	4.370	2.452	8.870
652.738	8.473	8.512	4.307	2.473	8.515
659.942	8.285	8.281	4.244	2.473	8.347
667.147	8.180	8.260	4.118	2.473	8.075
675.793	8.013	8.008	4.013	2.516	8.075
687.320	7.824	7.841	3.929	2.452	7.866
694.524	7.657	7.736	3.782	2.452	7.782
704.611	7.594	7.568	3.676	2.495	7.552
713.256	7.448	7.484	3.592	2.516	7.510
717.579	7.322	7.233	3.571	2.516	7.280
724.784	7.280	7.128	3.508	2.516	7.259
736.311	7.176	6.960	3.508	2.473	7.008
744.957	7.071	6.834	3.466	2.452	7.008
753.602	6.946	6.646	3.403	2.473	6.820
763.689	6.841	6.478	3.403	2.495	6.862
768.012	6.778	6.331	3.277	2.516	6.548
785.303	6.653	6.122	3.214	2.537	6.402
806.916	6.485	5.996	3.214	2.537	6.130
829.971	6.318	5.912	3.151	2.516	6.172
854.467	6.130	5.870	3.130	2.516	5.941
870.317	5.983	5.828	3.088	2.559	6.025
880.403	5.921	5.681	3.025	2.580	5.607
894.813	5.879	5.639	3.004	2.580	5.795
912.104	5.816	5.577	3.004	2.537	5.397
929.395	5.669	5.514	2.983	2.537	5.586
963.977	5.586	5.346	2.962	2.559	5.230

Table 5.4. Group velocity dispersion in reinforced composite.

f, 10^3 kHz	υ_g, 10^3 m/s				
	S1	A1	S0	A0	A1e
612.466	0.341	0.382	5.344	1.452	0.500
613.821	0.434	0.526	5.344	1.690	0.714
619.241	0.517	0.729	5.330	1.893	0.976
621.951	0.646	0.932	5.344	2.179	1.119
624.661	0.787	1.100	5.317	2.429	1.500
628.726	0.869	1.303	5.304	2.619	1.655
631.436	0.975	1.422	5.278	2.774	1.905
635.501	1.068	1.590	5.212	2.869	2.107
639.566	1.186	1.757	5.160	2.976	2.369
643.631	1.292	1.900	5.028	3.048	2.393
647.696	1.386	2.044	4.976	3.083	2.524
653.117	1.503	2.211	4.884	3.131	2.810
663.957	1.644	2.319	4.805	3.143	3.071
672.087	1.761	2.594	4.700	3.119	3.250
680.217	1.996	2.892	4.582	3.143	3.429
692.412	2.219	3.060	4.477	3.167	3.298
701.897	2.360	3.191	4.372	3.131	3.595
718.157	2.571	3.323	4.083	3.119	3.488
733.062	2.748	3.466	3.584	3.107	3.702
752.033	2.924	3.562	3.098	3.107	3.619
776.423	3.088	3.633	2.652	3.107	3.714
796.748	3.194	3.705	2.376	3.083	3.655
807.588	3.229	3.705	1.877	3.095	3.750
830.623	3.311	3.717	1.641	3.060	3.655
857.724	3.382	3.717	1.352	3.048	3.714
878.049	3.393	3.717	1.352	3.048	3.619
902.439	3.393	3.717	1.457	3.048	3.738
918.699	3.429	3.693	1.615	3.048	3.560
944.444	3.440	3.681	1.759	3.060	3.655
966.125	3.440	3.645	1.864	3.048	3.536

Table 5.5. Phase velocity dispersion in laminated composite.

f, 10^3 kHz	υ_p, 10^3 m/s				
	S1	A1	S0	A0	A1e
762.829	9.920	9.361	5.360	0.656	9.800
761.442	9.760	9.162	5.380	0.775	9.479
766.990	9.521	9.042	5.400	0.994	9.158
766.990	9.341	8.962	5.320	1.034	9.018
765.603	9.182	8.723	5.320	1.093	8.477
769.764	9.042	8.543	5.340	1.133	8.056
769.764	8.882	8.423	5.300	1.173	7.856
773.925	8.463	8.283	5.160	1.272	7.575
773.925	8.244	8.104	5.120	1.252	7.695
773.925	8.104	7.904	4.960	1.233	7.475
775.312	8.024	7.705	4.840	1.272	7.375
778.086	7.844	7.525	4.780	1.332	6.914
782.247	7.645	7.365	4.660	1.372	6.774
789.182	7.465	7.265	4.440	1.352	6.573
800.277	7.086	7.066	4.220	1.332	6.754
800.277	6.946	6.966	4.020	1.372	6.633
807.212	6.826	6.826	3.780	1.392	6.573
815.534	6.587	6.647	3.620	1.412	6.212
829.404	6.367	6.527	3.320	1.392	6.112
840.499	6.168	6.467	3.100	1.412	6.032
851.595	6.028	6.387	2.940	1.471	6.032
864.078	5.968	6.287	2.700	1.491	6.012
883.495	5.888	6.188	2.520	1.491	6.172
901.526	5.828	6.068	2.380	1.511	6.152
914.008	5.788	6.068	2.240	1.491	5.932
925.104	5.729	5.988	2.160	1.471	6.092
936.200	5.729	5.968	2.060	1.491	5.892
950.069	5.709	5.868	2.040	1.531	5.952
962.552	5.709	5.868	2.000	1.511	6.072
975.035	5.709	5.868	1.980	1.511	6.032

Table 5.6. Group velocity dispersion in laminated composite.

f, 10^3 kHz	υ_g, 10^3 m/s				
	S1	A1	S0	A0	A1e
798.540	0.377	0.696	5.774	1.040	0.532
802.920	0.616	0.987	5.774	1.190	0.709
805.839	0.780	1.190	5.774	1.290	0.899
810.219	1.057	1.506	5.774	1.466	1.253
811.679	1.208	1.709	5.736	1.503	1.430
818.978	1.497	1.924	5.762	1.553	1.709
823.358	1.723	2.101	5.749	1.578	1.937
826.277	1.887	2.278	5.762	1.603	2.127
832.117	2.101	2.430	5.762	1.528	2.506
839.416	2.340	2.595	5.736	1.566	2.734
843.796	2.541	2.696	5.661	1.578	2.975
843.796	2.704	2.949	5.686	1.541	3.025
851.095	2.881	3.127	5.649	1.516	3.228
854.015	3.107	3.544	5.573	1.516	3.367
862.774	3.245	3.646	5.485	1.541	3.671
870.073	3.509	3.848	5.297	1.441	4.038
872.993	3.673	4.089	5.146	1.466	4.038
880.292	3.849	4.253	4.858	1.466	4.127
886.131	3.962	4.380	4.506	1.453	4.418
889.051	4.075	4.456	4.079	1.466	4.354
897.810	4.151	4.582	3.715	1.466	4.582
903.650	4.289	4.620	3.402	1.466	4.759
909.489	4.390	4.684	2.862	1.466	4.899
913.869	4.478	4.759	2.209	1.478	4.987
925.547	4.642	4.772	1.757	1.453	4.823
928.467	4.730	4.797	1.067	1.415	4.797
941.606	4.818	4.835	0.590	1.441	5.051
950.365	4.918	4.861	0.577	1.403	4.899
960.584	5.006	4.911	0.715	1.415	5.076
981.022	5.157	4.911	0.879	1.390	4.962

The wavenumber can be determined from the equation

$$k = -\frac{i}{\Delta x_1} Ln(\lambda), \tag{5.37}$$

where the waveguide segment is

$$\lambda = \exp(ik\Delta x_1), \tag{5.38}$$

$Ln(\lambda)$ is the natural complex logarithm.

The results of calculations (and experiment – index "e") of phase and group velocities for reinforced and laminated composites are presented in Tables 5.3 - 5.6.

Analytical models for the finite element study of the scattering characteristics of the fundamental antisymmetric (A0) Lamb wave on delaminations in a quasi-isotropic composite laminate are implemented using the Mindlin plate theory and the Born approximation. The methodology is used to predict the scattering of the A0 Lamb wave on a delamination, which is modeled as an inhomogeneity, in an equivalent isotropic model of the composite laminate.

The literature presents the results of studies on the scattering characteristics of Lamb A0 waves on circular through-holes in composite laminates with different stacking sequences. It should be noted that the scattering patterns were found to be quite different for composite laminates that have the same number of lamellas but different stacking sequences.

However, the experimental verification has focused only on a limited number of ratios of defect diameter to incident wavelength (denoted by *R*). Therefore, it is of interest to conduct a comprehensive verification of the finite element model for a wide range of R values. In addition, the experimental results showed that the Lamb A0 wave has an increased sensitivity to small defects compared to the Lamb S0 and SH0 waves at the same excitation frequency.

The standard laminar composite flaw detection technique includes a model delamination object in the form of a discontinuity with reduced bending stiffness in the delamination region. The reduction in bending stiffness in the delamination region can be explained by the separation of the laminate in this region into upper and lower sublayers, in which the waveguide is divided into two separate subwaveguides. The presence of a discontinuity can cause both reflected and transmitted waves from the delamination. However, in composite laminates, the scattering of Lamb waves at delaminations is a rather complex phenomenon. In this regard, it is necessary to evaluate the accuracy of the equivalent isotropic model in predicting the scattering characteristics of the Lamb A0 wave at delaminations in composite laminates.

The method involves the analysis of the characteristics of scattered Lamb waves A0, which were obtained from a limited number of monitoring points by calculating the difference between the signal from the undamaged panel and the signal from the damaged panel.

At the next stage, the difference in the maximum absolute amplitude of the scattered Lamb waves A0 is estimated. Then, the procedure of normalization of all scattered Lamb waves A0 by the maximum absolute amplitude of the incident wave in the center of the defect zone for a given laminate layer is performed. The wavelength in the numerical integration method accounted for at least 20 - 30 nodes of the computational grid, which is sufficient for accurate prediction of the propagation and scattering of the Lamb wave A0 on defects in composite laminates.

The Born approximation is also applicable to defects with complex shapes. In addition, the Born approximation was used to approximate the scattered Lamb wave amplitude A0 and compared with analytical and experimentally verified predictions of numerical integration using the finite element method. The plate properties of the inhomogeneity region can be expressed in terms of the properties corresponding to the region outside the inhomogeneity

$$D^* = D(1+\delta_1), \tag{5.39}$$

$$\kappa^2 Gh^* = \kappa^2 Gh(1+\delta_2), \tag{5.40}$$

$$\rho I^* = \rho I(1+\delta_3), \tag{5.41}$$

$$\rho h^* = \rho h(1+\delta_4), \tag{5.42}$$

where

$D = f\,(E, I, \nu)$;

E is the Young's modulus;

I is the moment of inertia;

ν is the Poisson's ratio;

$\kappa = \pi(12)^{-0.5}$ is the shear correction factor;

G is the shear modulus;

ρ is the density;

h is the sample thickness;

δ_1 - δ_4 are the defect factors.

For a fixed signal frequency ω, the scattered Lamb wave A0, according to the Born approximation, can be expressed using the following relation

$$W^s = \iint \Big\{\delta_1 D\Gamma^{(i)}_{\beta\alpha} g_{3\alpha,\beta} + \Big[\delta_2\kappa^2\eta\Big(W^i_\alpha - \psi^i_\alpha\Big) + \delta_3\omega^2\rho I\psi^i_\alpha\Big]g_{3\alpha} +$$

$$+\delta_2\kappa^2 Gh\Big(W^i_\alpha - \psi^i_\alpha\Big)g_{33,\alpha} + \delta_4\rho h\omega^2 g_{33}\Big\}d\xi d\eta\,, \tag{5.43}$$

where

$\alpha, \beta = 1, 2$;

ξ, η represents point coordinates within fixed region;

Γ is the plate strain;
g i,k are the Green's functions:

$$g_{lm} = \gamma \frac{\partial H_0(k_1 r')}{\partial p}, \tag{5.44}$$

where H_0 is the Huncel function;

$$\gamma = \frac{i}{4D\left(k_1^2 - k_2^2\right)}, \tag{5.45}$$

$$r' = \left[(x-\xi)^2 + (y-\eta)^2\right]^{0.5}, \tag{5.46}$$

$$p = \begin{cases} x, \ (l=3, m=1) \\ y, \ (l=3, m=2). \\ z, \ (l=3, m=3) \end{cases} \tag{5.47}$$

The scattered Lamb wave can be represented by

$$W^s(r,\theta) = \left[\frac{2}{\pi k_1 r}\right]^{0.5} \exp\left[i\left(k_1 r - \frac{\pi}{4}\right)\right] \cdot T(\theta) \sum_{n=1}^{4} \delta_n P_n(\theta), \tag{5.48}$$

$$P_1(\theta) = -\gamma \lambda_1 k_1^2 D\left(\cos^2\theta + \nu \sin^2\theta\right), \tag{5.49}$$

$$P_2(\theta) = -\frac{\gamma k^2 G h (1-\lambda_1)^2}{\lambda_1} \cos\theta, \tag{5.50}$$

$$P_3(\theta) = \gamma \lambda_1 \rho I \omega^2 \cos\theta, \tag{5.51}$$

$$P_4(\theta) = \frac{\gamma \rho h \omega^2}{\lambda_1 k_1^2}, \tag{5.52}$$

$$T(\theta) = 2\pi k_1 a \frac{J_1\left[k_1 a (2 - 2\cos\theta)^{0.5}\right]}{(2 - 2\cos\theta)^{0.5}}. \tag{5.53}$$

An analytical model of Lamb A0 wave scattering by through-hole defects is used to verify the numerical accuracy of the finite element modeling performed in this study. The verification was performed for a limited number of *R* values.

The calculation model analyzes the range of R values and compares them with the analytical results. The normalization procedure is performed using the maximum absolute amplitude of the incident wave in the center of the defect zone in the intact laminated composite sample. The forward and backward scattered Lamb waves A0 have similar amplitudes. However, the forward scattered waves tend to have a larger amplitude with increasing *R*.

In addition, the dynamics of the normalized amplitudes of the forward and backscattered Lamb waves A0 for a range of R values is analyzed. The forward and backscattered amplitudes increase with a similar slope and magnitude for *R* less than 0.45, after which the backscattered amplitudes increase at a lower rate and with small variations.

The entire set of obtained analytical, approximate results for finite elements for scattering of Lamb waves A0 on delaminations was compared with the results predicted by the equivalent isotropic model, which is an approximation to the composite laminate $[45/45/0/90]_S$. The purpose of such a comparison is to analyze the suitability of the representation of delamination by inhomogeneity in the analytical model and the Born approximation.

It was shown that the A0 phase and group velocity are not sensitive to the fiber orientation in the composite laminate. Very good agreement was obtained in all three sets of results at different wave numbers for Lamb waves, thus confirming the approximation of the phase and group velocity in the composite laminate at low frequencies by an equivalent isotropic model. Analysis of the calculated results indicates that the Born approximation underestimates the forward scattering amplitudes of the Lamb wave, but it predicts the forward scattering amplitude trend well.

It is found that the backscatter amplitudes oscillate faster with R than the forward scatter amplitudes. The analytical, approximated backscatter amplitude results and the results of numerical integration using the finite element method have different oscillation patterns. The analytical results have the form of a sinusoidal function increasing with the incident wave amplitude. The approximated results oscillate between zero and maximum values and have an increasing behavior of a sinusoidal function.

It should be pointed out that the general trends of all three sets of results increase with the numerical value of R. Comparing the predictions of the forward and backscattering amplitudes, it can be stated that the inhomogeneity model represents the delamination in the forward scattering amplitudes well. However, for the backscattering amplitudes, there is a significant discrepancy in the amplitudes. A similar phenomenon has also been shown in the defect localization experiments in laminar composites for delaminations in composite beams.

A possible reason for the discrepancy between the analytical results and the results of numerical integration using the finite difference method is that the analytical model does not take into account multiple internal reflections in the delamination region. The discrepancy between the analytical results and the results of integration using the finite element method increases for R greater than 0.3. The reason for such an increase in discrepancies is that the effect of multiple reflections in the delamination region becomes sharper.

The functional dependences of the normalized amplitude A_n on the value of R for different scattering angles of the Lamb wave are shown in Figs. 5.3 - 5.8. The curves of the graphs correspond to different models: AM (analytical model), AP (approximation model), FE (equivalent model calculated using the finite element method), QI (quasi-isotropic laminate model).

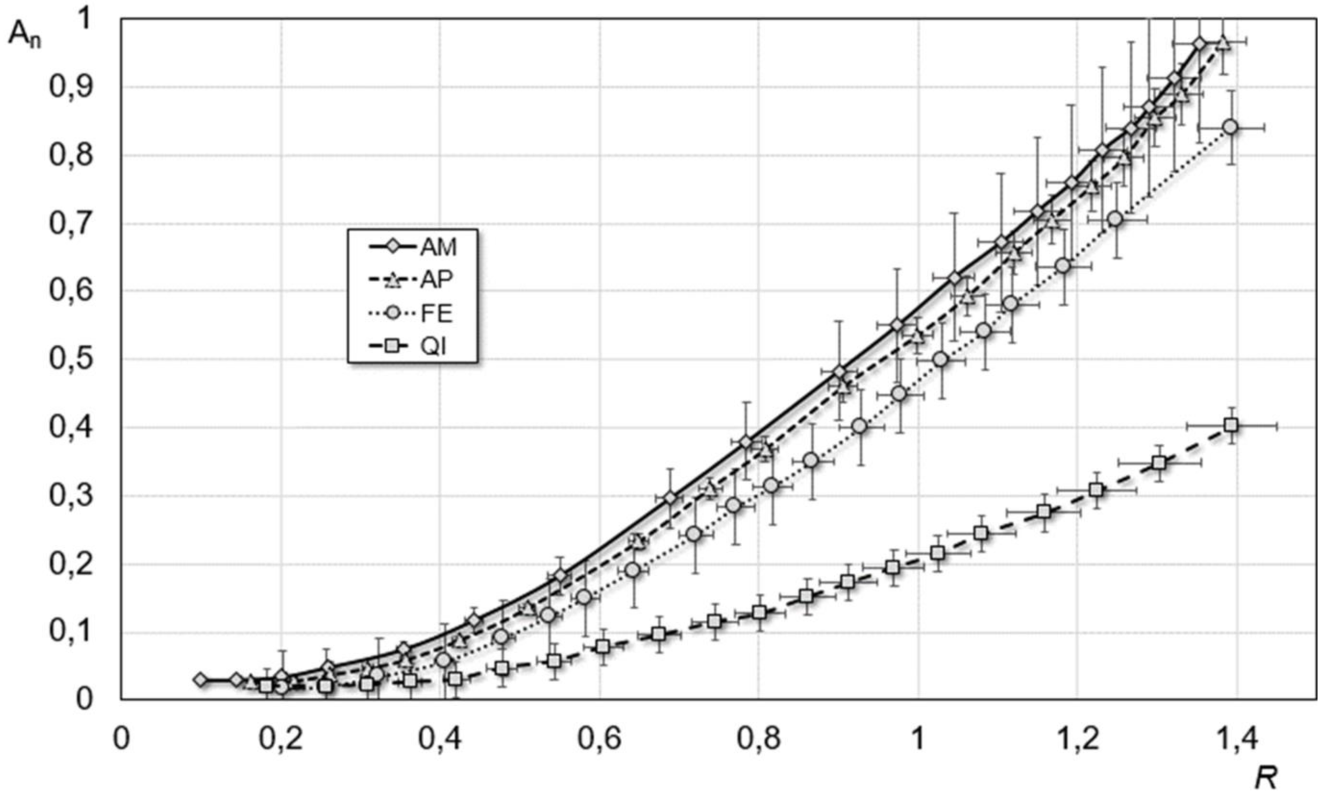

Figure 5.3. Dependence $A_n = A_n(R)$ for scattering angle $\theta = 0^0$.

In the quasi-isotropic laminated composite model, the deformation object is more conveniently represented as an elongated fiber located at a fixed angle to the surface of an individual layer. The orientation of each fiber affects the low-frequency Lamb wave. Analytical modeling and the Born approximation are used to calculate the scattered wave amplitudes in the equivalent isotropic model.

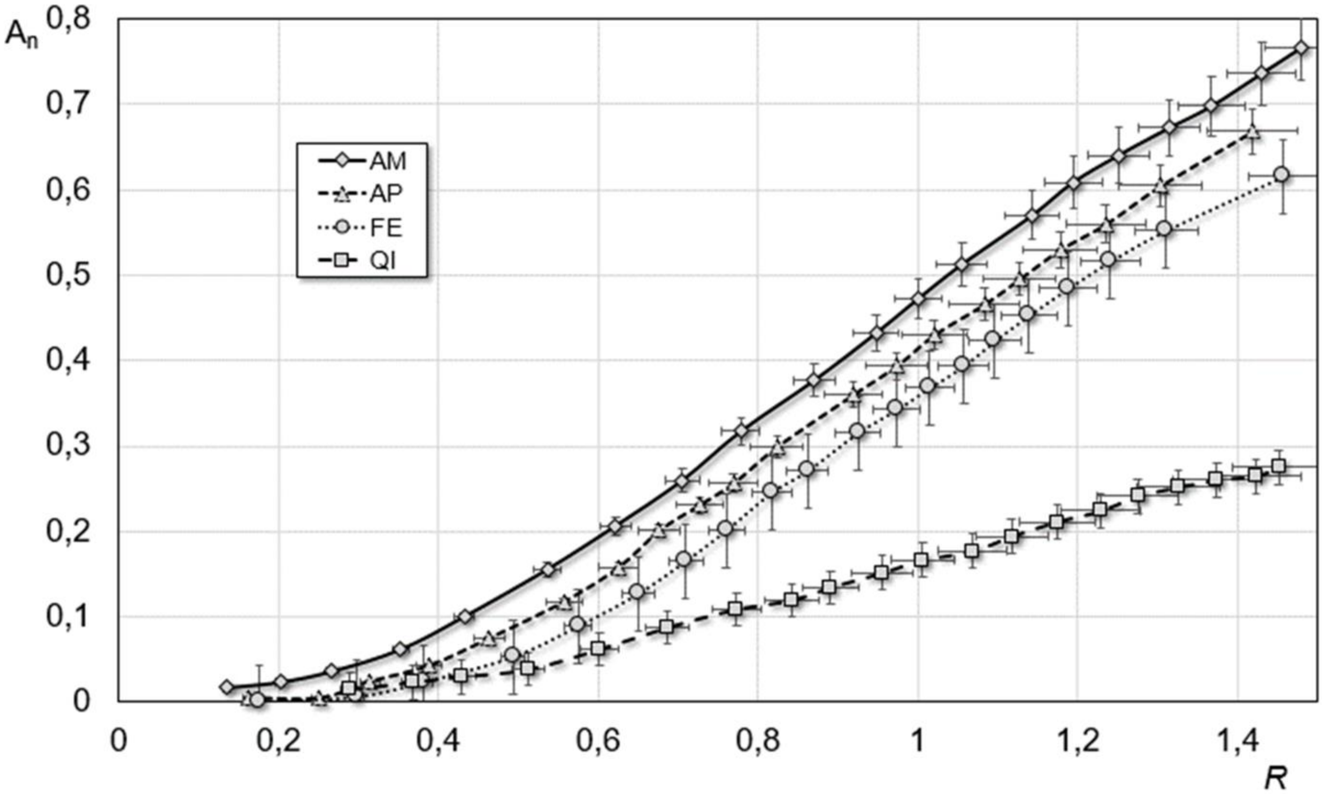

Figure 5.4. Dependence $A_n = A_n(R)$ for scattering angle $\theta = 20^0$.

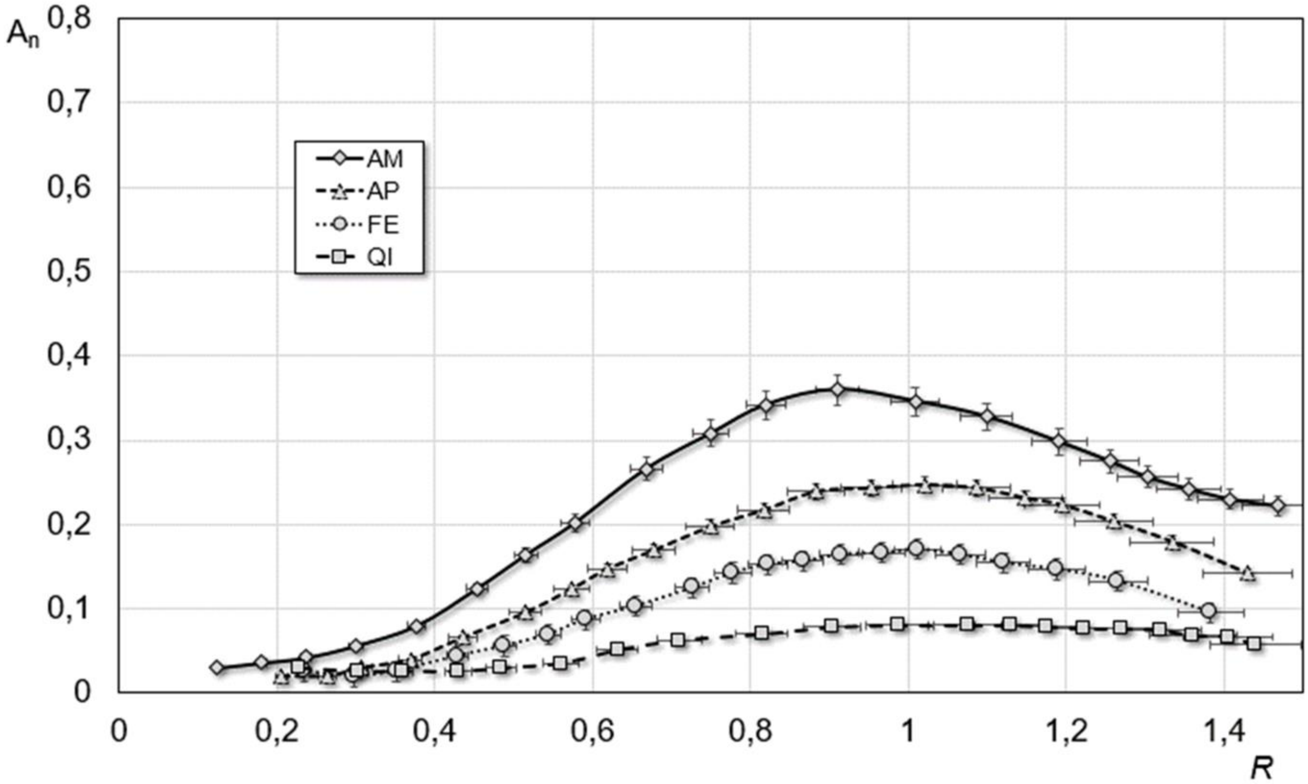

Figure 5.5. Dependence $A_n = A_n(R)$ for scattering angle $\theta = 40^0$.

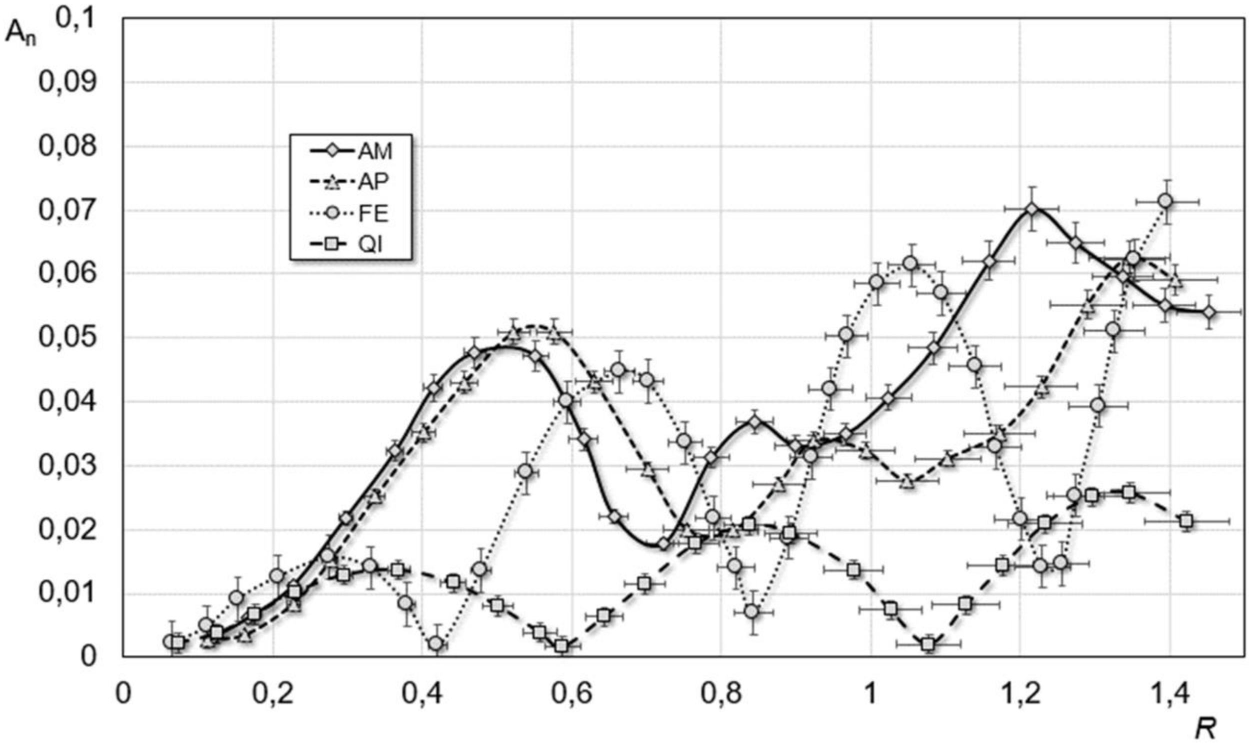

Figure 5.6. Dependence $A_n = A_n(R)$ for scattering angle $\theta = 180^0$.

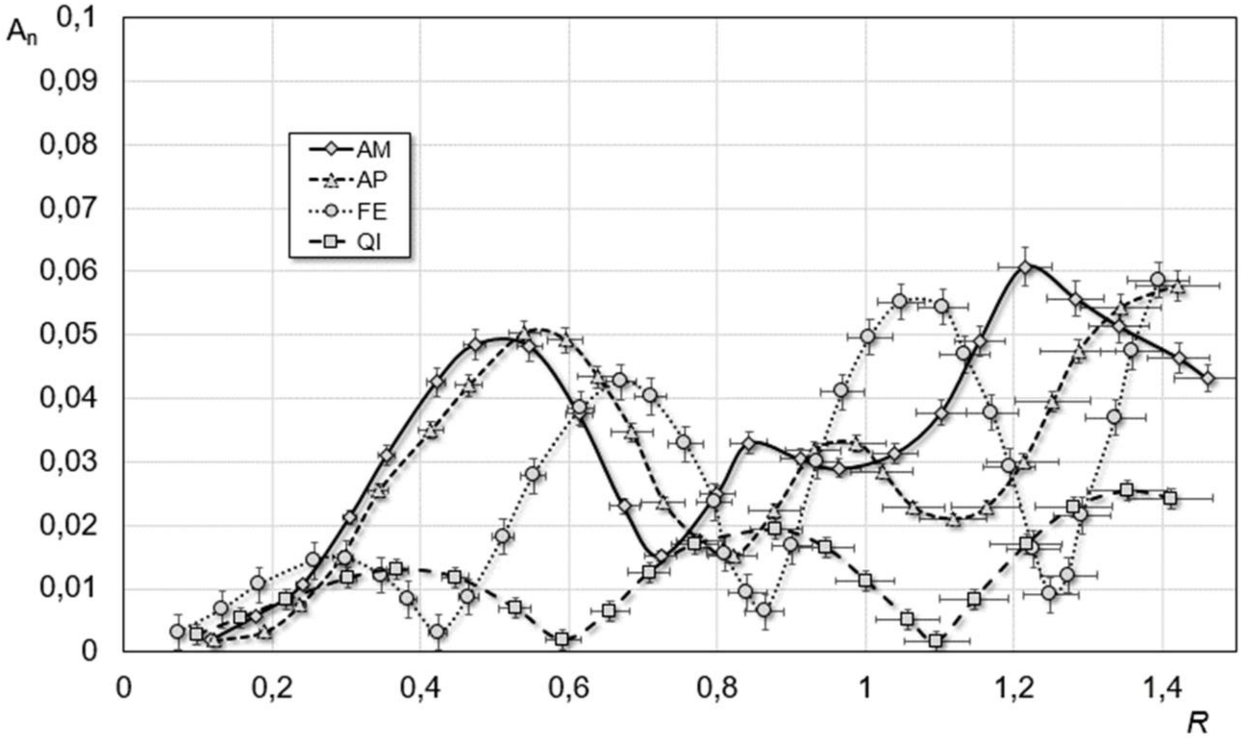

Figure 5.7. Dependence $A_n = A_n(R)$ for scattering angle $\theta = 200^0$.

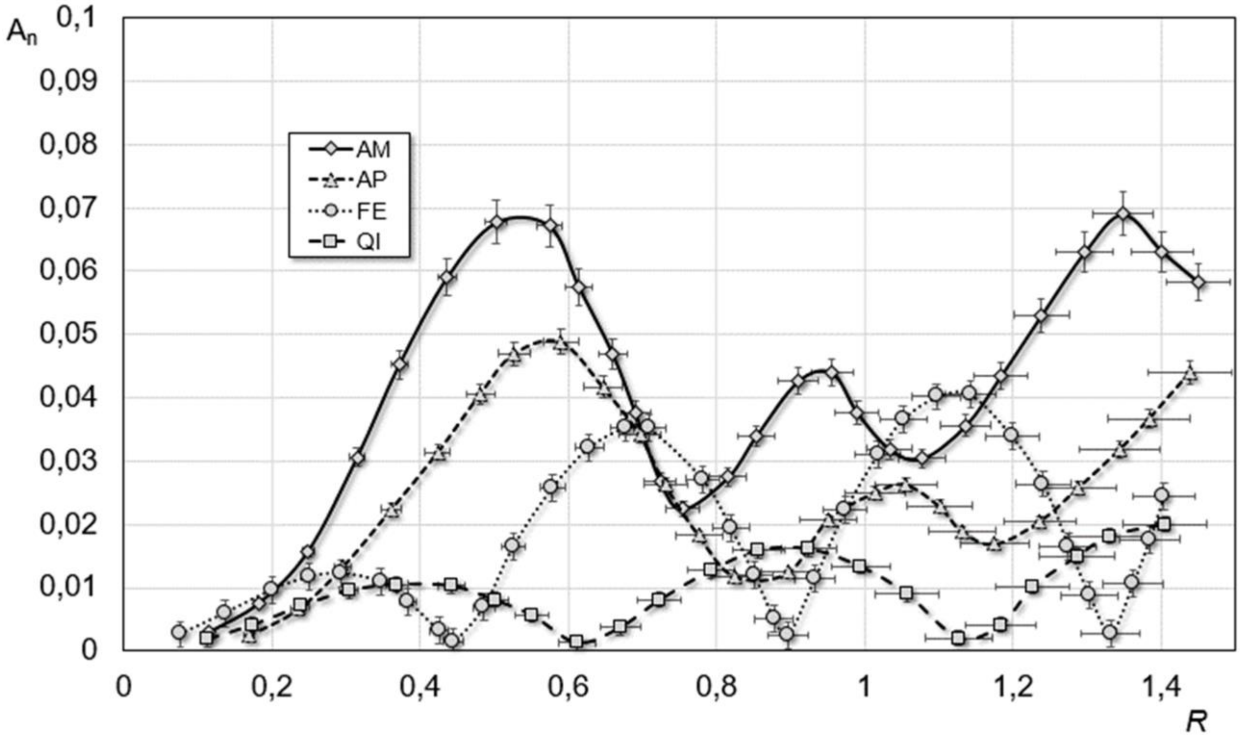

Figure 5.8. Dependence $A_n = A_n(R)$ for scattering angle $\theta = 220^0$.

Finite element modeling, in which each layer of the laminated composite is represented as a layer of solid elements with orientation in accordance with the fiber direction, is considered as the reference basic procedure. The agreement between analytical, approximate and finite element results is not very good. Satisfactory results in these models are observed for the case of a quasi-isotropic composite.

CHAPTER 6
STRUCTURAL HEALTH MONITORING TECHNIQUES

Non-destructive and continuous monitoring of structures can be defined as structural health monitoring. Such structures can be structures containing or entirely composed of composite material elements. Structural health monitoring can detect and control developing defects within their volume. A set of experimental studies conducted in recent years has shown that guided wave technology is an effective method for structural health monitoring. This is due to the high sensitivity of this technique and its versatility.

A guided wave can be generated by piezoelectric transducers on the composite structure under investigation. Such guided waves are sensitive to small-scale damage and can propagate over long distances. One such type of guided wave is the Lamb wave. The Lamb wave propagates due to the motion of particles between two surfaces in a thin plate-like medium of a laminar composite.

Using Lamb wave-based structure monitoring systems, there is no need to scan the entire object under investigation, and all data can be obtained from a single probe position. While defect detection and localization in simple thin-walled composite laminates has been widely studied, studies on the inspection of complex composite assemblies using Lamb wave-based systems lack sensitivity to defect localization in the composite volume.

The results of the composite structure monitoring experiments indicate that the structural integrity of composite joints is significantly dependent on the conditions and service life of the system as a whole. The connections of different elements in the structure can lead to abrupt failure with little advance warning. Therefore, it is necessary to develop structure monitoring methods that focus on continuous monitoring of composite joints. Recently, guided wave technology has been successfully applied to detect damage not only in mechanically fastened joints, but also in adhesive joints.

The numerical analysis of scattered Lamb waves can be used to evaluate the integrity of the composite joint. Ultrasonic guided waves are a good experimental tool for investigating the adhesive bonds between composite laminates. The study of the transient dynamics and wave propagation characteristics of adhesive composite joints is most effective using the wavelet spectral finite element model. Defect detection in composite joint types such as T-joint and L-joint can also be effectively performed using guided Lamb waves.

However, Lamb wave-based structure monitoring technologies for damage monitoring in composite local mechanical joints are not well developed. It is of interest to investigate composite local joints based on the Lamb wave propagation phenomenon. In particular, it is reasonable to consider two different types of local joints in a composite structure, differing in the length-to-width ratio of the joint.

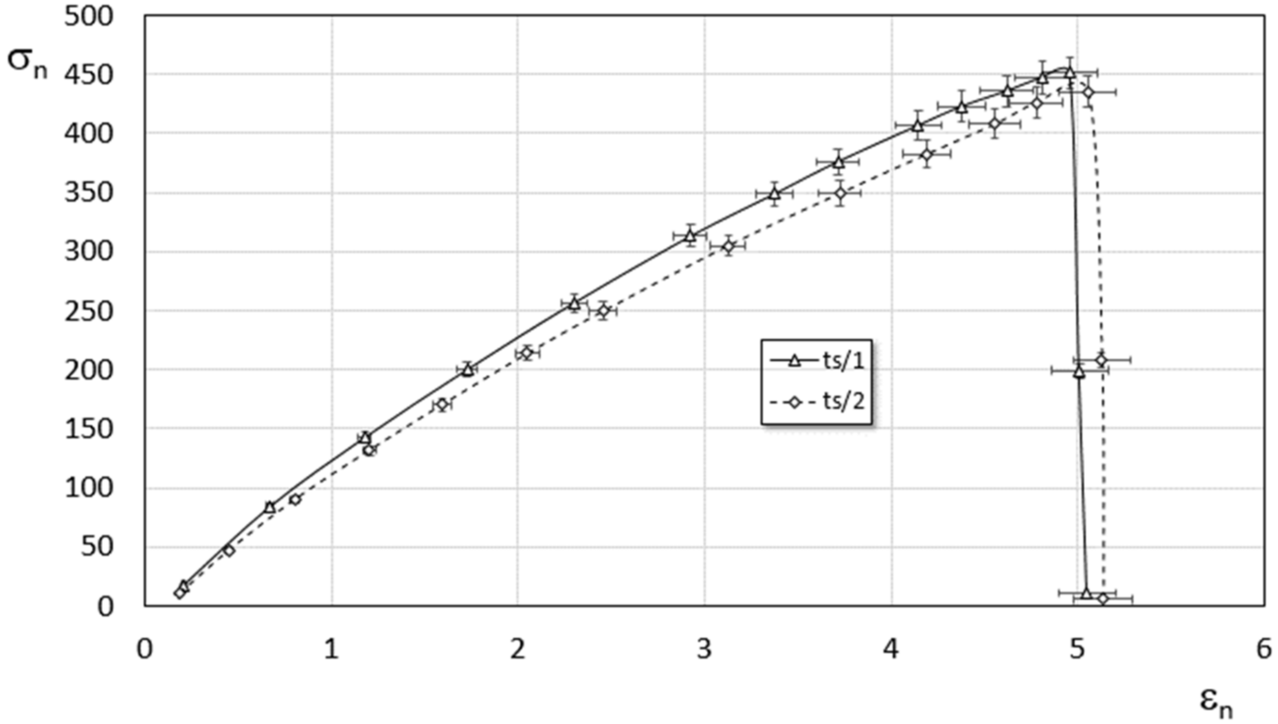

Figure 6.1. Stress-strain curves: ts/1 – 0^0 tensile; ts/2 – 90^0 tensile.

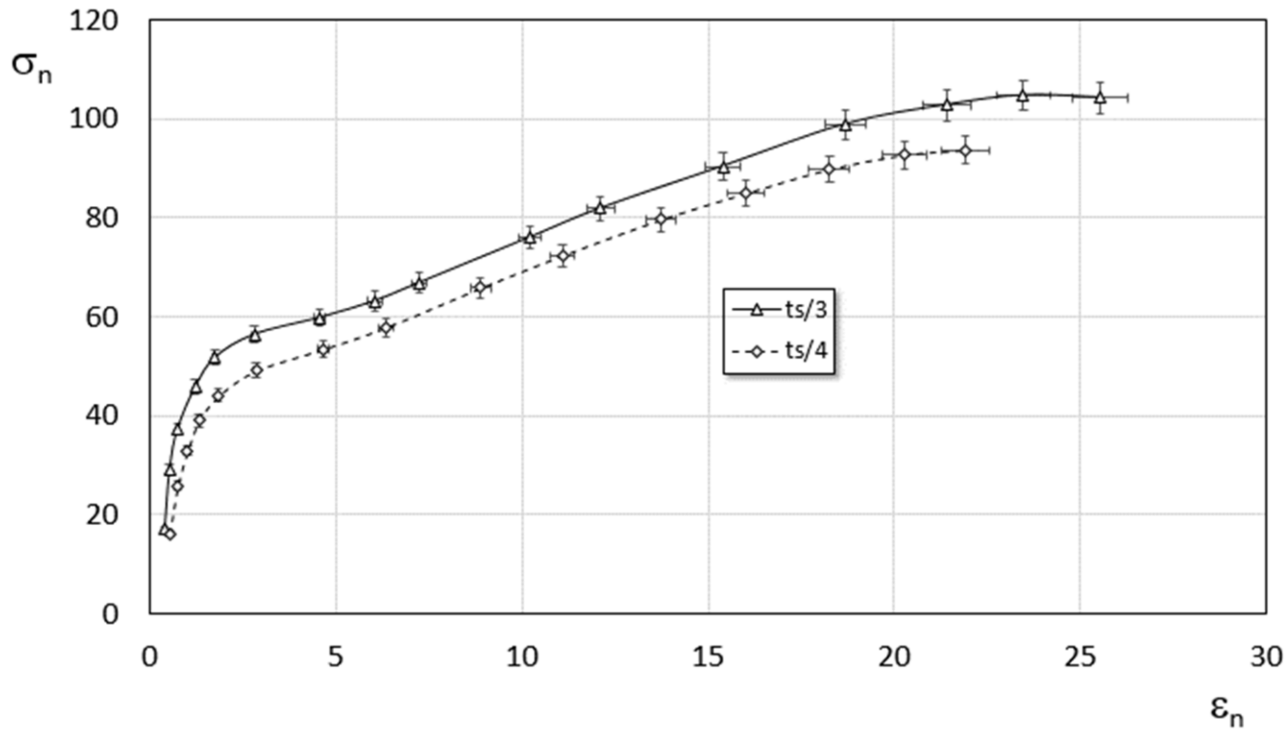

Figure 6.2. Stress-strain curves: ts/3 – |+45^0 tensile; ts/4 – |–45^0 tensile.

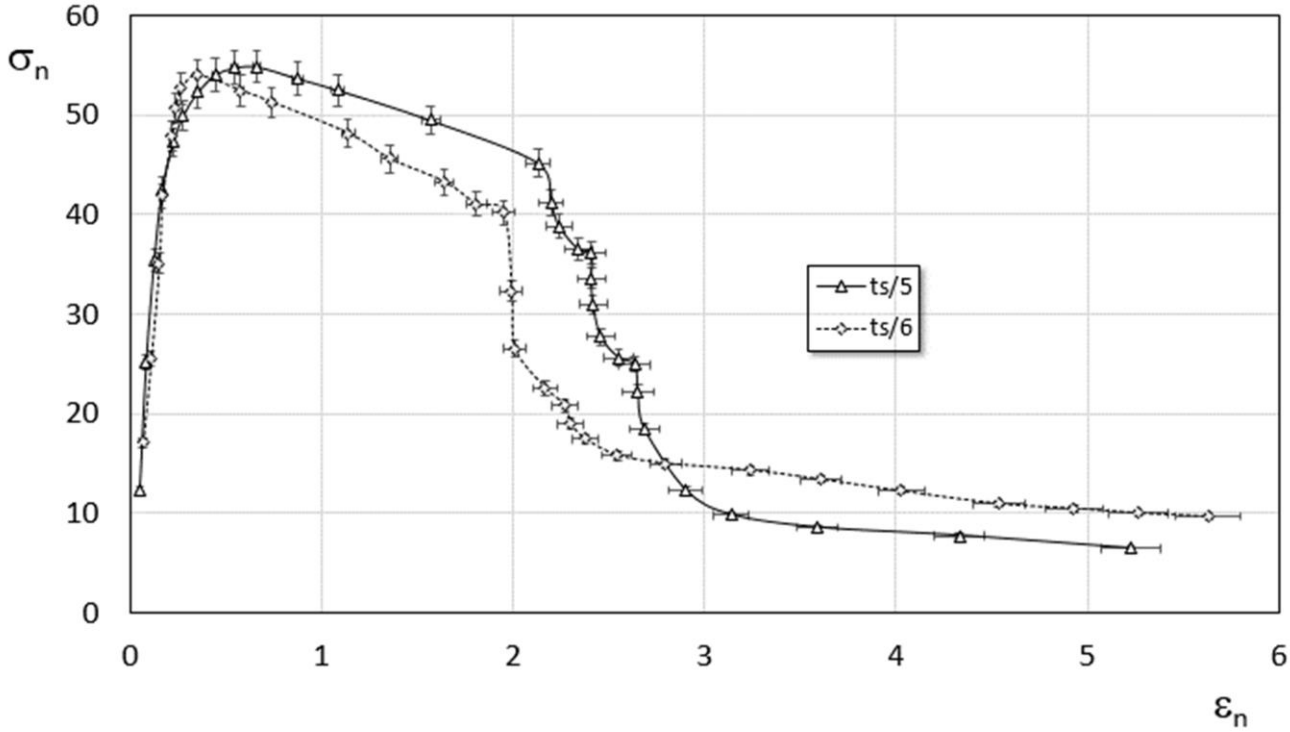

Figure 6.3. Stress-strain curves: ts/5 – 0^0 compression; ts/6 – 90^0 compression.

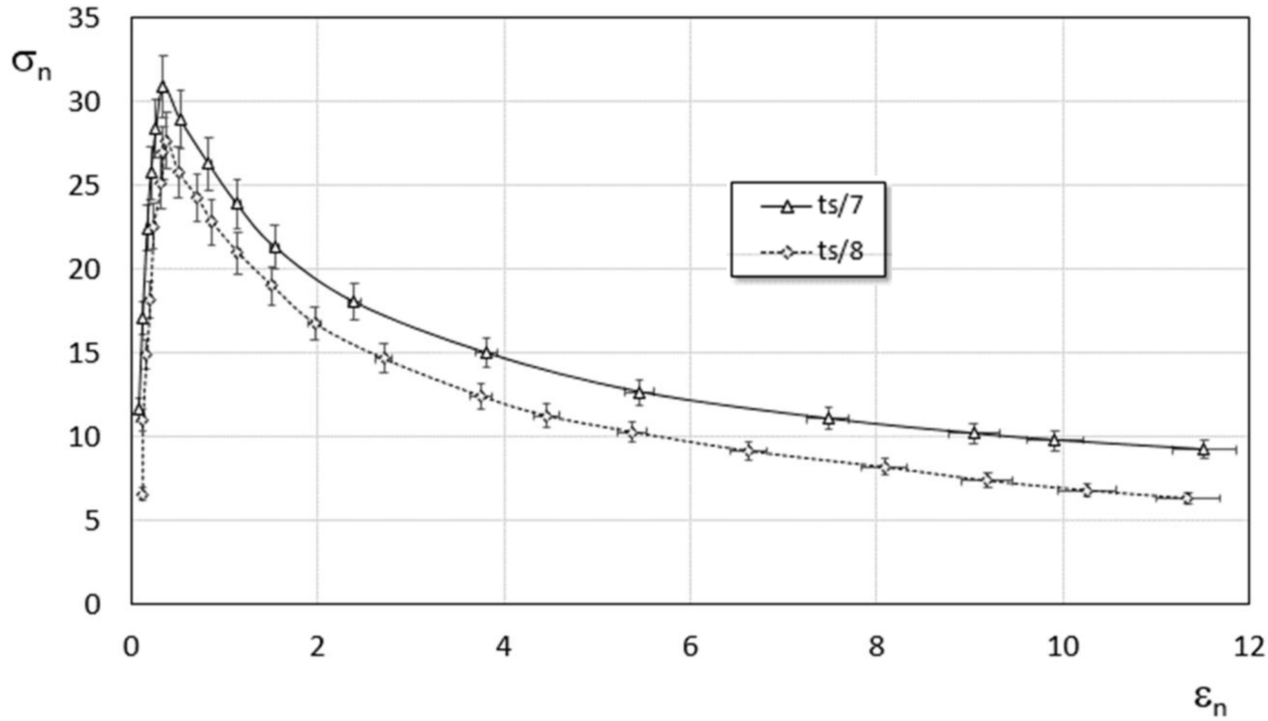

Figure 6.4. Stress-strain curves: ts/7 – |+45^0 compression; ts/8 – |-45^0 compression.

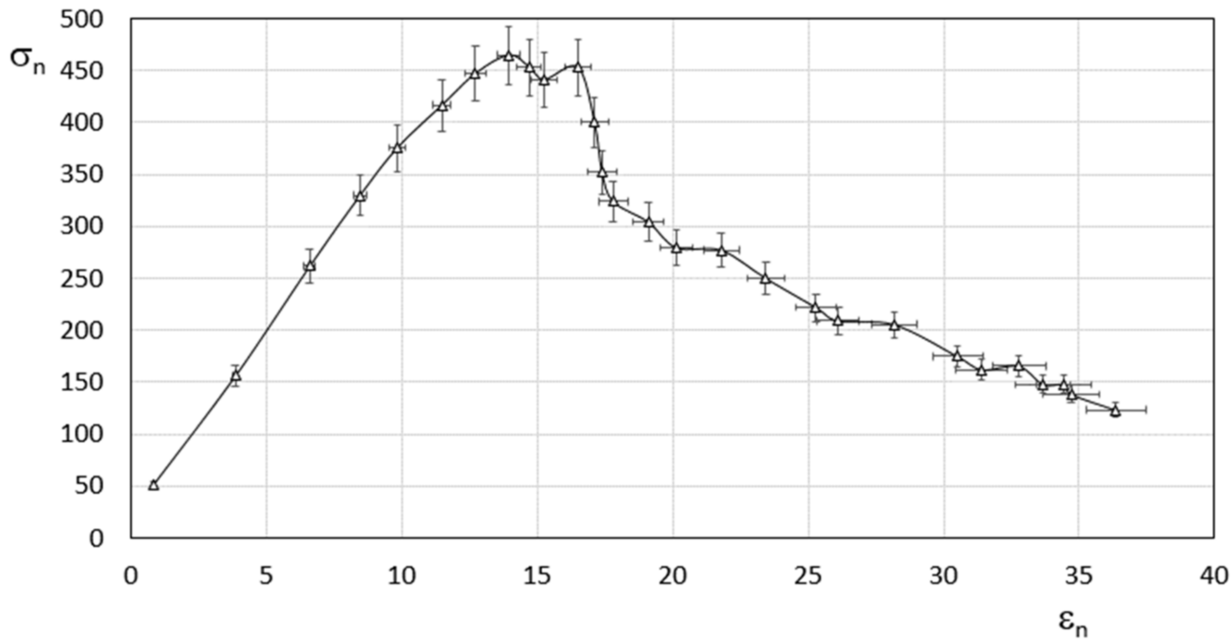

Figure 6.5. Stress-strain curve, three-point bending test.

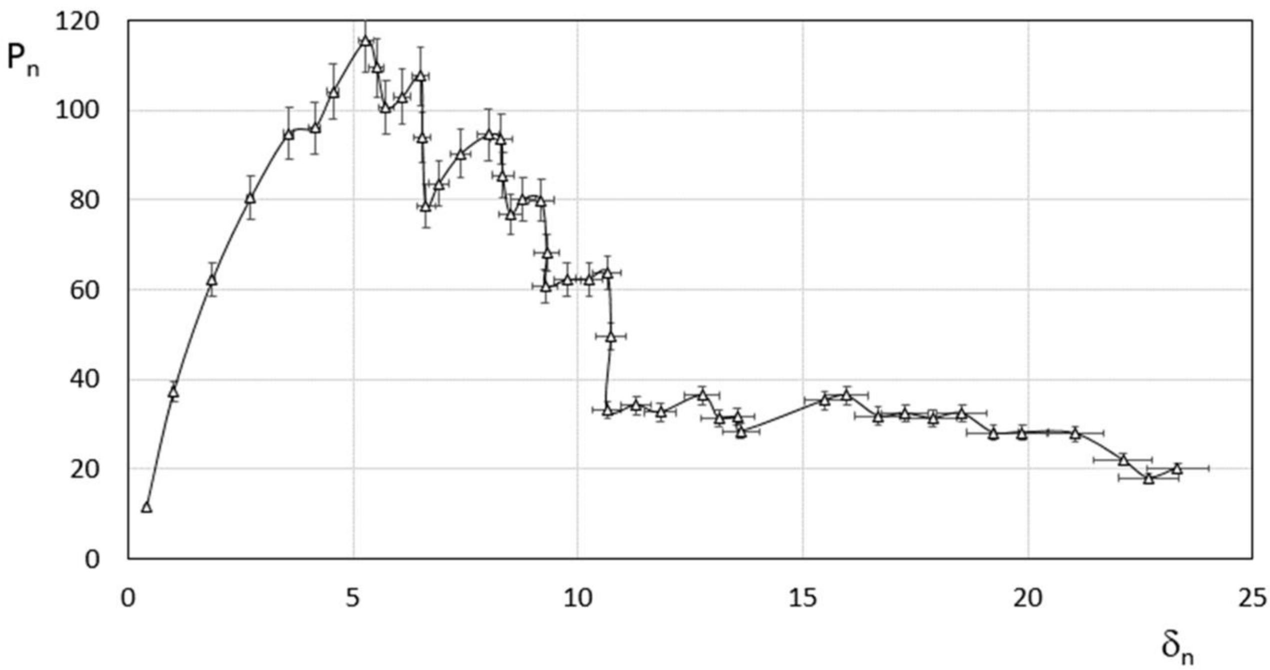

Figure 6.6. Fixed mode A fracture toughness test.

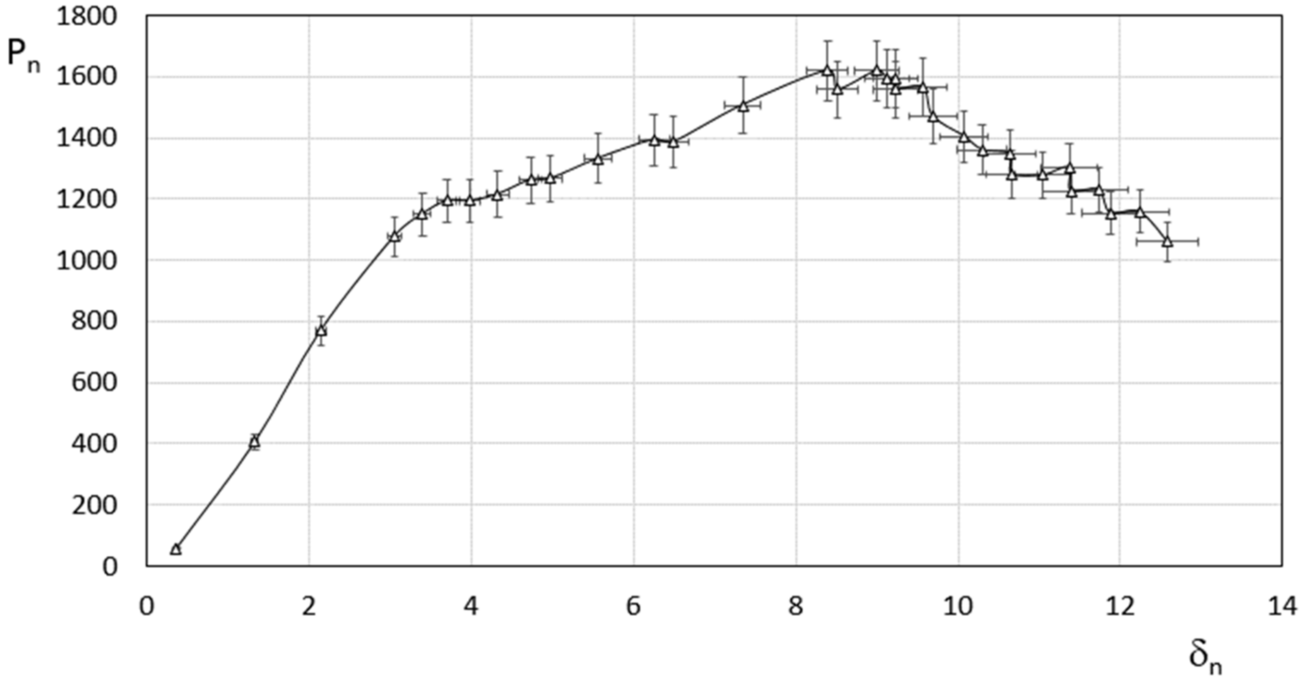

Figure 6.7. Fixed mode B fracture toughness test.

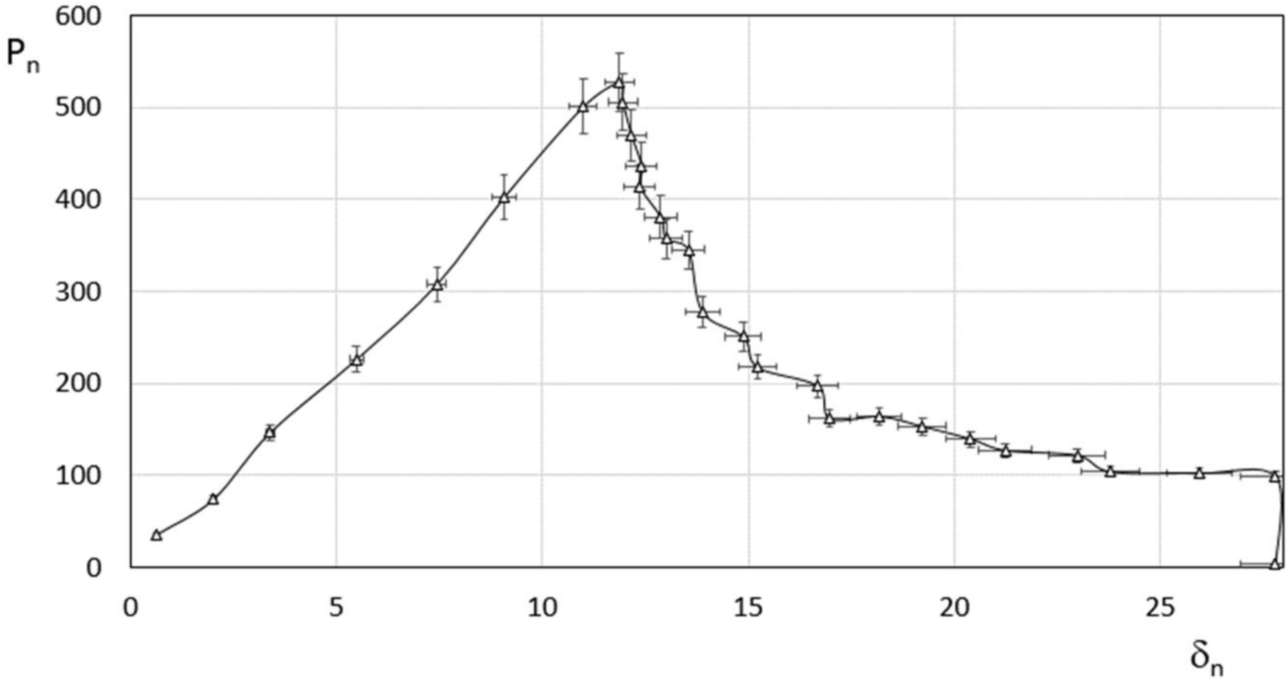

Figure 6.8. Fixed mode C fracture toughness test.

Mechanical effects on the surface of the composite sample naturally lead to a change in the deformation field and, accordingly, to a change in the characteristics of the Lamb waves scattered by defects. The propagation behavior of Lamb waves in joints, especially in the region of high mechanical local joint concentrations, was analyzed using three-dimensional finite element modeling. The numerical values of the parameters in the modeling were specified using the available results of the baseline experiments.

The results of numerical calculations were accumulated in the average stress-strain and load-displacement curves of the composite laminates for different types of mechanical loading. The stress-strain and compression curves (σ_n - ε_n) along 90^0, 0^0 and $\pm45^0$ fibers of the laminar composites are presented in Figs. 6.1 - 6.4. Figure 6.5 is the curve of the three-point bending test, and Figs. 6.5 - 6.8 are the normalized (index “n” in curves) load-displacement curves (P_n - δ_n) obtained in multimode tests.

Modes A, B and C in Fig. 6.6 - 6.8 are characterized by the following regimes: the origin of localized deformations in the form of cracks (mode A); the development of multiple cracks to their maximum geometric dimensions (mode B); the initial stage of the composite sample delamination caused by a set of developed cracks (mode C).

One of the quite effective methods for numerical modeling of the propagation of guided Lamb waves in composite laminates of arbitrary layup and cross-sectional geometry is the semi-analytical finite element method. It should be noted that the traditional finite element method in application to laminated composites is computationally expensive and may lead to numerical failure, especially in the case of short wavelengths.

The semi-analytical finite element method uses a finite element two-dimensional discretization of the cross-sectional area. The basic assumption in this model is that the displacements along the direction of propagation of the wave packet are assumed to have the form of a harmonic wave and are plane-polarized. Moreover, the typical planar geometry of laminates allows for further simplification in terms of one-dimensional modeling.

The calculation procedure considers the cross-sectional domain Ω of the laminated composite specimen, which is represented by a finite element system with domain Ω_e.

$$u(x,y,z,t)=\begin{bmatrix} u_x(x,y,z,t) \\ u_y(x,y,z,t) \\ u_z(x,y,z,t) \end{bmatrix} = \begin{bmatrix} u_x(y,z) \\ u_y(y,z) \\ u_z(y,z) \end{bmatrix} \exp[i(\xi x - \omega t)], \tag{6.1}$$

where ω is the angular temporal frequency.

The field of local displacements anisotropically located along the volume of the laminated composite is assumed to be harmonic along the *x*-propagation direction.

The characteristics of the displacement locations are described by spatial functions that are used to describe its amplitude in the *y-z* cross-sectional plane (6.1).

When using one-dimensional elements, a separate procedure was adopted for discretizing Ω. The discretized version of the displacement expressions over the element domain can be written in terms of shape functions, $N_k(y, z)$, and unknown nodal displacements, (U_{xk}, U_{yk}, U_{zk}) in the *x*, *y*, and *z* directions:

$$u^e(x,y,z,t)=\begin{bmatrix}\sum_{j=1}^{n} N_j(y,z)U_{xj}\\ \sum_{j=1}^{n} N_j(y,z)U_{yj}\\ \sum_{j=1}^{n} N_j(y,z)U_{zj}\end{bmatrix}\exp[i\xi x-\omega t]=N(y,z)q^e\exp[i\xi x-\omega t], \quad (6.2)$$

where

$$N(y,z)=\begin{bmatrix}N_1 & & & N_2 & & & \ddots & & & N_n & & \\ & N_1 & & & N_2 & & & \ddots & & & N_n & \\ & & N_1 & & & N_2 & & & \ddots & & & N_n\end{bmatrix} \quad (6.3)$$

$$q^e=[U_{x1},U_{y1},U_{z1},U_{x2},U_{y2},U_{z2},\ldots,U_{xn},U_{yn},U_{zn},], \quad (6.4)$$

n is the number of nodes per element.

Nodal displacements can be considered as arguments of some deformation vector

$$\varepsilon^e=\left[L_x\frac{\partial}{\partial x}+L_y\frac{\partial}{\partial y}+L_z\frac{\partial}{\partial z}\right]N(y,z)q^e\exp[i(k\,x-\omega t)]=$$

$$=(B_1+ikB_2)q^e\exp[i(k\,x-\omega t)], \quad (6.5)$$

where

$$B_1=L_yN_y+L_zN_z, \quad (6.6)$$

$$B_2=L_xN\,. \quad (6.7)$$

At the next stage, the technique requires writing down the discrete form of the formulation of Hamilton's equation (denoting by the symbol n_{el} the total number of elements of the cross section)

$$\int_{t_1}^{t_2}\left\{\bigcup_{e=1}^{n_{el}}\left[\int_{V_e}\delta\left(\varepsilon^{eT}\right)C_e\varepsilon^e dV_e+\int_{V_e}\delta\left(u^{eT}\right)\rho_e\ddot{u}^e dV_e\right]\right\}dt=0, \qquad (6.8)$$

where
C_e is the complex stiffness matrix;
ρ_e is the density.

Algebraic transformations of equations (6.5) and (6.8) lead to the following relations

$$\int_{V_e}\delta\left(\varepsilon^{eT}\right)C_e\varepsilon^e dV_e=$$

$$\int_{\Omega_e}\int_{x}\delta\left\{q^{eT}\left(B_1^T-ikB_2^T\right)\cdot\left[e^{i(kx-\omega t)}\right]^T\right\}C_e\left(B_1+ikB_2\right)q^e e^{i(kx-\omega t)}dxd\Omega=$$

$$=\int_{\Omega_e}\delta\left\{q^{eT}\left(B_1^T-ikB_2^T\right)\right\}C_e\left(B_1+ikB_2\right)q^e d\Omega_e=$$

$$=\delta q^{eT}\int_{\Omega_e}\left[B_1^TC_eB_1-ikB_2^TC_eB_1+ikB_1^TC_eB_2+k^2B_2^TC_eB_2\right]d\Omega_e q^e, \qquad (6.9)$$

where $i^T=-i$.

This numerical methodology assumes that the element stiffness matrix can be calculated by integrating only over the cross-sectional area Ω_e, since integration over x reduces to a unit factor due to the complex conjugate terms exp [± i ($kx - \omega t$)]. For viscoelastic materials, the strain energy consists of a real and an imaginary component. The real component of the strain energy describes the time-averaged elastic energy in the cross-section. The imaginary component of the strain energy is related to the time-averaged power dissipated by the cross-section.

The contribution of kinetic energy of mechanical displacement can be expressed by the ratio

$$\int_{V_e} \delta\left(u^{eT}\right)\rho_e \ddot{u}^e dV_e = \int_{\Omega_e}\int_x \delta\left(u^{eT}\right)\rho_e \ddot{u}^e dx d\Omega_e =$$

$$= -\omega^2 \delta q^{eT} \int_{\Omega_e} N^T \rho_e N d\Omega_e q^e \, . \tag{6.10}$$

In this case, equation (6.8) takes the form

$$\int_{t_1}^{t_2} \left\{ \bigcup_{e=1}^{n_{el}} \delta q^{eT} \left[k_1^e + ikk_2^e + k^2 k_3^e - \omega^2 m^e \right] q^e \right\} dt = 0 \, , \tag{6.11}$$

where

$$k_1^e = \int_{\Omega_e} B_1^T C_e B_1 d\Omega_e \, , \tag{6.12}$$

$$k_2^e = \int_{\Omega_e} \left[B_1^T C_e B_2 - B_2^T C_e B_1 \right] d\Omega_e \, , \tag{6.13}$$

$$k_3^e = \int_{\Omega_e} B_2^T C_e B_2 d\Omega_e \, , \tag{6.14}$$

$$m^e = \int_{\Omega_e} N^T \rho_e N d\Omega_e \, . \tag{6.15}$$

Applying the standard finite element procedure to equation (6.11), we get

$$\int_{t_1}^{t_2} \left\{ \delta U^T \left[K_1 + ikK_2 + k^2 K_3 - \omega^2 M \right] U \right\} dt = 0 \, , \tag{6.16}$$

where *U* is the global vector of nodal displacement and

$$K_1 = \bigcup_{e=1}^{n_{el}} k_1^e, \quad K_2 = \bigcup_{e=1}^{n_{el}} k_2^e, \quad K_3 = \bigcup_{e=1}^{n_{el}} k_3^e, \quad M = \bigcup_{e=1}^{n_{el}} m^e \, . \tag{6.17}$$

The homogeneous general wave equation has the form

$$\left[K_1 + ikK_2 + k^2K_3 - \omega^2 M\right]_M U = 0, \tag{6.18}$$

where M is the number of total degrees of freedom of the system.

The stiffness matrices K1 and K3 in the equation are symmetric. The matrix K2 is skew-symmetric and is related to the case where undamped motion is considered. For damped motion, all matrices Ki are usually complex. The matrix M is real symmetric and positive definite regardless of the type of motion (damped or undamped).

The matrix K1 is related to the strain transformation matrix B1, which is related to generalized plane strains. It should be noted that the matrix B1 describes the generalized plane strain behavior or transverse buckling. The matrix K3 describes the out-of-plane strain behavior since it depends on the matrix B2. The matrix K2 contains the matrices B1 and B2 and thus relates transverse buckling to out-of-plane strains.

The diagonal matrix T of the $M \times M$ transformation is introduced to eliminate the imaginary unit in the corresponding equations. The elements of T corresponding to the displacement components u_y and u_z are equal to 1, while the corresponding elements u_x are equal to the imaginary unit:

$$T = \begin{bmatrix} i & & & & & & \\ & 1 & & & & & \\ & & 1 & & & & \\ & & & \ddots & & & \\ & & & & i & & \\ & & & & & 1 & \\ & & & & & & 1 \end{bmatrix}. \tag{6.19}$$

This matrix has the properties TT = T* and T*T = TT* = I, where I is the identity matrix. In this case, the following relations are valid

$$T^T K_1 T = K_1, \quad T^T K_3 T = K_3, \quad T^T M T = M \ . \tag{6.20}$$

The property of the matrix K2 is that it mixes the components u_x with u_y and u_z, but does not mix the components u_y and u_z with each other

$$T^T K_2 T = -iK_2, \tag{6.21}$$

where K_2 is the symmetric matrix of undamped motion.

The final form of the special finite element eigenvalue method is

$$\left[K_1 + \xi K_2 + \xi^2 K_3 - \omega^2 M\right]_M U = 0 . \tag{6.22}$$

Results in terms of multiple modes and dispersion properties can be obtained in a numerically stable manner using the eigenvalue and eigenvector problem. Two quadratic finite elements were used on a model example of a laminar composite containing 18 plates. Each element has three degrees of freedom per node, associated with mechanical displacements U_x, U_y, U_z.

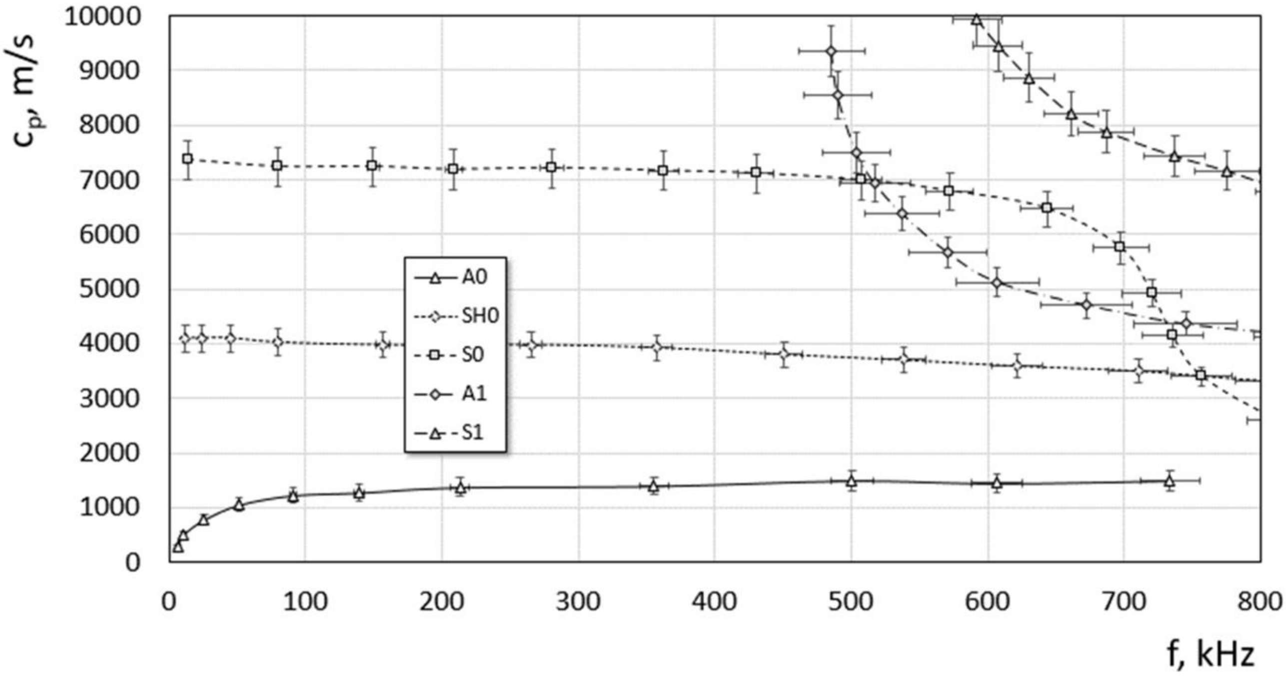

Figure 6.9. Dispesion curve $c_p = c_p$ (f) for $\theta = 0^0$ direction.

Figures 6.9 - 6.12 show the dispersion curves for the phase velocities $C_p = C_p$ (f). Considering the quasi-isotropic stacking and to quantify its anisotropy level, four different Lamb wave propagation directions (0°, 30°, 60°, and 90° relative to the *x*-coordinate of the laminate) were simulated. The basic assumption for the structure monitoring model is quasi-isotropy throughout the volume of the laminated composite.

The dispersion curve calculations revealed the presence of the so-called cutoff frequency f_c, which outlines the extension of the non-dispersive region where only three fundamental Lamb wave modes (S0, A0, and SH0) can exist. The velocity of the Lamb wave packets is almost constant in this range, except for the A0 wave close to the origin). It should be noted that the anisotropy level of the laminate is determined by the quasi-isotropic stacking sequence.

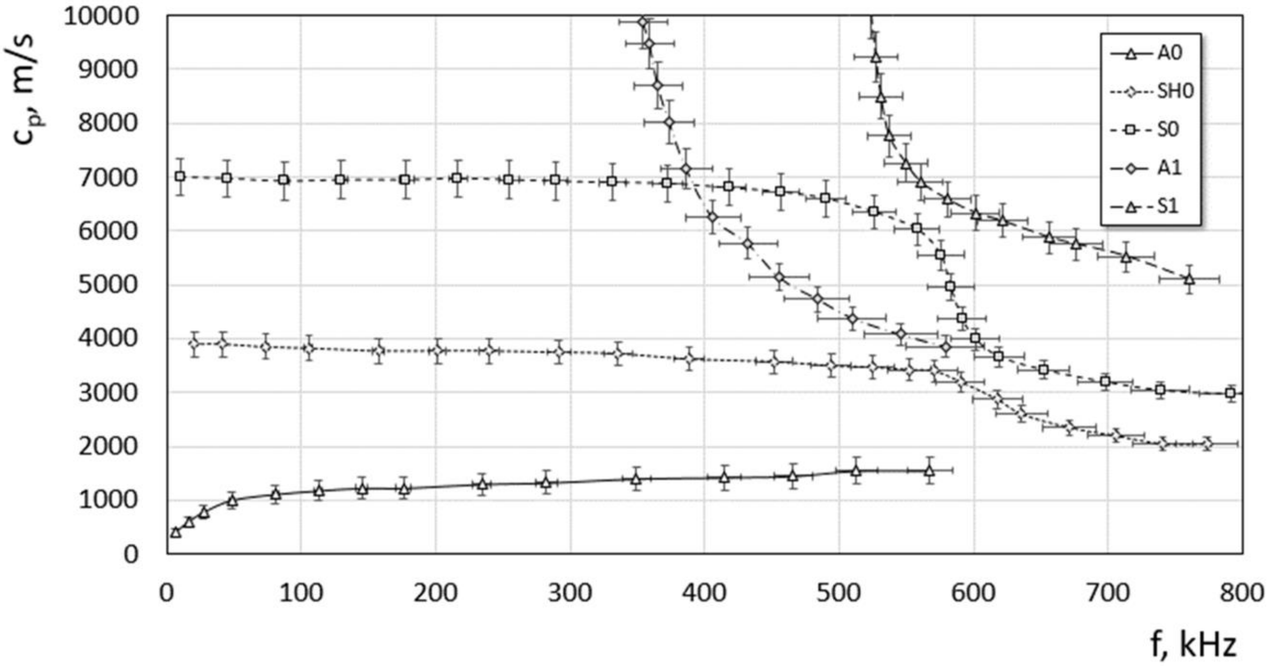

Figure 6.10. Dispesion curve $c_p = c_p$ (*f*) for $\theta = 30^0$

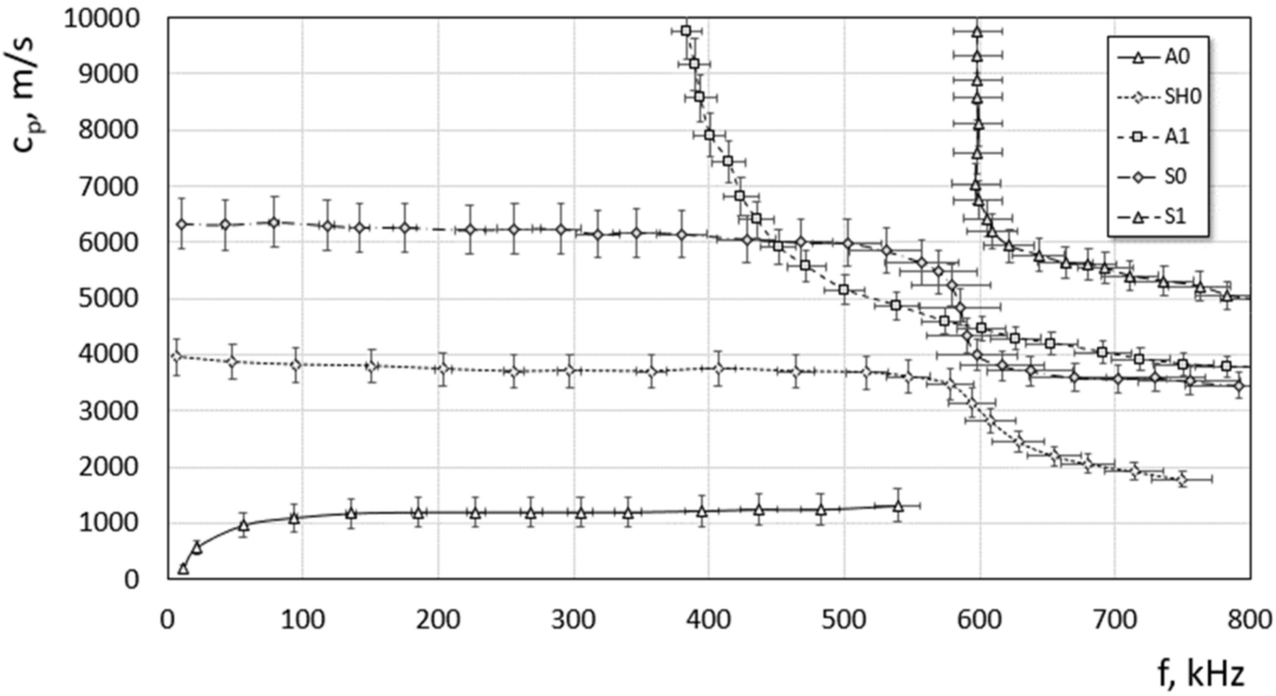

Figure 6.11. Dispesion curve $c_p = c_p$ (*f*) for $\theta = 60^0$

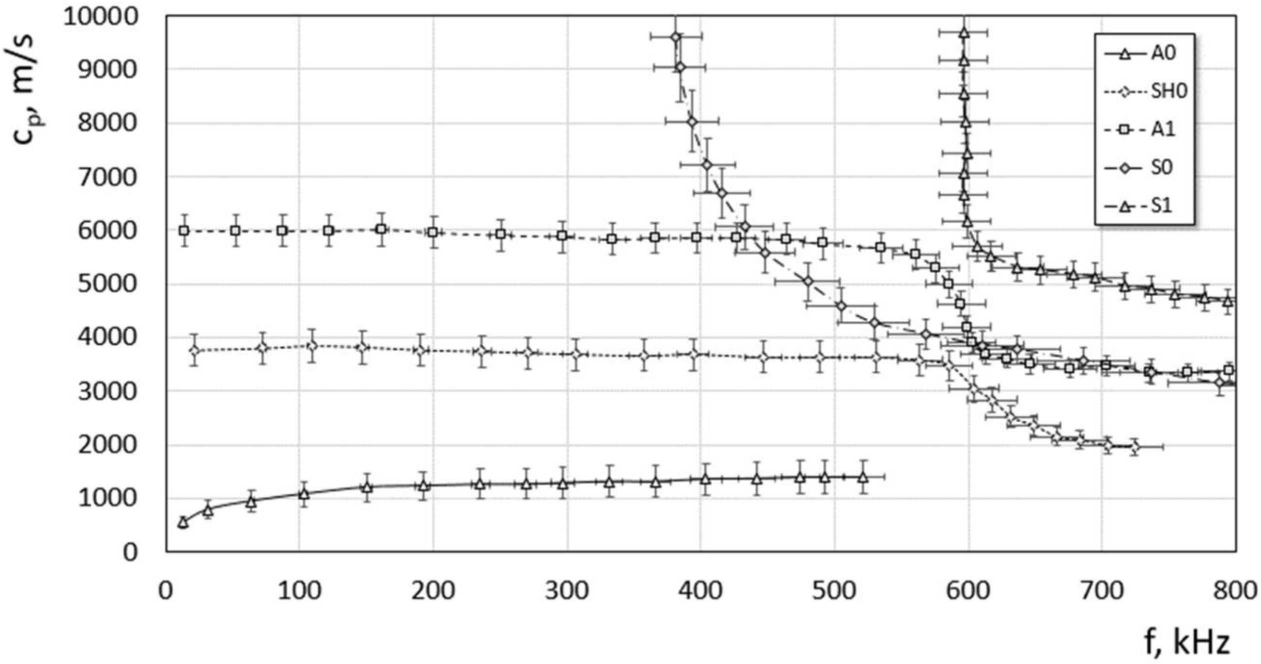

Figure 6.12. Dispesion curve c_p = c_p (f) for θ = 90^0

The characteristic value of the group velocity A0 is superimposed on the fluctuations. The amplitude values of the Lamb wave packets corresponding to the coordinate located at the midpoint of the laminate volume were processed through the Hilbert transform to extract the values of the group velocity Cg according to the formula

$$c_g = \frac{\Delta x}{f_c}, \tag{6.23}$$

where Δx is the wave propagation path.

The calculated values of the wave number based on the reference value of the circular frequency are the basis for determining the group velocity according to the formula

$$c_g = \frac{\partial \omega}{\partial k} = \frac{\Delta \omega}{\Delta k}. \tag{6.24}$$

CHAPTER 7
COMPARISON OF SCHEMES FOR LAMB WAVE MODELLING

Active diagnostics of composite materials often involves the use of transient Lamb waves for damage detection. This methodology involves preliminary analysis of the complex Lamb wave characteristics of composite laminates. Numerical studies of laminate damage characteristics such as delamination, matrix cracking, etc. always require the use of ply-by-ply theories or finite element models. These models have sufficient resolution in predicting local effects. However, they are computationally expensive, especially for modeling the entire laminated structure.

Among the large number of analytical studies, two key approaches to the study of global characteristics of Lamb wave propagation in composite laminates can be distinguished. The first approach is associated with the 3*D* elasticity theory, which is able to calculate exact solutions. The second technique is equivalent to the single-layer theory. The theory of one fixed layer can provide only approximate solutions.

Exact solutions can be obtained by analyzing the dispersion characteristics of Lamb waves in laminates. The dispersion results can be verified by the finite element method followed by analyzing the directional characteristics of Lamb waves in laminates. The complexity and computational cost of the 3D elasticity theory strongly depends on the stacking sequence of layers (along the plane of symmetry or not) and the number of layers of the laminated composite.

Approximate plate theory applied to laminated composite provides greater efficiency than 3D elasticity theory, especially for laminates with complex stacking sequences and a large number of layers. It should be noted that techniques of this type are effective for solving large-scale problems, such as reconstructing unknown stiffness coefficients in composites based on Lamb wave phase velocities.

A drawback of the first-order shear deformation theory, as well as of some higher-order shear deformation theories, is the absence of stress-free boundary conditions on the top and bottom surfaces of the panel. To overcome this drawback, a complex scheme was developed for calculating shear correction factors. The correction factors change their numerical values when the laminate properties (ply stacking sequence, number of plies and ply properties, etc.) are changed.

The standard method for determining the correction factors is to compare the fixed cutoff frequencies from the approximate theories with those obtained from the exact theory. The computational time required to implement this method for the conventional single plate equivalent theories should include the time required to calculate the exact solutions.

To avoid calculating complex shear correction factors, a correction is usually made to the displacement field. This takes into account the disappearance of transverse shear stresses at the top and bottom of a conventional laminate. However, for the case where Lamb wave packets propagate in composite panels, the stress-free state on the panel surfaces refers not only to the disappearance of transverse shear stresses, but also to the disappearance of normal stresses. Therefore, modified third-order plate theories should consider transverse shear strain and stress-free boundary conditions to effectively model Lamb waves in composite laminates. Lamb wave packets can be roughly divided into two groups of modes, which are generally represented by symmetric and antisymmetric modes in accordance with the symmetric characteristics of the displacement distribution.

Introducing a rectangular Cartesian coordinate system, it can be stated that *u*, *v* and *w* are the components of displacement in the *x*, *y* and *z* directions. In this case, the *u* and *v* displacement components of the antisymmetric modes have the property of being antisymmetric with respect to the *z*-axis. Due to this, the odd-order terms with respect to *z* in *u* and *v* describe antisymmetric modes. The even-order terms with respect to *z* in *w* also correspond to antisymmetric modes, because *w* is symmetric with respect to the *z*-axis for the antisymmetric modes. The even-order terms with respect to *z* in *u* and *v* together with the odd-order terms with respect to *z* in *w* describe symmetric modes.

Taking into account the effects of rotational inertia and shear deformation, it can be concluded that the displacement field defined in the base coordinate system taking into account the effects has the following components

$$u = z\varphi_x(x, y, t), \tag{7.1}$$

$$\upsilon = z\varphi_y(x, y, t), \tag{7.2}$$

$$w = w_0(x, y, t). \tag{7.3}$$

It should be noted that the bias field generates three antisymmetric modes and cannot be used to calculate any symmetric mode. A model example of a pseudospectral element of a plate with 5 degrees of freedom for a modified displacement field is described by the following relations

$$u = u_0(x, y, t) + z\varphi_x(x, y, t), \tag{7.4}$$

$$\upsilon = \upsilon_0(x, y, t) + z\varphi_y(x, y, t), \tag{7.5}$$

$$w = w_0(x, y, t), \tag{7.6}$$

where u_0 and υ_0 are the displacement components of the mid-plane.

The analysis shows that there are three antisymmetric modes and two symmetric modes in the displacement field of the laminated composite sample.

Splitting the characteristic matrix into two submatrices to solve the antisymmetric modes and symmetric modes separately can be done for laminar composites. Meanwhile, there is no term describing the symmetric modes in the w component, which means that the calculated two symmetric modes share a zero displacement component w. Therefore, the displacement field may not be suitable for predicting the symmetric modes.

The study of the motion of Lamb wave packets under tension of laminate composites can be effectively performed using a quadratic displacement field

$$u = u_0(x,y,t) + z\varphi_x(x,y,t) + z^2\varphi_x(x,y,t), \tag{7.7}$$

$$\upsilon = \upsilon_0(x,y,t) + z\varphi_y(x,y,t) + z^2\varphi_y(x,y,t), \tag{7.8}$$

$$w = w_0(x,y,t) + z\varphi_z(x,y,t) + z\varphi_z(x,y,t). \tag{7.9}$$

For this case, the Lamb wave propagation can be attributed to three antisymmetric modes and five symmetric modes. The third-order displacement field allows one to describe up to six antisymmetric Lamb wave modes and five symmetric Lamb wave modes

$$u = u_0(x,y,t) + z\psi_x(x,y,t) + z^2\varphi_x(x,y,t) + z^3\chi_x(x,y,t), \tag{7.10}$$

$$\upsilon = \upsilon_0(x,y,t) + z\psi_y(x,y,t) + z^2\varphi_y(x,y,t) + z^3\chi_y(x,y,t), \tag{7.11}$$

$$w = w_0(x,y,t) + z\psi_z(x,y,t) + z^2\varphi_z(x,y,t). \tag{7.12}$$

The procedure of equating the transverse components of the shear stress on the upper and lower surfaces to zero allowed us to modify the third-order theory

$$\begin{Bmatrix} \sigma_{yz} \\ \sigma_{xz} \end{Bmatrix}_{t1} = \begin{Bmatrix} \sigma_{yz} \\ \sigma_{xz} \end{Bmatrix}_{t2} = \begin{Bmatrix} 0 \\ 0 \end{Bmatrix}, \tag{7.13}$$

where
index “t1” corresponds the top surface of the layer;
index “t2” corresponds the bottom surface of the layer.

As a result, the displacement field gets the form

$$u = u_0 + z\varphi_x - z^2\left(\frac{1}{2}\frac{\partial\varphi_z}{\partial x}\right) -$$

$$-z^3\left[C_1\left(\frac{\partial w_0}{\partial x}+\varphi_x\right)+\frac{1}{3}\frac{\partial \varphi_z}{\partial x}\right], \tag{7.14}$$

$$\upsilon=\upsilon_0+z\varphi_y-z^2\left(\frac{1}{2}\frac{\partial \varphi_z}{\partial y}\right)-$$

$$-z^3\left[C_1\left(\frac{\partial w_0}{\partial y}+\varphi_y\right)+\frac{1}{3}\frac{\partial \varphi_z}{\partial y}\right], \tag{7.15}$$

$$w=w_0+z\varphi_z+z^2\varphi_z\,, \tag{7.16}$$

where
$C_1 = 4/(3h^2)$;
h is the laminate thickness.

The model example will consist of a laminar composite with a constant thickness h. The composite contains anisotropic plates that are ideally bonded together. The origin of the global Cartesian coordinate system is located in the mid-plane x-y, and the z-axis is perpendicular to the mid-plane. The two outer surfaces of the laminate are at $z = \pm h/2$. A packet of transient Lamb waves propagates in the composite laminate in an arbitrary direction θ, which is defined relative to the x-axis.

The fixed layer can be considered as a monoclinic material, having x-y as a plane of symmetry. In this case, the stress-strain relationships of an individual plate can be expressed in the following matrix form:

$$\begin{Bmatrix}\sigma_1\\\sigma_2\\\sigma_3\\\sigma_4\\\sigma_5\\\sigma_6\end{Bmatrix}=\begin{bmatrix}C_{11}&C_{11}&C_{11}&0&0&C_{11}\\C_{11}&C_{11}&C_{11}&0&0&C_{11}\\C_{11}&C_{11}&C_{11}&0&0&C_{11}\\0&0&0&C_{11}&C_{11}&0\\0&0&0&C_{11}&C_{11}&0\\C_{11}&C_{11}&C_{11}&0&0&C_{11}\end{bmatrix}\begin{Bmatrix}\varepsilon_1\\\varepsilon_2\\\varepsilon_3\\\varepsilon_4\\\varepsilon_5\\\varepsilon_6\end{Bmatrix}, \tag{7.17}$$

where
subscript “1” denotes x;
subscript “2” denotes y;
subscript “3” denotes z;
subscript “4” denotes yz;
subscript “5” denotes xz;
subscript “6” denotes xy.

The basic model assumes that the variables ϕ_x, χ_x , ϕ_y , χ_y , ψ_z and ϕ_z will be defined with the boundary condition that the mechanical stresses $\sigma_{zz} = \sigma_3$, $\sigma_{yz} = \sigma_4$ and $\sigma_{xz} = \sigma_5$ vanish at the top and bottom surfaces of the laminate panels.

In addition, the ratios $\sigma_4 = 0$ and $\sigma_5 = 0$ are equivalent to the corresponding strains (ε_4 and ε_5) being zero at the surfaces. However, for the condition $\sigma_3 = 0$ at the surfaces, the strain components (ε_1, ε_2, ε_3 and ε_6) are related to the stiffness coefficients (C_{13}, C_{23}, C_{33} and C_{36}) for the two plates at the top and bottom surfaces according to the characteristic equation. For parallel layers of laminar composite, the boundary condition can be expressed in the form of displacement parameters as

$$\left(\upsilon_z + \omega_y\right)_{z \pm \frac{h}{2}} = 0, \tag{7.18}$$

$$\left(u_z + \omega_z\right)_{z \pm \frac{h}{2}} = 0, \tag{7.19}$$

$$\left[Q_{13}u_x + Q_{23}\upsilon_y + Q_{33}\omega_z + Q_{36}\left(u_y + \upsilon_x\right)\right]_{z \pm \frac{h}{2}} = 0, \tag{7.20}$$

where

Q_{13} is the modified stiffness coefficient C_{13} of the two laminas on the top and the bottom surfaces;

Q_{23} is the modified stiffness coefficient C_{23} of the two laminas on the top and the bottom surfaces;

Q_{33} is the modified stiffness coefficient C_{33} of the two laminas on the top and the bottom surfaces;

Q_{36} is the modified stiffness coefficient C_{36} of the two laminas on the top and the bottom surfaces.

The generalized form of Lamb wave packets in the model example is described as follows

$$\left\{u_0, \psi_x, \varphi_x, \chi_x, \upsilon_0, \psi_y, \varphi_y, \chi_y, \omega_0, \psi_z, \varphi_z\right\} =$$

$$= \left\{U_0, \Psi_x, \Phi_x, X_x, V_0, \Psi_y, \Phi_y, X_y, W_0, \psi_z, \Phi_z\right\} \times$$

$$\times \exp\left[i\left(k_x x + k_y y - \omega t\right)\right], \tag{7.21}$$

where

ω is the angular frequency;

$k = [k_x, k_y]^T$ corresponds the direction of wave propagation in the x-y plane.

A set of quantities of six variables ϕ_x, χ_x, ϕ_y, χ_y, ψ_z and ϕ_z are functions of five arguments. In this case, the displacement field is then described by a system of equations

$$u = u_0 + z\psi_x + z^2\left(4Q_{13}u_{0,xx} + 4Q_{36}u_{0,xy}\right) +$$

$$+ 4Q_{36}\upsilon_{0,xx} + \frac{4Q_{23}\upsilon_{0,xy}}{a_1} +$$

$$+ z^3\left(-96Q_{33}\psi_x + 12h^2Q_{13}\psi_{x,xx} +\right.$$

$$+ 16h^2Q_{36}\psi_{x,xy} + 4h^2Q_{23}\psi_{x.yy} +$$

$$+ 8h^2Q_{36}\psi_{y,xx} + 6hQ_{23}\psi_{y,xy} -$$

$$\left. - 96Q_{33}\omega_{0,x}\right)/\,a_2, \tag{7.22}$$

$$\upsilon = \upsilon_0 + z\psi_y + z^2\left(4Q_{13}u_{0,xy} + 4Q_{36}u_{0,yy}\right) +$$

$$+ 4Q_{36}\upsilon_{0,xy} + \frac{4Q_{23}\upsilon_{0,yy}}{a_1} +$$

$$+ z^3\left(-96Q_{33}\psi_y + 12h^2Q_{23}\psi_{y,yy} +\right.$$

$$+ 16h^2Q_{36}\psi_{y,xy} + 4h^2Q_{13}\psi_{y.xx} +$$

$$+ 8h^2Q_{36}\psi_{x,yy} + 6hQ_{13}\psi_{x,xy} -$$

$$\left. - 96Q_{33}\omega_{0,y}\right)/\,a_2, \tag{7.23}$$

$$\omega = \omega_0 - z\left(8Q_{13}u_{0,x} + 6Q_{36}u_{0,y} + 5Q_{13}\upsilon_{0,x} +\right.$$

$$\left. + 8Q_{23}\upsilon_{0,y}\right)/\,a_1 + z^2\left(4Q_{13}\omega_{0,xx} +\right.$$

$$+ 8Q_{36}\omega_{0,xy} + 4Q_{23}\omega_{0,yy} -$$

$$-8Q_{13}\psi_{x,x}-8Q_{36}\psi_{x,y}-$$

$$-8Q_{23}\psi_{y,y}-8Q_{36}\psi_{y,x}\big)/\,a_3, \tag{7.24}$$

where

$$a_1=Q_{13}h^2k_x^2+2Q_{36}h^2k_xk_y+$$

$$+Q_{23}h^2k_y^2+8Q_{33}, \tag{7.25}$$

$$a_2=3Q_{13}h^4k_x^2+6Q_{36}h^4k_xk_y+$$

$$+3Q_{23}h^4k_y^2+72Q_{33}h^2, \tag{7.26}$$

$$a_3=Q_{13}h^2k_x^2+2Q_{36}h^2k_xk_y+$$

$$+Q_{23}h^2k_y^2+24Q_{33}\,. \tag{7.27}$$

The system of equations (7.22-7.27) defines the displacement field, which is associated with the stiffness coefficients of the two plates on the upper and lower surfaces and with the wave vector.

Hamilton's principle for virtual displacement can be used to derive the equation of motion of a higher order theory, provided that there are linear relations between deformation and displacement

$$\int_0^T\left(\delta U-\delta T+\delta W\right)dt=0, \tag{7.28}$$

where

U is the virtual strain energy;

T is the virtual kinetic energy;

W is the virtual work.

The Lamb wave packet modeling is performed under the condition that the mechanical stresses are free on the surfaces of the composite sample. In this case, the virtual work *W* is zero. Then the integral equation for the elasticity of the plate is given by

$$\int_0^T \int_{\Omega_0} \int_{-h/2}^{+h/2} (\sigma_1 \delta\varepsilon_1 + \sigma_2 \delta\varepsilon_2 + \sigma_3 \delta\varepsilon_3 + \sigma_4 \delta\varepsilon_4 +$$

$$+ \sigma_5 \delta\varepsilon_5 + \sigma_6 \delta\varepsilon_6) dzdAdt -$$

$$- \int_0^T \int_{\Omega_0} \int_{-h/2}^{+h/2} \rho \left(\dot{u} \delta\dot{u} + \dot{\upsilon} \delta\dot{\upsilon} + \dot{\omega} \delta\dot{\omega} \right) dAdt = 0 . \qquad (7.29)$$

The characteristic equation for the inertia of the plate and the resulting stress per unit length is as follows:

$$I = \sum_{k=1}^{N} \int_{z_k}^{z_{k+1}} \rho_k \left(1, z, z^2, z^3, z^4, z^5, z_6\right) dz , \qquad (7.30)$$

$$\left(N_i, M_i, P_i, S_i\right) = \sum_{k=1}^{N} \int_{z_k}^{z_{k+1}} \sigma_i \left(1, z, z^2, z^3\right) dz, \qquad \left(i = 1, \ldots, 6\right), \qquad (7.31)$$

where index “k” corresponds to the layer number in a composite laminate.

The matrix form of the equation of state of a laminate with arbitrary laying is as follows:

$$\begin{Bmatrix} N \\ M \\ P \\ S \end{Bmatrix} = \begin{bmatrix} [A] & [B] & [D] & [F] \\ & [D] & [E] & [F] \\ & & [F] & [H] \\ S* & & & [J] \end{bmatrix} \begin{Bmatrix} \varepsilon^0 \\ \varepsilon^1 \\ \varepsilon^2 \\ \varepsilon^3 \end{Bmatrix} . \qquad (7.32)$$

The stress and moment resultant vectors are defined as

$$N = \{N_1 \quad N_2 \quad N_3 \quad N_4 \quad N_5 \quad N_6\}^T , \qquad (7.33)$$

$$M = \{M_1 \quad M_2 \quad M_3 \quad M_4 \quad M_5 \quad M_6\}^T , \qquad (7.34)$$

$$P = \{P_1 \quad P_2 \quad P_3 \quad P_4 \quad P_5 \quad P_6\}^T , \qquad (7.35)$$

$$S = \{S_1 \quad S_2 \quad S_3 \quad S_4 \quad S_5 \quad S_6\}^T . \qquad (7.36)$$

The elements of the stiffness matrix and the moment of inertia are included in the following relationship

$$\left(A_{ij}, B_{ij}, D_{ij}, E_{ij}, F_{ij}, H_{ij}, J_{ij}\right) =$$

$$= \sum_{k=1}^{N} \int_{z_k}^{z_{k+1}} C_{ij} \left(1, z, z^2, z^3, z^4, z^5, z^6\right) dz \,,\ \left(i,\, j = 1, 2, 3, 4, 5, 6\right). \quad (7.37)$$

The components of the mechanical deformation vector are determined using deformation coefficients

$$\varepsilon_i = \left\{\varepsilon_1^i \quad \varepsilon_2^i \quad \varepsilon_3^i \quad \varepsilon_4^i \quad \varepsilon_5^i \quad \varepsilon_6^i\right\}^T, \qquad \left(i = 0, 1, 2, 3\right), \quad (7.38)$$

where

$$\varepsilon_j = \varepsilon_j^0 + z\varepsilon_j^1 + z^2\varepsilon_j^2 + z^3\varepsilon_j^3, \qquad \left(j = 1, 2, 3, 4, 5, 6\right). \quad (7.39)$$

Transformation of the equation of motion helps to solve the generalized eigenvalue problem. The characteristic matrix of order 5 × 5 defines five real positive eigenvalues associated with three antisymmetric and two symmetric modes of Lamb wave packets.

The set of functions of phase velocity (c_p), frequency (f) and direction of propagation (θ) are the components of the determinant of the matrix.

In turn, the determinant of the matrix allows one to write the characteristic equation, the solution of which gives the $c_p - f$ curves (dispersion curves) in the rectangular coordinate system for a given angle θ or the $c_p - \theta$ curves in the polar coordinate system for a given frequency f.

The results obtained from direct calculations using the finite element method and from the analysis of characteristic equations including the components of the stiffness matrix and mesic displacements were compared with the experimental data on a composite consisting of epoxy resin (35%) and graphite (65%) with a density of 1760 kg m^{-3}. The composite was a laminated structure of $[+45_6/-45_6]_S$. The thickness of each plate was 0.125 mm.

Based on the calculations, the phase velocity dispersion curves were constructed in rectangular coordinate systems. In the laminated composite, a fixed direction (300) of the phase velocity was considered. The results of the modified higher-order shear deformation theory were compared with the results obtained by several existing equivalent theories of a single plate of the laminated composite and exact solutions based on the three-dimensional theory of elasticity.

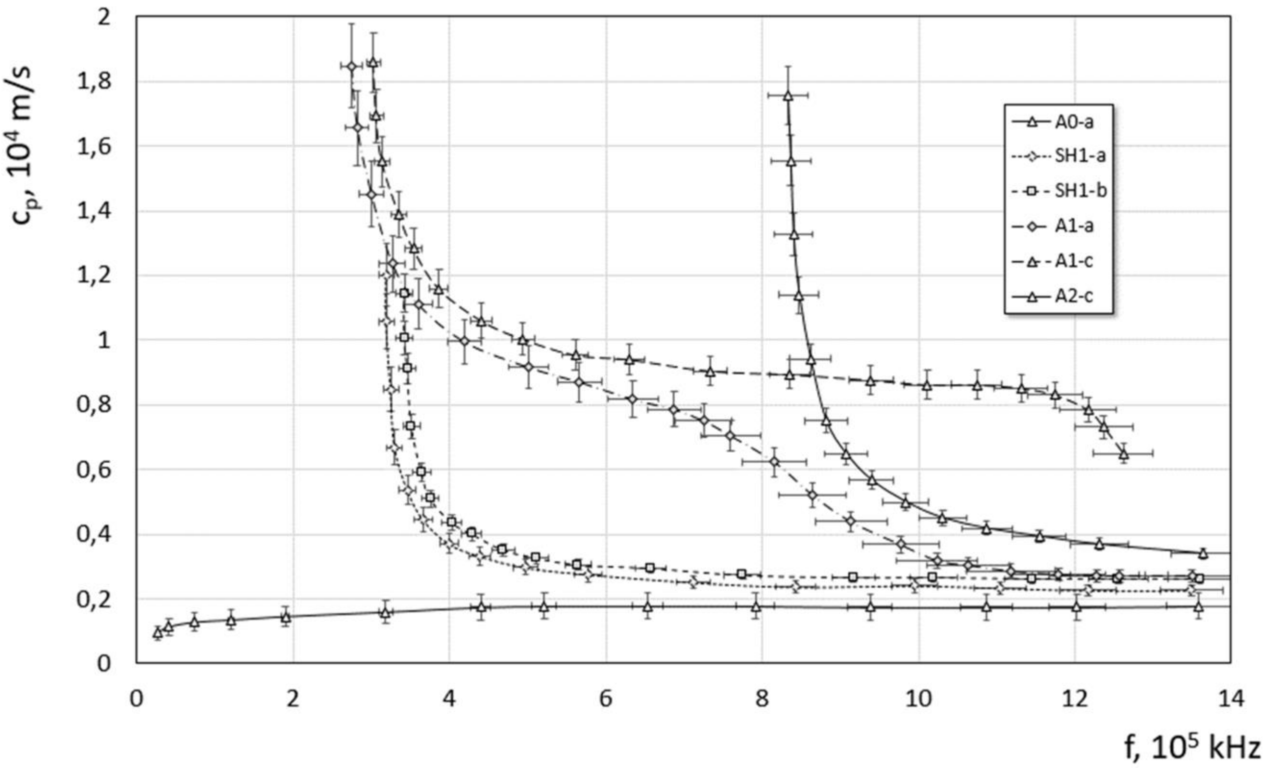

Figure 7.1. Dispersion curves for anti-symmetric curves, idexes: 1 – single plate equivalent theory; b – shear deformation theory of higher order; c – first order shear deformation theory.

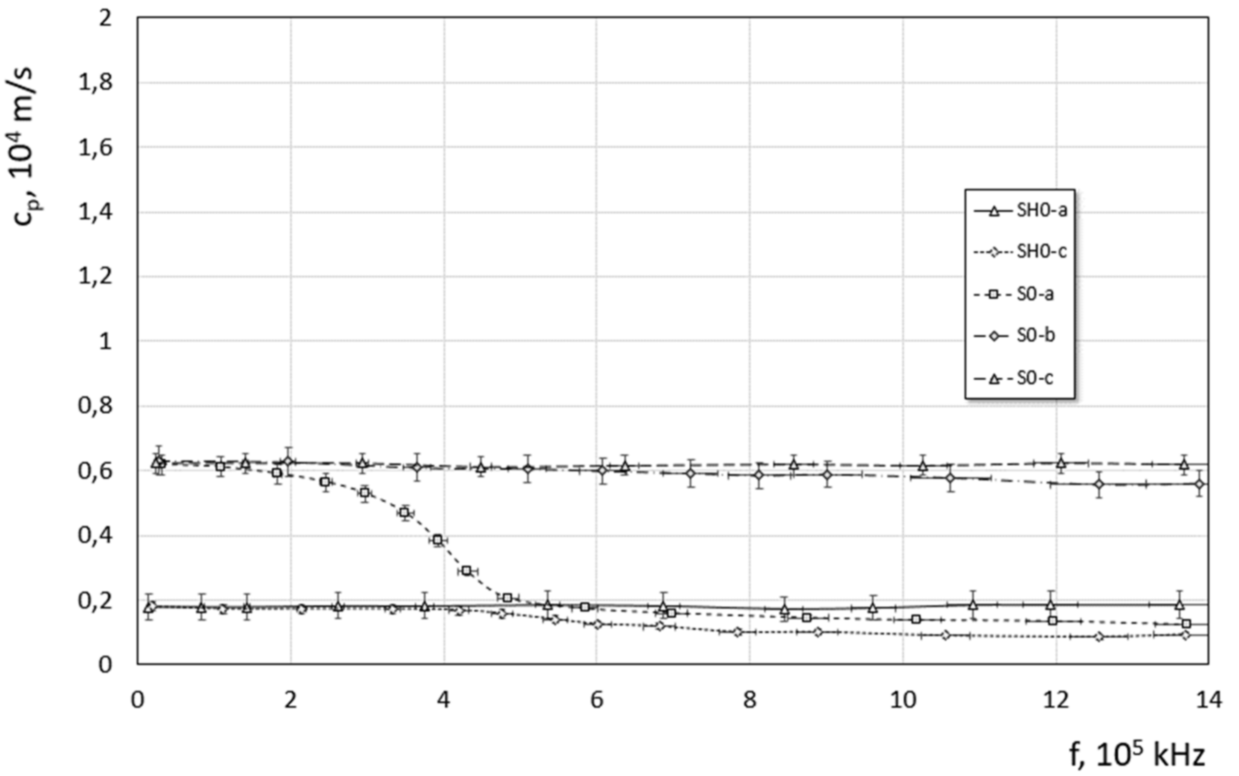

Figure 7.2. Dispersion curves for symmetric curves SH0, S0, idexes: 1 – single plate equivalent theory; b – shear deformation theory of higher order; c – first order shear deformation theory.

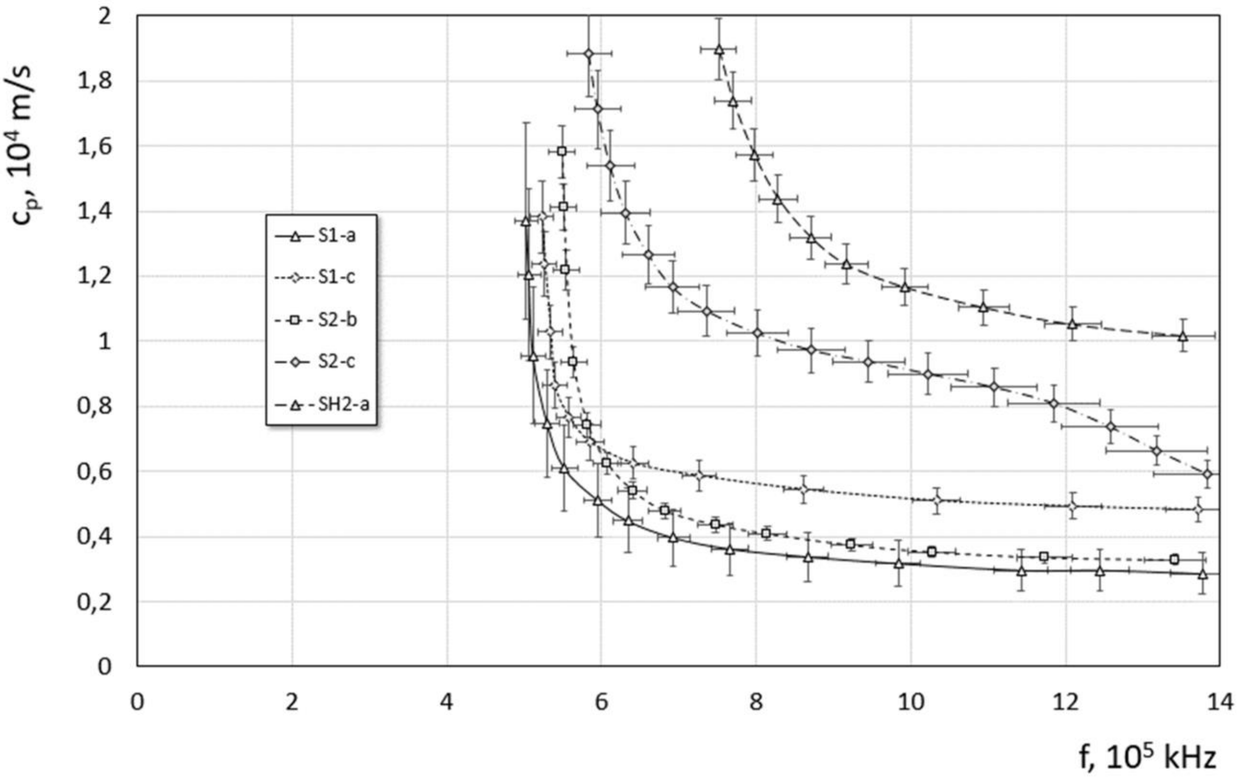

Figure 7.3. Dispersion curves for symmetric curves S1, S2, SH2, idexes: 1 – single plate equivalent theory; b – shear deformation theory of higher order; c – first order shear deformation theory.

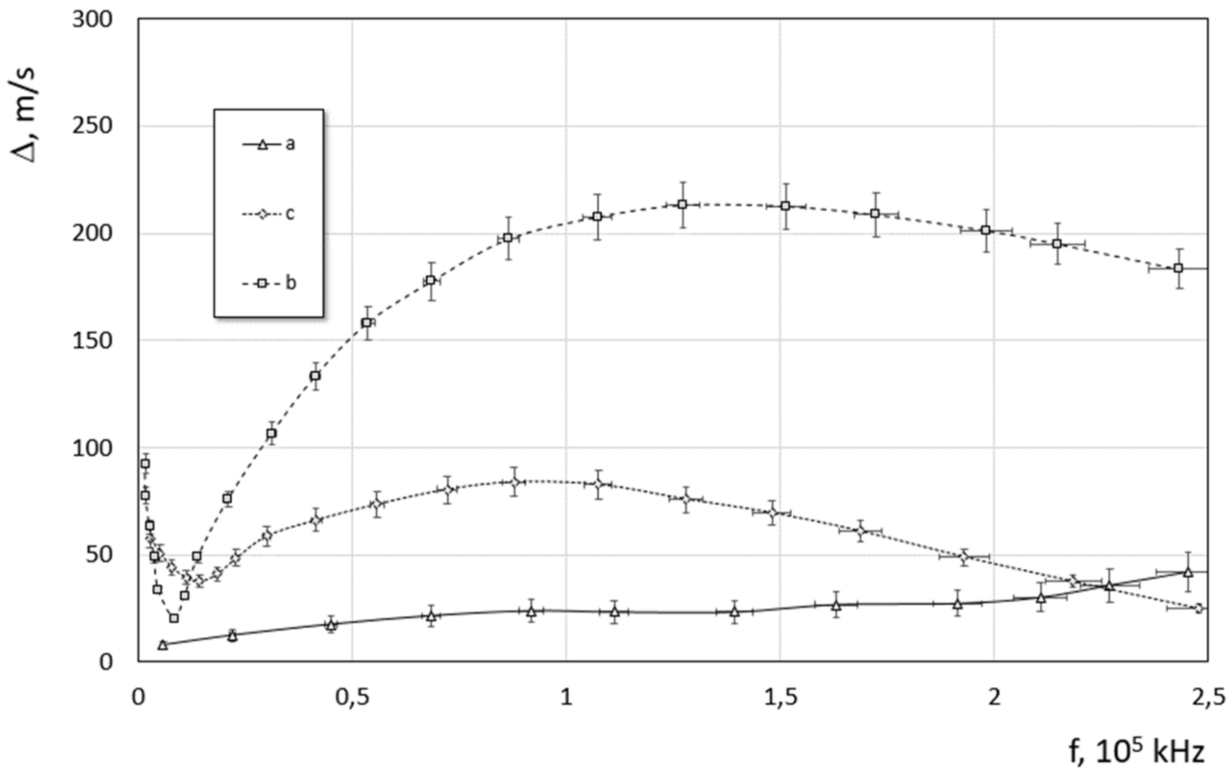

Figure 7.4. Difference Δ between the effective and fixed A0 modes, idexes: 1 – single plate equivalent theory; b – shear deformation theory of higher order; c – first order shear deformation theory.

The dispersion results were classified by the number of Lamb modes. In addition, the dispersion results for the three antisymmetric Lamb modes of the different theories were analyzed. Dispersion curves for symmetric and antisymmetric Lamb waves are shown in Figs. 7.1 - 7.4.

The analysis showed that the higher-order shear deformation theory has advantages over the single-plate equivalent theory of laminar composites. The shear theory predicts accurate solutions because there are no assumptions during the modeling process. In addition, this theory can predict an infinite number of Lamb modes as the frequency increases. For the single-plate equivalent theory, the number of Lamb modes is equivalent to the number of independent variables in the displacement fields. However, the higher-order shear deformation theory is quite time-consuming to calculate, especially for laminates with complex stacking sequences or a large number of layers.

In summary, it can be stated that the application of elastic wave propagation for damage detection in composite materials is most effective in the study of the interaction of Lamb modes with delaminations. The analysis of shear variable models revealed the presence of delamination effects on the fundamental symmetric Lamb mode in cross-laminated laminates.

It should be noted that the presence of strong dispersion of Lamb waves makes the damage localization process difficult. A way out of this situation may be the use of time-frequency analysis to facilitate damage localization. Such analysis allows to isolate individual frequency components of Lamb waves and, thus, allows to localize damage more effectively.

Time-frequency analysis based on short-time Fourier transform has also been found to be effective in obtaining the time of flight of diffracted waves. However, a large number of both theoretical and experimental studies still favor the wavelet transform, which is particularly suitable for localizing high-frequency components of mechanical stress waves. Unlike the Fourier transform, which uses sinusoidal functions as a basis, the wavelet transform uses more general basis functions. The location, size and orientation of damage can be determined using the delamination identification procedure. The methodology involves using the basic antisymmetric Lamb wave mode to detect delaminations in laminated composites. In the final stages of the analysis, a continuous wavelet transform was used to decompose the obtained results. Mechanical delaminations for each layer were localized based on the flight times of the damage-induced Lamb wave groups and their propagation velocities.

REFERENCES

1. Harb, M. S., & Yuan, F. G. (2016). Non-contact ultrasonic technique for Lamb wave characterization in composite plates. Ultrasonics, 64, 162-169.
2. Birchmeier, M., Gsell, D., Juon, M., Brunner, A. J., Paradies, R., & Dual, J. (2009). Active fiber composites for the generation of Lamb waves. Ultrasonics, 49(1), 73-82.
3. Pierce, S. G., Culshaw, B., Manson, G., Worden, K., & Staszewski, W. J. (2000). Application of ultrasonic Lamb wave techniques to the evaluation of advanced composite structures. In Smart Structures and Materials 2000: Sensory Phenomena and Measurement Instrumentation for Smart Structures and Materials (Vol. 3986, pp. 93-103). SPIE.
4. Sikdar, S., & Ostachowicz, W. (2019). Ultrasonic Lamb wave-based debonding monitoring of advanced honeycomb sandwich composite structures. Strain, 55(1), e12302.
5. Leonard, K. R., Malyarenko, E. V., & Hinders, M. K. (2002). Ultrasonic Lamb wave tomography. Inverse problems, 18(6), 1795.
6. Liu, T., Veidt, M., & Kitipornchai, S. (2002). Single mode Lamb waves in composite laminated plates generated by piezoelectric transducers. Composite Structures, 58(3), 381-396.
7. Luo, K., Chen, L., Chen, Y., Ye, L., & Yu, S. (2025). An ultrasonic Lamb wave-based non-linear exponential RAPID method for delamination detection in composites. Composite Structures, 352, 118701.
8. Ben, B. S., Yang, S. H., Ratnam, C., & Ben, B. A. (2013). Ultrasonic based structural damage detection using combined finite element and model Lamb wave propagation parameters in composite materials. The International Journal of Advanced Manufacturing Technology, 67, 1847-1856.
9. Giurgiutiu, V. (2005). Tuned Lamb wave excitation and detection with piezoelectric wafer active sensors for structural health monitoring. Journal of intelligent material systems and structures, 16(4), 291-305.
10. Wang, B., Shi, W., Zhao, B., & Tan, J. (2022). A modal decomposition imaging algorithm for ultrasonic detection of delamination defects in carbon fiber composite plates using air-coupled Lamb waves. Measurement, 195, 111165.
11. Ochôa, P., Villegas, I. F., Groves, R. M., & Benedictus, R. (2018). Experimental assessment of the influence of welding process parameters on Lamb wave transmission across ultrasonically welded thermoplastic composite joints. Mechanical Systems and Signal Processing, 99, 197-218.
12. Zou, X. Y., Liang, B., Chen, Q., & Cheng, J. C. (2009). Band gaps of lamb waves in one-dimensional piezoelectric composite plates: effect of substrate and

boundary conditions. IEEE transactions on ultrasonics, ferroelectrics, and frequency control, 56(2), 361-367.

13. Toyama, N., Ye, J., Kokuyama, W., & Yashiro, S. (2018). Non-contact ultrasonic inspection of impact damage in composite laminates by visualization of Lamb wave propagation. Applied Sciences, 9(1), 46.
14. Bellan, F. et al. (2005). A new design and manufacturing process for embedded Lamb waves interdigital transducers based on piezopolymer film. Sensors and Actuators A: Physical, 123, 379-387.
15. Schubert, K. J., & Herrmann, A. S. (2011). On attenuation and measurement of Lamb waves in viscoelastic composites. Composite Structures, 94(1), 177-185.
16. Wu, T. T., & Liu, Y. H. (1999). On the measurement of anisotropic elastic constants of fiber-reinforced composite plate using ultrasonic bulk wave and laser generated Lamb wave. Ultrasonics, 37(6), 405-412.
17. Dahmen, S., Amor, M. B., & Ghozlen, M. H. B. (2016). Investigation of the coupled Lamb waves propagation in viscoelastic and anisotropic multilayer composites by Legendre polynomial method. Composite Structures, 153, 557-568.
18. Ong, W. H., Rajic, N., Chiu, W. K., & Rosalie, C. (2016). Determination of the elastic properties of woven composite panels for Lamb wave studies. Composite Structures, 141, 24-31.
19. Lin, J., Gao, F., Luo, Z., & Zeng, L. (2016). High-resolution Lamb wave inspection in viscoelastic composite laminates. IEEE Transactions on Industrial Electronics, 63(11), 6989-6998.
20. Orta, A. H., Vandendriessche, J., Kersemans, M., Van Paepegem, W., Roozen, N. B., & Van Den Abeele, K. (2021). Modeling lamb wave propagation in visco-elastic composite plates using a fifth-order plate theory. Ultrasonics, 116, 106482.
21. Karmazin, A., Kirillova, E., Seemann, W., & Syromyatnikov, P. (2011). Investigation of Lamb elastic waves in anisotropic multilayered composites applying the Green's matrix. Ultrasonics, 51(1), 17-28.
22. Basri, R., & Chiu, W. K. (2004). Numerical analysis on the interaction of guided Lamb waves with a local elastic stiffness reduction in quasi-isotropic composite plate structures. Composite structures, 66(1-4), 87-99.
23. Seale, M. D., Smith, B. T., & Prosser, W. H. (1998). Lamb wave assessment of fatigue and thermal damage in composites. The Journal of the Acoustical Society of America, 103(5), 2416-2424.
24. Li, W., Cho, Y., & Achenbach, J. D. (2012). Detection of thermal fatigue in composites by second harmonic Lamb waves. Smart Materials and Structures, 21(8), 085019.

25. Ducousso, M., Dalodière, A., & Baillard, A. (2019). Evaluation of the thermal aging of aeronautical composite materials using Lamb waves. Ultrasonics, 94, 174-182.
26. Li, W., Xu, C., & Cho, Y. (2016). Characterization of degradation progressive in composite laminates subjected to thermal fatigue and moisture diffusion by lamb waves. Sensors, 16(2), 260.
27. Seale, M. D., & Madaras, E. I. (2000). Lamb wave evaluation of the effects of thermal-mechanical aging on composite stiffness. Journal of composite materials, 34(1), 27-38.
28. Seale, M. D., & Madaras, E. I. (1999). Lamb wave characterization of the effects of long-term thermal-mechanical aging on composite stiffness. The Journal of the Acoustical Society of America, 106(3), 1346-1352.
29. Cinquin, M., Castaings, M., Hosten, B., Brassier, P., & Pérès, P. (2005). Monitoring of the moisture content in carbon-epoxy plates using Lamb waves. NDT & E International, 38(1), 37-44.
30. Zimmermann, E., Eremin, A., & Lammering, R. (2018). Analysis of the continuous mode conversion of Lamb waves in fiber composites by a stochastic material model and laser vibrometer experiments. GAMM-Mitteilungen, 41(1), e201800001.
31. Lee, J., & Cho, Y. (2016). Using Lamb waves to monitor moisture absorption in thermally fatigued composite laminates. Journal of the Korean Society for Nondestructive Testing, 36(3), 175-180.
32. Su, Z., Ye, L., & Lu, Y. (2006). Guided Lamb waves for identification of damage in composite structures: A review. Journal of sound and vibration, 295(3-5), 753-780.
33. Chen, X., Li, X., Wang, S., Yang, Z., Chen, B., & He, Z. (2012). Composite damage detection based on redundant second-generation wavelet transform and fractal dimension tomography algorithm of lamb wave. IEEE transactions on instrumentation and measurement, 62(5), 1354-1363.
34. Paget, C. A., Grondel, S., Levin, K., & Delebarre, C. (2003). Damage assessment in composites by Lamb waves and wavelet coefficients. Smart materials and Structures, 12(3), 393.
35. Su, C., Jiang, M., Liang, J., Tian, A., Sun, L., Zhang, L., ... & Sui, Q. (2020). Damage assessments of composite under the environment with strong noise based on synchrosqueezing wavelet transform and stack autoencoder algorithm. Measurement, 156, 107587.
36. Lemistre, M., Gouyon, R., Kaczmarek, H., & Balageas, D. (1999). Damage localization in composite plates using wavelet transform processing on Lamb wave signals. Office National D Etudes Et De Recherches Aerospatiales Onera-Publications-TP.

37. Wu, J., Xu, X., Liu, C., Deng, C., & Shao, X. (2021). Lamb wave-based damage detection of composite structures using deep convolutional neural network and continuous wavelet transform. Composite Structures, 276, 114590.
38. Badcock, R. A., & Birt, E. A. (2000). The use of 0-3 piezocomposite embedded Lamb wave sensors for detection of damage in advanced fibre composites. Smart Materials and Structures, 9(3), 291.
39. Staszewski, W. J., Pierce, S. G., Worden, K., Philp, W. R., Tomlinson, G. R., & Culshaw, B. (1997). Wavelet signal processing for enhanced Lamb-wave defect detection in composite plates using optical fiber detection. Optical Engineering, 36(7), 1877-1888.
40. Kessler, S. S., Spearing, S. M., & Soutis, C. (2002). Damage detection in composite materials using Lamb wave methods. Smart materials and structures, 11(2), 269.
41. Ng, C. T., & Veidt, M. (2009). A Lamb-wave-based technique for damage detection in composite laminates. Smart materials and structures, 18(7), 074006.
42. Ben, B. S., Ben, B. A., Vikram, K. A., & Yang, S. H. (2013). Damage identification in composite materials using ultrasonic based Lamb wave method. Measurement, 46(2), 904-912.
43. Zheng, K., Li, Z., Ma, Z., Chen, J., Zhou, J., & Su, X. (2019). Damage detection method based on Lamb waves for stiffened composite panels. Composite Structures, 225, 111137.
44. Yang, B., Xuan, F. Z., Chen, S., Zhou, S., Gao, Y., & Xiao, B. (2017). Damage localization and identification in WGF/epoxy composite laminates by using Lamb waves: Experiment and simulation. Composite Structures, 165, 138-147.
45. Su, Z., Ye, L., Su, Z., & Ye, L. (2009). Fundamentals and analysis of lamb waves. Identification of Damage Using Lamb Waves: From Fundamentals to Applications, 15-58.
46. Mardanshahi, A., Shokrieh, M. M., & Kazemirad, S. (2020). Identification of matrix cracking in cross-ply laminated composites using Lamb wave propagation. Composite Structures, 235, 111790.
47. Mustapha, S., Ye, L., Wang, D., & Lu, Y. (2011). Assessment of debonding in sandwich CF/EP composite beams using A0 Lamb wave at low frequency. Composite structures, 93(2), 483-491.
48. Pieczonka, Ł., Ambroziński, Ł., Staszewski, W. J., Barnoncel, D., & Pérès, P. (2017). Damage detection in composite panels based on mode-converted Lamb waves sensed using 3D laser scanning vibrometer. Optics and lasers in engineering, 99, 80-87.
49. Gao, F., Zeng, L., Lin, J., & Shao, Y. (2018). Damage assessment in composite laminates via broadband Lamb wave. Ultrasonics, 86, 49-58.

50. Leleux, A., Micheau, P., & Castaings, M. (2013). Long range detection of defects in composite plates using Lamb waves generated and detected by ultrasonic phased array probes. Journal of Nondestructive Evaluation, 32, 200-214.
51. Kessler, S. S., Spearing, S. M., & Soutis, C. (2001, September). Optimization of Lamb wave methods for damage detection in composite materials. In Proceedings of the 3rd International Workshop on Structural Health Monitoring (pp. 870-879).
52. Zeng, L., Huang, L., & Lin, J. (2019). Damage imaging of composite structures using multipath scattering Lamb waves. Composite Structures, 216, 331-339.
53. Philibert, M., Soutis, C., Gresil, M., & Yao, K. (2018). Damage detection in a composite T-joint using guided Lamb waves. Aerospace, 5(2), 40.
54. Rauter, N., & Lammering, R. (2015). Impact damage detection in composite structures considering nonlinear lamb wave propagation. Mechanics of Advanced Materials and Structures, 22(1-2), 44-51.
55. Huang, L., Zeng, L., Lin, J., & Zhang, N. (2020). Baseline-free damage detection in composite plates using edge-reflected Lamb waves. Composite Structures, 247, 112423.
56. Lee, H., Lim, H. J., Skinner, T., Chattopadhyay, A., & Hall, A. (2022). Automated fatigue damage detection and classification technique for composite structures using Lamb waves and deep autoencoder. Mechanical Systems and Signal Processing, 163, 108148.
57. Diamanti, K., Hodgkinson, J. M., & Soutis, C. (2004). Detection of low-velocity impact damage in composite plates using Lamb waves. Structural Health Monitoring, 3(1), 33-41.
58. Kessler, S. S., Spearing, S. M., & Atalla, M. J. (2002, July). In-situ damage detection of composites structures using Lamb wave methods. In Proceedings of the first European workshop on structural health monitoring (pp. 10-12).
59. Toyama, N., Noda, J., & Okabe, T. (2003). Quantitative damage detection in cross-ply laminates using Lamb wave method. Composites science and technology, 63(10), 1473-1479.
60. Monnier, T. (2006). Lamb waves-based impact damage monitoring of a stiffened aircraft panel using piezoelectric transducers. Journal of Intelligent Material Systems and Structures, 17(5), 411-421.
61. Zhang, H., Wang, F., Lin, J., & Hua, J. (2024). Lamb wave-based damage assessment for composite laminates using a deep learning approach. Ultrasonics, 141, 107333.
62. Zhang, N., Zhai, M., Zeng, L., Huang, L., & Lin, J. (2023). Damage assessment in composite laminates with the Lamb wave factorization method. Composite Structures, 307, 116642.

63.Zeng, X., Liu, X., Yan, J., Yu, Y., Zhao, B., & Qing, X. (2022). Lamb wave-based damage localization and quantification algorithms for CFRP composite structures. Composite Structures, 295, 115849.
64.Amza, G., Moraru, A., Marinescu, M., Amza, C., & Melnic, L. V. (2008). Damage detection of composite materials with LAMB wave method. MATERIALE PLASTICE, 45(2), 203.
65.Su, Z., & Ye, L. (2005). Lamb wave propagation-based damage identification for quasi-isotropic CF/EP composite laminates using artificial neural algorithm: Part I-methodology and database development. Journal of intelligent material systems and structures, 16(2), 97-111.
66.Purekar, A. S., & Pines, D. J. (2010). Damage detection in thin composite laminates using piezoelectric phased sensor arrays and guided Lamb wave interrogation. Journal of Intelligent Material Systems and Structures, 21(10), 995-1010.
67.Dayal, V., & Kinra, V. K. (1991). Leaky Lamb waves in an anisotropic plate. II: Nondestructive evaluation of matrix cracks in fiber-reinforced composites. The Journal of the Acoustical Society of America, 89(4), 1590-1598.
68.Zhang, H., Hua, J., Gao, F., & Lin, J. (2020). Efficient Lamb-wave based damage imaging using multiple sparse Bayesian learning in composite laminates. NDT & E International, 116, 102277.
69.Toyama, N., Yashiro, S., Takatsubo, J., & Okabe, T. (2005). Stiffness evaluation and damage identification in composite beam under tension using Lamb waves. Acta materialia, 53(16), 4389-4397.
70.Luo, K., Liu, Y., Liang, W., Chen, L., & Yang, Z. (2024). Rapid damage reconstruction imaging of composite plates using non-contact air-coupled Lamb waves. NDT & E International, 143, 103047.
71.Huo, H., He, J., & Guan, X. (2021). A Bayesian fusion method for composite damage identification using Lamb wave. Structural Health Monitoring, 20(5), 2337-2359.
72.Driss, H., El Mahi, A., Bentahar, M., Beyaoui, M., & Haddar, M. (2023). Characterization of Tensile and Fatigue Damages in Composite Structures Using Lamb Wave for Improved Structural Health Monitoring. International Journal of Applied Mechanics, 15(02), 2350014.
73. Su, C., Jiang, M., Lv, S., Lu, S., Zhang, L., Zhang, F., & Sui, Q. (2019). Improved damage localization and quantification of CFRP using Lamb waves and convolution neural network. IEEE Sensors Journal, 19(14), 5784-5791.
74.Gao, F., Shao, Y., Hua, J., Zeng, L., & Lin, J. (2021). Enhanced wavefield imaging method for impact damage detection in composite laminates via laser-generated Lamb waves. Measurement, 173, 108639.
75.Su, C., Jiang, M., Liang, J., Tian, A., Sun, L., Zhang, L., ... & Sui, Q. (2019). Damage identification in composites based on Hilbert energy spectrum and

Lamb wave tomography algorithm. IEEE Sensors Journal, 19(23), 11562-11572.
76. Mal, A. K., Shih, F. J., Ricci, F., & Banerjee, S. (2005, May). Impact damage detection in composite structures using Lamb waves. In Health Monitoring and Smart Nondestructive Evaluation of Structural and Biological Systems IV (Vol. 5768, pp. 295-303). SPIE.
77. Liu, Y., Fard, M. Y., Kim, S. B., Chattopadhyay, A., & Doyle, D. (2011, April). Damage detection in composite structures using Lamb wave analysis and time-frequency approach. In Sensors and Smart Structures Technologies for Civil, Mechanical, and Aerospace Systems 2011 (Vol. 7981, pp. 1034-1048). SPIE.
78. Guo, J., Zeng, X., Liu, Q., & Qing, X. (2022). Lamb wave-based damage localization and quantification in composites using probabilistic imaging algorithm and statistical method. Sensors, 22(13), 4810.
79. Worden, K., Pierce, S. G., Manson, G., Philp, W. R., Staszewski, W. J., & Culshaw, B. (2000). Detection of defects in composite plates using Lamb waves and novelty detection. International Journal of Systems Science, 31(11), 1397-1409.
80. Tie, Y., Zhang, Q., Hou, Y., & Li, C. (2020). Impact damage assessment in orthotropic CFRP laminates using nonlinear Lamb wave: Experimental and numerical investigations. Composite Structures, 236, 111869.
81. Rahbari, A., Rébillat, M., Mechbal, N., & Canu, S. (2021). Unsupervised damage clustering in complex aeronautical composite structures monitored by Lamb waves: An inductive approach. Engineering Applications of Artificial Intelligence, 97, 104099.
82. Lu, Y., Ye, L., Wang, D., & Zhong, Z. (2009). Time-domain analyses and correlations of Lamb wave signals for damage detection in a composite panel of multiple stiffeners. Journal of Composite Materials, 43(26), 3211-3230.
83. Yu, F., Saito, O., & Okabe, Y. (2022). Detection of a single transverse crack in a CFRP cross-ply laminate by visualizing mode conversion of Lamb waves. Composite Structures, 283, 115118.
84. Hameed, M. S., & Li, Z. (2019). Transverse damage localization and quantitative size estimation for composite laminates based on Lamb waves. IEEE Access, 7, 174859-174872.
85. Gonzalez-Jimenez, A., Lomazzi, L., Junges, R., Giglio, M., Manes, A., & Cadini, F. (2024). Enhancing Lamb wave-based damage diagnosis in composite materials using a pseudo-damage boosted convolutional neural network approach. Structural Health Monitoring, 23(3), 1514-1529.
86. Bar-Cohen, Y., Mal, A. K., Lih, S. S., & Chang, Z. (1999, January). Composite materials stiffness determination and defects characterization using enhanced leaky Lamb wave dispersion data acquisition method. In

Nondestructive Evaluation of Aging Aircraft, Airports, and Aerospace Hardware III (Vol. 3586, pp. 250-255). SPIE.

87. Gao, Y., Sun, L., Song, R., Peng, C., Wu, X., Wei, J., ... & Zhang, L. (2024). Damage localization in composite structures based on Lamb wave and modular artificial neural network. Sensors and Actuators A: Physical, 377, 115644.
88. Hua, J., Zhang, H., Miao, Y., & Lin, J. (2022). Modified minimum variance imaging of Lamb waves for damage localization in aluminum plates and composite laminates. Ndt & E International, 125, 102574.
89. Nandyala, A. R., Darpe, A. K., & Singh, S. P. (2022). Damage severity assessment in composite structures using multi-frequency lamb waves. Structural Health Monitoring, 21(6), 2834-2850.
90. De Luca, A., Perfetto, D., De Fenza, A., Petrone, G., & Caputo, F. (2018). A sensitivity analysis on the damage detection capability of a Lamb waves based SHM system for a composite winglet. Procedia Structural Integrity, 12, 578-588.
91. Su, C., Jiang, M., Liang, J., Tian, A., Sun, L., Zhang, L., ... & Sui, Q. (2020). Damage localization of composites based on difference signal and lamb wave tomography. Materials, 13(1), 218.
92. Pysarenko A.M. (2024). Propagation of Lamb waves in laminar composites. International scientific conference "Global science and education in the modern realities '2024". Proconference in conjunction with KindleDP Seattle, Washington USA. No 24 on May 21 2024, 54 - 62.
93. Pysarenko O.M. (2024). Group Velocity Dispersion of Lamb Wave Modes in Laminar Composites. Comat 2024. 8th International Conference on Recent Trends in Structural Materials. Abstracts. September 10-12, 2024. Vienna House Easy by Wyndham, Pilsen, Cz, Eu, p. 14.
94. Wang, L., & Yuan, F. G. (2007). Group velocity and characteristic wave curves of Lamb waves in composites: Modeling and experiments. Composites science and technology, 67(7-8), 1370-1384.
95. Barouni, A. K., & Saravanos, D. A. (2016). A layerwise semi-analytical method for modeling guided wave propagation in laminated and sandwich composite strips with induced surface excitation. Aerospace Science and Technology, 51, 118-141.
96. Su, Z., & Ye, L. (2004). Selective generation of Lamb wave modes and their propagation characteristics in defective composite laminates. Proceedings of the institution of mechanical engineers, Part L: journal of materials: design and applications, 218(2), 95-110.
97. Wang, L., & Yuan, F. G. (2007). Group velocity and characteristic wave curves of Lamb waves in composites: Modeling and experiments. Composites science and technology, 67(7-8), 1370-1384.

98. Barouni, A. K., & Saravanos, D. A. (2017). A layerwise semi-analytical method for modeling guided wave propagation in laminated composite infinite plates with induced surface excitation. Wave Motion, 68, 56-77.
99. Yang, C., Ye, L., Su, Z., & Bannister, M. (2006). Some aspects of numerical simulation for Lamb wave propagation in composite laminates. Composite structures, 75(1-4), 267-275.
100. Yashiro, S., Takatsubo, J., & Toyama, N. (2007). An NDT technique for composite structures using visualized Lamb-wave propagation. Composites Science and Technology, 67(15-16), 3202-3208.
101. Mardanshahi, A., Shokrieh, M. M., & Kazemirad, S. (2022). Simulated Lamb wave propagation method for nondestructive monitoring of matrix cracking in laminated composites. Structural Health Monitoring, 21(2), 695-709.
102. Guo, N., & Cawley, P. (1993). Lamb wave propagation in composite laminates and its relationship with acousto-ultrasonics. Ndt&E International, 26(2), 75-84.
103. Samaratunga, D., & Jha, R. (2012, May). Lamb wave propagation simulation in smart composite structures. In SIMULIA Community Conference (pp. 1-11).
104. Weber, R., Hosseini, S. M. H., & Gabbert, U. (2012). Numerical simulation of the guided Lamb wave propagation in particle reinforced composites. Composite Structures, 94(10), 3064-3071.
105. Wang, L., & Yuan, F. G. (2007, April). Lamb wave propagation in composite laminates using a higher-order plate theory. In Nondestructive Characterization for Composite Materials, Aerospace Engineering, Civil Infrastructure, and Homeland Security 2007 (Vol. 6531, pp. 137-148). SPIE.
106. Sikdar, S., Fiborek, P., Kudela, P., Banerjee, S., & Ostachowicz, W. (2018). Effects of debonding on Lamb wave propagation in a bonded composite structure under variable temperature conditions. Smart Materials and Structures, 28(1), 015021.
107. Sherafat, M. H., Quaegebeur, N., Hubert, P., Lessard, L., & Masson, P. (2016). Finite element modeling of Lamb wave propagation in composite stepped joints. Journal of Reinforced Plastics and Composites, 35(10), 796-806.
108. Deng, P., Saito, O., Okabe, Y., & Soejima, H. (2020). Simplified modeling method of impact damage for numerical simulation of Lamb wave propagation in quasi-isotropic composite structures. Composite Structures, 243, 112150.
109. Rhee, S. H., Lee, J. K., & Lee, J. J. (2007). The group velocity variation of Lamb wave in fiber reinforced composite plate. Ultrasonics, 47(1-4), 55-63.

110. Castaings, M., & Hosten, B. (2003). Guided waves propagating in sandwich structures made of anisotropic, viscoelastic, composite materials. The Journal of the Acoustical Society of America, 113(5), 2622-2634.
111. Agostini, V., Delsanto, P. P., Genesio, I., & Olivero, D. (2003). Simulation of Lamb wave propagation for the characterization of complex structures. IEEE transactions on ultrasonics, ferroelectrics, and frequency control, 50(4), 441-448.
112. Voß, M., Ilse, D., Hillger, W., Vallée, T., Eppmann, M., de Wit, J., & von Dungern, F. (2020). Numerical simulation of the propagation of Lamb waves and their interaction with defects in C-FRP laminates for non-destructive testing. Advanced Composite Materials, 29(5), 423-441.
113. Lee, B. C., & Staszewski, W. J. (2007). Lamb wave propagation modelling for damage detection: I. Two-dimensional analysis. Smart Materials and Structures, 16(2), 249.
114. Noiret, D., & Roget, J. (1989). Calculation of wave propagation in composite materials using the Lamb wave concept. Journal of composite materials, 23(2), 195-206.
115. Han, J., Kim, C. G., & Kim, J. Y. (2006). The propagation of Lamb waves in a laminated composite plate with a variable stepped thickness. Composite structures, 76(4), 388-396.
116. Liu, H., Liu, S., Chen, X., Lyu, Y., & Liu, Z. (2020). Coupled Lamb waves propagation along the direction of non-principal symmetry axes in pre-stressed anisotropic composite lamina. Wave Motion, 97, 102591.
117. Pant, S. (2014). Lamb wave propagation and material characterization of metallic and composite aerospace structures for improved structural health monitoring (shm) (Doctoral dissertation, Carleton University).
118. Milosavljevic, D., Zmindak, M., Dekys, V., Radakovic, A., & Cukanovic, D. (2021). Approximate phase speed of Lamb waves in a composite plate reinforced with strong fibres. Journal of Engineering Mathematics, 129, 1-11.
119. Vasudeva, R. Y., & Govinda Rao, P. (1991). Influence of voids in interface zones on Lamb wave propagation in composite plates. The Journal of the Acoustical Society of America, 89(2), 516-522.
120. Collet, M., Ruzzene, M., & Cunefare, K. A. (2011). Generation of Lamb waves through surface mounted macro-fiber composite transducers. Smart Materials and Structures, 20(2), 025020.
121. Lee, B. C., & Staszewski, W. J. (2003). Modelling of Lamb waves for damage detection in metallic structures: Part I. Wave propagation. Smart materials and structures, 12(5), 804.
122. Rosalie, S. C., Vaughan, M., Bremner, A., & Chiu, W. K. (2004). Variation in the group velocity of Lamb waves as a tool for the detection of

delamination in GLARE aluminium plate-like structures. Composite Structures, 66(1-4), 77-86.

123. Pysarenko A.N. (2024). Lamb waves in multilayered anisotropic media. Міжнародна наукова інтернет-конференція "Інформаційне суспільство: технологічні та технічні аспекти становлення". Випуск 88. Секція 3. Технічні науки. 14-15 травня 2024. м. Тернопіль, Україна - м. Ополе Польща, 136-138.

124. Feng, B., Ribeiro, A. L., & Ramos, H. G. (2018). A new method to detect delamination in composites using chirp-excited Lamb wave and wavelet analysis. NDT & E International, 100, 64-73.

125. Tan, K. S., Guo, N., Wong, B. S., & Tui, C. G. (1995). Experimental evaluation of delaminations in composite plates by the use of Lamb waves. Composites science and technology, 53(1), 77-84.

126. Pant, S., Laliberte, J., Martinez, M., & Rocha, B. (2014). Derivation and experimental validation of Lamb wave equations for an n-layered anisotropic composite laminate. Composite Structures, 111, 566-579.

127. Birchmeier, M., Gsell, D., Juon, M., Brunner, A. J., Paradies, R., & Dual, J. (2009). Active fiber composites for the generation of Lamb waves. Ultrasonics, 49(1), 73-82.

128. Díaz Valdés, S. H., & Soutis, C. (2002). Real-time nondestructive evaluation of fiber composite laminates using low-frequency Lamb waves. The Journal of the Acoustical Society of America, 111(5), 2026-2033.

129. Okabe, Y., Fujibayashi, K., Shimazaki, M., Soejima, H., & Ogisu, T. (2010). Delamination detection in composite laminates using dispersion change based on mode conversion of Lamb waves. Smart materials and structures, 19(11), 115013.

130. Toyama, N., & Takatsubo, J. (2004). Lamb wave method for quick inspection of impact-induced delamination in composite laminates. Composites science and technology, 64(9), 1293-1300.

131. Yelve, N. P., Mitra, M., & Mujumdar, P. M. (2017). Detection of delamination in composite laminates using Lamb wave based nonlinear method. Composite Structures, 159, 257-266.

132. Su, Z., & Ye, L. (2004). Lamb wave-based quantitative identification of delamination in CF/EP composite structures using artificial neural algorithm. Composite Structures, 66(1-4), 627-637.

133. Watkins, R., & Jha, R. (2012). A modified time reversal method for Lamb wave based diagnostics of composite structures. Mechanical Systems and Signal Processing, 31, 345-354.

134. Tian, Z., Yu, L., & Leckey, C. (2015). Delamination detection and quantification on laminated composite structures with Lamb waves and wavenumber analysis. Journal of Intelligent Material Systems and Structures, 26(13), 1723-1738.

135. Bar-Cohen, Y., Lih, S. S., & Mal, A. K. (2001). NDE of composites using leaky lamb waves (LLW). Nondestructive Testing and Evaluation, 17(2), 91-119.
136. Xu, C., Yang, Z., Tian, S., & Chen, X. (2019). Lamb wave inspection for composite laminates using a combined method of sparse reconstruction and delay-and-sum. Composite Structures, 223, 110973.
137. Tao, C., Ji, H., Qiu, J., Zhang, C., Wang, Z., & Yao, W. (2017). Characterization of fatigue damages in composite laminates using Lamb wave velocity and prediction of residual life. Composite Structures, 166, 219-228.
138. Gao, F., Wang, L., Hua, J., Lin, J., & Mal, A. (2021). Application of Lamb wave and its coda waves to disbond detection in an aeronautical honeycomb composite sandwich. Mechanical Systems and Signal Processing, 146, 107063.
139. Pierce, S. G., Culshaw, B., Philp, W. R., Lecuyer, F., & Farlow, R. (1997). Broadband Lamb wave measurements in aluminium and carbon/glass fibre reinforced composite materials using non-contacting laser generation and detection. Ultrasonics, 35(2), 105-114.
140. Yilmaz, C., Topal, S., Ali, H. Q., Tabrizi, I. E., Al-Nadhari, A., Suleman, A., & Yildiz, M. (2020). Non-destructive determination of the stiffness matrix of a laminated composite structure with lamb wave. Composite Structures, 237, 111956.
141. Huang, L., Zeng, L., Lin, J., & Luo, Z. (2018). An improved time reversal method for diagnostics of composite plates using Lamb waves. Composite Structures, 190, 10-19.
142. Dayal, V., & Kinra, V. K. (1989). Leaky Lamb waves in an anisotropic plate. I: An exact solution and experiments. The Journal of the Acoustical Society of America, 85(6), 2268-2276.
143. Seale, M. D., Smith, B. T., Prosser, W. H., & Zalameda, J. N. (1998). Lamb wave assessment of fiber volume fraction in composites. The Journal of the Acoustical Society of America, 104(3), 1399-1403.
144. Singh, R. K., Ramadas, C., Shetty, P. B., & Satyanarayana, K. G. (2017). Identification of delamination interface in composite laminates using scattering characteristics of lamb wave: numerical and experimental studies. Smart Materials and Structures, 26(4), 045017.
145. Attar, L., Leduc, D., El Kettani, M. E. C., Predoi, M. V., Galy, J., & Pareige, P. (2020). Detection of the degraded interface in dissymmetrical glued structures using Lamb waves. NDT & E International, 111, 102213.
146. Cawley, P., & Alleyne, D. (1996). The use of Lamb waves for the long range inspection of large structures. Ultrasonics, 34(2-5), 287-290.
147. Gao, F., Hua, J., Wang, L., Zeng, L., & Lin, J. (2020). Local wavenumber method for delamination characterization in composites with sparse

representation of Lamb waves. IEEE Transactions on Ultrasonics, Ferroelectrics, and Frequency Control, 68(4), 1305-1313.

148. Ebrahiminejad, A., Mardanshahi, A., & Kazemirad, S. (2022). Nondestructive evaluation of coated structures using Lamb wave propagation. Applied Acoustics, 185, 108378.
149. Wandowski, T., Radzienski, M., & Kudela, P. (2024). Lamb wave S0/A0 mode conversion for imaging the internal structure of composite panel. Composite Structures, 118748.
150. Kang, K. T. Et al. (2011). Quantitative accessibility of delamination in composite using lamb wave by experiments and FEA. Advanced Composite Materials, 20(4), 361-373.
151. Attar, L., Leduc, D., El Kettani, M. E. C., Predoi, M. V., Galy, J., & Pareige, P. (2020). Detection of the degraded interface in dissymmetrical glued structures using Lamb waves. NDT & E International, 111, 102213.
152. Koh, Y. L., Chiu, W. K., & Rajic, N. (2002). Integrity assessment of composite repair patch using propagating Lamb waves. Composite structures, 58(3), 363-371.
153. Liu, Z., Zhong, X., Dong, T., He, C., & Wu, B. (2017). Delamination detection in composite plates by synthesizing time-reversed Lamb waves and a modified damage imaging algorithm based on RAPID. Structural Control and Health Monitoring, 24(5), e1919.
154. Petculescu, G., Krishnaswamy, S., & Achenbach, J. D. (2007). Group delay measurements using modally selective Lamb wave transducers for detectionand sizing of delaminations in composites. Smart Materials and Structures, 17(1), 015007.
155. Yu, L., Xiao, W., Mei, H., & Giurgiutiu, V. (2023). Delamination imaging in composites using cross-correlation method by non-contact air-coupled Lamb waves. Smart Materials and Structures, 32(10), 105013.
156. Ryuzono, K., Yashiro, S., Onodera, S., & Toyama, N. (2023). Lamb wave mode conversion and multiple-reflection mechanisms for simply and reliably evaluating delamination in composite laminates. Advanced Composite Materials, 32(5), 749-766.
157. Liu, Z., Yu, H., Fan, J., Hu, Y., He, C., & Wu, B. (2015). Baseline-free delamination inspection in composite plates by synthesizing non-contact air-coupled Lamb wave scan method and virtual time reversal algorithm. Smart Materials and Structures, 24(4), 045014.
158. Pysarenko O. (2024). Dispersion of Lamb waves in multilayer structures. Mechanics and Mathematical Methods, VI (2), 124–135.
159. Alleyne, D. N., & Cawley, P. (1992). The interaction of Lamb waves with defects. IEEE transactions on ultrasonics, ferroelectrics, and frequency control, 39(3), 381-397.

160. Guo, N., & Cawley, P. (1993). The interaction of Lamb waves with delaminations in composite laminates. The Journal of the Acoustical Society of America, 94(4), 2240-2246.
161. Munian, R. K., Mahapatra, D. R., & Gopalakrishnan, S. (2018). Lamb wave interaction with composite delamination. Composite Structures, 206, 484-498.
162. Pant, S., Laliberte, J., Martinez, M., Rocha, B., & Ancrum, D. (2015). Effects of composite lamina properties on fundamental Lamb wave mode dispersion characteristics. Composite Structures, 124, 236-252.
163. Baid, H., Schaal, C., Samajder, H., & Mal, A. (2015). Dispersion of Lamb waves in a honeycomb composite sandwich panel. Ultrasonics, 56, 409-416.
164. Ng, C. T., Veidt, M., Rose, L. F., & Wang, C. H. (2012). Analytical and finite element prediction of Lamb wave scattering at delaminations in quasi-isotropic composite laminates. Journal of Sound and Vibration, 331(22), 4870-4883.
165. Ramadas, C., Balasubramaniam, K., Joshi, M., & Krishnamurthy, C. V. (2010). Interaction of guided Lamb waves with an asymmetrically located delamination in a laminated composite plate. Smart Materials and Structures, 19(6), 065009.
166. Ng, C. T., & Veidt, M. (2011). Scattering of the fundamental anti-symmetric Lamb wave at delaminations in composite laminates. The Journal of the Acoustical Society of America, 129(3), 1288-1296.
167. Pudipeddi, G. T., Ng, C. T., & Kotousov, A. (2019). Mode conversion and scattering of Lamb waves at delaminations in composite laminates. Journal of Aerospace Engineering, 32(5), 04019067.
168. Ramadas, C., Balasubramaniam, K., Hood, A., Joshi, M., & Krishnamurthy, C. V. (2011). Modelling of attenuation of Lamb waves using Rayleigh damping: Numerical and experimental studies. Composite Structures, 93(8), 2020-2025.
169. Patra, S., Ahmed, H., Saadatzi, M., & Banerjee, S. (2019). Evidence of dissipative and growing nonlinearity in Lamb waves due to stress-relaxation and material degradation in composites. Ultrasonics, 96, 224-231.
170. Soleimanpour, R., & Ng, C. T. (2022). Scattering analysis of nonlinear Lamb waves at delaminations in composite laminates. Journal of Vibration and Control, 28(11-12), 1311-1323.
171. Devillers, D., Taillade, F., Osmont, D., Balageas, D., & Royer, D. (2002). Interaction of Lamb waves with defects in composite sandwich structures. OFFICE NATIONAL D ETUDES ET DE RECHERCHES AEROSPATIALES ONERA-PUBLICATIONS-TP, (172).

172. Draudviliene, L., Aider, H. A., Tumsys, O., & Mazeika, L. (2018). The Lamb waves phase velocity dispersion evaluation using an hybrid measurement technique. Composite Structures, 184, 1156-1164.
173. Ono, K., & Gallego, A. (2012). Attenuation of Lamb Waves in CFRP Plates. Journal of Acoustic emission, 30.
174. Chiu, W. K., Rose, L. F., & Nadarajah, N. (2017). Scattering of the fundamental anti-symmetric Lamb wave by a mid-plane edge delamination in a fiber-composite laminate. Procedia Engineering, 188, 317-324.
175. Duflo, H., Morvan, B., & Izbicki, J. L. (2007). Interaction of Lamb waves on bonded composite plates with defects. Composite structures, 79(2), 229-233.
176. Ramadas, C. (2014). Three-dimensional modeling of Lamb wave attenuation due to material and geometry in composite laminates. Journal of Reinforced Plastics and Composites, 33(9), 824-835.
177. Veidt, M., & Ng, C. T. (2011). Influence of stacking sequence on scattering characteristics of the fundamental anti-symmetric Lamb wave at through holes in composite laminates. The Journal of the Acoustical Society of America, 129(3), 1280-1287.
178. Park, H. W., Sohn, H., Law, K. H., & Farrar, C. R. (2007). Time reversal active sensing for health monitoring of a composite plate. Journal of Sound and Vibration, 302(1-2), 50-66.
179. Philibert, M., Yao, K., Gresil, M., & Soutis, C. (2022). Lamb waves-based technologies for structural health monitoring of composite structures for aircraft applications. European Journal of Materials, 2(1), 436-474.
180. Carboni, M., Gianneo, A., & Giglio, M. (2015). A Lamb waves based statistical approach to structural health monitoring of carbon fibre reinforced polymer composites. Ultrasonics, 60, 51-64.
181. Diaz Valdes, S. H., & Soutis, C. (2000). Health monitoring of composites using Lamb waves generated by piezoelectric devices. Plastics, Rubber and Composites, 29(9), 475-481.
182. Cardoni, M., Gianneo, A., & Giglio, M. (2014). A low frequency lamb-waves based structural health monitoring of an aeronautical carbon fiber reinforced polymer composite. Journal of Acoustic Emission, 32, 1.
183. Balasubramaniam, K. (2014). Lamb-wave-based structural health monitoring technique for inaccessible regions in complex composite structures. Structural Control & Health Monitoring, 21(5).
184. Gorgin, R., Luo, Y., & Wu, Z. (2020). Environmental and operational conditions effects on Lamb wave based structural health monitoring systems: A review. Ultrasonics, 105, 106114.
185. Rajagopalan, J., Balasubramaniam, K., & Krishnamurthy, C. V. (2006). A phase reconstruction algorithm for Lamb wave based structural health

monitoring of anisotropic multilayered composite plates. The Journal of the Acoustical Society of America, 119(2), 872-878.

186. Zeng, L., Lin, J., & Huang, L. (2017). A modified Lamb wave time-reversal method for health monitoring of composite structures. Sensors, 17(5), 955.
187. Yang, B., Xuan, F. Z., Xiang, Y., Li, D., Zhu, W., Tang, X., ... & Luo, C. (2017). Lamb wave-based structural health monitoring on composite bolted joints under tensile load. Materials, 10(6), 652.
188. Gangadharan, R., Murthy, C. R. L., Gopalakrishnan, S., & Bhat, M. R. (2011). Time Reversal Health Monitoring of Composite Plates using Lamb waves. International Journal of Aerospace Innovations, 3(3).
189. Sekhar, B. S., Balasubramaniam, K., & Krishnamurthy, C. V. (2006). Structural health monitoring of fiber-reinforced composite plates for low-velocity impact damage using ultrasonic Lamb wave tomography. Structural Health Monitoring, 5(3), 243-253.
190. Schubert, K. J., Brauner, C., & Herrmann, A. S. (2014). Non-damage-related influences on Lamb wave–based structural health monitoring of carbon fiber–reinforced plastic structures. Structural Health Monitoring, 13(2), 158-176.
191. Zhao, J., Ji, H., & Qiu, J. (2014). Modeling of Lamb waves in composites using new third-order plate theories. Smart materials and structures, 23(4), 045017.
192. Zhao, J., Qiu, J., Ji, H., & Hu, N. (2013). Four vectors of Lamb waves in composites: Semianalysis and numerical simulation. Journal of Intelligent Material Systems and Structures, 24(16), 1985-1994.
193. Moulin, E., Assaad, J., Delebarre, C., & Osmont, D. (2000). Modeling of Lamb waves generated by integrated transducers in composite plates using a coupled finite element–normal modes expansion method. The Journal of the Acoustical Society of America, 107(1), 87-94.
194. Pysarenko A.N. Application of wavelet transforms for inhomogeneous structures. Monograph. Odesa. 2024, 134 p.
195. Veidt, M., Liu, T., & Kitipornchai, S. (2002). Modelling of Lamb waves in composite laminated plates excited by interdigital transducers. Ndt&E International, 35(7), 437-447.
196. Hong, M., Mao, Z., Todd, M. D., & Su, Z. (2017). Uncertainty quantification for acoustic nonlinearity parameter in Lamb wave-based prediction of barely visible impact damage in composites. Mechanical Systems and Signal Processing, 82, 448-460.
197. Kulkarni, G., & Mitra, M. (2012). Simulation of time reversibility of Lamb wave in symmetric composite laminate. International journal of mechanical sciences, 54(1), 277-286.

198. Schmidt, D., Sinapius, M., & Wierach, P. (2013). Design of mode selective actuators for Lamb wave excitation in composite plates. CEAS Aeronautical Journal, 4, 105-112.
199. Xu, C., Yang, Z., Zuo, H., & Deng, M. (2021). Minimum variance Lamb wave imaging based on weighted sparse decomposition coefficients in quasi-isotropic composite laminates. Composite Structures, 275, 114432.
200. Willberg, C., Koch, S., Mook, G., Pohl, J., & Gabbert, U. (2012). Continuous mode conversion of Lamb waves in CFRP plates. Smart Materials and Structures, 21(7), 075022.
201. Mahfoud, E., & Harb, M. (2023). Numerical lamb wave modeling and analysis for cure cycle shortening of carbon fiber composites. Journal of Composite Materials, 57(9), 1683-1703.
202. Lin, C. M., Chen, Y. Y., & Pisano, A. P. (2010). Theoretical investigation of Lamb wave characteristics in AlN/3C–SiC composite membranes. Applied Physics Letters, 97(19): 193506 - 193506-3.

INDEX

Наукове видання
Scientific publication

Писаренко О.М.
Pysarenko O.M.

LAMB WAVE-BASED TECHNIQUES
FOR NONDESTRUCTIVE MONITORING I
N LAYERED COMPOSITES

Монографія
Monograph

(англійською мовою)
(in English)

Signed for printing on 04/24/2025
Format 60×84/16 Offca paper Times Font
Digital printing. Conditiona printing sheets 9.65.
Circulation 50 copies. Order No. 25-3

Publisher and manufacturer:
Odesa State Academy of Civil Engineering and Architecture
Certificate No. 4515 dated 04/01/2013
Ukraine, 65029, Odesa, 4, Didrikhson St.
tel.: (048) 729-85-34, e-mail: rio@odaba.edu.ua

Printed in the author’s edition from a ready-made original layout
In the editorial and publishing department of OSACEA

Підписано до друку 24.04.2025 р.
Формат 60×84/16 Папір офісний Гарнітура Times
Цифровий друк. Ум. -друк. арк.9,65
Наклад 50 прим. Зам. № 25-3

Видавець і виготовлювач:
Одеська державна академія будівництва та архітектури
Свідоцтво ДК № 4515 від 01.04.2023 р.
Україна, 65029б м. Одеса, вул Дідрихсона, 4
Тел.: (048) 729-85-34, e-mail: rio@odaba.edu.ua

Надруковано в авторській редакції з готового орігінал-макету
В редакційно-видавничому відділі ОДАБА